



저작자표시-비영리-변경금지 2.0 대한민국

이용자는 아래의 조건을 따르는 경우에 한하여 자유롭게

- 이 저작물을 복제, 배포, 전송, 전시, 공연 및 방송할 수 있습니다.

다음과 같은 조건을 따라야 합니다:



저작자표시. 귀하는 원저작자를 표시하여야 합니다.



비영리. 귀하는 이 저작물을 영리 목적으로 이용할 수 없습니다.



변경금지. 귀하는 이 저작물을 개작, 변형 또는 가공할 수 없습니다.

- 귀하는, 이 저작물의 재이용이나 배포의 경우, 이 저작물에 적용된 이용허락조건을 명확하게 나타내어야 합니다.
- 저작권자로부터 별도의 허가를 받으면 이러한 조건들은 적용되지 않습니다.

저작권법에 따른 이용자의 권리는 위의 내용에 의하여 영향을 받지 않습니다.

이것은 [이용허락규약\(Legal Code\)](#)을 이해하기 쉽게 요약한 것입니다.

[Disclaimer](#)

**Ph.D. DISSERTATION**

**Anchoring Plasmonic Octahedral Au  
Nanoparticles for Solar Water Splitting  
Application**

**Cheon Woo Moon**

**February 2018**

**SEOUL NATIONAL UNIVERSITY  
COLLEGE OF ENGINEERING  
DEPARTMENT OF MATERIALS SCIENCE AND  
ENGINEERING**

# **Anchoring Plasmonic Octahedral Au Nanoparticles for Solar Water Splitting Application**

Advisor: Prof. Ho Won Jang

by

Cheon Woo Moon

A thesis submitted to the Graduate Faculty of Seoul National University

in partial fulfillment of the requirements for the

Degree of Doctor of Philosophy

Department of Materials Science and Engineering

February 2018

Approved

By

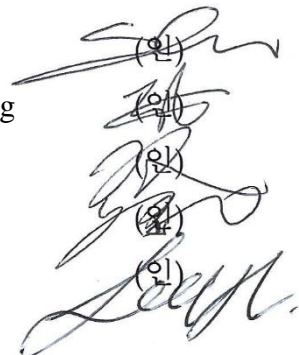
Chairman of Advisory Committee: Seungwu Han

Vice-chairman of Advisory Committee: Ho Won Jang

Advisory Committee: Jin Young Kim

Advisory Committee: Soo Young Kim

Advisory Committee: Chul-Ho Lee



(인)  
(인)  
(인)  
(인)  
(인)

## Abstract

---

Due to their localized surface plasmon resonances in visible spectrum, noble metal nanostructures have been considered for improving the photoactivity of wide bandgap semiconductors. Improved photoactivity is attributed to localized surface plasmon relaxations such as direct electron injection and resonant energy transfer. However, the details on the plasmonic solar water splitting through near electromagnetic field enhancement have not been fully understood. The performance of plasmonic Au nanostructure/metal oxide heterointerface shows great promise in enhancing photoactivity, due to its ability to confine light to the small volume inside the semiconductor and modify the interfacial electronic band structure. Therefore, the shape control of Au nanoparticles (NPs) is crucial for moderate band gap semiconductors, because plasmonic resonance by interband excitations or intraband excitations overlaps above or below the absorption edge of semiconductors,

This thesis presents about plasmon enhanced photoelectrochemical water splitting, based on semiconductor photoanode in three main chapters. The first chapter focus on a plasmon enhanced photoelectrochemical water splitting for band-edge non-straddle semiconductor (mainly  $\text{TiO}_2$ ) by deprotonation method. The second chapter focus on a plasmon enhanced photoelectrochemical water splitting for band-edge straddle semiconductor (mainly  $\text{BiVO}_4$ ). The last chapter includes the high-coverage octahedral Au nanoparticle decoration method from ligand exchange via phase transfer. The high-coverage octahedral Au nanoparticle decorated  $\text{BiVO}_4$  film overcome theoretical efficiency.

At the first, I report that shape-controlled gold nanoparticles on wide bandgap semiconductors improve the water-splitting photoactivity of the semiconductors with over-bandgap photon energies compared to sub-bandgap photon energies. It is revealed that hot hole injection into the oxygen evolution reaction potential is the rate-limiting step in plasmonic solar water splitting. The proposed concept of photooxidation catalysts derived from an ensemble of gold nanoparticles having sharp vertices is applicable to various photocatalytic semiconductors and provides a theoretical framework to explore new efficient plasmonic photoelectrodes.

At the second, I firstly study the plasmonic effects of shape-controlled Au NPs on bismuth vanadate ( $\text{BiVO}_4$ ), and report a largely enhanced photoactivity of  $\text{BiVO}_4$  by introducing the octahedral Au NPs. The octahedral Au NPs/ $\text{BiVO}_4$  achieves  $2.4 \text{ mA/cm}^2$  at the  $1.23 \text{ V}$  vs. reversible hydrogen electrode, which is the 3-fold enhancement compared to  $\text{BiVO}_4$ . It is the highest value among the previously reported plasmonic Au NPs/ $\text{BiVO}_4$ . Improved photoactivity is attributed to the localized surface plasmon resonance; direct electron transfer (DET), plasmonic resonant energy transfer (PRET). The PRET can be stressed over DET when considering the moderate band gap semiconductor. Enhanced water oxidation induced by the shape-controlled Au NPs is applicable to moderate semiconductors, and shows a systematic study to explore new efficient plasmonic solar water splitting cells.

At the last, the essential benefit of introducing gold nanoparticles is an enhanced light energy conversion by generating plasmon. The plasmon decay

induces various phenomena such as heat generation, near-field enhancement, hot electron injection, and resonance energy transfer. Shape-controlled octahedral gold nanoparticles having sharp vertices can maximize the efficiency of these processes. For practical plasmonic gold nanoparticle engineering, a high-coverage decoration method of octahedral gold nanoparticles comparable to physical vapor deposition on a semiconductor nanostructure is indispensable. However, the ligand exchange reaction to attach octahedral gold nanoparticles is limited in aqueous solution due to the inactivity of gold (111) surface by densely-packed cetyltrimethylammonium bilayer structure. Here, we report a controllable high coverage surface decoration method of octahedral gold nanoparticles on the targeted semiconductor nanostructures. The thiolated polyethylene glycol adsorption in gold (111) surface is achieved via phase transfer by ethanol-dichloromethane medium. In the application of solar water splitting, a high-coverage decoration of BiVO<sub>4</sub> film resulted over the theoretical photocurrent. I expect that our results deliver an innovative platform for future plasmonic gold nanoparticle applications.

**Keywords:** Solar water splitting, Plasmon, Localized surface plasmon, Plasmon enhanced solar water splitting, Octahedral gold nanoparticles, Catalytic hole transfer, Hot electron injection, Resonant electron transfer, PEGylation, Thiolated PEG, (111) facet, Ligand exchange, FDTD simulation

**Student Number:** 2012-23142

CHEON WOO MOON

# Table of Contents

---

Abstract .....	i
Table of Contents.....	iv
List of Tables.....	x
List of Figures .....	xi
Chapter 1 .....	1
Emergence of Golden Age with Gold Nanoparticles.....	1
<b>1.1. Introduction</b> .....	2
<b>1.1.1 Lycurgus Cup (Roman era)</b> .....	4
<b>1.1.2 Stained Glass (Medieval era)</b> .....	7
<b>1.1.3 Michel Faraday’s Discovery (Early-modern era)</b> .....	9
<b>1.2. Modern Era</b> .....	11
<b>1.2.1 Finite-difference Time-domain (FDTD) Method</b> .....	12
<b>1.2.2 Local Field Enhancement Calculation by FDTD</b> .....	16
<b>1.2.3 Various Shape of Gold Nanoparticles</b> .....	17
Chapter 2.....	19
Synthesis and Characterization of Gold Nanoparticles.....	19
<b>2.1. Gold Nanoparticle Synthesis with Citrate Reduction</b> .....	20
<b>2.1.1 Turkevich Method</b> .....	20
<b>2.1.2 Frens Method</b> .....	20
<b>2.1.3 pH Dependence</b> .....	21
<b>2.1.4 Consecutive Ostwald Ripening</b> .....	23
<b>2.1.5 Growth Mechanism</b> .....	26
<b>2.2. Seed-mediated Growth Method</b> .....	27
<b>2.2.1 Electrochemical Synthesis</b> .....	27
<b>2.2.2 Seed-Mediated Synthesis</b> .....	28
<b>2.3 Seedless Growth Method</b> .....	29
<b>2.4 Shape-Controlled Gold Nanoparticles via Seed-Mediated Growth Method</b> .....	32

2.4.1	<b>Magic Numbers</b> .....	32
2.4.2	<b>Understanding of Anisotropic Growth by LaMer Model</b> .....	33
2.4.3	<b>Unit Stereographic Triangle of Gold Nanoparticles</b> ..	34
2.4.4	<b>Surface Energy</b> .....	35
2.4.5	<b>Shape of Seeds</b> .....	37
2.4.6	<b>Effect of the Halide Ions.</b> .....	38
2.4.7	<b>Effect of the Ascorbic Acid Concentration.</b> .....	41
2.4.8	<b>Effect of the CTAB concentration.</b> .....	42
2.5	<b>Capping Layer of Gold Nanoparticles</b> .....	44
2.5.1	<b>Zeta Potential</b> .....	44
2.5.2	<b>Capping layer in Gold Nanoparticles</b> .....	46
2.5.3	<b>Linker Molecule (Gold Surface Absorber)</b> .....	48
2.5.4	<b>Linker Molecule (Semiconductor Surface Absorber)</b>	49
2.5.5	<b>Molecules for the Gold Nanoparticle Attachment</b> .....	49
2.6	<b>Synthesis of Quasi-Spherical Gold Nanoparticles</b> .....	50
2.7	<b>Synthesis of Octahedral Gold Nanoparticles</b> .....	51
2.7.1	<b>Synthesis of CTAC-capped Au seeds</b> .....	51
2.7.2	<b>Growth of octahedral Au nanoparticles</b> .....	51
2.8	<b>Characterization of Gold Nanoparticles.</b> .....	52
2.9	<b>Attachment of Gold Nanoparticles.</b> .....	54
<b>Chapter 3</b> .....		56
<b>Gold for Plasmon Resonance</b> .....		56
3.1.	<b>Wood's Anomalies</b> .....	57
3.1.1	<b>Anomalous Diffraction Gratings</b> .....	57
3.1.2	<b>Fano Type Resonance in Metal Gratings</b> .....	59
3.2.	<b>Dielectric Function in a Metal</b> .....	62
3.3.	<b>Maxwell's Equations</b> .....	65
3.4.	<b>Electromagnetic Response in Bulk Metal (Volume Plasmon Polariton)</b> .....	67

<b>3.5. Electromagnetic Response in Metal-Dielectric Interfaces (Surface Plasmon Polariton)</b> .....	76
<b>3.6. Electromagnetic Response in Confined Metal-Dielectric Interfaces (Localized Surface Plasmon)</b> .....	88
<b>3.7. Graphical Summary of Plasmon Resonance in Gold</b> .....	92
<b>3.8. Candidate Materials for Localized Surface Plasmon Resonances</b> .....	94
<b>3.9. Modulations of Extinction Spectra</b> .....	96
<b>Chapter 4</b> .....	99
<b>Photoelectrochemical Water Splitting</b> .....	99
<b>4.1. Introduction</b> .....	100
<b>4.1.1 Configurations</b> .....	100
<b>4.1.2 The Potentiostat</b> .....	103
<b>4.1.3 Reference Electrodes</b> .....	104
<b>4.1.4 Conversion of Potentials</b> .....	106
<b>4.1.5 AM 1.5 G Standard</b> .....	109
<b>4.2. Principles of Solar Water Splitting</b> .....	111
<b>4.2.1 Semiconductor-Liquid Junction</b> .....	112
<b>4.2.2 Electrical Double Layer Structures</b> .....	114
<b>4.2.3 Band Structure of Photoelectrochemical Water Splitting with n-type Photoanode</b> .....	115
<b>4.3. Candidate Materials for Solar Water Splitting</b> .....	120
<b>4.3.1 Considering Band-Edge Positions</b> .....	120
<b>4.3.2 Corrosion Level</b> .....	122
<b>4.3.3 Pourbaix Diagram</b> .....	123
<b>4.5. Polarization of Photoelectrode</b> .....	130
<b>4.5.1 Photoexcitation</b> .....	130
<b>4.5.2 Thermodynamic Consideration</b> .....	132
<b>4.5.3 Polarization Curve (<i>I-V</i>)</b> .....	132
<b>4.5.4 Light illumination directions</b> .....	135
<b>4.6. Determination of Flat Band Potential</b> .....	136

4.7. Marcus Theory.....	138
4.8. Shockley and Queisser (SQ) Limit.....	141
<b>Chapter 5.....</b>	<b>145</b>
<b>Enlightening Solar Water Splitting with Plasmonic Gold Nanoparticles .....</b>	<b>145</b>
5.1. Plasmon Relaxation Process .....	146
5.1.1 Spontaneous and Stimulated Emission .....	146
5.1.2 Radiative decay.....	148
5.1.3 Non-Radiative Decay (Landau Damping).....	148
5.1.4 Resonant Energy Transfer .....	149
5.1.5 Modeling.....	150
5.1.6 Summary of the Plasmon Relaxation .....	151
5.2. Plasmon Induced Charge Generation .....	152
5.3. Excitation of Semiconductor by Localized Surface Plasmon Resonance of Gold Nanoparticles .....	154
5.4.1 Photoactivity Enhancement from Light Intensity ....	158
5.4.2 Transient Negative Ion (TNI) States.....	160
5.5. Exceeding Theoretical Efficiency (SQ Limit) .....	161
5.6. Band Transitions in Conduction Band .....	163
5.7. Utilization of Conduction Band Electrons in Au 5d Orbital .....	166
5.8. Photocurrent Degradations in Plasmonic Photoanode .....	170
5.8.1 Photocurrent Degradation on Au-TiO <sub>2</sub> .....	170
5.8.2 Photocurrent Degradation on Au-Fe <sub>2</sub> O <sub>3</sub> .....	172
<b>Chapter 6.....</b>	<b>174</b>
<b>Plasmonic Octahedral Gold Nanoparticles of Maximized Near Electromagnetic Fields for Enhancing Catalytic Hole Transfer in Solar Water Splitting .....</b>	<b>174</b>
6.1. Motivation .....	175
6.2. Introduction .....	175
6.3. Benefit of Au Interband Transition for Solar Water Splitting .....	178

6.4. Optimization of Shape (Near Field Enhancements).....	181
6.5. Gold Nanoparticle Decorated TiO <sub>2</sub> Films .....	186
6.7. Photocurrent Action Spectra.....	192
6.8. Wavelength Dependence of Photoactivity .....	197
6.9. Impedance Analysis.....	201
6.10. Qualitative Modeling of Plasmon Enhanced Solar Water Splitting .....	203
6.11. Detection of Oxygen Evolution Reaction with Gold Nanoparticle Decorated TiO <sub>2</sub> Nanorod .....	205
6.12. Conclusion .....	208
6.13. Experimental Characterizations .....	208
<b>Chapter 7</b> .....	<b>211</b>
<b>Dominance of Plasmonic Resonant Energy Transfer over Direct Electron Transfer in Substantially Enhanced Water Oxidation Activity of BiVO<sub>4</sub> by Shape-Controlled Au Nanoparticles</b> .....	<b>211</b>
7.1. Motivation .....	212
7.2. Introduction .....	215
7.3. Near-Field Enhancements.....	220
7.4. Gold Nanoparticle Decorated BiVO <sub>4</sub> Films .....	224
7.6. Coverage Control of Octahedral Gold Nanoparticles in BiVO <sub>4</sub> /FTO film.....	231
7.7. Stability Test .....	239
7.8. Photoactivity .....	240
7.9. Energy Band Diagram for Plasmon Enhanced Solar Water Splitting in BiVO <sub>4</sub> .....	244
7.10. Conclusion .....	248
7.11. Experimental Characterizations .....	249
<b>Chapter 8</b> .....	<b>254</b>
<b>Siege of Metal Oxide Surface with {111} form Au Nanoparticles Using PEGylation</b> .....	<b>254</b>
8.1. Motivation .....	255
8.2. Introduction .....	255

<b>8.2. Near-Field Enhancements</b> .....	261
<b>8.3. Agglomeration of Gold Nanoparticles</b> .....	263
<b>8.5. Gold Nanoparticle Attachment by phase Transfer</b> .....	268
<b>8.6. Raman Spectra Analysis</b> .....	271
<b>8.7. FT-IR Spectra Analysis</b> .....	275
<b>8.8. Attachment Mechanism</b> .....	277
<b>8.9. Exceeding the Theoretical SQ Limit</b> .....	279
<b>8.10. Conclusion</b> .....	280
<b>8.11. Experimental Details</b> .....	281
<b>Chapter 9 Summary</b> .....	285
<b>References</b> .....	289
<b>Closing Remarks</b> .....	307
<b>Acknowledgments</b> .....	308
<b>List of Publications</b> .....	310
<b>Curriculum vitae</b> .....	320

## List of Tables

---

Table 1. Chemical composition of the Lycurgus Cup. ....	6
Table 2. Definition for the Air Mass (AM) global illumination.....	110
Table 3. Field enhancement of hemispherical Au NPs and octahedral Au NPs under 350 nm, 430 nm and 550 nm. ....	219
Table 4. Circuit analysis of the EIS spectra for various octahedral Au NPs/BiVO <sub>4</sub> photoelectrodes. ....	234
Table 5. Vibrational activity of the CTA <sup>+</sup> molecule in Au NPs solution. .	269

## List of Figures

---

Figure 1. Fragment of diatretum in reflected (a) and transmitted (b) light. ....	4
Figure 2. Image of Lycurgus Cup from Roman era for reflected (left) and transmitted (right) light. ....	5
Figure 3. Transmission electron microscopy image of nanoparticles incorporated in Lycurgus Cup (Left, NaCl; Right, $\text{Ag}_{0.7}/\text{Au}_{0.3}$ ). ....	6
Figure 4. Reenacted glass in Lycurgus Cup in reflected (a) and transmitted (b) light. ....	7
Figure 5. Stained glass in Troyes Cathedral, France (17th century). ....	7
Figure 6. Stained glass in United Presbyterian Church of Morning Sun, Iowa. ....	8
Figure 7. The origin of colored stained glass in Medieval era. ....	9
Figure 8. Michel Faraday's colloidal gold solution. ....	10
Figure 9. Light pass through solution (left) and colloid (right). ....	11
Figure 10. Representation of Yee's cell in a specific position (m, n, p). ....	13
Figure 11. Electric/magnetic field nodes in a space-time. ....	14
Figure 12. Yee's cell and boundary condition in FDTD method. ....	15
Figure 13. Shape-controlled gold nanoparticles. <sup>9</sup> ....	17
Figure 14. Tunable color of gold nanoparticle solution. ....	18
Figure 15. Electron microscope image of size controlled gold by Frens (1973). ....	21
Figure 16. pH variation for the ratio of salts. Dominating species related with the reaction is shown as red. <sup>13</sup> ....	22
Figure 17. Two reaction pathways for the synthesis of gold nanoparticles by citrate reduction. <sup>13</sup> ....	23
Figure 18. LaMer model of Nucleation and Growth. ....	24
Figure 19. Growth of monodisperse gold nanoparticles by seeded-growth. ....	25
Figure 20. Schematic of configuration. ....	26
Figure 21. Deduced gold nanoparticle formation process by citrate reduction method. ....	27
Figure 22. TEM images of gold nanorods synthesized by the electrochemical method with CTAB. ....	28
Figure 23. Shape of gold nanoparticles via seeded growth method using CTAB. ....	29
Figure 24. Micelle template induced nanoparticle synthesis by seedless growth. ....	30

Figure 25. Monodisperse gold nanoparticles synthesized by seedless growth technique. ....	31
Figure 26. TEM images of gold nanorods synthesized by seedless method. ....	31
Figure 27. Various shape controlled gold nanoparticles with seedless growth technique. ....	32
Figure 28 Full-shell magic number formation. ....	33
Figure 29. LaMer model for monodisperse particle formation and seed-mediated growth particle formation. ....	34
Figure 30. Unit stereographic triangle showing crystal structure have single atomic facet. ....	35
Figure 31. Variations of surface energy according to the facets and metals: trisoctahedron (TOH), trapezohedron (TPH), rhombic dodecahedron (RD), tetrahexahedron (THH), and cube. <sup>26</sup> .....	36
Figure 32 (a) Exchange current density for platinum electrode according to the facet. (b) Reduction of 4-nitroaniline according to the facet. ....	37
Figure 33. The schematic illustration of the reaction pathways of anisotropic gold nanoparticles. <sup>28</sup> .....	38
Figure 34. CTAB/C distribution on gold surface by molecular simulations. ....	39
Figure 35. Chloride containing surfactant results in (720) facets and bromide containing surfactant results in (730) facet. ....	40
Figure 36. Formation of Au nanoplatelet via addition of iodide ions. <sup>31</sup> .....	41
Figure 37. Polyhedral gold nanoparticles according to the rate or reduction. <sup>32</sup> .....	42
Figure 38. Polyhedral gold nanoparticles according to the rate or reduction. <sup>33</sup> .....	42
Figure 39. Morphology evolution of gold nanoparticles with a function of CTAB and ascorbic acid. ....	43
Figure 40 Graphical representation of zeta potential. ....	44
Figure 41. The difference of zeta potential of gold nanoparticles (in form of depletion interaction potential) with shape. <sup>35</sup> .....	45
Figure 42 Capping layer structure in gold nanoparticles. ....	46
Figure 43. Amphiphilic structure of CTAB molecule. ....	47
Figure 44. Graphical representation of CTAC bilayer structure (CTAB is also similar). ....	47
Figure 45. Functionalized group for surface absorber. ....	48
Figure 46. Surface absorption structure of the molecule having oxygen in function group. ....	49

Figure 47. Structure of 3-mercaptopropionic acid.....	50
Figure 48. The SEM-TEM image of quasi-spherical and octahedral gold nanoparticles.....	53
Figure 49 (a) Diameter (for quasi-spherical) and edge length (for octahedral) distribution of Au NPs (please note that the diameter of a circumscribing sphere of octahedron is $\sqrt{2}$ times greater than edge length). (b) Normalized absorbance of synthesized solutions containing Au NPs. Dotted line (...) indicates corresponding absorbance on TiO <sub>2</sub> film. ....	53
Figure 50. Schematic representation of the process. ....	55
Figure 51. Example of He-Ne laser induced diffraction grating pattern. ....	57
Figure 52. Spectra of a continuous light source by metal grating. ....	58
Figure 53. Lorentzian (a) and Fano (b) resonance model.....	60
Figure 54 Explanation of the meaning of the Fano formula. ....	60
Figure 55 Fano resonances in a metallic photonic crystal, consisting of a gold nanowire grating on a single-mode indium tin oxide (ITO) slab waveguide, in which the light is incident normal to the structure. a, Extinction in TE polarization (E-field parallel to the gold wires). A single Fano resonance owing to grating coupling into the waveguide is visible. b, Extinction in TM polarization (E-field perpendicular to the wires). Two polariton branches that exhibit a Fano lineshape owing to the coupling of the narrow waveguide resonance to the broad particle plasmon in the gold wires are visible. <sup>48</sup> .....	61
Figure 56. Energy (frequency) dependent real and imaginary components of the dielectric function for an Drude metal. ....	73
Figure 57. Dispersion relationship of bulk metal in Drude model .....	76
Figure 58 (a) Wave propagation at a dielectric-metal interface and, (b) geometry of the system.....	77
Figure 59 (a) Transverse magnetic wave propagation. (b) Transverse electric wave propagation.....	78
Figure 60 Dispersion relation of surface plasmon polariton in metal-dielectric interface. True line (—) indicates dispersion relation at air and dotted line (--) indicates dispersion relation at dielectric medium. ....	85
Figure 61 Scattering mechanisms according the particle size.....	89
Figure 62 Dielectric function of nanostructured metal sphere (localized surface plasmon).....	91
Figure 63 Graphical representation of resonance for summary of three plasmon modes. ....	92

Figure 64 FDTD calculation of electric field around a single metal groove.....	93
Figure 65 Dark field image of plasmonic nanoparticles.....	93
Figure 66 Optical extinction of metals and conducting oxide by LSPR. ....	95
Figure 67 Extinction spectra of metal nanoparticles according to their size.....	96
Figure 68. Glutathione-protected gold clusters exhibit size-dependent excited state and electron transfer properties. ....	97
Figure 69 (a) Simulated dielectric constant (refractive index) dependence. (b) Resonance change upon metal nanostructure displacement with substrate.....	98
Figure 70. 2-electrode configuration of electrode. ....	100
Figure 71. 3-electrode configuration of electrode. ....	101
Figure 72. 3-electrode configuration with Ruggin capillary. ....	102
Figure 73. The simplified diagram of a potentiostat. ....	104
Figure 74. AM 1.5 G (global) spectra. ....	109
Figure 75. Explanation of Air Mass (AM) standard on Earth. ....	110
Figure 76 Semiconductor-liquid junction.....	112
Figure 77 Electrical double layer structure suggested in history.....	114
Figure 78. Band structure of photoanode with the illumination.....	116
Figure 79. Water splitting potential including overpotential according to a pH. ....	119
Figure 80. Possibility of water splitting reaction related to the band edge positions.....	121
Figure 81. Explanation of a photocorrosion possibility from the semiconductor photoelectrode.....	122
Figure 82. Pourbaix diagram of hematite. ....	123
Figure 83. Two pinning condition under positive bias. Band edge pinning (left) and Fermi level pinning (right) is depicted. ....	125
Figure 84.n-type semiconductor with Fermi level pinning. (a) Electrode at $V_{FB}$ . (b) Weak anodic bias empties the surface state but band bending does not occur. (c) High anodic bias initiates the band bending of semiconductor. <sup>65</sup> .....	126
Figure 85. The photovoltage behavior according to the pinning conditions. ....	127
Figure 86. Semiconductors do/do not exhibit Fermi level pinning. ...	128
Figure 87. n-type Semiconductor illumination with bias for two pinning conditions. ....	128

Figure 88. p-type Semiconductor illumination with bias for two pinning conditions. ....	129
Figure 89. Excitation of carrier by external electrochemical potential. The electrochemical potential is achieved from the light (semiconductor) and bias (metal). ....	130
Figure 90. Photovoltage benchmarks. ....	131
Figure 91. Polarization curve of photoanode. ....	133
Figure 92. Reaction coordinate of water splitting. ....	138
Figure 93. Interfacial electron transfer model by Marcus theory. ....	140
Figure 94. Theoretical efficiency limit in p-n junction solar cells. ....	142
Figure 95. Dependence of the theoretical maximum solar-to-hydrogen efficiency and photocurrent density according to the bandgap in AM 1.5 G illumination. <sup>60</sup> .....	143
Figure 96. Theoretical efficiency of photoelectrochemical water splitting. ....	144
Figure 97. Schematic of photon emission mechanisms.....	146
Figure 98. Schematic of phonon emission mechanism. ....	147
Figure 99. The incident light is grazed, and the emitted photon is collected normal to the surface. ....	147
Figure 100. Plasmon relaxation via non-radiative decay. ....	149
Figure 101. Phenomological plasmonic model. <sup>78</sup> .....	150
Figure 102. Density matrix model. <sup>79</sup> .....	151
Figure 103. Plasmon relaxation process. ....	151
Figure 104. Plasmon induced charge generation process. ....	152
Figure 105. Band diagram for a n-type semiconductor-liquid junction. ....	155
Figure 106. Band diagram for a n-type semiconductor-metal-liquid junction. ....	155
Figure 107. Possible band alignments of semiconductor-metal junction. ....	156
Figure 108. Preferred carrier move direction upon contact and illumination.....	156
Figure 109. Excitation states of plasmonic metal nanoparticles and semiconductor junction. ....	157
Figure 110. Photocatalytic activity enhanement from light intensity modulation.....	159
Figure 111. Absorption of transient negative ions on plasmonic metal nanoparticle (mechanism of plasmon photocatalysis).....	160
Figure 112. Optical absorption spectra of semiconductor.....	161
Figure 113. Plasmon induced absorption enhancement. <sup>79</sup> .....	162

Figure 114. The theoretical efficiency (SQ limit) and plasmon induced efficiency enhancement. ....	163
Figure 115. Bandstructure of gold <sup>78</sup> and corresponding electron transitions (interband and interband). <sup>89</sup> .....	164
Figure 116. Schematic of band transitions in gold. <sup>90</sup> .....	164
Figure 117. Absorption of light in gold according to the band transitions. <sup>52</sup> .....	165
Figure 118. The energy relaxation process from interband transition in gold. <sup>91</sup> .....	165
Figure 119. The effect of 5d to 6sp interband transition in gold nanoparticles. <sup>92</sup> .....	166
Figure 120. Selective oxidation of organic molecules by light irradiation in gold nanoparticle supported composites. ....	167
Figure 121. Synergetic promotion of hydrogen evolution in TiO <sub>2</sub> -gold nanoparticle composites. ....	168
Figure 122. Dual-sided photocatalytic efficiency enhancement control by plasmonic gold nanoparticles for TiO <sub>2</sub> composite. ....	169
Figure 123. Utilization of holes in Au 5d orbital by iridium oxide co-catalysts. ....	170
Figure 124. Photocurrent enhancement and degradation with irradiation of UV and visible light. ....	171
Figure 125. Analysis of IPCE enhancement on Au-TiO <sub>2</sub> composite. ....	171
Figure 126. Photocurrent degradations in over-bandgap region of Fe <sub>2</sub> O <sub>3</sub> with surface configuration of gold nanoparticles. ....	172
Figure 127. (a) Photocurrent enhancement from gold nanoparticles embedded in Fe <sub>2</sub> O <sub>3</sub> film. (b) Photocurrent degradation from gold nanoparticles on the surface of the Fe <sub>2</sub> O <sub>3</sub> nanorod.....	173
Figure 128. Hole reaction model for comprehensive descriptions of photocatalytic activity. Schematic illustration of photocatalytic activity enhancement mechanism in the TiO <sub>2</sub> /Au octahedral system where $\Phi_B$ is reaction potential barrier, $k_{6sp}$ is the hole transfer constant for intraband transition, $k_{5d}$ is the hole transfer constant for interband transition, $h$ is the Flank's constant, $\omega_p$ is localized surface plasmon resonance frequency of Au NPs and $E_g$ is band gap energy of TiO <sub>2</sub> .....	179
Figure 129. Summary of the results of FDTD simulation performed on six representative shapes (semicircle, triangle, circle, cube, hexagon and rhombus).....	181
Figure 130. FDTD simulation results of near field enhancement for various shapes of Au NPs on the TiO <sub>2</sub> flat film in water. (a) Field enhancement under 550 nm photons. (b) Field enhancement under 350	

nm photons (octahedral vertical, octahedral tilt, sphere and hemisphere configurations are shown). .....	182
Figure 131. FDTD simulation results of near field enhancement for various shapes of Au NPs on the TiO <sub>2</sub> flat film in water under 405 nm photons (octahedral vertical, octahedral tilt, sphere and hemisphere configurations are shown). The maximum field enhancements of corresponding shapes were recorded as 3.34, 3.17, 2.59 and 1.7.....	183
Figure 132. FDTD simulation results of near field in the absence of Au NPs. (a) Field enhancement under 550 nm wavelength. (b) Field enhancement under 350 nm wavelength. ....	184
Figure 133. Schematic representation of Au nanoparticle FDTD configurations on TiO <sub>2</sub> thin film in Figure 2a,b is represented. (a) Octahedral Au nanoparticle vertical. (b) Octahedral Au nanoparticle tilt. (c) Sphere Au nanoparticle. (d) Hemisphere Au nanoparticle. ....	185
Figure 134. FDTD simulation results of absorption, scattering and extinction cross section of various Au NP shapes.....	186
Figure 135. (a) SEM image of quasi-spherical Au NPs. (b) SEM image of self-assembled octahedral Au NPs. (c) TEM image of quasi-spherical Au NPs. (d) TEM image of octahedral Au NPs. (e) Diameter (for quasi-spherical) and edge length (for octahedral) distribution of Au NPs (please note that the diameter of a circumscribing sphere of octahedron is $\sqrt{2}$ times greater than edge length). (f) Normalized absorbance of synthesized solutions containing Au NPs. Dotted line (...) indicates corresponding absorbance on TiO <sub>2</sub> film.....	188
Figure 136. (a) TEM image of Au NPs together with a fast Fourier transform (FFT) pattern in selected area. (b) TEM image of octahedral Au NPs. Inset is provided to give readers better recognition of attachment configuration. (c) TEM image of quasi-spherical Au NPs together with a FFT pattern in selected area. (d) TEM image of quasi-spherical Au NPs. ....	189
Figure 137. Cross-section TEM image of as-deposited 80-nm-thick TiO <sub>2</sub> film on silicon. Note that, TiO <sub>2</sub> film was deposited on Si to clearly show the thickness and uniformity. False colors (blue and yellow) were added in TEM image to enhance visibility. ....	190
Figure 138. Schematic representation of deprotonation process.....	191
Figure 139. SEM image of coverage controlled Au NPs above 80-nm-thick TiO <sub>2</sub> film on FTO/Glass substrates. (a) quasi-spherical Au NPs with moderate coverage. (b) quasi-spherical Au NPs with low coverage. (c) Octahedral Au NPs with moderate coverage. (d) Octahedral Au NPs with low coverage. The image is taken after measurement.....	191

Figure 140. Grazing incidence X-ray diffraction (GIXRD) spectra of 80-nm-thick TiO<sub>2</sub> film on FTO/Glass substrate sample annealed at 700 °C.

..... 192

Figure 141. Linear sweep curves for Au attached to fluorine doped tin oxide (FTO)/TiO<sub>2</sub> 80 nm samples over various coverage (low, moderate and high). (a) SEM image of quasi-spherical Au NPs attached to FTO/TiO<sub>2</sub> 80 nm sample with high coverage. (b) Linear sweeps in dark/with photo for various coverage of quasi-spherical Au NPs. (c) SEM image of octahedral Au NPs attached to FTO/TiO<sub>2</sub> 80 nm sample with high coverage. (d) Linear sweeps in dark/with photo for various coverage of octahedral Au NPs. (e) Hemispherical Au NPs from E-beam evaporator (3 nm Au) over FTO/TiO<sub>2</sub> 80 nm sample. (f) Linear sweep in dark/with photo for annealed Au NPs from E-beam evaporator (5.0, 3.0, 1.5 and 0.7 nm Au). In linear sweep data (b), (d) and (f), dashed line (- -) indicates linear sweep data of TiO<sub>2</sub> film without Au NPs, dotted line (...) indicates corresponding dark currents, orange arrow indicates the tendency of current behavior with Au NPs and purple arrow indicates the tendency of onset potential with Au NPs. Schematic of Au NPs configurations on TiO<sub>2</sub> are also drawn as inset in the SEM images... 194

Figure 142. (a) SEM image of annealed e-beam deposited Au NPs (0.7 nm) over FTO / TiO<sub>2</sub> 80 nm sample. (b) SEM image of annealed e-beam deposited Au NPs (1.5 nm) over FTO / TiO<sub>2</sub> 80 nm sample. (c) SEM image of annealed e-beam deposited Au NPs (5.0 nm) over FTO / TiO<sub>2</sub> 80 nm sample. (d) SEM image of e-beam deposited Au NPs (20.0 nm) over FTO / TiO<sub>2</sub> 80 nm sample. .... 195

Figure 143. Linear sweep curves for 20 nm Au thin film 80-nm-thick TiO<sub>2</sub> film on FTO/Glass substrate. The sample does not show effective photocurrent under AM 1.5 G illumination (consider the current gain is almost zero). .... 196

Figure 144. The detailed information about coverage and the number of Au NPs is summarized. .... 197

Figure 145. (a) Photocurrent transient at 1.23 V vs. RHE with monochromatic 10 mW/cm<sup>2</sup> fluence at 532 nm. (b) Photocurrent transient at 1.23 V vs. RHE with monochromatic 10 mW/cm<sup>2</sup> fluence at 405 nm. (c) Photovoltage gains of samples at open circuit potential. (d) IPCE spectra of above mentioned samples at 1.23 V vs. RHE. Moderate coverage of quasi-spherical Au NPs, moderate coverage of octahedral Au NPs and 3.0 nm E-beam evaporated Au on 80-nm-thick TiO<sub>2</sub> samples were used for the measurements. The vertical dotted line (...) indicates

the band gap energy of  $\text{TiO}_2$ . Inset is also shown to clarify the photocurrents in the visible light are within the noise level. .... 199

Figure 146. Photovoltage gain profiles of samples (quasi-spherical Au NPs attached FTO/ $\text{TiO}_2$  80 nm with moderate coverage sample, octahedral Au NPs attached to FTO/ $\text{TiO}_2$  80 nm with moderate coverage sample and annealed e-beam deposited Au NPs (3nm) over FTO/ $\text{TiO}_2$  80 nm sample. (a) Photovoltage gain at OCP with the fluence of  $10 \text{ mW/cm}^2$  at 405 nm. (b) Photovoltage gain at OCP with the fluence of  $10 \text{ mW/cm}^2$  at 532 nm. .... 200

Figure 147. Nyquist plots at 1.23 V vs. RHE under AM 1.5G illumination. Equivalent circuit analyses are summarized in the table where  $R_{dp}$  is the resistance of depletion region in semiconductor,  $CPE_{dp}$  is the capacitance of depletion region in semiconductor,  $R_h$  is the resistance of Helmholtz diffusion layer and  $CPE_h$  is the capacitance of Helmholtz diffusion layer. .... 202

Figure 148. Qualitative diagram of the photocatalytic activity enhancement by shape-controlled Au NPs. The overall enhancement is calculated by subtraction for the activity of Au NPs with high LSPR-EF and activity of shading effect from Au NPs. Each component enhances and deteriorates photocatalytic activity subsequently. .... 205

Figure 149. Gas chromatography measurements for  $\text{TiO}_2$  NRs. (a) Low coverage of octahedral Au NPs on the  $\text{TiO}_2$  NRs. Yellow arrow indicates octahedral Au NPs. (b) Linear sweep of corresponding samples. (c) The amount of oxygen produced and faradaic efficiencies with respect to time. (d) Photocurrent transient at 1.4 V vs. RHE in AM 1.5G illumination. .... 206

Figure 150. SEM image of octahedral Au NPs on  $\text{TiO}_2$  film after 3-hour illumination (AM 1.5 G) at 1.4 V vs. RHE. .... 207

Figure 151. Photoactivity curves for other oxide n-type photoelectrode materials with or without octahedral Au NPs under 1-sun illumination. (a) For  $\text{Fe}_2\text{O}_3$  40 nm. (b) Corresponding IPCE spectra for  $\text{Fe}_2\text{O}_3$  40 nm with or without octahedral Au NPs. (c) For  $\text{WO}_3$  80 nm. (d) For Nb 0.01 % doped  $\text{SrTiO}_3$  single crystal. Dashed line (- -) corresponds to dark currents. .... 212

Figure 152. The shown  $J^2$ -V analysis is drawn from data from Fig. 151 to analyze onset potential. (a) For  $\text{Fe}_2\text{O}_3$  40 nm thin film. (b) For  $\text{WO}_3$  80 nm thin film. (c) For Nb 0.01 % doped  $\text{SrTiO}_3$  single crystal..... 215

Figure 153. The absorption spectrum of octahedral Au NPs. .... 220

Figure 154. Schematic representation of Au Nanoparticle Finite-difference time-domain (FDTD) configurations on  $\text{BiVO}_4$  film. (a)

Hemispherical Au nanoparticle. (b) Octahedral Au nanoparticle. FDTD simulation results of near field enhancement for hemispherical and octahedral Au NPs on the flat BiVO <sub>4</sub> film in water. (c) Field enhancement for hemispherical Au NPs under 550 nm photons. (d) Field enhancement for octahedral Au NPs under 550 nm photons. (e) Field enhancement for hemispherical Au NPs under 430 nm photons. (f) Field enhancement for octahedron Au NPs under 430 nm photons. (g) Field enhancement for hemispherical Au NPs under 350 nm photons. (h) Field enhancement for octahedral Au NPs under 350 nm photons. ....	222
Figure 155. Model used in finite-difference time-domain (FDTD) for the simulation. (a) Hemispherical Au NPs. (b) Octahedral Au NPs .....	223
Figure 156. FDTD simulation results of near field enhancement for flat BiVO <sub>4</sub> film in water. (a) Field distribution of BiVO <sub>4</sub> under 550 nm photons. (b) Field distribution of BiVO <sub>4</sub> under 430 nm photons. (c) Field distribution of BiVO <sub>4</sub> under 530 nm photons.....	223
Figure 157. (a) SEM and TEM (inset) images of octahedral Au NPs. (b) Enlarged TEM images of octahedral Au NPs. (c) Fast Fourier transform (FFT) pattern of octahedral Au NP. (d) Cross sectional EDS image of the octahedral Au NPs attached to BiVO <sub>4</sub> film. (e) False-colour scanning electron microscopy (SEM) image of octahedral Au NPs attached to BiVO <sub>4</sub> films with optimum coverage. (f) SEM image of the hemispherical Au NPs from E-beam evaporator (1.5 nm) attached to BiVO <sub>4</sub> film. (g) Photographic images of FTO, BiVO <sub>4</sub> , .....	226
Figure 158. (a) SEM image of octahedral Au NPs. (b) SEM image of octahedral Au NPs attached to BiVO <sub>4</sub> with optimum coverage. (c),(d) EDS images of octahedral Au NPs.....	227
Figure 159. SEM image of the hemispherical Au NPs from E-beam evaporator attached to BiVO <sub>4</sub> film. (a) 0.7 nm, (b) 1.5 nm and (c) 5 nm thickness. Photocurrent density of hemispherical Au NPs/BiVO <sub>4</sub> with (d) 0.7nm, (e) 1.5 nm and (f) 5 nm.....	227
Figure 160. X-ray diffraction (XRD) pattern of BiVO <sub>4</sub> film. ....	228
Figure 161. (a) Linear sweep voltammograms for BiVO <sub>4</sub> film, hemispherical Au NPs/BiVO <sub>4</sub> and octahedral Au NPs/BiVO <sub>4</sub> photoelectrodes measured in 0.5 M phosphate buffer with 1 M Na <sub>2</sub> SO <sub>3</sub> at a scan rate of 10mV/s under 1.5 G solar light under the chopped light condition. (b) Mott-Schottky plot of bare BiVO <sub>4</sub> and octahedral Au NPs/BiVO <sub>4</sub> photoelectrode measured under light off. The inset is enlarged Mott-Schottky plot of bare BiVO <sub>4</sub> and octahedral Au NPs/BiVO <sub>4</sub> in the grey region. * Frequency: 1 kHz, Amplitude : 10 mV. ....	230

Figure 162. SEM image of octahedral Au NPs/BiVO <sub>4</sub> photoelectrode after photoelectrochemical measurement. ....	230
Figure 163. (a)-(c) SEM images of the octahedral Au NPs changing coverage according to dipping time, 0h, 4h and 6h, respectively. (d)-(f) SEM images of the octahedral Au NPs changing coverage according to amount of the MPA precipitation solution. Scale bar is 200 nm.....	232
Figure 164. (a) Number of octahedral Au NPs in the selected area (grey region, shown in the Supplementary figure S8. (a)-(c) (see Fig. S8, ESI†)) according to the dipping time. (b) Number of octahedral Au NPs in the selected area (grey region, shown in the Figure 163. (d)-(f) according to amount of the MPA precipitation solution. (c), (d) Photocurrent density of Au NPs/BiVO <sub>4</sub> photoelectrodes controlled the dipping time and amount of the MPA precipitation solution at 1.23 V vs. RHE, respectively. (e), (f) Electrochemical impedance spectra (EIS) for various Au NPs/BiVO <sub>4</sub> photoelectrodes. The solid line was fitted by the ZSimpWin software using the proposed equivalent circuit model. The EIS was measured at 1.23 V vs. RHE under simulated solar illumination in 0.5 M phosphate buffer with 1 M Na <sub>2</sub> SO <sub>3</sub> . Inset shows equivalent circuits for various Au NPs/BiVO <sub>4</sub> photoelectrodes. ....	232
Figure 165. (a) Linear sweep voltammograms (LSVs) data of octahedral Au NPs/BiVO <sub>4</sub> photoelectrodes with different dipping time and amount of MPA solution. (b) Electrochemical impedance spectra (EIS) for comparing BiVO <sub>4</sub> film and Au NPs/BiVO <sub>4</sub> photoelectrode with extreme conditions. The solid line was fitted by the ZSimpWin software using the proposed equivalent circuit model. The inset shows equivalent circuits for various Au NPs/BiVO <sub>4</sub> photoelectrodes. (c) Amperometric current density-time profiles for BiVO <sub>4</sub> film and octahedral Au NPs/BiVO <sub>4</sub> photoelectrodes according to change of the dipping time. (d) Amperometric current density-time profiles for bare BiVO <sub>4</sub> and octahedral Au NPs/BiVO <sub>4</sub> photoelectrodes according to change of the amount of the MPA solution. The EIS and J-t curves were measured at 0.63 V (vs. Ag/AgCl) under simulated solar illumination in 0.5 M phosphate buffer with 1 M Na <sub>2</sub> SO <sub>3</sub> .....	233
Figure 166. The shown J <sup>2</sup> -V analysis is drawn from data from Fig. 165 to analyze onset potential. ....	235
Figure 167. Stability test of octahedral Au NPs/SiO <sub>2</sub> (1nm)/BiVO <sub>4</sub> measured in 0.5 M phosphate buffer solution with 1M Na <sub>2</sub> O <sub>3</sub> at 1.10 V vs. RHE.....	239
Figure 168. (a) and (b) Amperometric current density-time profiles for bare BiVO <sub>4</sub> and octahedral Au NPs/BiVO <sub>4</sub> photoelectrodes at 1.23 V vs.	

RHE with the fluence of  $10 \text{ mW/cm}^2$  at 532 nm and 405 nm, respectively.

(c) and (d) Absorption of the bare  $\text{BiVO}_4$  and octahedral Au NPs/ $\text{BiVO}_4$  films by estimating the transmission and reflection spectra using an integrating sphere (Absorbance =  $1 - \text{Transmittance} - \text{Reflectance}$ ) (e) IPCE spectra of bare  $\text{BiVO}_4$  and octahedral Au NPs/ $\text{BiVO}_4$  photoelectrodes at 1.23 V vs. RHE. (f) IPCE Enhancement of octahedral Au NPs/ $\text{BiVO}_4$  photoelectrodes. .... 240

Figure 169. Photovoltage gains of octahedral Au NPs/ $\text{BiVO}_4$  at (a) constant current of  $500 \mu\text{A}$  under 405 nm, (b) constant current of  $10 \mu\text{A}$  405 nm under 532 nm. .... 242

Figure 170. Photovoltage gains of octahedral Au NPs/ $\text{BiVO}_4$  at open circuit potential (a) 405 nm, (b) 532 nm. .... 243

Figure 171. (a) IPCE spectra at 1.23 V vs. RHE. Octahedral Au NPs were decorated on 80-nm-thick  $\text{TiO}_2$  film. The vertical dotted line (--) indicates the band gap energy of  $\text{TiO}_2$ . Inset indicates that the photocurrent enhancement for the visible light is below the noise level. .... 243

Figure 172. Schematic for the energy band diagram of the octahedral Au NPs/ $\text{BiVO}_4$  system to show that both DET and PRET mechanisms work in the system. .... 247

Figure 173. (a) IPCE enhancement in the octahedral Au NPs/ $\text{BiVO}_4$  photoelectrode. (b) Energy distribution of electrons and holes in the conduction and valence bands of  $\text{BiVO}_4$ . The highest electron and hole concentrations are  $1/2 \text{ kT}$  away from  $E_c$  and  $E_v$ . .... 248

Figure 174. Agglomeration of octahedral Au nanoparticles on  $\text{TiO}_2/\text{FTO}$  on glass substrate. (a) Moderately agglomerated Au nanoparticles ( $\sim 50 \%$ ). (b) Heavily agglomerated Au nanoparticles ( $\sim 100 \%$ ). .... 260

Figure 175. FDTD simulation results ( $|\mathbf{E}/\mathbf{E}_0|$ ) of the three kinds of Au nanoparticles (octahedral, truncated octahedral and cuboctahedral) at various incident wavelengths. (100) and (111) facets are denoted as yellow and blue, respectively. (a) Schematic configurations of Au nanoparticles. (b) Field enhancement at 350 nm photons. (c) Field enhancement at 450 nm photons. (c) Field enhancement at 550 nm photons. (b) Field enhancement at 650 nm photons. .... 262

Figure 176. The maximum electric field enhancement ( $\mathbf{E}/\mathbf{E}_0$ ) from twelve finite-difference time-domain (FDTD) simulations. The value is arranged in either grape and table. .... 263

Figure 177. Agglomerated (a) octahedral, (b) truncated octahedral and (c) cuboctahedral Au nanoparticles on  $\text{TiO}_2$  thin films. (d) A schematic of the Au NPs attachment procedure based on phase transfer to organic

medium via PEGylation. (e) A schematic for the process of anchoring Au nanoparticles for the semiconductor nanostructure attachment using PEGylation in aqueous phase and phase transfer to organic medium. (f) Phase transfer to organic medium according to the PEGylation time. (g) Image of octahedral Au nanoparticle attached vial. ....	266
Figure 178. Calculated coverage of three equilateral shaped Au NPs (octahedral, truncated octahedral and truncated cube) for (100) and (111) facets. (Equilateral is assumed.) .....	267
Figure 179. PEGylated octahedral Au NPs taken by negative staining technique. (a) Low magnification. (b) High magnification.....	267
Figure 180. (a) Normalized absorbance of synthesized solutions containing three shape-controlled Au NPs (octahedral, truncated octahedral and cuboctahedral). Dotted lines indicate the absorbance of solutions after PEGylation. Peak positions are also included as inset. (b) Attached octahedral Au NPs density on Si by the process by dipping time and concentration. (c) SEM image of highest coverage of octahedral Au NPs from the conditions. (d) Octahedral Au NPs decoration on Au nanorod by phase transfer to organic medium via PEGylation. (Octahedral Au NPs in the SEM images are depicted as false yellow color.).....	269
Figure 181. (a) The Au NPs solution (organic phase, EtOH-DCM) after Au octahedral NPs attachment (transparent). (b) The original (aqueous phase) as-synthesized Au octahedral NPs solution (purple). ....	270
Figure 182. Octahedral Au NPs decorated TiO <sub>2</sub> nanorods on planar view. ....	270
Figure 183. Octahedral Au NPs attachment on various semiconductors. ....	271
Figure 184. Normalized Raman spectroscopic analysis of the three shape-controlled Au NPs solutions from (600 to 3,000) cm <sup>-1</sup> . Smoothed data is also included (numbers indicate peak positions).....	273
Figure 185. RAMAN spectra of CTAB 200 mM solution. ....	274
Figure 186. Normalized FTIR spectroscopic analysis of the three shape-controlled Au NPs solutions before and after the PEGylation from (2,000 to 3,950) cm <sup>-1</sup> .....	276
Figure 187. (a) FTIR spectra of dried CTAB (black) and PEG-TH solution on glass substrate. (b) Peak designation of CTA <sup>+</sup> molecule in FTIR spectra. ....	277
Figure 188. Schematic of the CTA <sup>+</sup> bilayer structure according to the facet of Au NPs. ....	278

Figure 189. Photocurrent enhancement with high-coverage of octahedral gold nanoparticles formed by ligand exchange method with PEG-TH. The result is shown with the previous result. .... 279

Figure 190. Theoretical photocurrent of BiVO<sub>4</sub>. .... 280

# Chapter 1

## Emergence of Golden Age with Gold Nanoparticles

### Quote

**Michel Faraday**

“Part of the gold is reduced in exceedingly fine particles, which becoming diffused, produce a beautiful ruby fluid.” (1857)

## 1.1. Introduction

In these days, we always celebrate the Christmas (especially the Christmas is ahead; 2017.11). When the day come, the famous sing “Look out the window” is widely being heard. To enjoy such a period, the beautiful scenery with an ornament is essential. The beauty of world is attributed to the light interaction with matters. Not only beauty but also practical view, without light interaction with matters, we cannot achieve modern day civilization.

The advance of science in history was made with the understanding of light interaction with matter. Since the ‘Principia’, which is announced by Sir Issac Newton, understanding of the nature is partially achieved. He made a great advance for photonics in his book ‘Opticks’. He regarded light as fine particles. He initiated the science revolution in Renaissance era.

But this view had been great conflict with wave property of light. In the 17<sup>th</sup> century Christiaan Huygens explained light interaction with matter (reflection, refraction and diffraction) with as a light wave. In the 19<sup>th</sup>, double slit experiment (Thomas Young, 1803) and Maxwell’s equations for electromagnetic theory (James Clerk Maxwell, 1855) revealed the property of light as a wave.

A long time later, one more genius was born in 1879. He is the Albert Einstein. He made great progress of understanding for the nature in history of humanity. From the Newtonian era, light has been regarded as a particle. But the Albert Einstein changed this view into wave-particle duality by photoelectric effect (1905). As a result, based on profound understandings, numerous phenomena

in the nature has been analyzed by posterity researchers. Even many progresses have been made, the understanding is not yet complete and still going forward.

In the 20<sup>th</sup> century, there was a great scientific revolution in the era. Quantum mechanics is arranged by many scientists such as Louis de Brogile, Erwin Schrödinger, Werner Karl Heisenberg, Paul Adrien Maurice Dirac, Richard Phillips Feynman and etc. As a result, a representative interpretation so called ‘Copenhagen interpretation’ has been set. Development of nanotechnology with quantum mechanics leads to the understanding of material as a totally new view.

After the innovation of transistor by John Bardeen, William Shockley and Walter Brattain (1947), the understanding of electronic properties of the material has been essential. Researchers and scientists stacked a wide variety of knowledge related to the semiconductor physics. These historical advancements are the base for modern advancements of science and engineering.

Recently, researches deal light-matter interaction in nanoscale. Metal nanoparticle–light interaction is the area people interest due to their abnormal photoelectrical property with light. Recently we call this area as ‘plasmonics’. In history, the technology has been used as a beauty. Nowadays, due to the higher momentum of plasmon than light in matter, many benefits has been expected and investigated. Before the investigation, I will address some of historical aspects of the phenomena.

### 1.1.1 Lycurgus Cup (Roman era)

Even though there are many developments from the ancients in Roman era, one of the astonishing output has been made. They dedicated their knowledge to deal with glass product. For the beauty, they made spectacular glass cup which is called as a 'diatretum'. One of the example of glass is shown in Figure 1.<sup>1</sup> The diatretum is a dichromic glass cup consist of decorative cage. People has been pronounced it as "the most spectacular glass of the periods, fittingly decorated, which we know to have existed".



Figure 1. Fragment of diatretum in reflected (a) and transmitted (b) light.

The essence of their technology is concentrated on a 'Lycurgus Cup' which is made in 4<sup>th</sup> century in Roman era. It (165 mm high and 15 mm thick) is only of perfect legacy of Roman era remain in modern era. The decoration of cup is related to myth of the legend of King Lycurgus from the Homer's Iliad. They expressed praise the triumph of Dinysus over Lycurgus. The British museum achieved the right of cup from Rothchiled in 1958 by aid of the National Art Collection Fund. The glass part is consisted with dichromic glass. The greatest part of the cup is its color. When the light is reflected from the cup, it shows dim-green color. While, when the light is transmitted from the cup, it looks like

bloody-red color. The image from the British museum is incorporated in Figure 2.



Figure 2. Image of Lycurgus Cup from Roman era for reflected (left) and transmitted (right) light.

The secret of the color change has not been revealed until 1990. In 1990, D. J. Barber and I. C. Freestone from United Kingdom investigated the reason using transmission electron microscopy based on chemical elemental analysis.<sup>2</sup> For the reference, the chemical analysis is summarized in Table 1.

SiO <sub>2</sub>	73.5	Fe <sub>2</sub> O <sub>3</sub>	1.5	SnO <sub>2</sub>	<0.01
Na <sub>2</sub> O	13-15	P <sub>2</sub> O <sub>5</sub>	0,2	B <sub>2</sub> O <sub>5</sub>	0.1
CaO	6.5	MnO	0.45	TiO <sub>2</sub>	0.07
K <sub>2</sub> O	0.9	Sb <sub>2</sub> O <sub>3</sub>	0.3	Ag	0.03
MgO	0.5-0.6	CuO	0.04	Au	0.004

---

Table 1. Chemical composition of the Lycurgus Cup.

The chemical analysis shown that the glass is typical soda-lime-silica glass which have metal impurities (Ag and Au). From the analysis from the sampling of Lycurgus Cup fragment, two kinds of nanoparticle are discovered as shown in Figure 3.

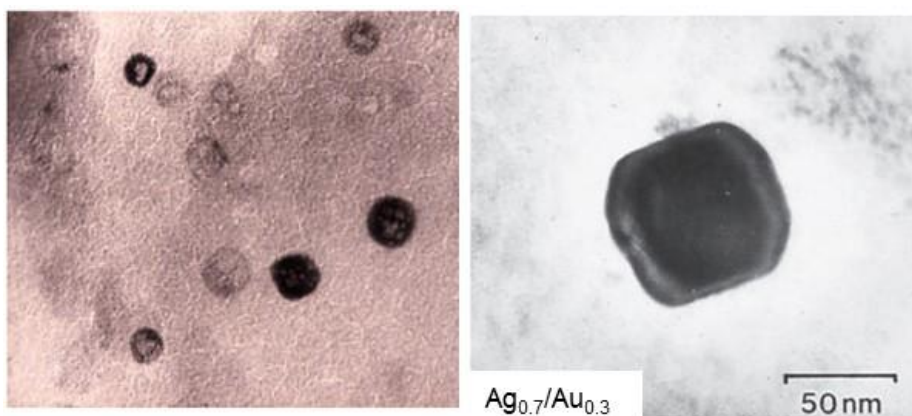


Figure 3. Transmission electron microscopy image of nanoparticles incorporated in Lycurgus Cup (Left, NaCl; Right, Ag<sub>0.7</sub>/Au<sub>0.3</sub>).

At that time, people already know the fact that NaCl (also metal oxides) could not be responsible for the color. So, color source should be the metal nanoparticles incorporated in Lycurgus Cup. The chemical analysis of metallic nanoparticle shows their composition as Ag<sub>0.7</sub>/Au<sub>0.3</sub>. At that time, the color of colloidal metal Au nanoparticles is already known. They concluded that Au and Ag is introduced while production of dichromic glass. Modern people have succeeded to reenact the dichromic glass in Roman era by the knowledge as shown in Figure 4.

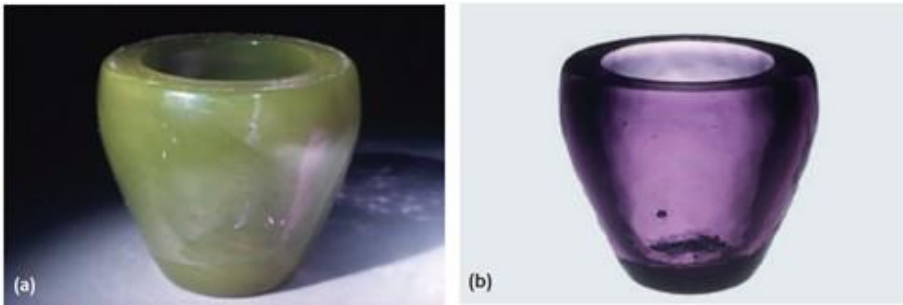


Figure 4 Reenacted glass in Lycurgus Cup in reflected (a) and transmitted (b) light.

### 1.1.2 Stained Glass (Medieval era)

In the western Europe, stained glass spread into the major ornament form in the cathedral. The golden age of colored glass was that era. That was widely used in lofty and Gothic form cathedral in Medieval era. The stained glass does not show effective color by reflection of light. But when the light transmitted into the glass, it shows brilliant color. The visual example is shown on the Figure 5.

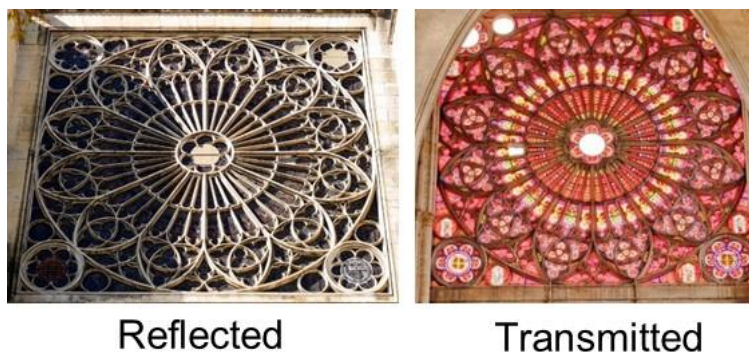
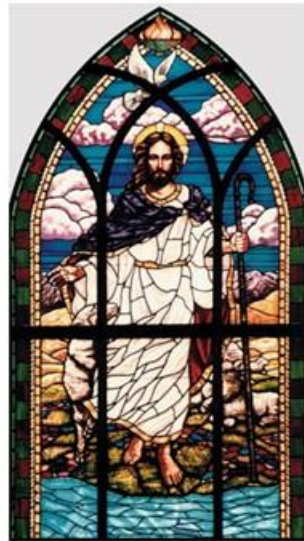


Figure 5. Stained glass in Troyes Cathedral, France (17th century).

At that time, the artists, artisans and craftsman does not recognize that the usage of nanotechnology. The stained glass is being used as an art even in a recent day as shown on Figure 6. The combination of contemporary art and previous ancient art forms great advancement.



Reflected



Transmitted

Figure 6. Stained glass in United Presbyterian Church of Morning Sun, Iowa.

The origin of the color glass is revealed in quite recent days (~ 2003). The shape and size dependence of particles are treated recently,<sup>3</sup> and the New York Times summarized the secret of color glass in news (2005. 05. 22). Nowadays, we recognize that the color of stained glass has an origin with gold and silver nanoparticles. For example, 100 nm silver nanotriangle emits red light when the light is transmitted. The ancient workers must be recognized the color generation in glass by impurity metals (gold and silver). The informative pictorial page is incorporated here below in Figure 7.

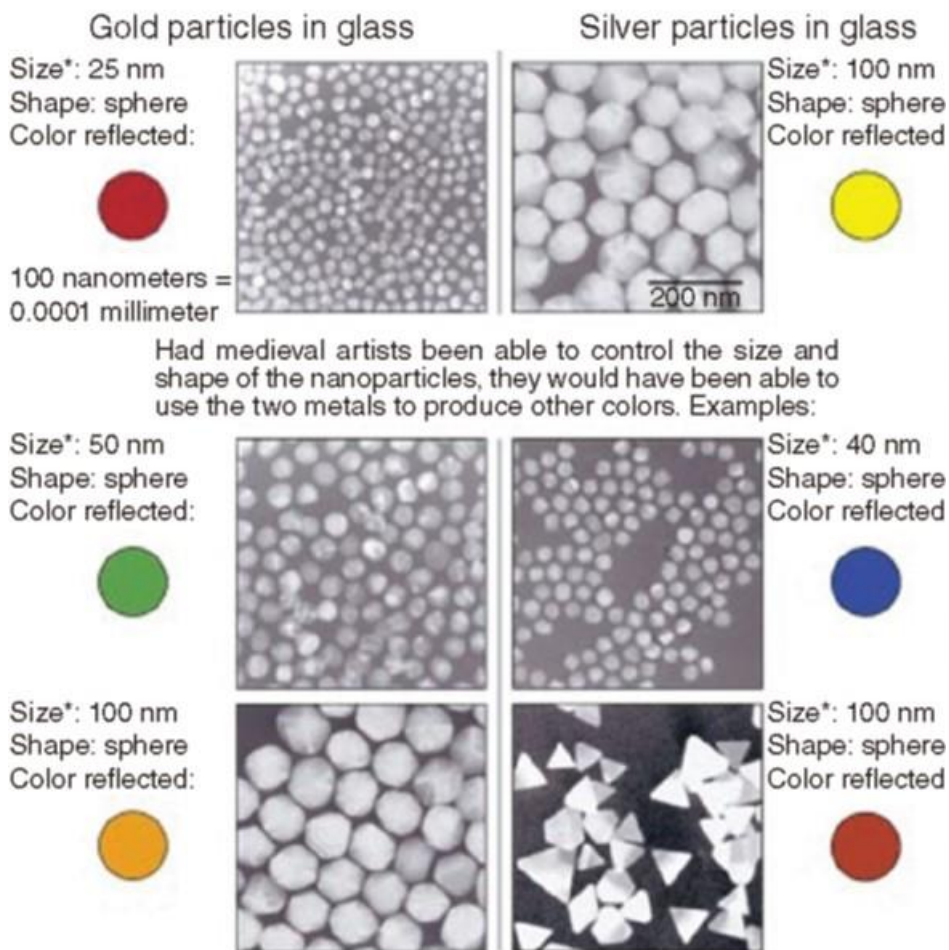


Figure 7. The origin of colored stained glass in Medieval era.

### 1.1.3 Michel Faraday's Discovery (Early-modern era)

Colloidal gold is a colloidal suspension of gold nanoparticles in a solvent (usually in aqueous system). The modern synthesis is not developed until the Faraday's approach begins. In 1856, he accidentally succeeds to synthesis nano-sized gold by reduction of an aqueous solution of chloroaurate ( $\text{AuCl}_4^-$ ) by phosphorus in  $\text{CS}_2$ .<sup>4</sup> The yellow chloroaurate solution become red by

reduction with phosphorus in  $\text{CS}_2$ . In the article, he said ‘Part of the gold is reduced in exceedingly fine particles, which becoming diffused, produce a beautiful ruby fluid.’. The particle solution is survived until the 2<sup>nd</sup> world war, and the solution is accidentally broken by attack. The picture is incorporated into Figure 8. Long time later for the colloidal gold formation, Turkevich achieved gold nanoparticles according to the Faraday’s method and analyzed the particles with electron microscopy.<sup>5</sup> The result shows that Faraday succeeded to synthesize around 6 nm range gold nanoparticles.



Figure 8. Michel Faraday's colloidal gold solution.

After the innovation, he tested light scattering property of the solution.<sup>6</sup> Named after the discovery with light scattering is called as Faraday-Tyndall effect (or simply, Tyndall effect). If the light shines the gold colloidal solution, due to the scattering, the beam path is visible and solution become much brighter. The longer waves become more transmitted and shorter waves become scattered like Rayleigh scattering. The exemplary picture is attached.<sup>7</sup>

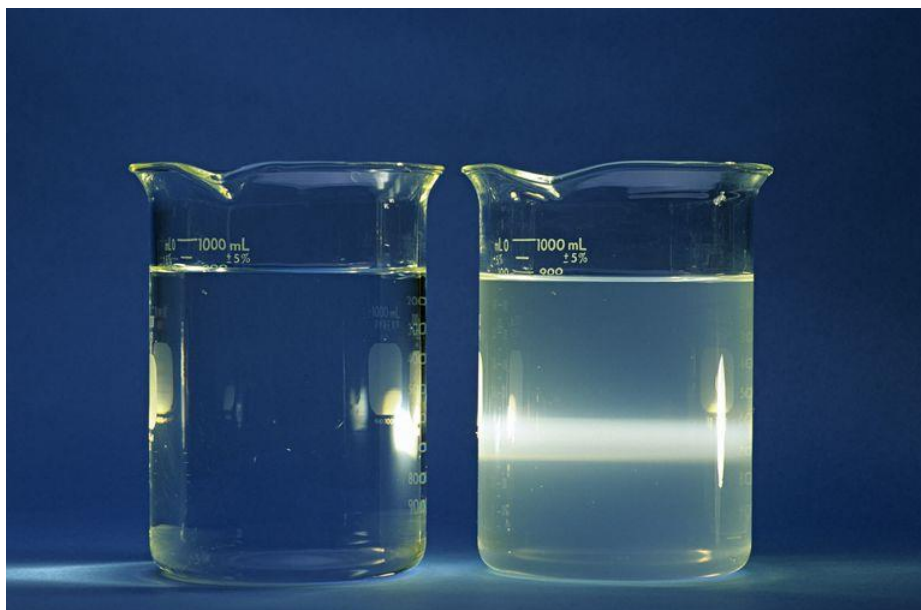


Figure 9. Light pass through solution (left) and colloid (right).

## 1.2. Modern Era

Recent studies for gold nanoparticles and nanostructures conducted with incorporation of computational methods and experimental approaches.

The characteristics are designed previous of the synthesis.

## 1.2.1 Finite-difference Time-domain (FDTD) Method

Finite-difference time-domain method is a computational method to solve Maxwell's electromagnetic differential equation. In an approximation in the unit cell, the electric/magnetic field components in specific time is solved. According to Maxwell's equation, electric/magnetic field induces magnetic/electric field in the space. Reader can refer Formula 1.1 in below.

### Formula 1.1 Maxwell's equation

Faraday's law and Ampere's law is written as below partial differential form.

$$\mu \frac{\partial H_y}{\partial t} = \frac{\partial E_x}{\partial x}, \quad \varepsilon \frac{\partial E_z}{\partial t} = \frac{\partial H_y}{\partial x}$$

The electromagnetic behavior is solved until the desired equilibrium. The Chinese American mathematician Kane S. Yee (born 1934) provided numerical computational analysis techniques. In the calculated space, the cell has electric/magnetic vector components in three directions. The algorithm is summarized in Formula 1.2 in below.

### Formula 1.2 Yee's algorithms

1. Replace all the derivatives in Ampere's and Faraday's laws with finite differences. Discretize space and time so that the electric and magnetic fields are staggered in both space and time.

2. Solve the resulting difference equations to obtain “update equations” that express the (unknown) future fields in terms of (known) past fields.
3. Evaluate the magnetic fields one time-step into the future so they are now known (effectively they become past fields).
4. Evaluate the electric fields one time-step into the future so they are now known (effectively they become past fields).
5. Repeat the previous two steps until the fields have been obtained over the desired duration.

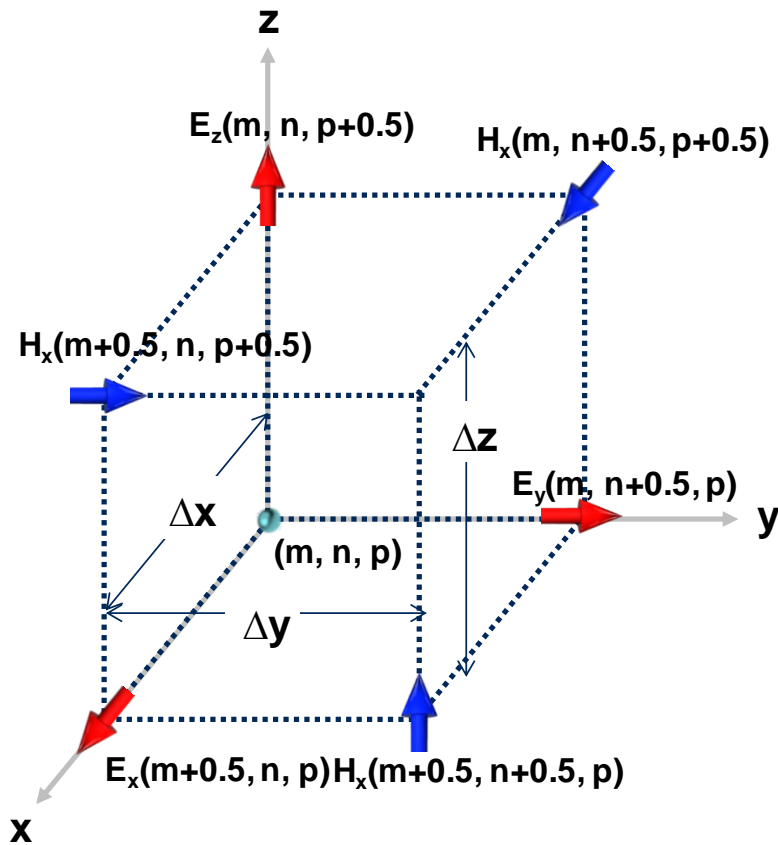


Figure 10 Representation of Yee's cell in a specific position  $(m, n, p)$ .

The cell according to Yee's method is called as Yee's cell (Figure 10). Electric and magnetic field components are placed in a half step in time (Figure 11). As explained in previous paragraph, Electric field induces magnetic field and magnetic field induced electric field in sequence. Current electric/magnetic field components are seed of future magnetic/electric field components.

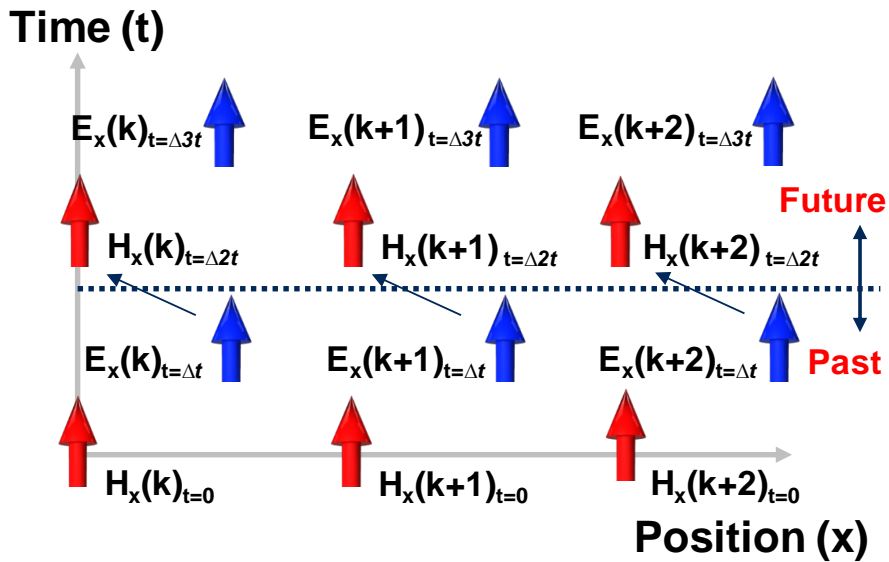


Figure 11 Electric/magnetic field nodes in a space-time.

If the calculated region and boundary condition is defined, the given electromagnetic field components can be solved by explicit method in a space-time. As a boundary condition, well-known boundary conditions are metal, periodic, (anti-)symmetric, Bloch, perfectly matched crystal (PMC) and perfectly matched layer (PML). In 1994, Berenger devised the method to solve Maxwell's equation.<sup>8</sup> In usual situation, the PML condition is widely adopted. PML is synthetic absorbing layer of electromagnetic wave. To solve problem

efficiently (reduce time) in the boundary the electromagnetic wave solving variables changed as below.

<b>Formula 1.3 Perfectly matched layer (PML)</b>
$\frac{\partial}{\partial x} \rightarrow \frac{1}{1 + \frac{i\sigma(x)}{\omega}} \quad x \rightarrow x + \frac{1}{\omega} \int \sigma(x') dx'$
$\exp i(kx - \omega t) \rightarrow \exp i(kx - \omega t) - \frac{k}{\omega} \sigma(x') dx'$

The electromagnetic properties of materials such as extinction (absorption and scattering), field distribution, power distribution (poynting vector) and etc. can be solved efficiently. Graphical representation of the method summary is provided in Figure 12.

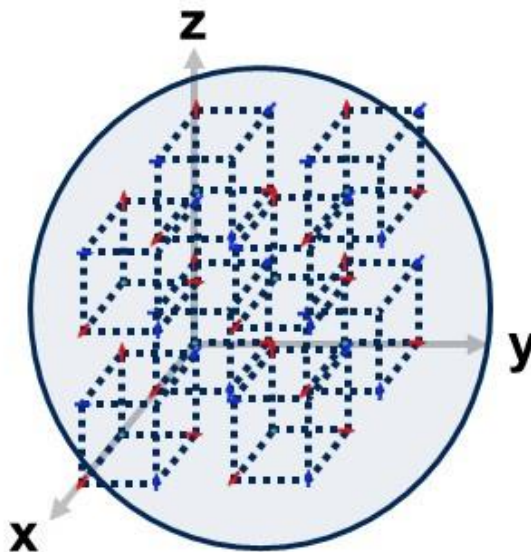


Figure 12 Yee's cell and boundary condition in FDTD method.

## 1.2.2 Local Field Enhancement Calculation by FDTD

To solve time-dependent equation (Maxwell's equation) into analytic form, Fourier transformation of the wave equation is required (Formula 1.4).

### Formula 1.4 Fourier Transformation of Wave Equation

$$E(x, y, x, t) = E_0(x, y, z_0) s(t)$$

↔ (Fourier)

$$E(x, y, x, \omega) = E_0(x, y, z_0)$$

(Refer that,  $s(\omega) = \int \exp(i\omega t) s(t) dt$ )

The field enhancement can be calculated by signal integration into specific time or steady-state interval. Using continuous wave normalization (CWNORM), spectral averaging is achieved. Field enhancement is calculated as below.

### Formula 1.4 Fourier Transformation of Wave Equation

$$\langle |E(\omega)|^2 \rangle = \frac{\int_0^\infty |s(\omega)|^2 |E(\omega)|^2 d\omega}{\int_0^\infty |s(\omega)|^2 d\omega}$$

$$\text{Enhancement} = \sqrt{\frac{\langle |E(\omega)|^2 \rangle}{\langle |E_0(\omega)|^2 \rangle}}$$

### 1.2.3 Various Shape of Gold Nanoparticles

In modern days, the synthesis method of gold nanoparticle is tremendous. The desired shape can be synthesized by understanding the growth mechanism. Shape is controlled by the growth kinetic control of facet. Usual circumstances, dissolved gold salt is efficiently reduced with capping agents. Examples of shape-controlled gold nanoparticles depicted in the Figure 13.

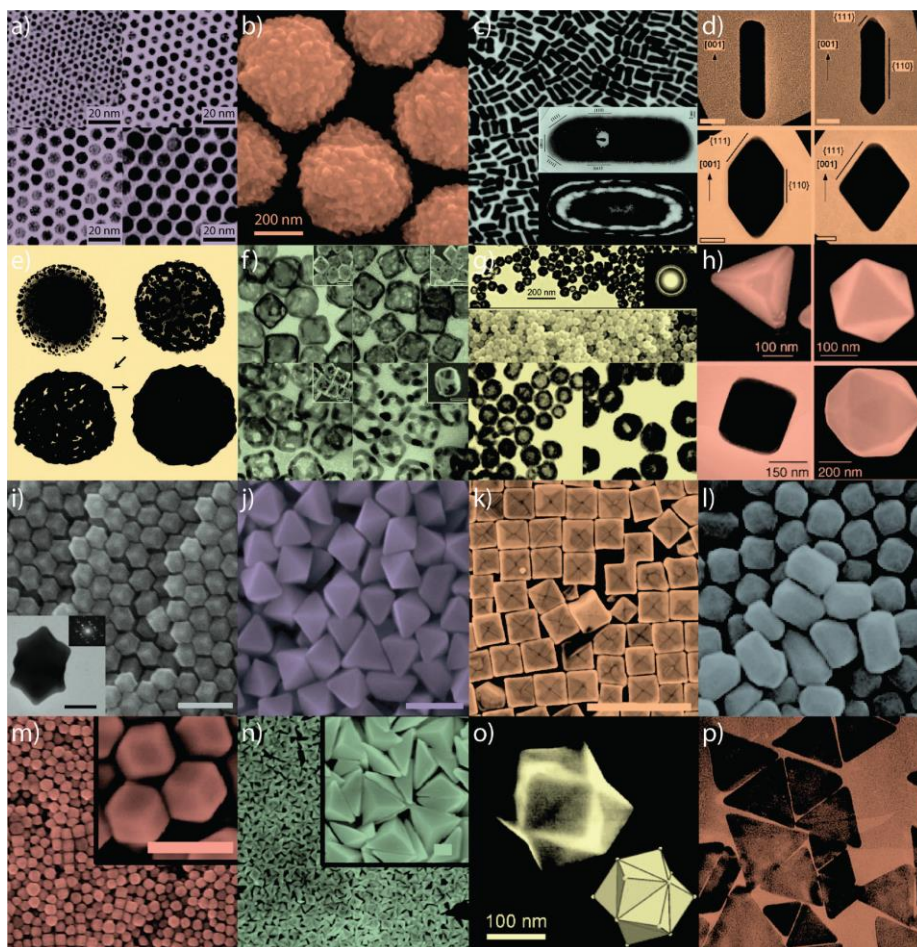


Figure 13. Shape-controlled gold nanoparticles.<sup>9</sup>

According to the shape, size and composition of gold nanoparticle, the color of solution can be tuned besides red. All visible spectrum is available as shown in Figure 14.

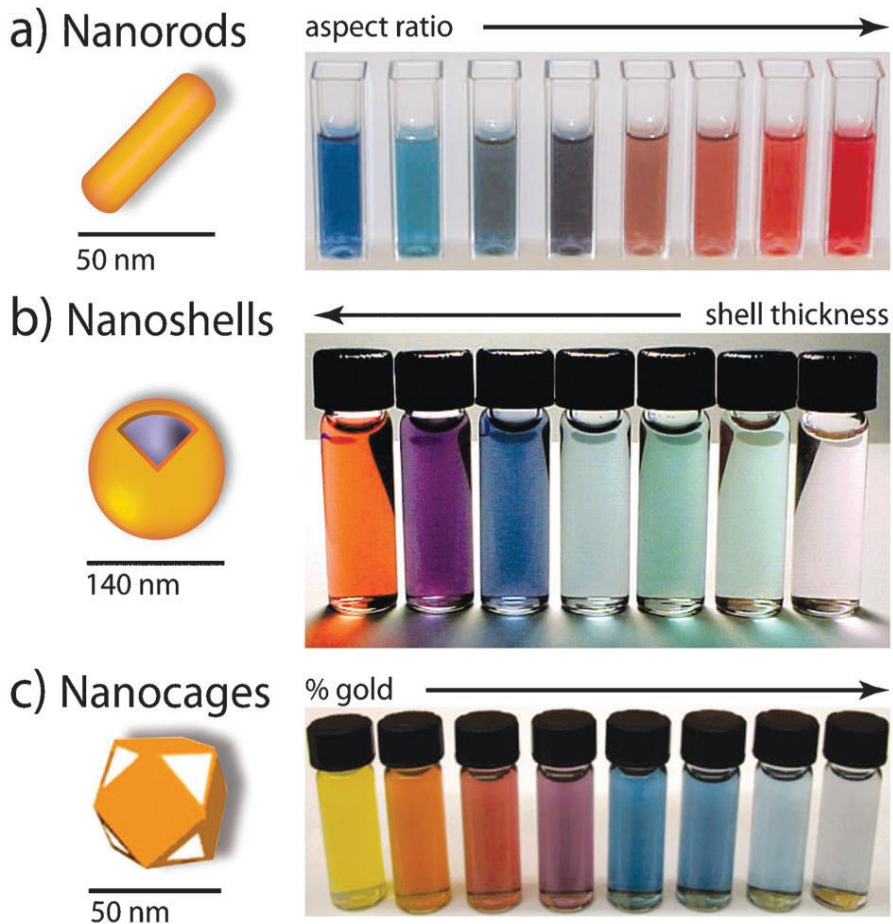


Figure 14 Tunable color of gold nanoparticle solution.

## **Chapter 2**

# **Synthesis and Characterization of Gold Nanoparticles.**

### **Quote**

**Richard P. Feynman**

"There's Plenty of Room at the Bottom" (1959, Lecture)

## **2.1. Gold Nanoparticle Synthesis with Citrate Reduction**

### **2.1.1 Turkevich Method**

Previously, Faraday succeeded the synthesis of gold nanoparticles in two phase. But in the aqueous phase, the aqueous solution phase of gold nanoparticles is not achieved until 1951. J. Turkevich presented the synthesis of gold nanoparticles in one aqueous phase in Discussions of the Faraday Society.<sup>10,11</sup> He synthesized gold nanoparticle as follows. Chloroauric acid solution 50 ml (contains 50 mg Au) is mixed with 45 mL distilled water and 5 mL 0.1 M KOH solutions. Then the solution is mixed with phosphorus-ether solution.

### **2.1.2 Frens Method**

In 1973, Frens revised the Turkevich method.<sup>12</sup> Frens assumed that the reduction of gold chloride with sodium citrate in aqueous solution is a proper way to synthesize monodisperse gold nanoparticle solution. He wants to control the rate of nucleation and growth by modulating amount of reactants. To generate gold nanoparticles by Frens Method, the following procedure is utilized. The first, salt solution of  $\text{HAuCl}_4$  ( $10^{-2}$  weight %) is heated to boiling. And the second, salt solution of sodium citrate ( $\text{Na}_3$ -citrate, 1 weight %) is added. In a few second, the solution turns into blue color due to the nucleation process and red color due to the formation of gold nanoparticles. The particle size become large by reducing the amount of citrate salt. The atypical spherical gold nanoparticle with a size distribution in specific range is achieved according to the method. They showed that the growth of gold nanoparticle in a citrate reduction method is governed by the number of nuclei as shown in Figure 15.

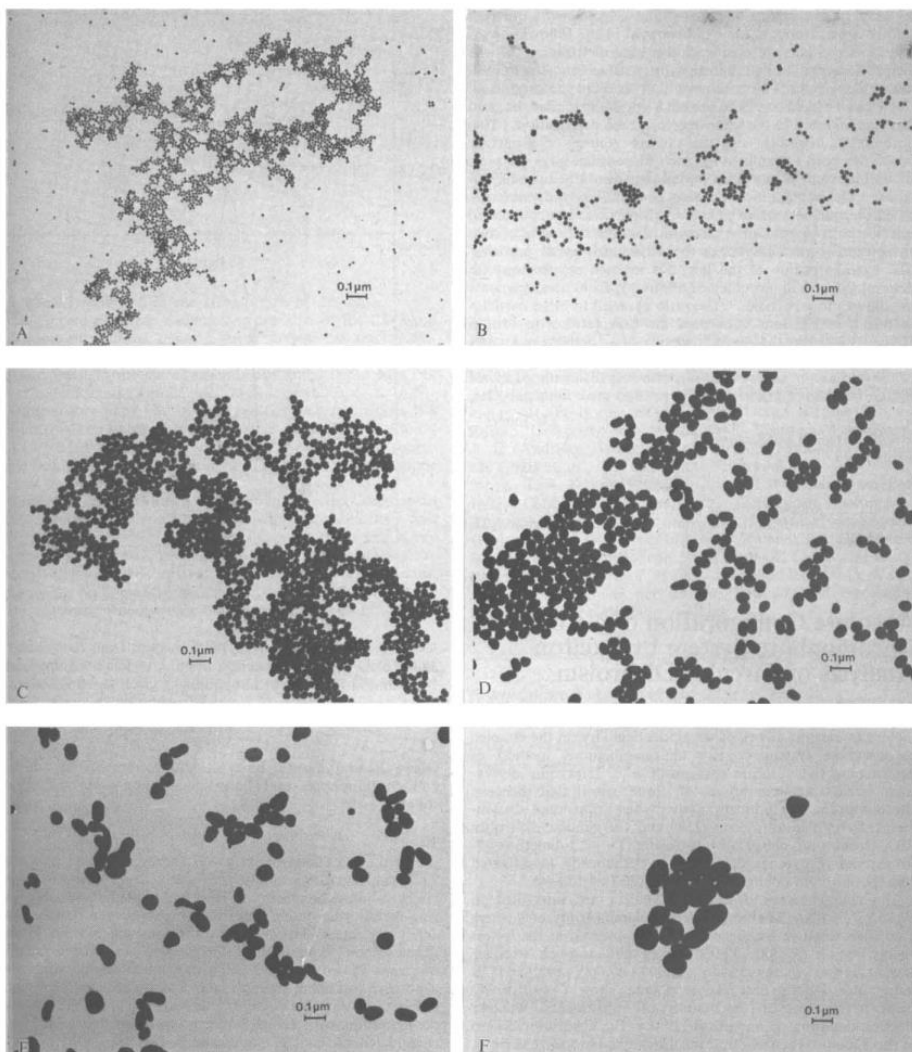


Figure 15. Electron microscope image of size controlled gold by Frens (1973).

### 2.1.3 pH Dependence

In the Frens method, the size distribution become broader when the size of gold nanoparticle become increase. Ji et al. provided the detailed description for this view.<sup>13</sup> The  $\text{Na}_3\text{-citrate}$  precursor has reactivity switching points at  $\text{pH} = 6.2$  and  $7.1$ . Also, according to the  $\text{pH}$ , the reactivity and ionic structure of auric complex are change. In the synthesis procedure the citrate precursor also acts

the pH controller. So the role of Na<sub>3</sub>-citrate should be reconsidered. The information is provided in Figure 16.

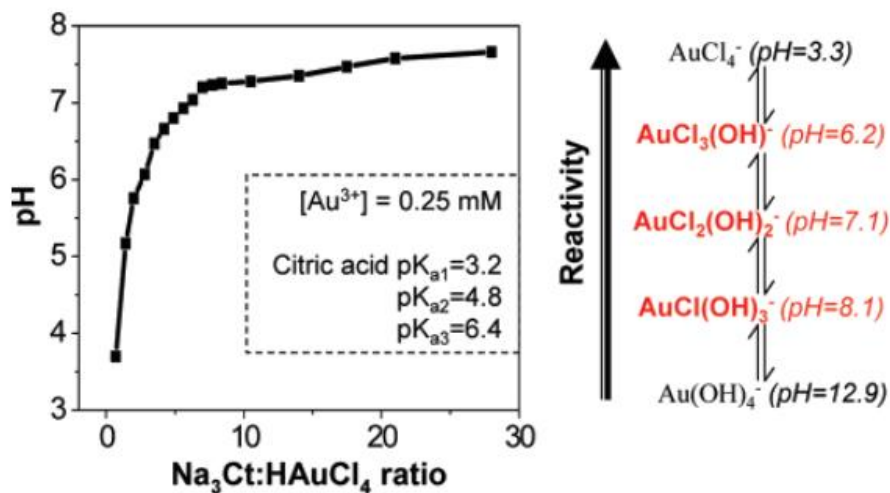


Figure 16 pH variation for the ratio of salts. Dominating species related with the reaction is shown as red.<sup>13</sup>

Without the pH control, the synthesis route provided fast nucleation of nanoparticles. As a result, random attachment, aggregation, intra-particle ripening occurred to minimize a surface energy of gold nanocrystals. While under high pH condition, nucleation and growth is controlled by diffusion. As a result, monodisperse size of gold nanoparticle is provided. In the research, they succeed to achieved monodisperse gold nanoparticles with sized from 20 to 40 nm. The schematic illustration of reaction pathway is shown in Figure 17.

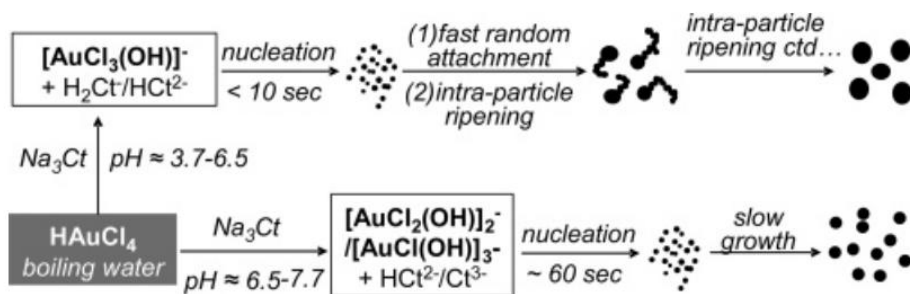


Figure 17. Two reaction pathways for the synthesis of gold nanoparticles by citrate reduction.<sup>13</sup>

### 2.1.4 Consecutive Ostwald Ripening

A growth process of monodisperse gold nanoparticle is well-explained under consideration of LaMer mechanism (homogeneous nucleation).<sup>14</sup> In the model, at the first stage, precipitation occurs. If the concentration is enough above the nucleation at some point of supersaturation, the burst and rapid nucleation begins to reduce the concentration of solution. The process is called as the focusing period which the mean radius of particles increase fast. After the period growth process by diffusion occurs to reduce the concentration of solution to the solubility of the solution. The particle growth near the saturation concentration is called as Ostwald ripening (roughly Ostwald ripening refers diffusion-controlled nanoparticle growth process). The period is called as the defocusing period, where the growth rates reduce severely. The size distribution of nanoparticles become broader according to the time before the saturation due to the Ostwald ripening process under the growth period. The graphical representation of the Lamer process is shown on **Figure 18**.<sup>15</sup>

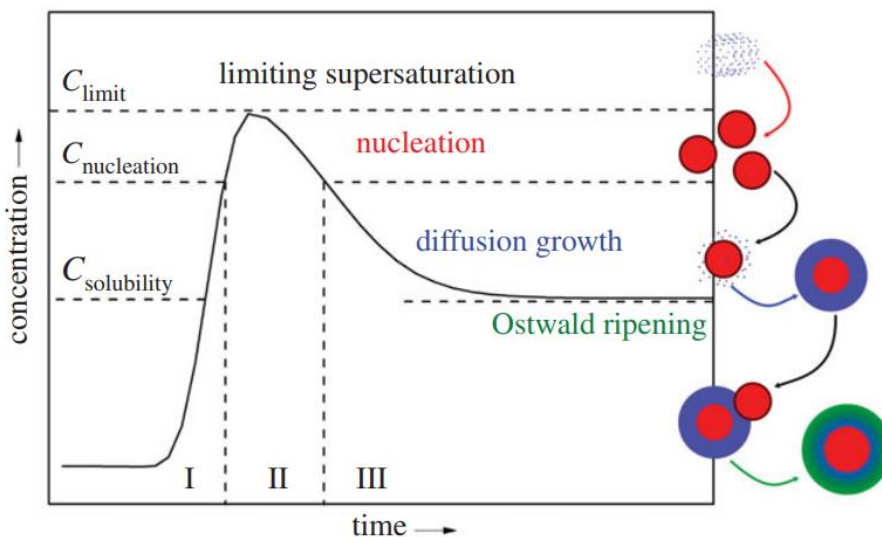


Figure 18. LaMer model of Nucleation and Growth.

Neus et al. provided the growth method of monodisperse citrate reduced gold nanoparticle by consecutive Ostwald ripening.<sup>16</sup> Through prohibiting secondary nucleation, they succeed to synthesize the monodisperse gold nanoparticles of up to 200 nm by seeded growth method. In a summary, the first, they synthesized gold nanoseeds. A solution of 2.2 mM sodium citrate in distilled water (150 mL) is heated under vigorous stirring. After boiling had commenced, 1 mL of  $\text{HAuCl}_4$  (25 mM) was injected. The color of the solution changed from yellow to gray-blue and then to soft pink in 10 min. The second, Seeded Growth of Au NPs is commenced. After the synthesis of the Au seeds, the reaction was controlled to slow by adjusting the solution temperature to 90 °C. Then, 1 mL of sodium citrate (60 mM) and 1 mL of a  $\text{HAuCl}_4$  solution (25 mM) were sequentially injected. By repeating this process (sequential addition of 1 mL of 60 mM sodium citrate and 1 mL of 25 mM  $\text{HAuCl}_4$ ), gold particles of progressively larger sizes were grown. After 14 progress, 1 mL of

a HAuCl<sub>4</sub> solution (25 mM) was injected and 30 min were given. After that, the diluted sample (by extracting 55 mL of sample and adding 53 mL of distilled water and 2 mL of 60 mM sodium citrate) was used as a seed solution for process and repeated again. The schematic of process and the representative nanoparticle images are given in Figure 19.

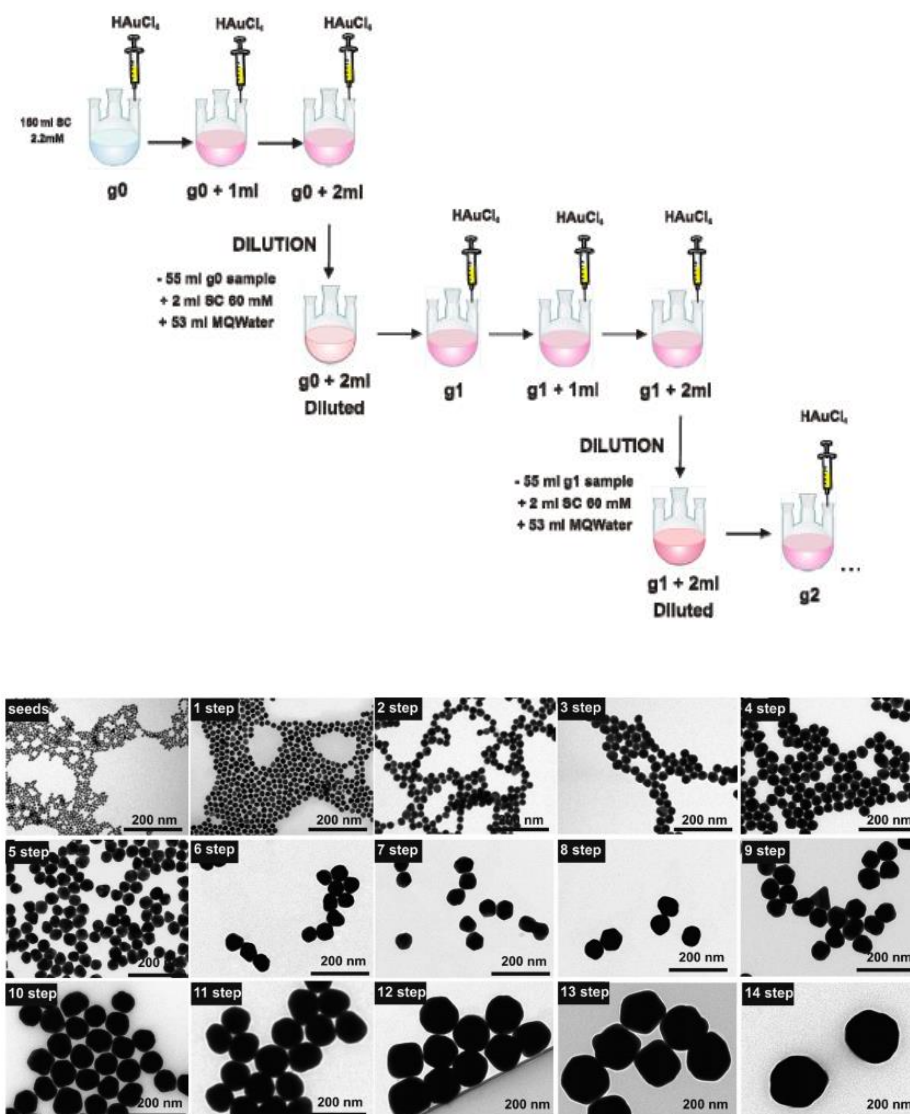


Figure 19. Growth of monodisperse gold nanoparticles by seeded-growth.

## 2.1.5 Growth Mechanism

To unearth the growth mechanism of gold nanoparticles by citrate reduction method by experimentally, Polte et al. incorporated small-angle X-ray scattering (SAXS) and X-ray absorption near-edge spectroscopy (XANES) during synthesis.<sup>17</sup> Droplets levitated in an acoustic levitator as shown in Figure 20.

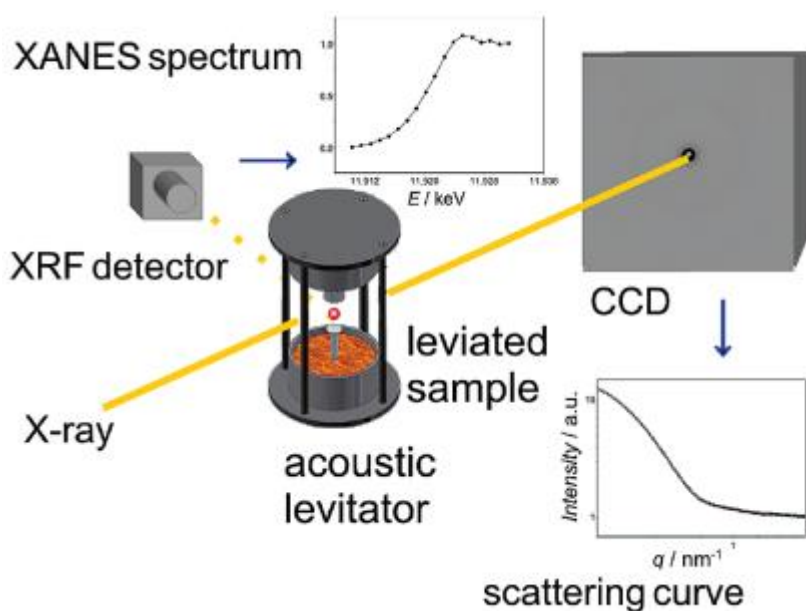


Figure 20 Schematic of configuration.

The experiment drives us to recognize the detail of nanoparticle growth mechanism in detail. Rapid initial reduction of fraction of precursor is occur in initial stage. Then both coalescence and precursor reduction contributes to the particle growth. The revealed mechanism is not complete agreement with classical LaMer mechanism. In the classical view, the number of particles are constant at certain time. On the contrary, the number of nucleated particles

decrease after nucleation and coalescence dominates the growth. The schematic of the process is shown in Figure 21.

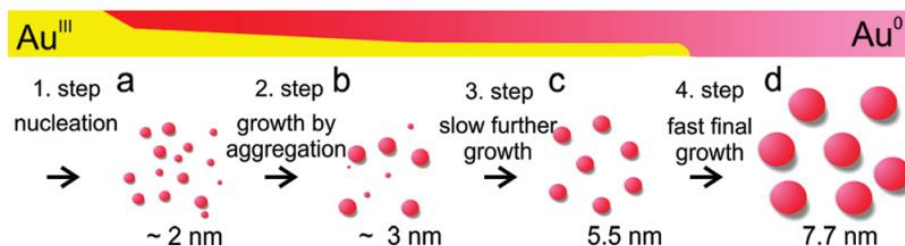


Figure 21. Deduced gold nanoparticle formation process by citrate reduction method.

## 2.2. Seed-mediated Growth Method

### 2.2.1 Electrochemical Synthesis

Though many electrochemical syntheses had been conducted to synthesize gold nanoparticles, use of hexadecyltrimethylammonium bromide ( $\text{C}_{16}\text{TAB}$ ) was firstly reported in the group of Chris Wang in the Journal of Physical Chemistry B in 1997 as far as we know.<sup>18</sup> They recognized that the CTAB acts not only as a electrolyte and but also as a stabilizer for the growth of gold nanorod. Using two electrode configuration with gold (anode) and platinum (cathode) metal plate, they succeed to synthesize nanorods with aspect ratio 2.6 to 7.6. The figure of the synthesized gold nanorod is shown on the Figure 22. Based on the finding, seed-mediated growth has birthed.

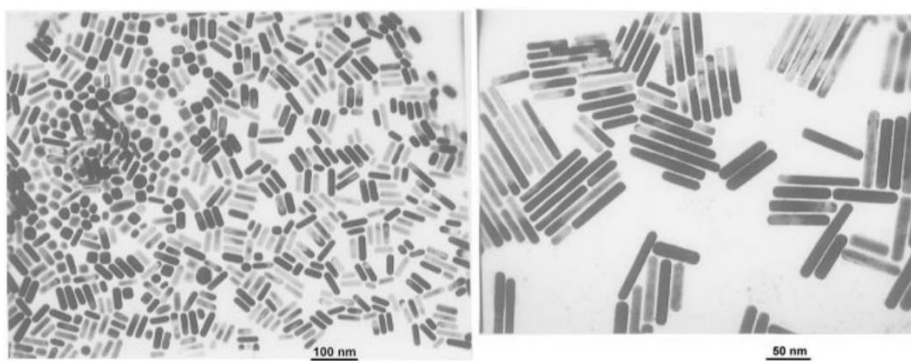


Figure 22. TEM images of gold nanorods synthesized by the electrochemical method with CTAB.

### **2.2.2 Seed-Mediated Synthesis**

In 2001, Catherine J. Murphy's group (R. Jana et al.) reported the seed-mediated growth approach for shaped controlled gold nanoparticles in the *Advanced Materials*.<sup>19</sup> Before the research, the shape-controlled gold nanoparticles have been synthesized using a template such as porous alumina and micelles. The critical point was that the deformation of a template under reaction environments. They achieved different size and shaped gold nanoparticles using controlled nucleation and growth. To initialize seed-mediated method, they prepared small-sized borohydride reduced gold nanoparticles with 3 to 4 nm. The reason for using seed was the increase the kinetic reaction and growth rate. They provided an idea to use an ascorbic acid as a mild reduction agent to start reaction. To control the morphology and increase the yield, they introduced silver ions from silver nitrate ( $\text{AgNO}_3$ ). The shapes of

synthesized gold nanoparticles are taken from TEM as shown in below Figure 23.

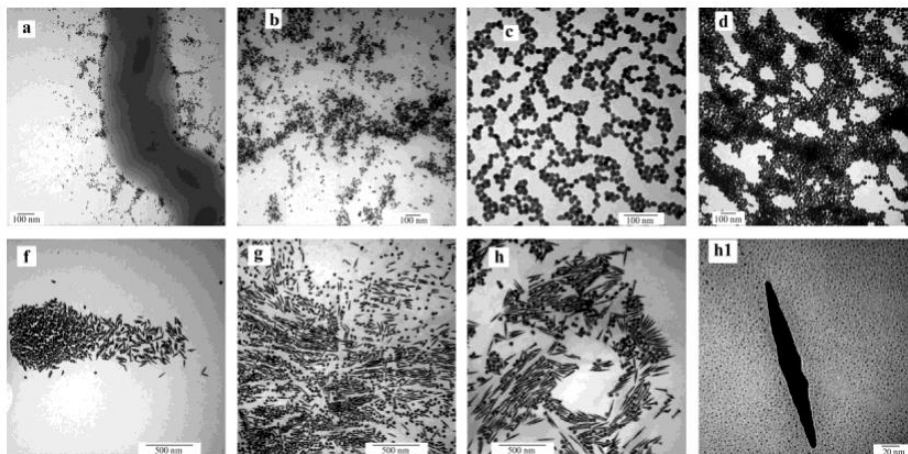


Figure 23 Shape of gold nanoparticles via seeded growth method using CTAB.

From the investigation of the process from El-sayed group,<sup>20</sup> extensive studies provided to reveal the synthesis procedure and structure of nanoparticles in the scientific society.

### 2.3 Seedless Growth Method

R. Jana made a breakthrough for the synthesis of gold nanoparticles in 2005. In the classical seed-mediated growth method needs two essential stages. The first is the synthesis of a seed and the second is the growth of the seeds. Anisotropic monodisperse shape-controlled gold nanoparticles were synthesized by the mixture of strong and weak reducing agent into metal salt. A ratio of borohydride was crucial to control the nucleation kinetic. High ratio of borohydride induced spherical shape from rapid nucleation. While, low ratio of borohydride has slow nucleation so that broad size and shape distribution in

the solution. In addition, the concentration of CTAB was crucial because the shape of micellar structure transition occurs around the 2<sup>nd</sup> critical micelle concentration. Seed concentration and size also contributed a shape of gold nanoparticles. These conditions are deeply investigated in the research. The proposed mechanism according to the various conditions is summarized in Figure 24. The important thing to satisfy the mechanism is the growing nanoparticle should be fixed to the micelle surface (if additive is needed, Ag<sup>+</sup> ions can be added into the solution).

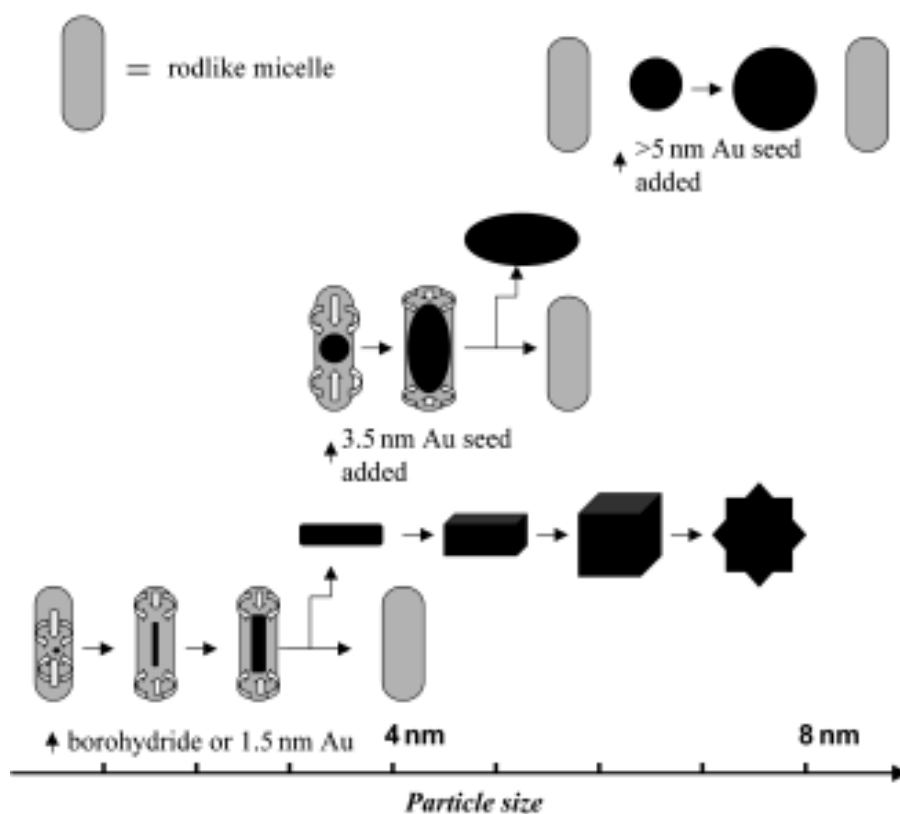


Figure 24 Micelle template induced nanoparticle synthesis by seedless growth.

Further advancement was made after 2012. Moustafa R. K. Ali (El-Sayed group) added hydrochloric acid to enhance the yield and aspect ratio.<sup>21</sup> Due to

the slowed kinetics by lowering pH by hydrochloric acid, they provided more monodisperse solution. However, their synthesis was efficiently activated for small sized gold nanorod. The image of Synthesized gold nanorod is shown on Figure 25.

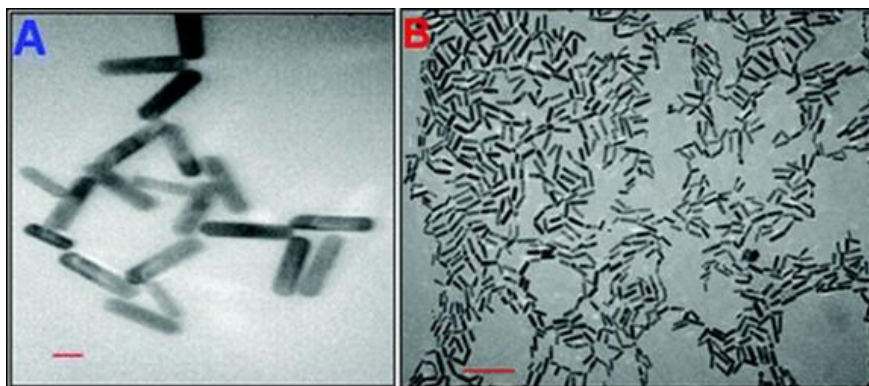


Figure 25. Monodisperse gold nanoparticles synthesized by seedless growth technique.

Xiaolong Xu et al. achieved high aspect ratio gold nanorods in a practical dimension with high yield.<sup>22</sup> By introducing a paradioxybenzene (reducing agent) substitute for a ascorbic acid, the solution overcame the kinetic barrier from pH (hydrochloric acid) and succeed to form high ratio gold nanorods as shown in Figure 26.

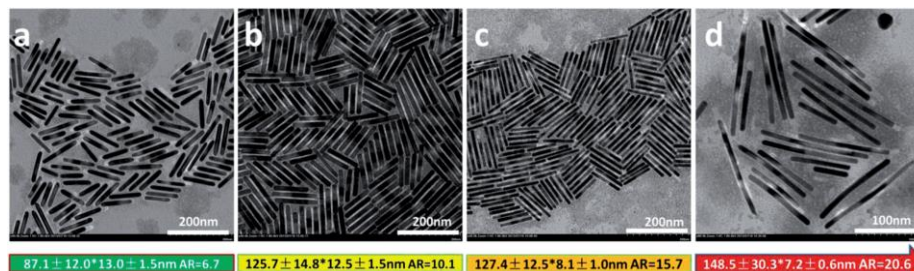


Figure 26. TEM images of gold nanorods synthesized by seedless method.

Various controlled shapes are achieved by precise control of amount in precursor. In the research, concave cubic, cubic, trisoctahedral, nanorods and quasi-spherical gold nanoparticle forms are achieved as shown in below Figure 27.

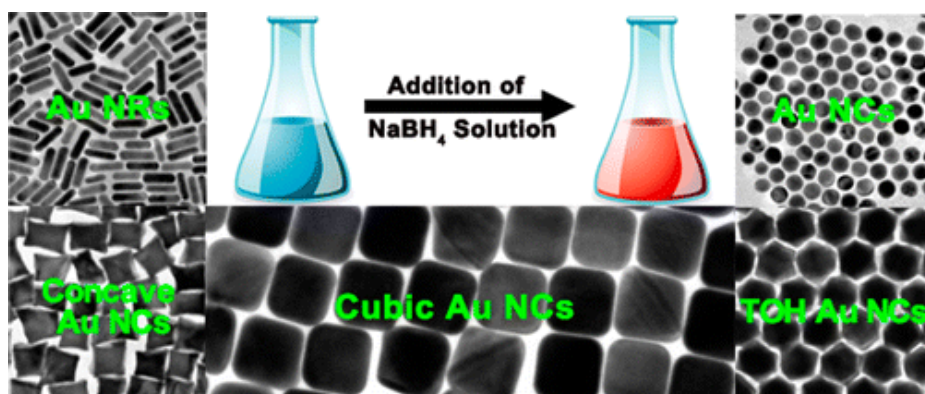


Figure 27. Various shape controlled gold nanoparticles with seedless growth technique.

## 2.4 Shape-Controlled Gold Nanoparticles via Seed-Mediated Growth Method

### 2.4.1 Magic Numbers

Many metals (Al, Ni, Pt, Ag, Cu, Au, and Pb) have face centered cubic (FCC) lattice structure. Candidate noble metals for plasmon resonance are in the FCC structure. Especially, the lattice constant of gold in (100) facet is  $4.078 \text{ \AA}$ . Very small sized gold nanoparticles is called as cluster rather than nanoparticles. These small particles can be synthesized from organic medium due to the necessity of spherical micelle for the synthesis. Even the clusters are not used in the seed-mediated growth method, it can be further utilized in the future. In

addition, the shape in the basic to understand the seed-mediated growth of gold nanoparticles. Someone can refer the details on the review article for metal clusters.<sup>23</sup> The stable and available gold nanoparticle form is given in the below Figure 28. With increasing the size, the percentage of the surface atoms become decrease. The atoms in nanoclusters is calculated as in Formula 2.1

Full-Shell "Magic Number" Clusters					
Number of shells	1	2	3	4	5
Number of atoms in cluster	M <sub>13</sub>	M <sub>55</sub>	M <sub>147</sub>	M <sub>309</sub>	M <sub>561</sub>
Percentage surface atoms	92%	76%	63%	52%	45%

Figure 28 Full-shell magic number formation.

<b>Formula 2.1 Magic number</b>
Magic number for the cluster and surface of the cluster.
$N = 1/3 (10 n^3 - 15n^2 + 11n - 3)$
$N_{\text{surf}} = 10 n^2 - 20n + 12$

## 2.4.2 Understanding of Anisotropic Growth by LaMer Model

The explanation is adopted from recent perspective article.<sup>24</sup> General nanoparticle seed formation is described in Figure 29 (section A). If surplus monomer above the solubility level is provided, the solution become saturated and nucleation starts at certain concentration level. At the high level, monomer clusters are in the equilibrium. The equilibrated clusters are the seed for the

generation of gold nanoparticles in solution. As a result, the clusters become nanoparticles and the monomer concentration become saturated. In comparison, the nanoparticle formation from the seed mediated growth is depicted in Figure 29 (section B). The concentration below critical concentration does not occur seed generation normally. Because self-induced nucleation is not activated. If we add some seed in the solution, the seed formation process can be neglected. In addition, due to the anisotropy of seed particle, saturation concentration and activation energy become reduced. So at the stage with seed particles, growth is available.

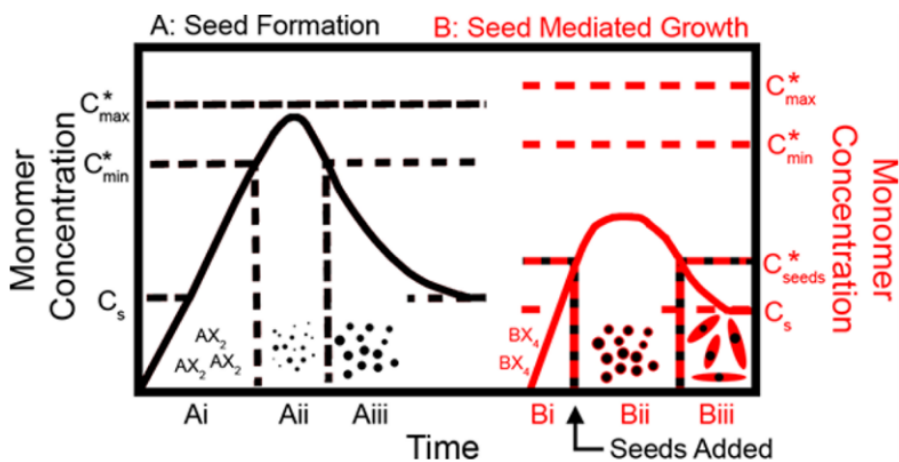


Figure 29. LaMer model for monodisperse particle formation and seed-mediated growth particle formation.

### 2.4.3 Unit Stereographic Triangle of Gold Nanoparticles

For gold (FCC crystal), the three low-index planes ((111), (100) and (110)) are represented at the vertex of the triangle. The coordination number of the plane is 9, 8 and 7. The possible crystal structure having

single atomic facet is elucidated in Figure 30.<sup>25</sup> Actual possible shape is more complicated due to the entwining of facets across the surfaces and twins. For example, the mixture of octahedron and cube shape would be truncated octahedron. From multiple twinned seed, icosahedron is also possible. This indicates the possible shape is not much confined the unit stereographic crystals.

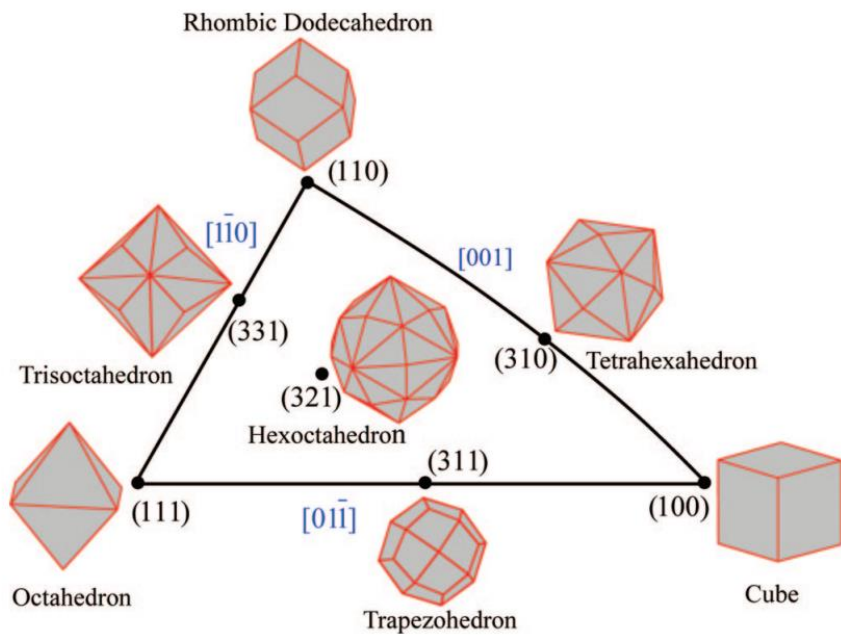


Figure 30. Unit stereographic triangle showing crystal structure have a single atomic facet.

#### 2.4.4 Surface Energy

The surface energies ( $\gamma$ ) for FCC metals showing similar tendency. It is usually  $\gamma(111) < \gamma(100) < \gamma(110) < \gamma(hkl)$  as are shown in Figure 31. The calculation shows that gold has lowest surface energy. It indicates that high chemical

activity for the solution process. While, the high surface energy of Rh indicates, the metal Rh is hard to synthesize from solution process due to the high surface energy.

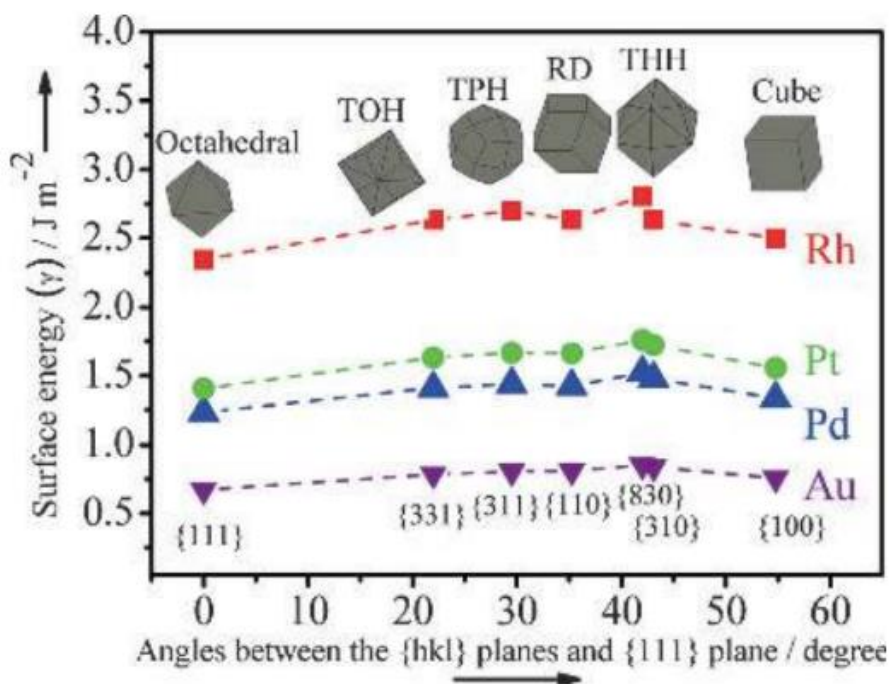


Figure 31. Variations of surface energy according to the facets and metals: trisoctahedron (TOH), trapezohedron (TPH), rhombic dodecahedron (RD), tetrahexahedron (THH), and cube.<sup>26</sup>

Above calculation is well fitted to experimental results in Figure 32. Figure 32 (a) shows exchange current density for oxygen reduction reaction of platinum electrode in sulfuric acid (H<sub>2</sub>SO<sub>4</sub>). The activity was lowest at (111) surface which is identical to the tendency for the surface energy.<sup>27</sup> Similarly, for organic molecule reduction, the octahedral gold nanoparticles showed lowest catalytic

activity to 4-nitroaniline reduction. Overall result indicates that the catalytic activity is analogous to the tendency the surface energy of facet.

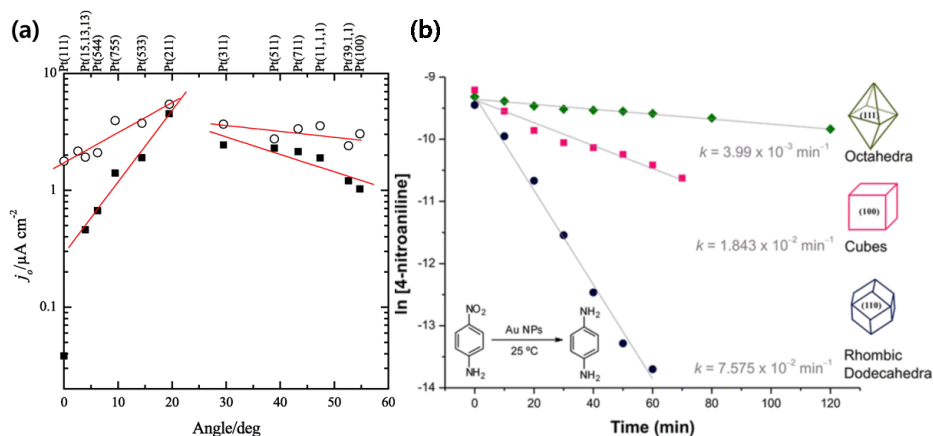


Figure 32 (a) Exchange current density for platinum electrode according to the facet. (b) Reduction of 4-nitroaniline according to the facet.

## 2.4.5 Shape of Seeds

The final shape is determined by several factors including kinetics, thermodynamics, additives such as capping agents. Depending on the growth rates of the specific direction, anisotropic shape is achieved. (100) and (111) facet is mainly considered. The yellow indicates the (111) facet and green indicates the (100) facet. R indicates the growth rates of directions ([100] / [111]). The single crystal seeds can evolve into the octahedron, cuboctahedron and cube. With selective activation, the single-crystal rod and bar also formatted. With twinned crystal, the shape with low symmetry is possible. Right bipyramid, decahedron and icosahedron is also possible. Plate-like shape is also possible with kinetic control of growth by prohibition of evolution into specific facet.

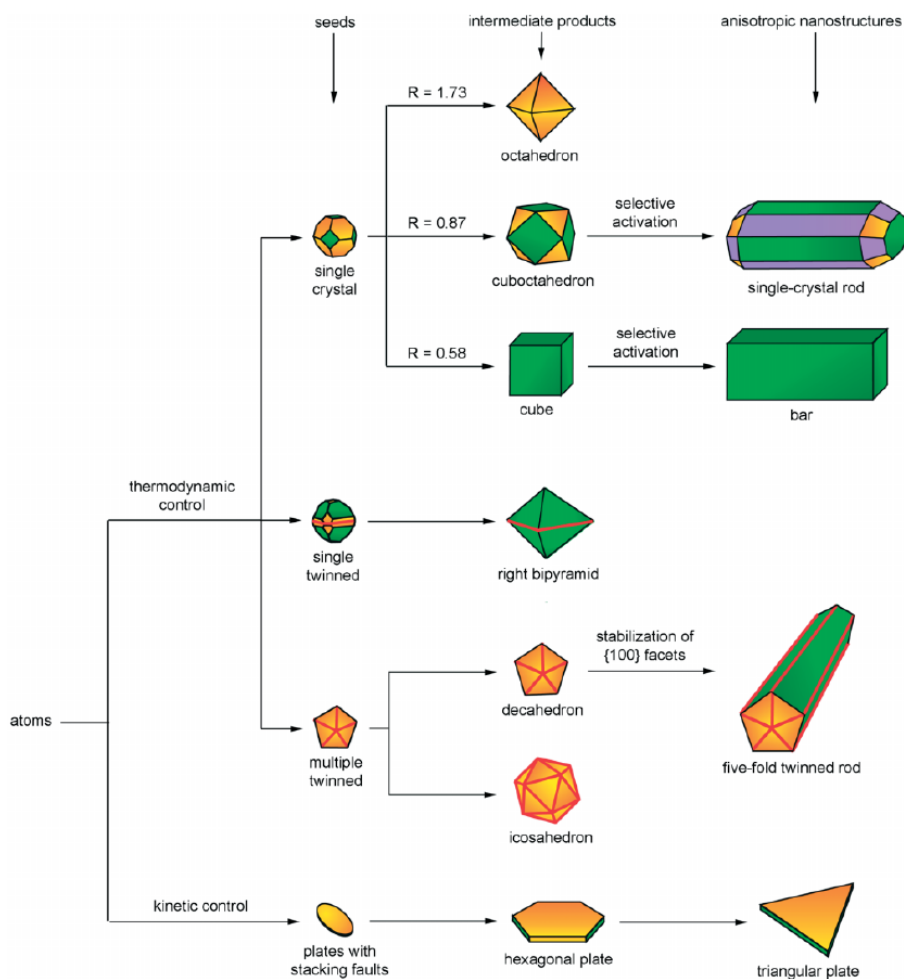


Figure 33. The schematic illustration of the reaction pathways of anisotropic gold nanoparticles.<sup>28</sup>

## 2.4.6 Effect of the Halide Ions.

Three kinds of halide ( $\text{Cl}^-$ ,  $\text{Br}^-$ ,  $\text{I}^-$ ) are adopted for the synthesis of gold nanoparticles via seed-mediated growth method. A binding strength of the halides to the gold surface is increasing in the following sequence  $\text{Cl}^- < \text{Br}^- < \text{I}^-$ .<sup>29</sup> Besides the binding strength, the reduction potential of Au-halide complex

$[\text{AuX}_2]^-$  decreases in order  $(1.154 ([\text{AuCl}_2]^-) > 0.960 ([\text{AuBr}_2]^-) > 0.578 ([\text{AuI}_2]^-))$ .

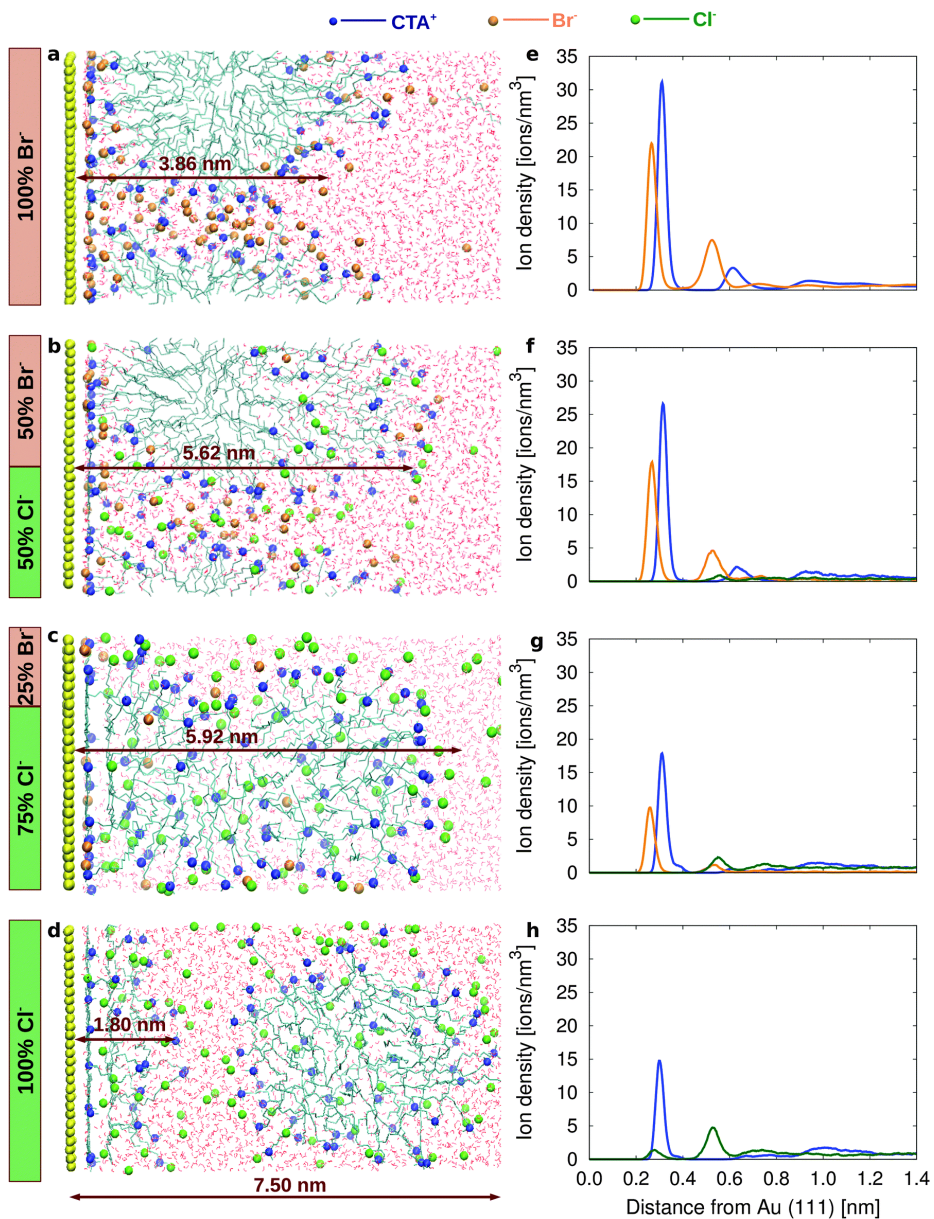


Figure 34. CTAB/C distribution on gold surface by molecular simulations.

The growth control of gold nanoparticles with halide is investigated by molecular simulations. The CTAB molecule formed a dense micellar layer on

the gold surface. While the CTAC molecules does not effectively absorbed on the surface. The molecular absorption is supported by experimental evidence.<sup>30</sup> Due to the high reduction potential with chloride, the rate of gold ion reduction is slower than other halide. So lower-energy surface facet is preferred. Iodide considered to have strong binding to (111) facets.<sup>31</sup> For example, in the identical conditions, the shape of product particle is changed according to the halide ions as shown in Figure 35.

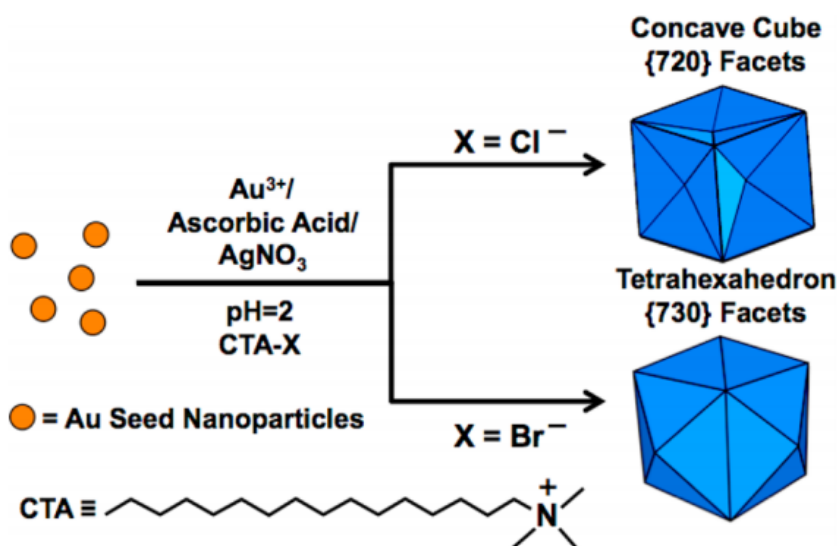


Figure 35. Chloride containing surfactant results in (720) facets and bromide containing surfactant results in (730) facet.

With increasing the concentration of iodide, as shown in Figure 36, the (111) facet dominant plate shape is arisen. The preferential binding into (111) facet can be shown via XPS analysis for  $\text{I}^-$  3d orbital.

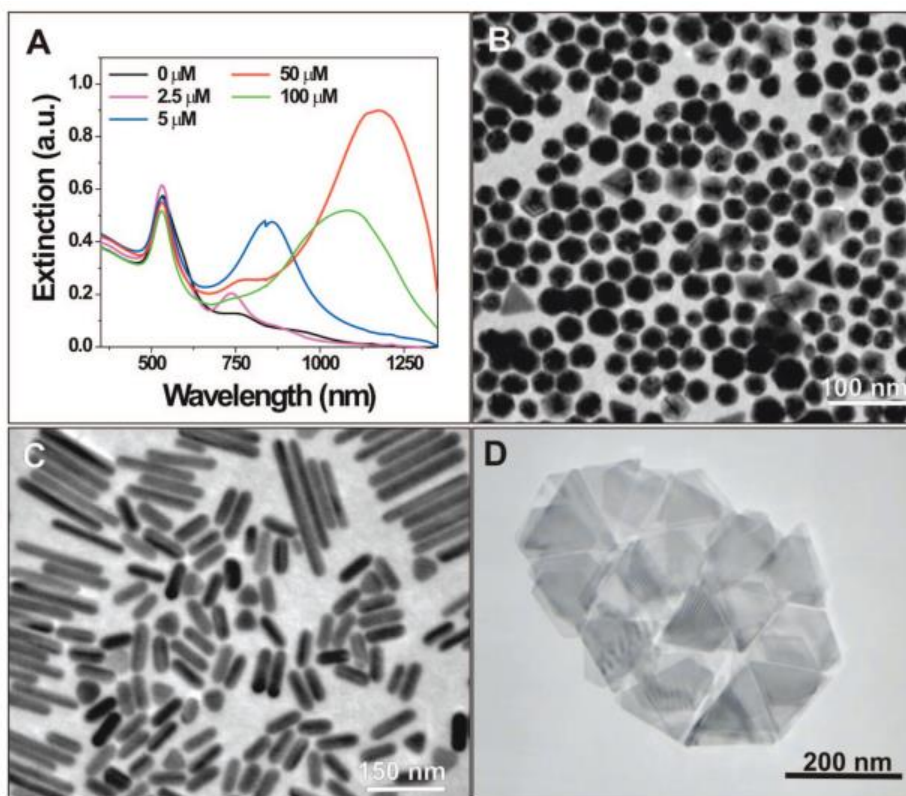


Figure 36. Formation of Au nanoplatelet via addition of iodide ions.<sup>31</sup>

### 2.4.7 Effect of the Ascorbic Acid Concentration.

In the seed-mediated growth method, the introduction of ascorbic acid to reduce gold ions (III) to gold ion (I) state is essential. The addition of ascorbic acid is related to the kinetic growth of gold nanoparticles. Higher concentration of ascorbic acid induces fast gold ion reduction, guiding to the high index facets. The experimental evidence is included in Figure 37 and 38.

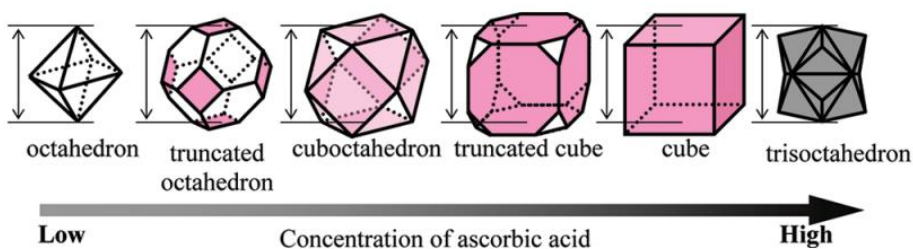


Figure 37. Polyhedral gold nanoparticles according to the rate or reduction.<sup>32</sup>

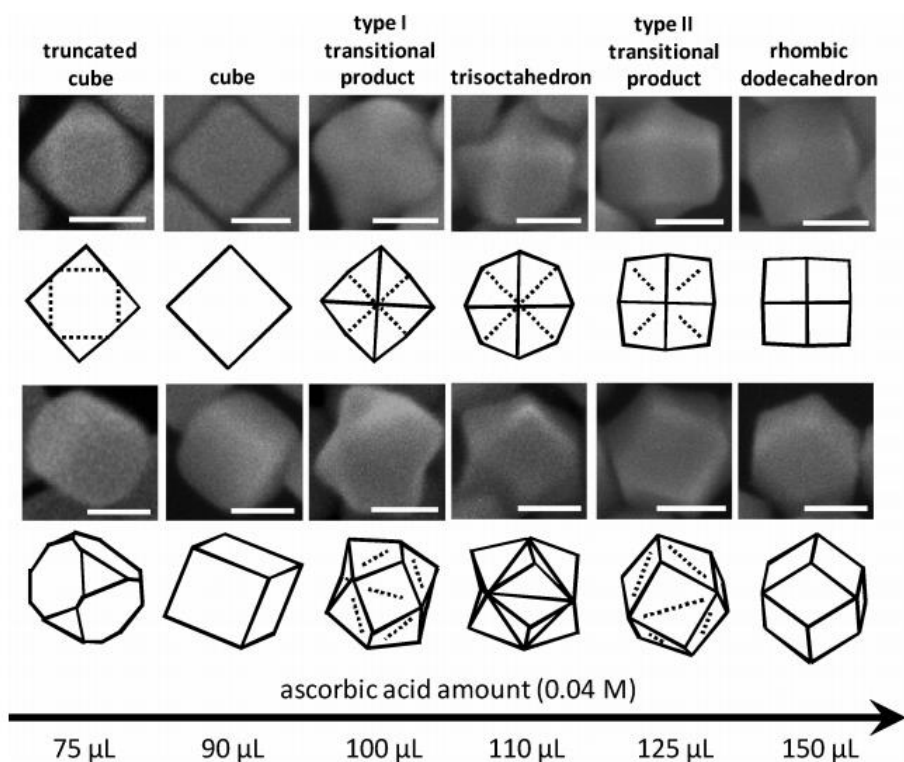


Figure 38. Polyhedral gold nanoparticles according to the rate or reduction.<sup>33</sup>

## 2.4.8 Effect of the CTAB concentration.

Without addition of CTAC in the solution, the synthesized product shape is highly dependent on not only ascorbic acid concentration but also CTAB capping agent concentration. Because the suppression of the growth with CTAB precursor for the (100) surface, synthesized gold nanoparticles prefer to

enclose by (110) facets. Rhombic dodecahedra shape is preferred in a high concentration of CTAB and nanorods-plate mixture is preferred in a low concentration of CTAB. The general tendency for the synthesis is described in Figure 39.<sup>34</sup> Note that, octahedral shape is not possible to synthesis from the procedure due to the depression of generation of (111) facet.

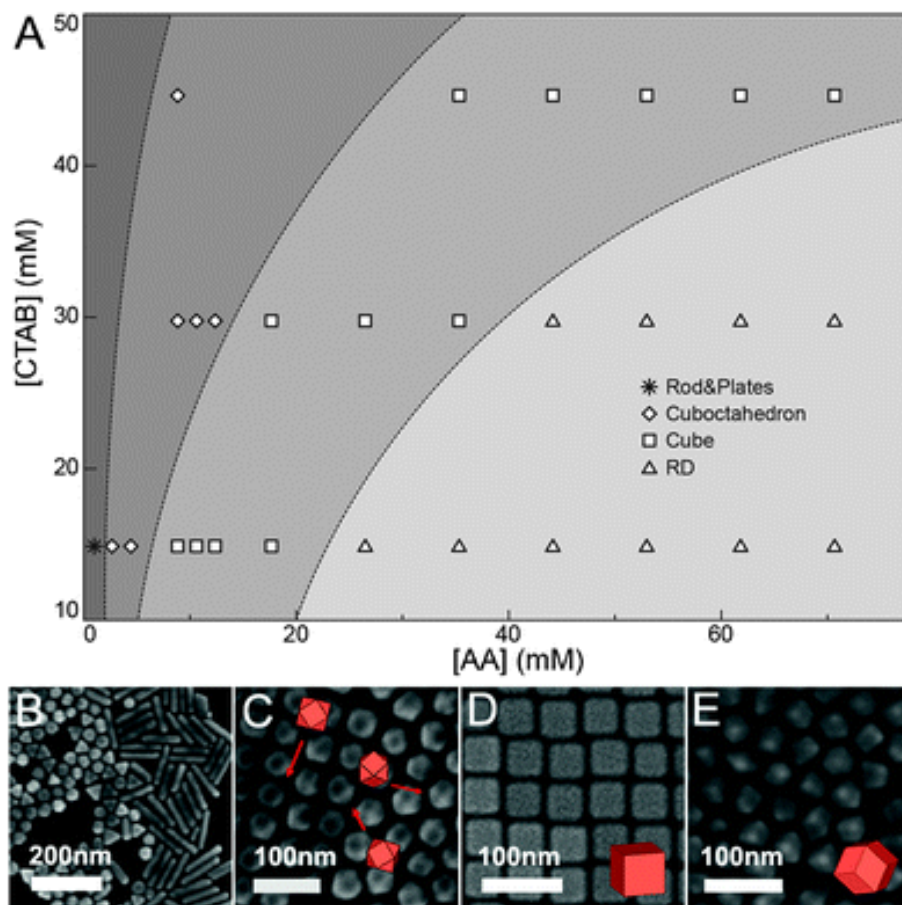


Figure 39. Morphology evolution of gold nanoparticles with a function of CTAB and ascorbic acid.

## 2.5 Capping Layer of Gold Nanoparticles

### 2.5.1 Zeta Potential

The shape of material is thermodynamically controlled to have minimum surface energy. This criterion indicates that the generation of nanoparticle is an unfavorable thermodynamic process. To overcome this barrier, the change of surface energy is required to prevent agglomeration by thermodynamic criteria. This is achieved by introducing capping layer to stabilize gold nanoparticles. The potential related to the surface charge, we call it as zeta potential. If the surface of gold nanoparticle is charged with positive charges, the zeta potential is positive and vice versa. The graphical representation of the zeta potential in the gold nanoparticles is provided in Figure 40.

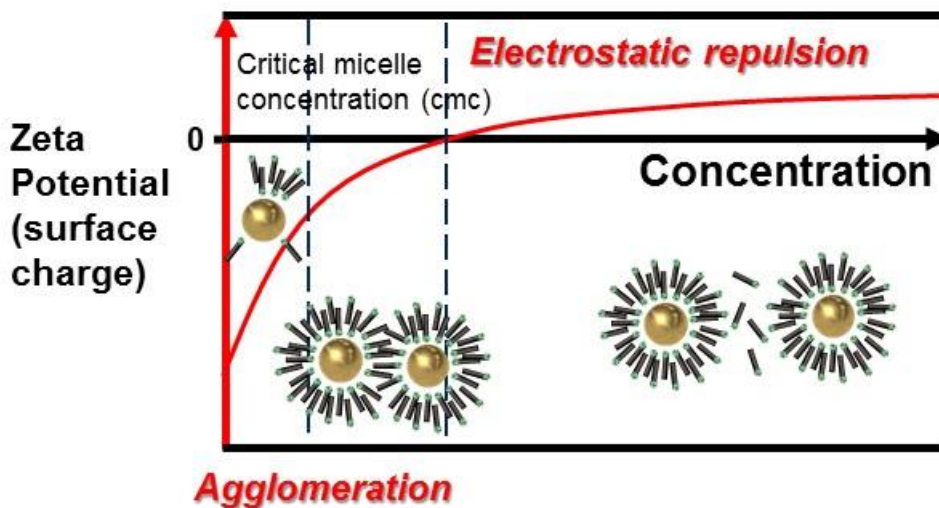


Figure 40 Graphical representation of zeta potential.

Zeta potential is closely related to the stability of the micelle on the surface of gold nanoparticles. Below the critical micelle concentration, the particles

cannot be existing into separated states and become coalescence with aggregating some portion of gold nanoparticles. The critical micelle concentration means zero charge (zeta potential) at the surface of gold nanoparticles. At some concentration much below than critical micelle concentration, the gold nanoparticles in water do not exist even in a coalescence form. The gold nanoparticles in the state become totally agglomerate and the color of solution become blue pale or transparent due to the precipitation of all gold nanoparticles. In addition, the zeta potential of gold nanoparticles is different slightly according to the shape shown as below Figure 41.

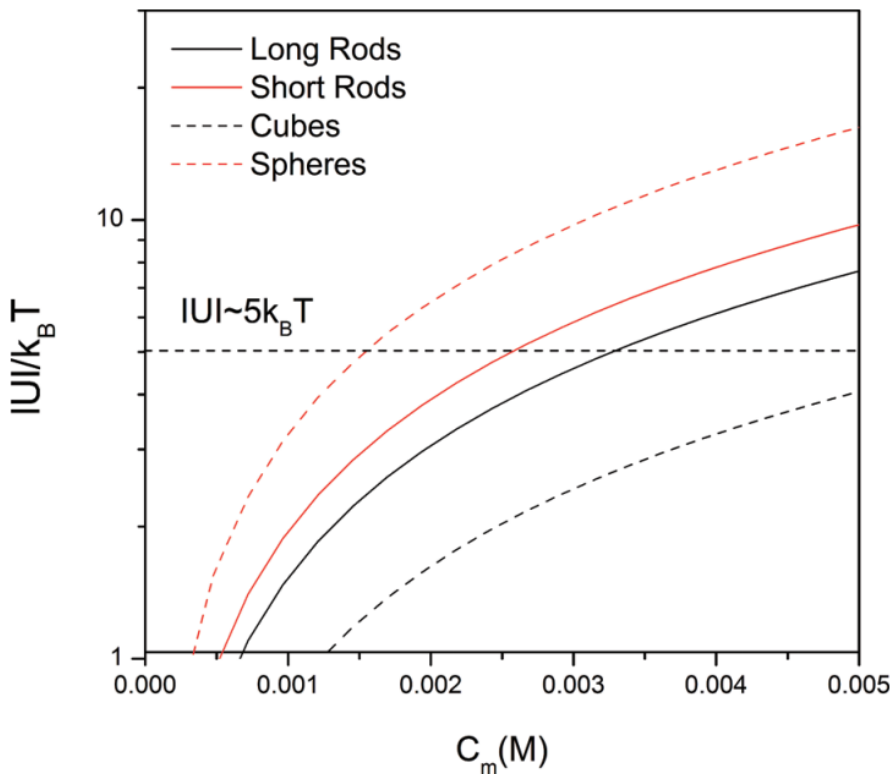


Figure 41. The difference of zeta potential of gold nanoparticles (in form of depletion interaction potential) with shape.<sup>35</sup>

Anisotropic shape has much lower critical micelle concentration according to the result. This property can be used the separation of nanoparticle shapes in gold nanoparticle colloids.

## 2.5.2 Capping layer in Gold Nanoparticles

The well-known particle two synthesis method is the citrate reduction method and the seed-mediated growth method. The two methods use different molecules to stabilize gold nanoparticles on the surface. Citrate reduction method uses a sodium citrate ( $\text{Na}_3\text{-Cit}$ ) as a reduction and capping agent. Seed-mediated growth method uses CTAB/C as a capping agent. As a result of ionic structure of two molecules, the nanoparticles become charged with negative and positive. The schematic feature is expressed on Figure 42.

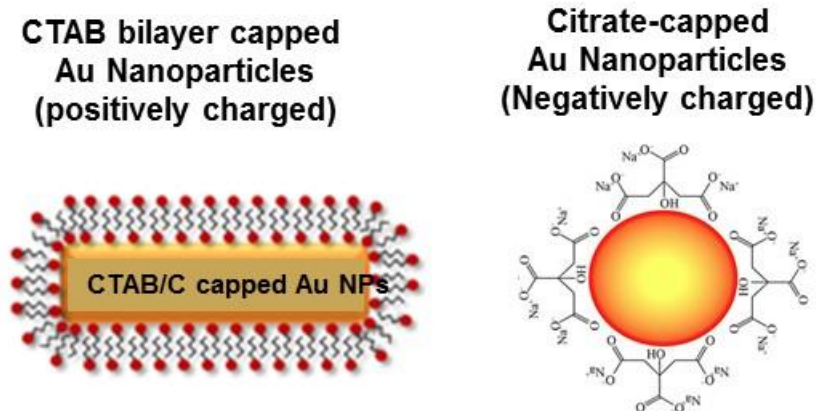


Figure 42 Capping layer structure in gold nanoparticles.

The molecules are bounded to gold surface due to the ionic nature. Especially, CTAB/C molecule is quite special. They exist as a bilayer structure on the

surface of gold nanoparticles. To explain the reason, the structure of CTAB is shown on Figure 43.

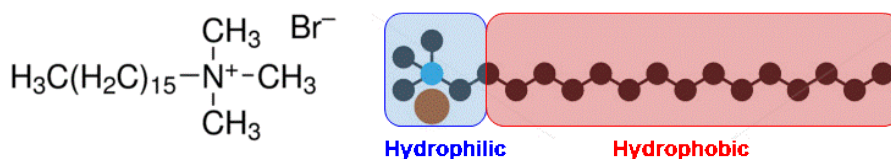


Figure 43. Amphiphilic structure of CTAB molecule.

Due to the amphiphilic property from the long hydrocarbon chain of hydrophobic in the tail, the CTAB molecule do not solely absorb onto the surface of gold surface. Hydrophobic chain should be in close together to provide hydrophilic property on the surface of gold nanoparticles (as a reference, the bilayer structure in the organic phase is reverse).

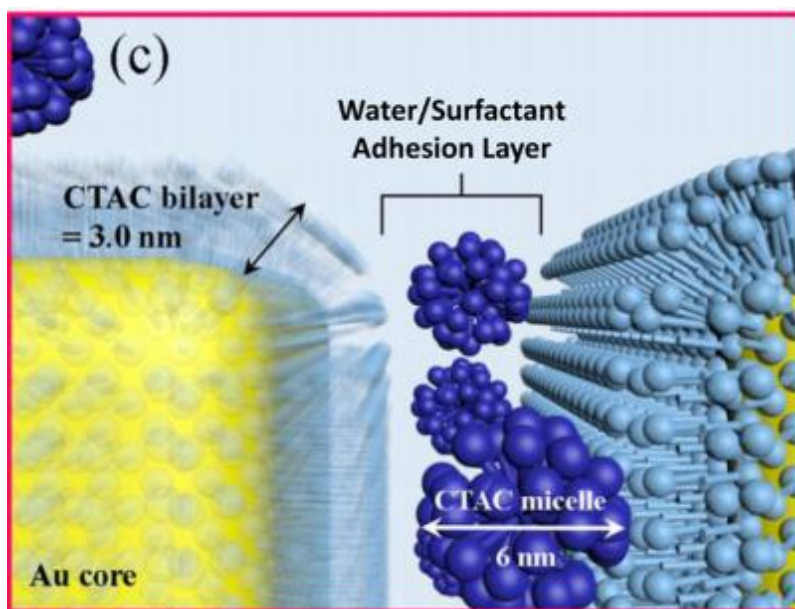


Figure 44. Graphical representation of CTAC bilayer structure (CTAB is also similar).

The structure is investigated with time and spatially resolved X-ray scattering technique recently (small angle scattering of X-rays/neutrons, SAXS/SANS).<sup>36</sup> They revealed the bilayer structure of gold nanoparticle on (100) facet as 32 Å . Graphical representation is adopted from the article in Figure 44.

### 2.5.3 Linker Molecule (Gold Surface Absorber)

There are four types of surface absorber terminal group is widely known for a stabilization of gold nanoparticles. Two types (carboxyl and nitrogen ion) are initialized by ionic property (ionic bonding). And other two types (phosphor and thiol) are initialized by electron affinity (covalent bonding). Molecule having those structure can be attached into the gold surface as shown below example Figure 45.

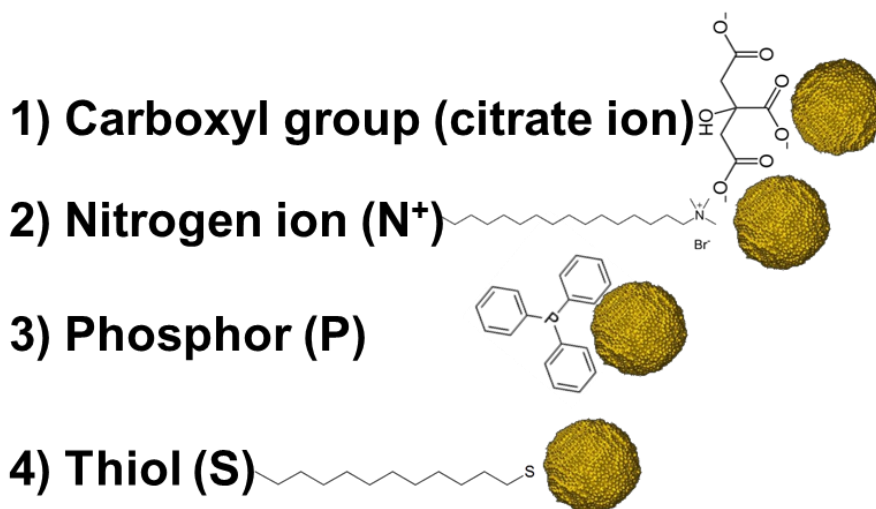


Figure 45. Functionalized group for surface absorber.

### 2.5.4 Linker Molecule (Semiconductor Surface Absorber)

A surface adsorption of molecule into semiconductor is usually initiated by an oxygen dissociation into the surface. To realize the surface absorption into the semiconductor, the surface absorber molecule should be oxygen functional group at the terminal. Three functional group (silicic, hydroxide and carboxylate) is widely adopted for this procedure. The adsorption structure is given at the Figure 46.

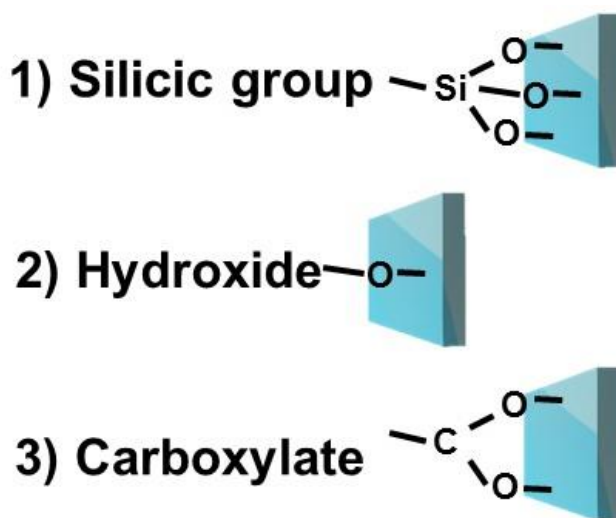


Figure 46. Surface absorption structure of the molecule having oxygen in function group.

### 2.5.5 Molecules for the Gold Nanoparticle Attachment

To attach gold nanoparticles on the targeted semiconductor, above considerations should be reconsidered. Especially, the linker molecule for this purpose should fulfill the conditions given in section 2.5.3 and 2.5.4. Fortunately, sodium citrate itself fulfills the requirement. While the CTAB molecule is not. So additional linker molecule should be hosted for the process.

In the research, 3-mercaptopropionic acid (HS-(CH<sub>2</sub>)<sub>2</sub>-COOH) is adopted for the purpose. The molecular structure is given in the below Figure 47.

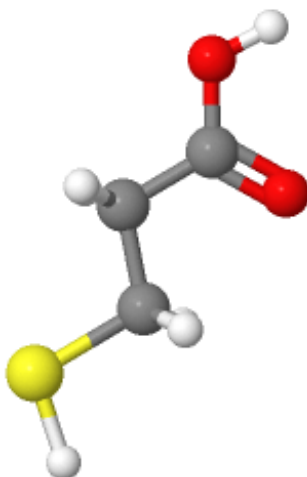


Figure 47. Structure of 3-mercaptopropionic acid.

## 2.6 Synthesis of Quasi-Spherical Gold Nanoparticles

The synthesis of citrate-stabilized quasi-spherical Au nanoparticles was proceeded based on the method reported in *Langmuir* (2011).<sup>37</sup> 2.2 mM sodium citrate aqueous solution (50 mL) was heated in a beaker under vigorous stirring at 90 °C. After the solution had formed, 25 mM HAuCl<sub>4</sub> aqueous solution (0.35 mL) was injected. The solution was left for around 15 min to generate the Au seeds. Next, 18.35 mL of the solution was discarded, then 60 mM sodium citrate aqueous solution (0.65 mL) and water (17.7 mL) were added to the seed solution. This solution was then left for around 15 min. 0.35 mM HAuCl<sub>4</sub> aqueous solution (0.35 mL) was then injected, and the solution was left for around 15 min. Then, 0.35 mM HAuCl<sub>4</sub> aqueous solution (0.35 mL) was again injected into the solution and the solution was left for around 15 min. This entire

process was twice, at the temperature condition of 90 °C. The resulting solution contains citrate-stabilized quasi-spherical Au nanoparticles of around 30 nm diameter.

## **2.7 Synthesis of Octahedral Gold Nanoparticles**

### **2.7.1 Synthesis of CTAC-capped Au seeds.**

A seed-mediated growth method is used for the synthesis of shape-controlled Au nanoparticles. First, CTAB-capped Au seeds were synthesized from a strong reduction agent ( $\text{NaBH}_4$ ). 10 mM ice-cold  $\text{NaBH}_4$  aqueous solution (0.6 mL) was added to a 10.0 mL aqueous solution (incorporating 0.25 mM  $\text{HAuCl}_4$  and 100 mM CTAB). The brownish seed solution was stirred for 2 hours at 30 °C to decompose the remaining  $\text{NaBH}_4$ . Next, CTAC-capped Au seeds were synthesized from the CTAB-capped Au seeds. Then, 100 mM (1.5 mL) AA was added to another aqueous mixture solution (incorporating 5 mM  $\text{HAuCl}_4$  (0.2 mL), 200 mM CTAC (2 mL) and water (1.8 mL)). After the color change of the mixture solution from yellow to transparent, 100  $\mu\text{L}$  CTAB-capped Au seed solution was promptly injected. The solution was left in room temperature until a red-wine color was seen. The as-synthesized Au seeds were concentrated by centrifugation and redispersed in 1 mL of 20 mM aqueous CTAC solution.

### **2.7.2 Growth of octahedral Au nanoparticles.**

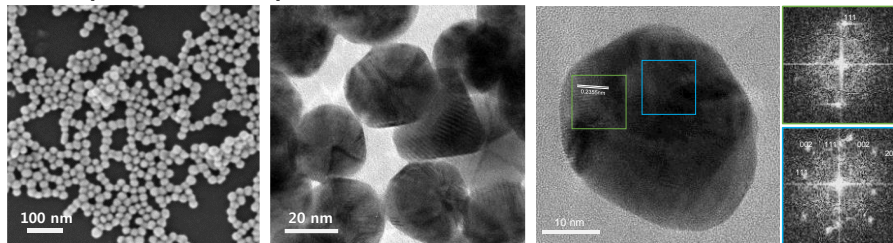
100  $\mu\text{L}$  of the redispersed CTAC seed solution was rapidly injected into the transparent aqueous growth solution (incorporating 5 mM  $\text{HAuCl}_4$  (0.4 mL),

200 mM CTAB (0.5 mL), 200 mM CTAC (4.5 mL), 100 mM AA (60  $\mu$ L) and water (4.3 mL)). Stirring was vigorously performed during the growth process.

## **2.8 Characterization of Gold Nanoparticles.**

As shown in Figure 48, quasi-spherical and octahedral Au NPs were well synthesized using seed-mediated growth methods<sup>37,38</sup> and consisted of the lowest energy facets of (111) planes.<sup>39</sup> The image on the figure is produced with the SEM-TEM. Au NPs synthesized from citrate stabilization were nearly spherical and their averaged size estimated to be 31.1 nm, whereas the octahedral Au NPs synthesized from cetyltrimethylammonium bromide/chloride (CTAB/C) stabilization were in a highly monodisperse manner and their averaged-size was around 33.5 nm (Figure 49a). The UV-VIS absorption spectra of the synthesized Au nanoparticle solutions containing quasi-spherical and octahedral Au NPs exhibited a LSPR peak at 520 and 550 nm, respectively (Figure 49b). The discrepancy with plasmon resonance wavelength between the shapes is mainly attributed to the sharp edges and vertices of shape in octahedral Au NPs.<sup>40</sup> These peaks were red-shifted on the surface of the TiO<sub>2</sub> films due to dielectric constant change.<sup>41</sup>

### Quasi-spherical Au nanoparticles



### Octahedral Au nanoparticles

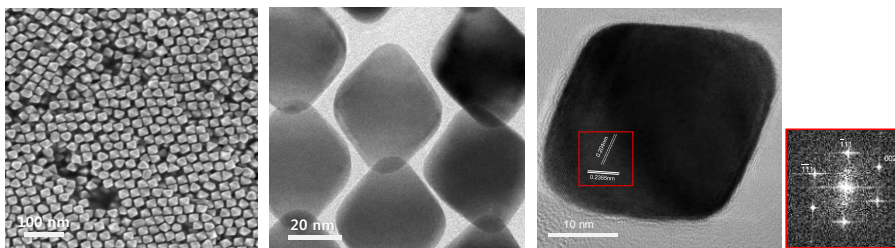


Figure 48. The SEM-TEM image of quasi-spherical and octahedral gold nanoparticles

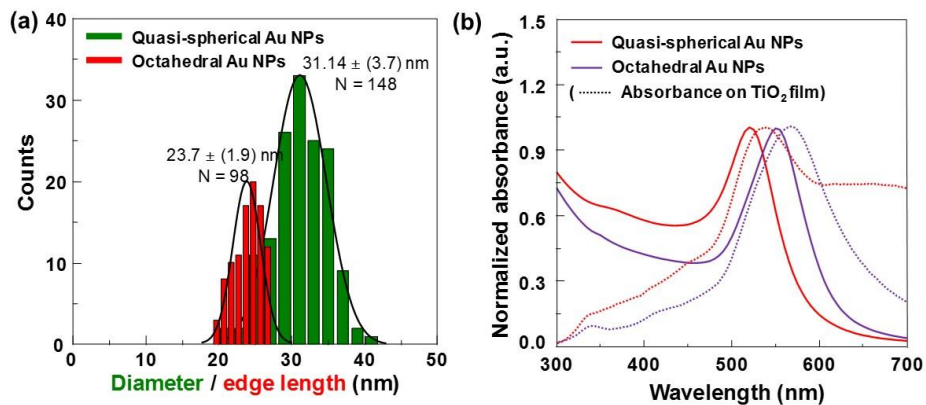


Figure 49 (a) Diameter (for quasi-spherical) and edge length (for octahedral) distribution of Au NPs (please note that the diameter of a circumscribing sphere of octahedron is  $\sqrt{2}$  times greater than edge length). (b) Normalized absorbance of synthesized solutions containing Au NPs. Dotted line (...) indicates corresponding absorbance on  $\text{TiO}_2$  film.

## 2.9 Attachment of Gold Nanoparticles.

This process was developed on the basis of the sodium citrate absorption process reported in *JACS* (2010)<sup>42</sup>. Octahedral shaped Au decoration was carried out as follows. 1 mL octahedral shaped Au nanoparticle solution was added to a 10mL scintillation vial. The objective samples were immersed into the octahedral shaped Au nanoparticle solution. Then, a solution containing 0.5 M mercaptopropionic acid (MPA) and 0.5 M sodium hydroxide (NaOH) was added to the octahedral shaped Au nanoparticle solution. Similarly, 1 mL quasi-spherical Au nanoparticle solution was added to a 10 mL scintillation vial. The objective samples were immersed into the quasi-spherical Au nanoparticle solution. A solution containing 1 M citric acid was then added to the quasi-spherical Au nanoparticle solution. The coverage of the octahedral shaped Au nanoparticle on the samples is controlled by changing the volume of the mixture solution. A precipitator solution was directly added to precipitate nanoparticles (0.5 M MPA and 0.5 M NaOH, 1 M citric acid aqueous solution). Schematic of the process is provided in Figure 50.

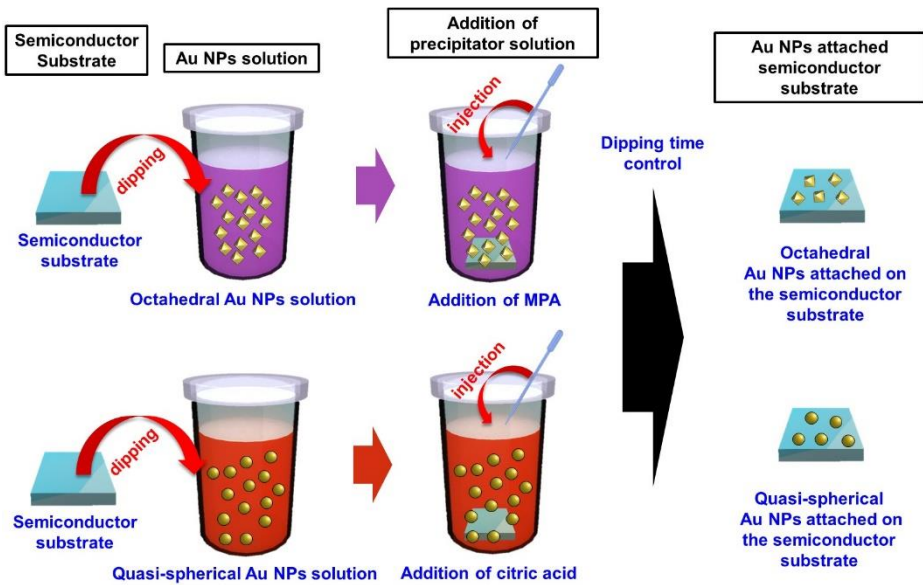


Figure 50. Schematic representation of the process.

## Chapter 3

### Gold for Plasmon Resonance

#### Quote

**R. H. Ritchie**

"This distribution exhibits both collective interaction characteristics and individual interaction characteristics, and is more general than the result obtained by other workers." (1957, Physical Review)

### 3.1. Wood's Anomalies

#### 3.1.1 Anomalous Diffraction Gratings

If diffraction grating is inserted into the path of incident light, pattern having maxima/minima is generated according to the diffraction grating theory (by the Fourier transform). The light is unequally positioned through the space. One of the good image is attached in Figure 5 for the understanding.<sup>43</sup> According to diffraction formula, Rayleigh expected pattern position according to the Formula 4.1.

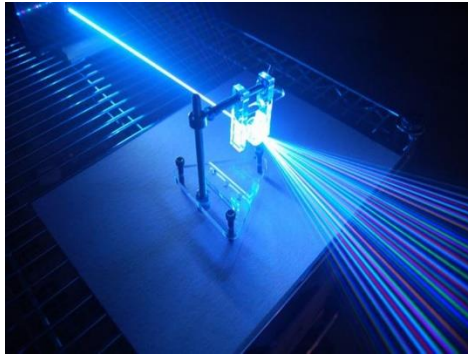


Figure 51. Example of He-Ne laser induced diffraction grating pattern.

#### Formula 3.1 Diffraction grating formula

$$\frac{n\lambda}{d} = -\sin\theta \pm 1, (n = \pm 1, \pm 2, \pm 3 \dots)$$

In 1902, Wood tested diffraction property with metal gratings.<sup>44</sup> While the experiment, he found anomalies (French word: strange things) for the diffraction pattern. He used incandescent light (continuous spectra over visible wavelength). He putted grating on the way of light path and changed the

incident angle will make change of the position of diffracted wave. He recorded the pattern by camera in the Figure 6 (adopted from the Wood's investigation). As we expected, position of the diffracted wave should be changed according the incident wave angle.

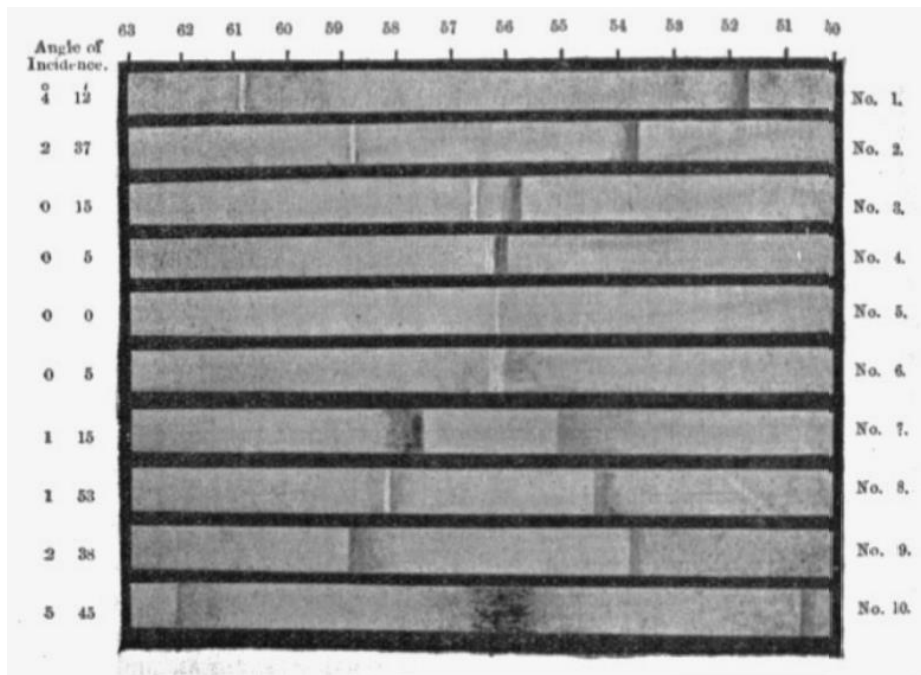


Figure 52. Spectra of a continuous light source by metal grating.

From number 1 to number 5, the appeared line patterns (bright line (610 nm) and dark line (520 nm)) in number 1 become contacted at normal incident (number 5). Two Dark lines appear while rotating the incident ray in reverse direction. As we seen at number 7 the dark line at 580 nm become extremely dark than other position. The dark line at number 7 become extremely white (like a white light at center position) at number 8. After the circumstances, the lines changed to original state as expected. The sudden intensity change is seen only narrow range. In the shiny region, light is totally transparent from metal

grating. And in the dark region, light is totally reflected from metal gratings. In addition, he tested with polarized light at grating. The result was very strange. Only p-polarized light evokes the phenomena. The further investigation has been given in his life to explain the anomalies.<sup>45</sup>

### **3.1.2 Fano Type Resonance in Metal Gratings**

In the history, many resonance phenomena have been interpreted with harmonic motion model in classical system. These resonances are frequently described by Lorentzian resonances. It has been considered the fundamental resonance model in a long time. The resonance is induced by independent resonator which have its own vibration system fixed into the background. The interaction between the resonator has not been considered in the classical system. However, an emergence of quantum mechanics totally changed the system. In 1961, Ugo Fano announced a different type of resonance model in the Physical Review (recently we call the model as Fano type resonance).<sup>46</sup> The essential part of disparity between two model is resonator interaction. A mathematical description of the models is given in the Formula 3.2 and graphical description of the models are given in the Figure 7. Fano explained the Wood's anomalies using his model. The unexpected position at the metal

diffraction grating can be explained using a forced resonance related to the leaky waves supported by the grating.

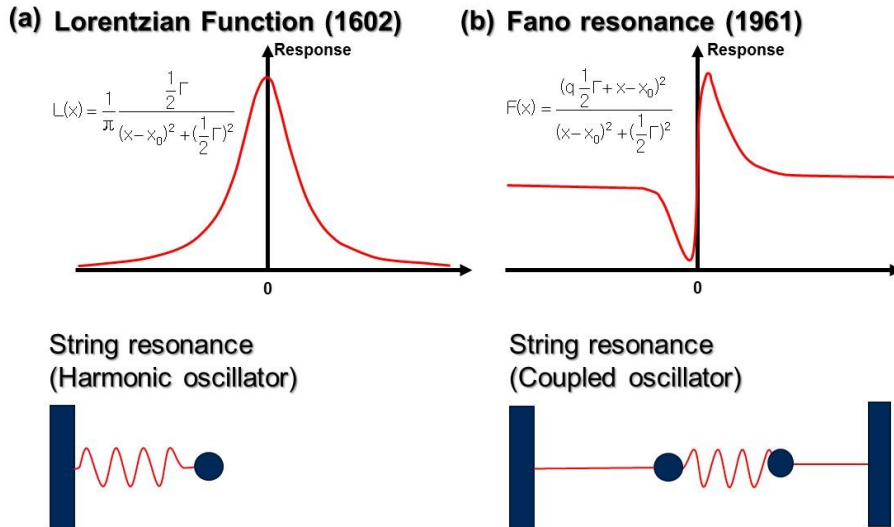


Figure 53. Lorentzian (a) and Fano (b) resonance model

Detailed explanation of the model is given in recent review.<sup>47</sup> Fano resonance is the quantum interference of two resonate states. In detail, the Fano resonance mode is the result of discrete state (interaction) and continuum state (quantum mechanics) of two process as shown in the Figure 8.

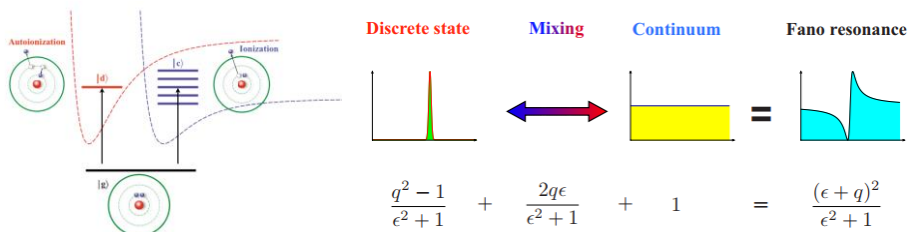


Figure 54 Explanation of the meaning of the Fano formula.

In the plasmonics, due to the interaction of metallic atom and electrons in the system Fano resonance is observed. Even a well-known light scattering property anticipate the resonance of the Plasmonic system, it is not sufficient. The exact, detailed and multipole resonance mode is achieved with Fano resonance with quantum mechanical description. The excellent example from the review is incorporated into the manuscript in Figure 9.<sup>48</sup>

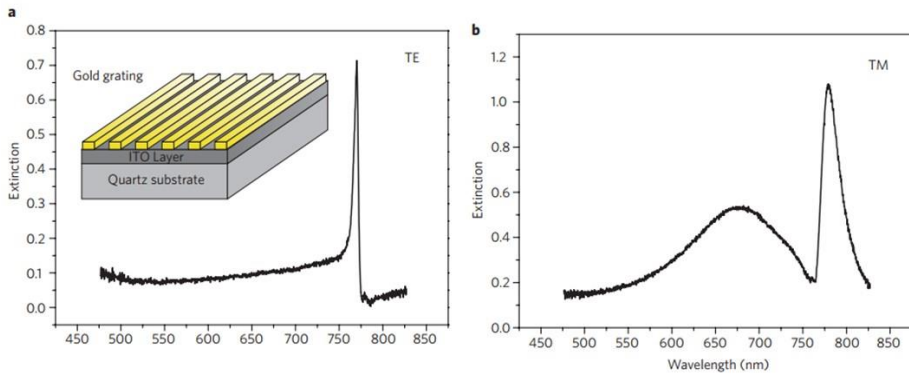


Figure 55 Fano resonances in a metallic photonic crystal, consisting of a gold nanowire grating on a single-mode indium tin oxide (ITO) slab waveguide, in which the light is incident normal to the structure. a, Extinction in TE polarization (E-field parallel to the gold wires). A single Fano resonance owing to grating coupling into the waveguide is visible. b, Extinction in TM polarization (E-field perpendicular to the wires). Two polariton branches that exhibit a Fano lineshape owing to the coupling of the narrow waveguide resonance to the broad particle plasmon in the gold wires are visible.<sup>48</sup>

### 3.2. Dielectric Function in a Metal

By assuming electrons in a metal as gas similar to a kinetic gas theory given by Maxwell-Boltzmann statistics, we can describe the motion of electrons in metal by Drude model. According to Ohm's law, we can describe physical properties of electrons in metal qualitatively.

#### Formula 3.2 Ohm's law

Let's suppose a metal wire which cross-sectional area as A.

According to Ohm's law the current density is described as below.

$$J = \sigma E = -Ne^2 \tau E$$



(J: current density,  $\sigma$ : conductivity of metal, E: electric field

, N: electrons per unit volume, e: unit charge of electron

, m: unit mass of electron,  $\tau$ : relaxation time by damping ( $\gamma = 1/\tau$ ))

By the differential unit, we can describe the quantity dN, dQ as

$$dN = NAvdt, \quad dQ = -edN = -NevAdt$$

So average velocity of electrons and DC-Drude conductivity is given as below.

$$v = -\frac{e\tau}{m} E, \quad \sigma_0 = -\frac{Ne^2\tau}{m}$$

Upper calculation anticipates the characteristics of electrons in metal in a DC field. By considering the electron motions in an alternating electric field with angular frequency  $\omega$  and damping constant  $\gamma$  we can set up force balance

equation. By solving the equation with harmonic external electric field, the electron displacement ( $\mathbf{x}$ ) can be solved.

### Formula 3.3 Electron displacement in metal from harmonic AC field

Force-balance equation is achieved by considering the electron motions in a harmonic field.

$$m\ddot{x} + m\gamma\dot{x} = -eE$$

This equation can be solved as a momentum ( $\mathbf{p}$ ) by harmonic AC field as below.

1) Harmonic field (angular frequency as  $\omega$ )

$$E = E_0 e^{-i\omega t}, \quad P = P_0 e^{-i\omega t}$$

2) Momentum equation

$$p' = -\frac{p}{\tau} - eE$$

By insert the harmonic field equation into the force-balance derived momentum equation the differential equation can be solved.

$$-i\omega p_0 = -\frac{p_0}{\tau} - eE_0$$

$$p_0 = \frac{eE_0}{\left(-\frac{1}{\tau} + i\omega\right)} = \frac{eE_0\tau}{(i\omega\tau - 1)}$$

Previous section, we derived Ohm's law according to the valuables as below.

$$J = \sigma E = -NEv = -\frac{Ne^2\tau}{m}E, \quad p = mv = -e\tau E$$

So current equation of J can be converted into the equation having angular frequency  $\omega$ .

$$J = -\frac{Ne\mu}{m} = \frac{Ne^2\tau}{m(i\omega\tau - 1)}E$$

From the equation AC-Drude conductivity can be rewritten as below.

$$\sigma_0 = \frac{Ne^2\tau}{m}, \quad J = \frac{\sigma_0}{(i\omega\tau - 1)}E = \sigma(\omega)E$$

We should connect this microscopic view to macroscopic view. So to, we can use electric displacement (D) and macroscopic polarization (P).

#### **Formula 3.4 Dielectric displacement and polarization in medium**

Dielectric displacement

$$D = \epsilon E = \epsilon_0 E + P$$

Polarization

$$P = -Nex$$

The macroscopic and microscopic view can be merged with complex dielectric function ( $\epsilon(\omega)$ ) using above Formula 3.4.

#### **Formula 3.5 Derivation of complex dielectric function in a harmonic**

**AC field**

Considering harmonic electron displacement, the displacement can be written as below.

$$X = X_0 e^{-i\omega t}$$

Putting the equation into the force-balance equation we achieve relationship as below.

$$X = \frac{e}{m(\omega^2 + i\gamma\omega)} E$$

Thus dielectric function is derived as below.

$$D = \epsilon E = \epsilon_0 E - \frac{Ne^2}{m(\omega^2 + i\gamma\omega)} E = \epsilon_0 E + P = \epsilon_0 \epsilon(\omega) E$$

$$D = \epsilon_0 E - \epsilon_0 \frac{Ne^2}{\epsilon_0 m (\omega^2 + i\gamma\omega)} E = \epsilon_0 \left( 1 - \frac{Ne^2}{\epsilon_0 m (\omega^2 + i\gamma\omega)} \right) E$$

If we define plasmon frequency ( $\omega_p$ ) as below, dielectric function is defined.

$$\omega_p^2 = \frac{Ne^2}{\epsilon_0 m}$$

$$\epsilon(\omega) = 1 - \frac{Ne^2}{\epsilon_0 m (\omega^2 + i\gamma\omega)} = 1 - \frac{\omega_p^2}{(\omega^2 + i\gamma\omega)}$$

By separation of variables into the real number and complex number, the formula is arranged into below formula.

$$\epsilon(\omega) = \left( 1 - \frac{\omega_p^2 \tau^2}{1 + \omega^2 \tau^2} \right) + i \left( \frac{\omega_p^2 \tau^2}{\omega (1 + \omega^2 \tau^2)} \right)$$

### 3.3. Maxwell's Equations

Maxwell equation is a combination of differential equations for electric field (E) and magnetic field (B). It is consisted of four equations (Gauss's law for electric/magnetic field, Faraday's law and Ampere's law) as below.

**Formula 3.6 Maxwell's equations (differential form)**

Curl (Faraday's law and Ampere's law)

$$\nabla \times E = -\frac{\partial B}{\partial t}, \quad \nabla \times B = \mu_0 J + \mu_0 \epsilon_0 \frac{\partial E}{\partial t}$$

Divergence (Gauss's law for electric/magnetic field)

$$\nabla \cdot E = \frac{\rho}{\epsilon_0}, \quad \nabla \cdot B = 0$$

Optical medium (non-conducting and without charging) above reduces to below.

$$\nabla \times E = -\frac{\partial B}{\partial t}, \quad \nabla \times B = \mu \epsilon \frac{\partial E}{\partial t}$$

$$\nabla \cdot E = 0, \quad \nabla \cdot B = 0$$

From the above differential equation, equivalent calculation on the formula can be achieved by the mathematical treatment.

**Formula 3.7 Equivalent calculation by Fourier transformation**

Considering harmonic electric/magnetic field.

For electric field

$$ik \times E \equiv i\omega B$$

For magnetic field

$$ik \times B \equiv \mu_0 J - \frac{i\omega}{c^2} E$$

For time dependence

$$\frac{\partial}{\partial t} \equiv -i\omega$$

The relationship is reduced as below for optical medium.

$$ik \times B \equiv -\frac{i\omega}{c^2} E$$

To understand electromagnetic properties in metal, we should settle up wave equation in medium.

#### **Formula 3.8 Wave equations**

From a fundamental vector calculus, the triple outer product can be solved as below.

$$\nabla \times \nabla \times A = \nabla(\nabla \cdot A) - (\nabla \cdot \nabla)A = \nabla(\nabla \cdot A) - \nabla^2 A$$

Considering for the optical medium, above vector calculus can be reduced to below equations.

$$\nabla \times \nabla \times E = -\nabla^2 E, \quad \nabla \times \nabla \times H = -\nabla^2 H$$

### **3.4. Electromagnetic Response in Bulk Metal (Volume Plasmon Polariton)**

To remove del ( $\nabla$ ) operator using harmonic wave equation, a widely known Fourier-transform-factor can be used. The linear form of electric field equation can be achieved.

#### **Formula 3.9 Derivation of linear form of wave equations**

From the below form, apply outer product with  $\mathbf{k}$  vector (wave vector).

$$i\mathbf{k} \times \mathbf{E} \equiv i\omega \mathbf{B}$$

$$i\mathbf{k} \times (\mathbf{k} \times \mathbf{E}) = \omega (i\mathbf{k} \times \mathbf{B}) = \omega \mu_0 \mathbf{J} - \frac{i\omega^2}{c^2} \mathbf{E}$$

$$\mathbf{k} \times (\mathbf{k} \times \mathbf{E}) + i\omega \mu_0 \mathbf{J} + \frac{\omega^2}{c^2} \mathbf{E} = 0$$

By applying the vector calculus formula in Formula 3.8, above equation can be reduced to as below.

$$\mathbf{k}(\mathbf{k} \cdot \mathbf{E}) - \mathbf{E}(\mathbf{k} \cdot \mathbf{k}) + i\omega \mu_0 \mathbf{J} + \frac{\omega^2}{c^2} \mathbf{E} = 0$$

$$\mathbf{k}(\mathbf{k} \cdot \mathbf{E}) - \mathbf{E}(\mathbf{k} \cdot \mathbf{k}) + i\omega \mu_0 \sigma \mathbf{E} + \frac{\omega^2}{c^2} \mathbf{E} = 0$$

$$\mathbf{k}(\mathbf{k} \cdot \mathbf{E}) - \mathbf{E}(\mathbf{k} \cdot \mathbf{k}) + (i\omega \mu_0 \sigma + \frac{\omega^2}{c^2}) \mathbf{E} = 0$$

Above relationship can be reduced using dielectric function induced by Maxwell's equation based on harmonic electric function.

**Formula 3.10 Derivation of frequency-dependent dielectric function based on Ampere's law**

Let's suppose harmonic electric field as below.

$$\mathbf{E}(\mathbf{r}, t) = \mathbf{E}_0 e^{i(\mathbf{k} \cdot \mathbf{r} - \omega t)}$$

From the Maxwell's equation (Ampere's law), below relationship is valid.

$$\frac{1}{\mu_0} \nabla \times \mathbf{B} = \mathbf{J} + \epsilon_0 \frac{\partial \mathbf{E}}{\partial t} = \sigma \mathbf{E} + \epsilon_0 \frac{\partial \mathbf{E}}{\partial t} = \epsilon_0 \epsilon \frac{\partial \mathbf{E}}{\partial t}$$

$$\sigma + \epsilon_0(-i\omega) = \epsilon_0 \epsilon(-i\omega)$$

$$\varepsilon = \frac{\sigma}{-i\varepsilon_0\omega} + 1$$

$$\varepsilon \frac{\omega^2}{c^2} = \frac{\sigma}{-i\varepsilon_0\omega} \frac{\omega^2}{c^2} + \frac{\omega^2}{c^2}$$

$$\varepsilon \frac{\omega^2}{c^2} = i\omega\mu_0\sigma + \frac{\omega^2}{c^2}$$

Above calculation leads to the linear form of the wave equation of electric field.

### Formula 3.11 Wave equation of electric field (linear form)

Based on the conclusions of Formula in 3.8 and 3.9, two equations can be merged into one equation as below.

$$\mathbf{k}(\mathbf{k} \cdot \mathbf{E}) - k^2\mathbf{E} + \varepsilon \frac{\omega^2}{c^2} \mathbf{E} = 0$$

The linear form of wave equation indicates the possible case of the wave propagation in medium (metal). Considering the 3-directional propagation, the variables can be considered with the system of matrix equations.

### Formula 3.12 Solutions of wave equations

Above formula can be reduced to the matrix equation as below if we consider the matrix term in A as below

If propagation in z direction ( $\mathbf{k}$  value along  $\mathbf{z}$  direction) is supposed, the matrix contains below numbers.

$$A = \left\{ k^2 - k^2 + \frac{\omega^2}{c^2} \epsilon \right\}$$

$$\begin{pmatrix} 0 & 0 & 0 \\ 0 & 0 & 0 \\ 0 & 0 & k^2 \end{pmatrix} - \begin{pmatrix} k^2 & 0 & 0 \\ 0 & k^2 & 0 \\ 0 & 0 & k^2 \end{pmatrix} + \begin{pmatrix} \frac{\omega^2}{c^2} \epsilon & 0 & 0 \\ 0 & \frac{\omega^2}{c^2} \epsilon & 0 \\ 0 & 0 & \frac{\omega^2}{c^2} \epsilon \end{pmatrix} = A$$

The details are given in below.

$$\begin{pmatrix} A_{xx} & A_{xy} & A_{xz} \\ A_{yx} & A_{yy} & A_{yz} \\ A_{zx} & A_{zy} & A_{zz} \end{pmatrix} \begin{pmatrix} E_x \\ E_y \\ E_z \end{pmatrix} = 0$$

Then Formula 3.9 is reduced as below.

$$A \cdot E = 0$$

To have nontrivial solution, we should consider determinant of the matrix A.

The condition for nontrivial solution existence is inferred from the determinant of above matrix as below.

$$\det | A | = 0$$

$$\det | A | = \left( \frac{\omega^2}{c^2} \epsilon - k^2 \right)^2 \frac{\omega^2}{c^2} \epsilon = 0$$

Above equation let us know existence of the two possible solutions.

A) In case of

$$\left( \frac{\omega^2}{c^2} \epsilon - k^2 \right) = 0$$

Matrix equation is reduced to as below.

$$\begin{pmatrix} 0 & 0 & 0 \\ 0 & 0 & 0 \\ 0 & 0 & \frac{\omega^2}{c^2} \epsilon \end{pmatrix} \begin{pmatrix} E_x \\ E_y \\ E_z \end{pmatrix} = 0$$

Above result indicates  $E_z = 0$ , which means  $\mathbf{k} \cdot \mathbf{E} = 0$

The relationship indicates transverse wave form.



B) In case of

$$\frac{\omega^2}{c^2} \epsilon = 0$$

Matrix equation is reduced to as below.

$$\begin{pmatrix} \frac{\omega^2}{c^2} \epsilon - k^2 & 0 & 0 \\ 0 & \frac{\omega^2}{c^2} \epsilon - k^2 & 0 \\ 0 & 0 & 0 \end{pmatrix} \begin{pmatrix} E_x \\ E_y \\ E_z \end{pmatrix} = 0$$

Above result indicates  $E_z = 0$ , which means  $\mathbf{k} \times \mathbf{E} = 0$

The relationship indicates longitudinal wave form.



The analysis of wave equation is now possible based on the above conclusions. Different physical property is expected from transverse and longitudinal wave according to the wave equations. In wavevector-frequency domain, the

electromagnetic response is analyzable. First we should recognize the reduced form of electromagnetic response in metal from the frequency dependent dielectric function as in Formula 3.13. The general graphical form of dielectric function in real and imaginary region is given in **Figure 7**. Near the plasmon frequency ( $\omega_p$ ) region, the real part of dielectric function become 0.

### Formula 3.13 Electromagnetic response in metal

From Formula 3.5,

$$\varepsilon(\omega) = \left( 1 - \frac{\omega_p^2 \tau^2}{1 + \omega^2 \tau^2} \right) + i \left( \frac{\omega_p^2 \tau^2}{\omega(1 + \omega^2 \tau^2)} \right)$$

a) If,

$$\omega > \omega_p, \text{ then } \varepsilon(\omega) \cong 1 + i \cdot 0, \text{ Re}(\varepsilon(\omega)) > 0$$

b) If,

$$\omega < \omega_p$$

For  $\omega\tau \gg 1$

$$\varepsilon(\omega) \cong \left( 1 - \frac{\omega_p^2 \tau^2}{(\omega\tau)^2} \right) + i \left( \frac{\omega_p^2 \tau}{\omega(\omega\tau)^2} \right) = \left( 1 - \frac{\omega_p^2}{\omega^2} \right) + i \cdot 0$$

For  $\omega\tau \ll 1$

$$\varepsilon(\omega) \cong \left( 1 - \frac{\omega_p^2 \tau^2}{1 + (\omega\tau)^2} \right) + i \left( \frac{\omega_p^2 \tau}{\omega(1 + (\omega\tau)^2)} \right)$$

$$= (1 - \omega_p^2 \tau^2) + i \left( \frac{\omega_p^2 \tau}{\omega} \right)$$

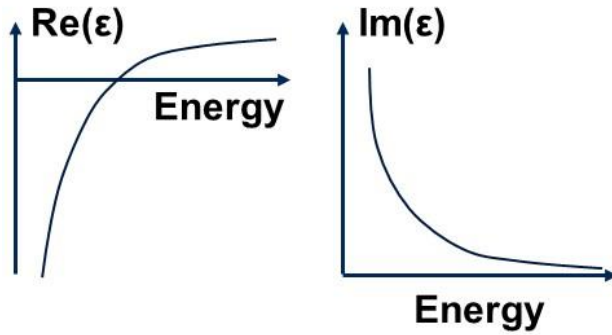


Figure 56. Energy (frequency) dependent real and imaginary components of the dielectric function for an Drude metal.

The transverse and longitudinal wave function now can be analyzed by considering above relationships.

#### Formula 3.14 Transverse volume plasmon mode

In case of metal, valid wave equation is given as below.

$$k(k \cdot E) - k^2 E + \varepsilon \frac{\omega^2}{c^2} E = 0$$

By putting  $k \cdot E = 0$  into the wave equation, the wave equation is reduced to as below.

$$k^2 = \varepsilon(k, \omega) \frac{\omega^2}{c^2}$$

From Formula 3.13,

For  $\omega\tau \gg 1$

$$\varepsilon(\omega) \cong \left( 1 - \frac{\omega_p^2}{\omega^2} \right) + i \cdot 0$$

is applicable.

So, above dispersion relationship is reduced to as below.

$$k^2 = \left(1 - \frac{\omega_p^2}{\omega^2}\right) \frac{\omega^2}{c^2}$$

$$k^2 c^2 = \omega^2 - \omega_p^2, \quad \omega^2 = \omega_p^2 + k^2 c^2$$

$$\frac{\omega}{\omega_p} = \sqrt{1 + \frac{k^2 c^2}{\omega_p^2}}$$

### Formula 3.15 Longitudinal volume plasmon mode

In case of metal, valid wave equation is given as below.

$$k(k \cdot E) - k^2 E + \varepsilon \frac{\omega^2}{c^2} E = 0$$

In case of  $\mathbf{k} \times \mathbf{E} = 0$ ,

$$\frac{\omega^2}{c^2} \varepsilon = 0$$

is valid.

To exist wave,  $\varepsilon(k, \omega) = 0$  is possible.

So in the macroscopic view, below is valid.

$$D = \varepsilon_0 E + P = \varepsilon_0 \varepsilon(\omega) E = 0,$$

$$E = -\frac{P}{\varepsilon_0}$$

For the phase velocity, there are no limitation of the value

$$V_{\text{phase}} = \frac{\omega}{k}$$

In addition, for the group velocity, result means stationary condition.

$$v_{\text{group}} = \frac{d\omega}{dk} = 0$$

Moreover, the longitudinal mode is the limit of transverse wave at the plasmon frequency.

$$\varepsilon(\omega_p) = 0 \cong \left(1 - \frac{\omega_p^2}{\omega^2}\right)$$

And

$$0 = k^2 c^2, \quad 0 = k$$

Above conclusions made the analysis of electromagnetic behavior in the metal. In above plasmon frequency, metals mainly conducting which means wave propagates through the metal and seems transparent for incident wave. In the below plasmon frequency, with  $\omega\tau \gg 1$ , metal become perfect conductor (no apparent absorption). And with  $\omega\tau \ll 1$ , imaginary part of dielectric function makes metal absorb incident light. Due to the high damping, propagation do not occur. Near the plasmon frequency, wave behavior can be tracked with according to the wave equation from Maxwell's relationships. Because  $\omega^2 = \omega_p^2 + \mathbf{K}^2 \mathbf{C}^2$  is valid at  $\omega > \omega_p$ , transverse mode of wave propagation is allowed over  $\omega > \omega_p$ . At the plasmon frequency, wave propagation is allowed with longitudinal mode. Metal have pure depolarization field ( $\mathbf{D} = 0$ ) with no damping. And collective electron displacement from harmonic electric field leads to oscillations of charge in homogeneous motion. This oscillation is called

as volume plasmons. The analysis is expressed as a graph in Figure 8.

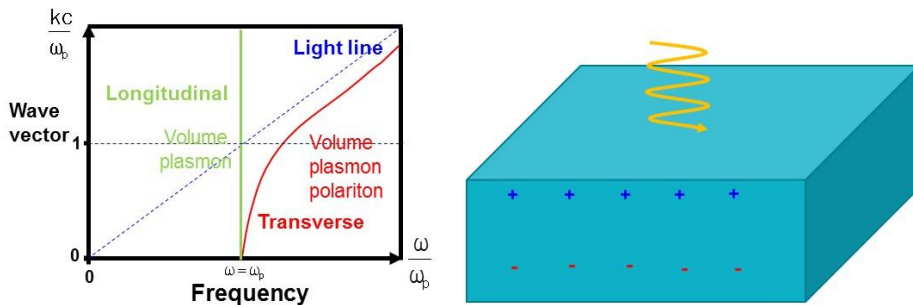


Figure 57. Dispersion relationship of bulk metal in Drude model

### 3.5. Electromagnetic Response in Metal-Dielectric Interfaces (Surface Plasmon Polariton)

When electric field enters the interface between metal and dielectric, a new type of electron-light interaction can happen. We call it as surface plasmon polariton (SPP). As a result, the excited electromagnetic field propagates at the interface by confinement. The electromagnetic field propagation is dissipated as evanescent field perpendicular to the interface. The situation is depicted in Figure 12(a). To investigate the property, the wave equations in Formula 3.8 should be deeply investigated. Wave propagation into x direction is depicted with vector  $\mathbf{k}$ . Permittivity of dielectric is  $\epsilon_D$ . To describe frequency dependent response of electromagnetic field in metal, permittivity is written as dielectric function  $\epsilon(\omega)$ . The situation is depicted in Figure 12(b).

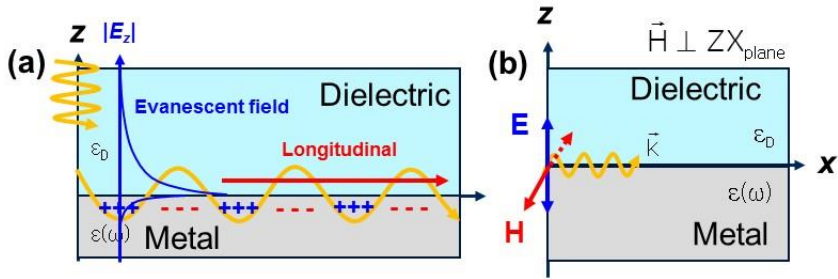


Figure 58 (a) Wave propagation at a dielectric-metal interface and, (b) geometry of the system.

### Formula 3.16 Helmholtz equation from wave equations

The validity of below equation is proved in previous section with wave equation.

$$\nabla \times \nabla \times \mathbf{E} = -\nabla^2 \mathbf{E}, \quad \nabla \times \nabla \times \mathbf{H} = -\nabla^2 \mathbf{H}$$

Above equation is reduced to Helmholtz equation with Maxwell's equation.

$$\text{a) } \nabla \times \nabla \times \mathbf{E} = -\frac{\partial(\nabla \times \mathbf{B})}{\partial t} = -\mu\epsilon \frac{\partial^2 \mathbf{E}}{\partial t^2}$$

$$\nabla \times \nabla \times \mathbf{E} = -\nabla^2 \mathbf{E}$$

Above two are equivalent, so rearranged as below.

$$\nabla^2 \mathbf{E} - \mu\epsilon \frac{\partial^2 \mathbf{E}}{\partial t^2} = 0, \quad \nabla^2 \mathbf{E} - \frac{\omega^2}{c^2} \epsilon(\omega) \mathbf{E} = 0$$

$$\nabla^2 \mathbf{E} - k_0^2 \epsilon(\omega) \mathbf{E} = 0$$

$$\text{b) } \nabla \times \nabla \times \mathbf{H} = \frac{\partial(\nabla \times \mathbf{E})}{\partial t} = -\epsilon \frac{\partial^2 \mathbf{B}}{\partial t^2} = -\mu\epsilon \frac{\partial^2 \mathbf{H}}{\partial t^2}$$

$$\nabla \times \nabla \times \mathbf{H} = -\nabla^2 \mathbf{H}$$

Above two are equivalent, so rearranged as below.

$$\nabla^2 \mathbf{H} - \mu\epsilon \frac{\partial^2 \mathbf{H}}{\partial t^2} = 0, \quad \nabla^2 \mathbf{H} - \frac{\omega^2}{c^2} \epsilon(\omega) \mathbf{H} = 0$$

$$\nabla^2 \mathbf{H} - k_0^2 \epsilon(\omega) \mathbf{H} = 0$$

Above Formula 3.16 can be analyzed with transverse magnetic wave and transverse electric wave. Configuration of electromagnetic wave at the interface is depicted in Figure 13. Further arrangement is conducted in the Formula 3.17.

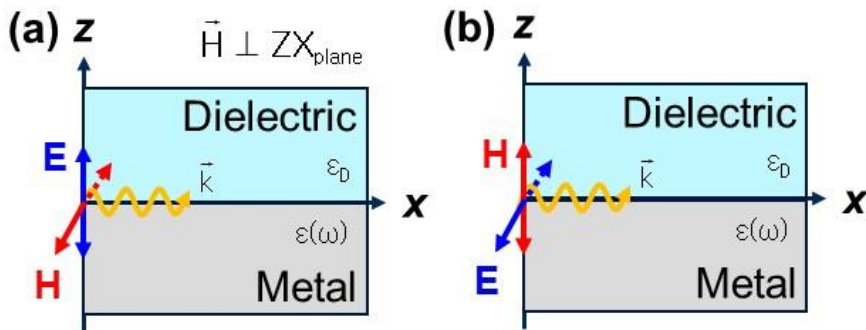


Figure 59 (a) Transverse magnetic wave propagation. (b) Transverse electric wave propagation.

#### Formula 3.17 Helmholtz equation from wave equations

Let us suppose propagating wave at  $z = 0$  plane into  $x$  direction which has propagation constant  $\mathbf{k}_x = \beta$ .

$$E/H(x,y,z) = E/H(z)e^{i\beta x}$$

In this case, differentials related with directional component are written as below.

$$\frac{\partial}{\partial x} \equiv i\beta, \quad \frac{\partial}{\partial y} \equiv 0, \quad \frac{\partial}{\partial t} \equiv -i\omega$$

$$\nabla^2 E - k_0^2 \epsilon(\omega) E = 0, \quad \nabla^2 H - k_0^2 \epsilon(\omega) H = 0$$

(a) For the transverse magnetic wave (TM)

$$H(x,y,z) = H_y e^{i\beta x}$$

$$(i^2 \beta^2) H_y e^{i\beta x} + \frac{\partial^2 H_y}{\partial z^2} e^{i\beta x} + k_0^2 \epsilon H_y e^{i\beta x} = 0$$

$$\frac{\partial^2 H_y}{\partial z^2} + (k_0^2 \epsilon - \beta^2) H_y = 0$$

(b) For the transverse electric wave (TE)

$$E(x,y,z) = E_y e^{i\beta x}$$

$$(i^2 \beta^2) E_y e^{i\beta x} + \frac{\partial^2 E_y}{\partial z^2} e^{i\beta x} + k_0^2 \epsilon E_y e^{i\beta x} = 0$$

$$\frac{\partial^2 E_y}{\partial z^2} + (k_0^2 \epsilon - \beta^2) E_y = 0$$

To calculate spatial explicit expressions for different field components, harmonic wave in different directions for  $\mathbf{x}$ ,  $\mathbf{y}$  and  $\mathbf{z}$  is inserted. System of equations are achieved for the arrangement.

$$\frac{\partial E_z}{\partial y} - \frac{\partial E_y}{\partial z} = i\omega \mu_0 H_x, \quad \frac{\partial E_x}{\partial z} - \frac{\partial E_z}{\partial x} = i\omega \mu_0 H_y,$$

$$\frac{\partial E_y}{\partial x} - \frac{\partial E_x}{\partial y} = i\omega\mu_0 H_z, \quad \frac{\partial H_z}{\partial y} - \frac{\partial H_y}{\partial z} = -i\omega\varepsilon E_x,$$

$$\frac{\partial H_x}{\partial z} - \frac{\partial H_z}{\partial x} = -i\omega\varepsilon E_y, \quad \frac{\partial H_y}{\partial x} - \frac{\partial H_x}{\partial y} = -i\omega\varepsilon E_z.$$

Above is reduced to below.

$$\frac{\partial E_y}{\partial z} = -i\omega\mu_0 H_x, \quad \frac{\partial E_x}{\partial z} - i\beta = i\omega\mu_0 H_y, \quad i\beta E_y = i\omega\mu_0 H_z$$

$$\frac{\partial H_y}{\partial z} = i\omega\varepsilon E_x, \quad \frac{\partial H_x}{\partial z} - i\beta H_z = -i\omega\varepsilon E_y, \quad i\beta H_y = -i\omega\varepsilon E_z.$$

To calculate field profile and dispersion relation at the metal-dielectric interface, harmonic field profile including the propagation direction and evanescent field in perpendicular direction is substituted for transverse magnetic/electric waves.

### **Formula 3.18 Governing equation for metal-dielectric interface in the transverse magnetic (TM) wave**

TM wave can be written as below

$$H(x, y, z) = H_y e^{i\beta x}$$

In  $z > 0$ , wave belongs to the dielectric domain.

Wave equation of magnetic field in dielectric domain is written as below.

$$H_y(z) = A_2 e^{i\beta x} e^{-k_2 z}$$

By analyzing spatial explicit equation in Formula 3.17 leads to below conclusions.

$$E_x(z) = iA_2 \frac{1}{\omega \epsilon_D} k_2 e^{i\beta x} e^{-k_2 z} \quad , \quad E_z(z) = -A_2 \frac{\beta}{\omega \epsilon} e^{i\beta x} e^{-k_2 z}$$

$$k_2^2 = \beta^2 - k_0^2 \epsilon_D$$

In  $Z < 0$ , wave belongs to the metal domain.

Wave equation of magnetic field in metal domain is written as below.

$$H_y(z) = A_1 e^{i\beta x} e^{k_1 z}$$

By analyzing spatial explicit equation in Formula 3.17 leads to below conclusions.

$$E_x(z) = -iA_1 \frac{1}{\omega \epsilon(\omega)} k_1 e^{i\beta x} e^{k_1 z} \quad , \quad E_z(z) = -A_1 \frac{\beta}{\omega \epsilon(\omega)} e^{i\beta x} e^{k_1 z}$$

$$k_1^2 = \beta^2 - k_0^2 \epsilon(\omega)$$

In the position at  $\mathbf{z} = 0$ , field component should have continuity.

From the magnetic field condition at  $z = 0$ , below is valid.

$$H_y(0) = A_2 e^{i\beta x} \quad , \quad H_y(0) = A_1 e^{i\beta x}$$

$$\text{So, } A_1 = A_2 .$$

From the electric field condition at  $\mathbf{z} = 0$ , below is valid.

$$E_x(0) = iA_2 \frac{1}{\omega \epsilon_D} k_2 e^{i\beta x} \quad , \quad E_x(0) = -iA_1 \frac{1}{\omega \epsilon(\omega)} k_1 e^{i\beta x}$$

$$\text{So, } \frac{k_2}{\epsilon_D} = -\frac{k_1}{\epsilon(\omega)} \quad \text{or} \quad k_2 = -\frac{\epsilon_D}{\epsilon(\omega)} k_1 .$$

Wavevector-frequency equation from  $Z < 0$  and  $Z > 0$  can be combined to below way.

From  $k_2^2 = \beta^2 - k_0^2 \epsilon_D$  equation, below is valid.

$$\left( \frac{\epsilon_D}{\epsilon(\omega)} \right)^2 k_1^2 = \beta^2 - k_0^2 \epsilon_D$$

Take a proportion of below two equations as below.

$$k_1^2 = \beta^2 - k_0^2 \epsilon(\omega), \quad \left( \frac{\epsilon_D}{\epsilon(\omega)} \right)^2 k_1^2 = \beta^2 - k_0^2 \epsilon_D$$

$$\frac{k_1^2}{\left( \frac{\epsilon_D}{\epsilon(\omega)} \right)^2 k_1^2} = \frac{\beta^2 - k_0^2 \epsilon(\omega)}{\beta^2 - k_0^2 \epsilon_D}, \quad \left( \frac{\epsilon(\omega)}{\epsilon_D} \right)^2 = \frac{\beta^2 - k_0^2 \epsilon(\omega)}{\beta^2 - k_0^2 \epsilon_D}$$

Above is arranged to as below.

$$\epsilon(\omega)^2 \beta^2 - \epsilon(\omega)^2 k_0^2 \epsilon_D = \epsilon_D^2 \beta^2 - \epsilon_D^2 k_0^2 \epsilon(\omega)$$

$$(\epsilon(\omega)^2 - \epsilon_D^2) \beta^2 = k_0^2 \epsilon(\omega) \epsilon_D (\epsilon(\omega) - \epsilon_D)$$

$$\beta^2 = k_0^2 \frac{\epsilon(\omega) \epsilon_D}{\epsilon(\omega) + \epsilon_D}$$

Propagation constant at the interface between a metal and dielectric is written as below.

$$\beta = k_0 \sqrt{\frac{\epsilon(\omega) \epsilon_D}{\epsilon(\omega) + \epsilon_D}}$$

**Formula 3.19 Governing equation for metal-dielectric interface in the transverse electric (TE) wave**

TE wave can be written as below

$$E(x, y, z) = E_y e^{i\beta x}$$

In  $z > 0$ , wave belongs to the dielectric domain.

Wave equation of electric field in dielectric domain is written as below.

$$E_y(z) = A_2 e^{i\beta x} e^{-k_2 z}$$

By analyzing spatial explicit equation in Formula 3.17 leads to below conclusions.

$$H_x(z) = -iA_2 \frac{1}{\omega\mu_0} k_2 e^{i\beta x} e^{-k_2 z} \quad , \quad H_z(z) = A_2 \frac{\beta}{\omega\mu_0} e^{i\beta x} e^{-k_2 z}$$

$$k_2^2 = \beta^2 - k_0^2 \epsilon_D$$

In  $Z < 0$ , wave belongs to the metal domain.

Wave equation of electric field in metal domain is written as below.

$$E_y(z) = A_1 e^{i\beta x} e^{k_1 z}$$

By analyzing spatial explicit equation in Formula 3.17 leads to below conclusions.

$$H_x(z) = iA_1 \frac{1}{\omega\mu_0} k_1 e^{i\beta x} e^{k_1 z} \quad , \quad H_z(z) = A_1 \frac{\beta}{\omega\mu_0} e^{i\beta x} e^{k_1 z}$$

$$k_1^2 = \beta^2 - k_0^2 \epsilon(\omega)$$

In the position at  $z = 0$ , field component should have continuity.

From the electric field condition at  $z = 0$ , below is valid.

$$E_y(z) = A_2 e^{i\beta x} \quad , \quad E_y(z) = A_1 e^{i\beta x}$$

$$\text{So, } A_1 = A_2 .$$

From the magnetic field condition at  $z = 0$ , below is valid.

$$H_x(0) = -iA_2 \frac{1}{\omega\mu_0} k_2 e^{i\beta x} \quad , \quad H_x(0) = iA_1 \frac{1}{\omega\mu_0} k_1 e^{i\beta x}$$

$$\text{So, } iA_1 \frac{1}{\omega\mu_0} k_1 e^{i\beta x} + iA_2 \frac{1}{\omega\mu_0} k_2 e^{i\beta x} = 0$$

Above equation is reduced to as below.

$$A_1(k_1 + k_2) = 0$$

The propagation constant is not zero in metal-dielectric interface.

Due to the condition of  $\text{Re}(k_1, k_2) > 0$ , it satisfies  $A_1 = A_2 = 0$ .

Analysis in Formula 3.19 indicates that inexistence of surface plasmon with TE wave. Above result is summarized as dispersion relation in Figure 14. In a dielectric medium, the slope of the light line become decrease according to the dielectric constant of medium. Frequency above the  $\omega_p$  is the transparent region of metal. So incident wave in this region pass through the metal without degradation. At the frequency in  $\omega_p$ , volume plasmon evolve on metal. The phenomena are same as previous bulk metal case. There is more separation of region according to the frequency below  $\omega_p$ . We solved TM equation for surface wave. We achieved propagation constant ( $\beta = k_0 (\epsilon(\omega)\epsilon_D / (\epsilon(\omega) + \epsilon_D))$ ). If  $(\epsilon(\omega) + \epsilon_D)$  approaches to 0 value, propagation constant become infinity. The frequency where  $(\epsilon(\omega) = \epsilon_D)$  satisfy, we call there as surface plasmon frequency  $\omega_{sp}$ . Infinity value of propagation constant means, group velocity ( $V_g = d\omega / dk$ ) become zero. So, in the surface plasmon frequency, the behavior of surface plasmon is electrostatic. The equation for surface plasmon frequency is given below for Formula 3.20. Between the surface plasmon frequency and volume

plasmon frequency, there are no propagation around x direction due to the imaginary number of  $k_x$ .

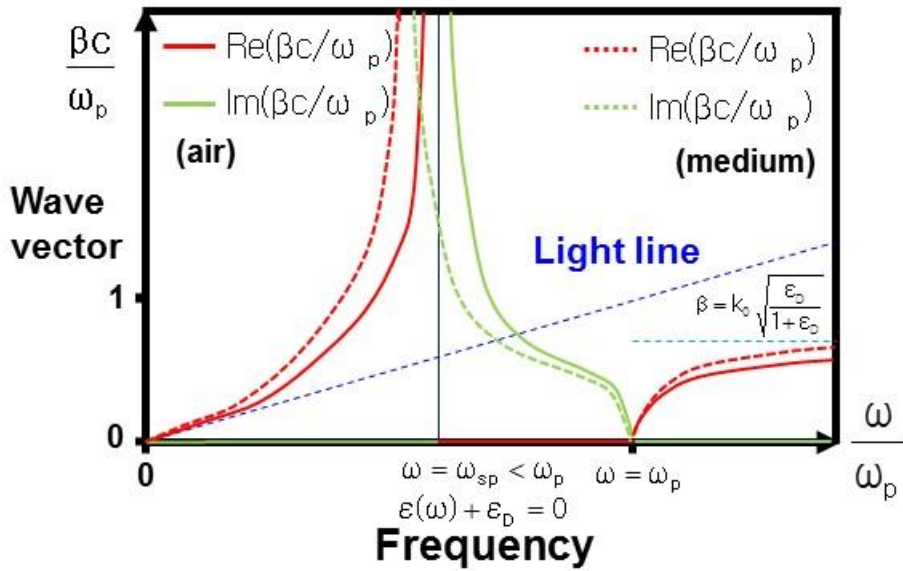


Figure 60 Dispersion relation of surface plasmon polariton in metal-dielectric interface. True line (–) indicates dispersion relation at air and dotted line (–) indicates dispersion relation at dielectric medium.

**Formula 3.20 Derivation of surface plasmon resonance frequency**

From TM wave, propagation constant can be written as below.

$$\beta = k_0 \sqrt{\frac{\epsilon(\omega)\epsilon_D}{\epsilon(\omega) + \epsilon_D}}$$

The propagation constant become infinity when satisfies the condition.

$$\epsilon(\omega) + \epsilon_D = 0$$

Below condition satisfies in metal inherently at the frequency region.

For ,  $\omega < \omega_p$ .

And,  $\omega\tau \gg 1$ .

$$\varepsilon(\omega) \cong \left(1 - \frac{\omega_p^2 \tau^2}{(\omega\tau)^2}\right) + i \left(\frac{\omega_p^2 \tau}{\omega(\omega\tau)^2}\right) = \left(1 - \frac{\omega_p^2}{\omega^2}\right) + i \cdot 0$$

By combining the factors, below is satisfied.

$$-\varepsilon_D = \left(1 - \frac{\omega_p^2}{\omega_{SP}^2}\right)$$

$$\omega_{SP} = \frac{\omega_p}{\sqrt{1 + \varepsilon_D}}$$

The surface plasmon resonance frequency is lower than volume plasmon resonance frequency.

Overall dispersion relation in  $k$ - $\omega$  space is summarized in below Formula 3.21.

### Formula 3.21 dispersion relation in $k$ - $\omega$ space

(1) Waveform

at  $z > 0$

$$H_d = (0, H_{y_d}, 0) \exp i(k_{x_d}x + k_{z_d}z - \omega t)$$

$$E_d = (E_{x_d}, 0, E_{z_d}) \exp i(k_{x_d}x + k_{z_d}z - \omega t)$$

at  $z < 0$

$$H_m = (0, H_{y_m}, 0) \exp i(k_{x_m}x + k_{z_m}z - \omega t)$$

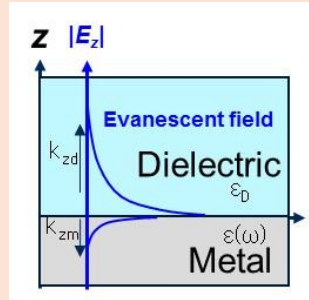
$$E_m = (E_{x_m}, 0, E_{z_m}) \exp i(k_{x_m}x + k_{z_m}z - \omega t)$$

(2) Boundary condition

$$E_{xd} = E_{xm}, H_{yd} = H_{ym}, D_{zd} = D_{zm} \quad (\epsilon_d E_{zd} = \epsilon_m E_{zm})$$

(3) Existence of SPP

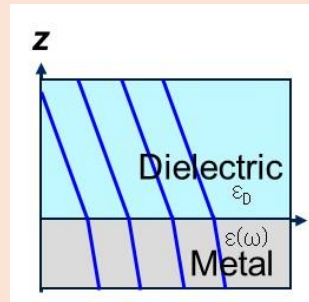
$$\frac{k_{zm}}{\epsilon_m} = \frac{k_{zd}}{\epsilon_d}$$



(4) Continuity (wavevector form at  $x$  direction)

$$k_x = k_{xm} = k_{xd}$$

$$k_x = \beta = k_0 \sqrt{\frac{\epsilon(\omega)\epsilon_D}{\epsilon(\omega) + \epsilon_D}}$$



(5) Wavevector calculation (directional)

$$k^2 = k_x^2 + k_{zm}^2 = k_x^2 + k_{zd}^2$$

(6) Wavevector form at  $z$  direction

$$k_{zd} = k_0 \sqrt{\frac{\epsilon_D^2}{\epsilon(\omega) + \epsilon_D}} \quad k_{zm} = k_0 \sqrt{\frac{\epsilon(\omega)^2}{\epsilon(\omega) + \epsilon_D}}$$

(7) Lightline slope in  $k(y)$ - $\omega(x)$  plane

$$\frac{\sqrt{\epsilon_d}}{ck_x}$$

(8) Complex wavenumber in frequency domain

(a) Radiative modes

$$\omega > \omega_p, \epsilon(\omega) > 0$$

$$k_x = \text{Re}(k_x), k_z = \text{Re}(k_z)$$

(b) Quasi-bound modes

$$\omega_p > \omega > \omega_{sp}, 0 > \epsilon(\omega) > -\epsilon_d$$

$$k_x = \text{Im}(k_x), k_z = \text{Re}(k_z)$$

(c) Bound-modes

$$\omega_{sp} > \omega, -\epsilon_d > \epsilon(\omega)$$

$$k_x = \text{re}(k_x), k_z = \text{Im}(k_z)$$

### 3.6. Electromagnetic Response in Confined Metal-Dielectric Interfaces (Localized Surface Plasmon)

Similar to the dielectric-metal interface, metal nanostructure can generate plasmons. However, due to the restriction at the interface (confinement effect) the surface plasmon polariton changes its property. There are significant extinction property exists in nanostructure such as absorption and scattering. Scattering indicates light deviation from straight beam path after interaction with matter. There are three scattering types (geometric scattering, Mie scattering and Rayleigh scattering) according to their size parameters which is shown in Figure 15.

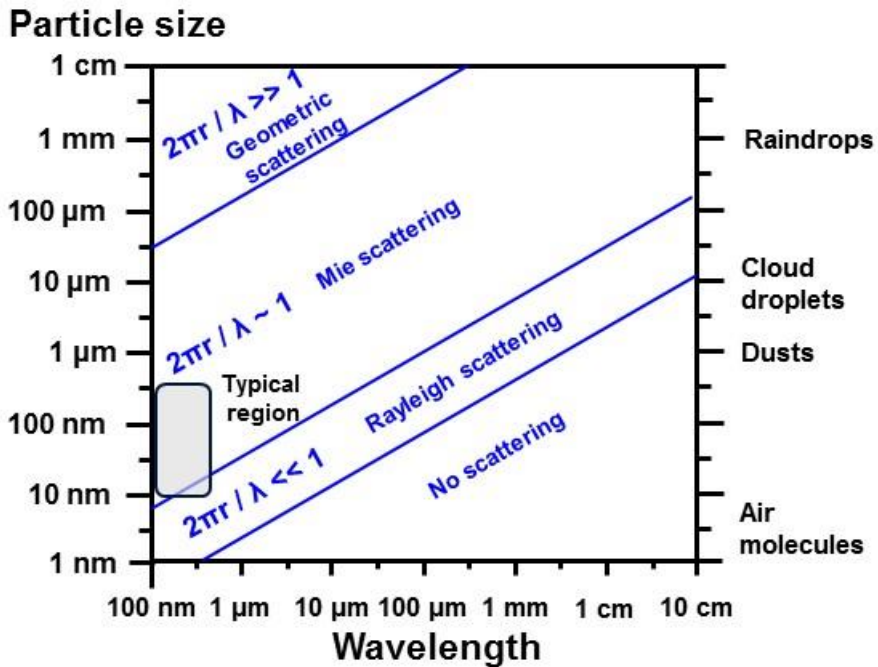


Figure 61 Scattering mechanisms according the particle size

If incident light beam wavelength is more than ten times of longer than the size of matter (especially particles), Rayleigh scattering occurs in every-direction and its intensity is proportional to the  $1/\lambda^4$ . So the scattering mechanism is effective in short wavelength region. The shape of scattering pattern has symmetry on the center of particle. And elastic scattering occurs around particles. But the light interaction with gold nanoparticles is not in the region of the Rayleigh.

Another important scattering mechanism is Mie scattering. If the particle is not much smaller than the incident light, Mie scattering mechanism occurs (even the Mie scattering contains Rayleigh scattering, here, the mechanism is separated). This scattering have a great effect on longer wavelength compared to Rayleigh scattering. The shape of scattering pattern does not have symmetry

on the center of particle. Its intensity is proportional to the  $1/\lambda^p$ . The interaction of light with gold nanostructures are in the region of the Mie scattering mechanism. To find dielectric property of gold nanoparticles, the Mie scattering theory is combined with Maxwell's electromagnetic theory.

To analyze the dispersion relation of localized surface plasmon, metal sphere is introduced. This metal sphere has some polarizability and it is known as Clausius-Mossotti relation as in Formula 3.22. The polarizability is related to response of metal sphere with external field to generate dipole moment.

**Formula 3.22 Clausius-Mossotti relation**

Dipole moment of metal sphere can be written as below.

$$\vec{p} = \epsilon_0 \epsilon_m \alpha \vec{E}$$

From Mie theory, the polarizability ( $\alpha$ ) is written as below.

$$\alpha = 4 \pi \epsilon_0 a^3 \frac{\epsilon_{\text{metal}} - \epsilon_{\text{surround}}}{\epsilon_{\text{metal}} + 2 \epsilon_{\text{surround}}}$$

Resonance occurs at highest dipole moment state. To be, the polarizability should be maximum. So that, denominator term of dielectric function should be minimum. Around the resonance, there are negligible value of metal dielectric function in imaginary part exists. The condition is called as Fröhlich's condition.

**Formula 3.22 Fröhlich's condition**

Resonance at

$$|\epsilon_{\text{metal}} + 2 \epsilon_{\text{surround}}|_{\text{min}}, \text{Re}(\epsilon_m) = -2 \epsilon_d$$

The resonance condition of dielectric function of metal can be shown via graph (based on Drude model) in Figure 16. The resonance frequency of localized surface is  $3^{-0.5}$  times lower than the volume plasmon resonance frequency. The detailed calculation of extinction (energy loss) cross-section is conducted on below.

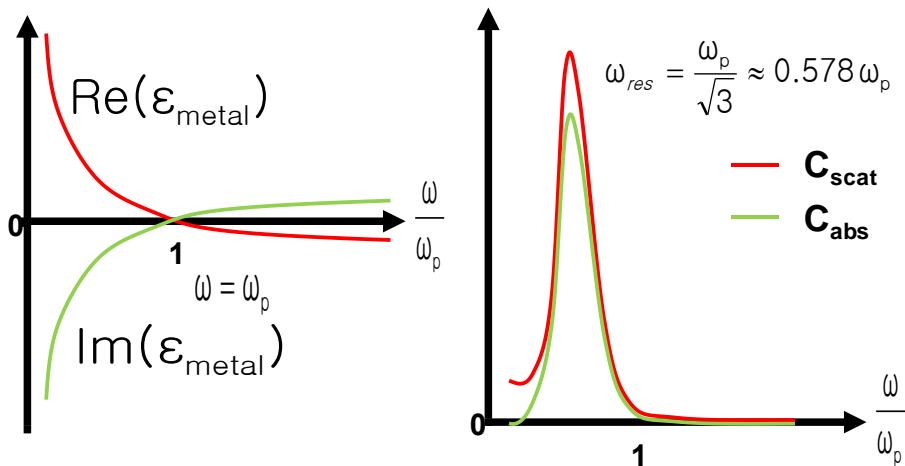


Figure 62 Dielectric function of nanostructured metal sphere (localized surface plasmon)

### Formula 3.23 Extinction cross section in metal nanosphere

Let us define the cross section in metal nanosphere.

$$C_{\text{scat}} = \frac{I_{\text{scat}}}{I}, \quad C_{\text{abs}} = \frac{I_{\text{abs}}}{I}$$

It can be calculated as below.

$$C_{\text{scat}} = \frac{8\pi}{3} k^4 a^6 \left| \frac{\epsilon_{\text{metal}} - \epsilon_{\text{surround}}}{\epsilon_{\text{metal}} + 2\epsilon_{\text{surround}}} \right|^2 = \frac{k^4}{6\pi} |\alpha|$$

$$C_{\text{abs}} = 4\pi k^4 a^3 \text{Im} \left\{ \frac{\epsilon_{\text{metal}} - \epsilon_{\text{surround}}}{\epsilon_{\text{metal}} + 2\epsilon_{\text{surround}}} \right\} = k \text{Im} \{ \alpha \}$$

### 3.7. Graphical Summary of Plasmon Resonance in Gold

The electric fields and charges in resonance for bulk, surface and localized plasmon are expressed in the Figure 17.

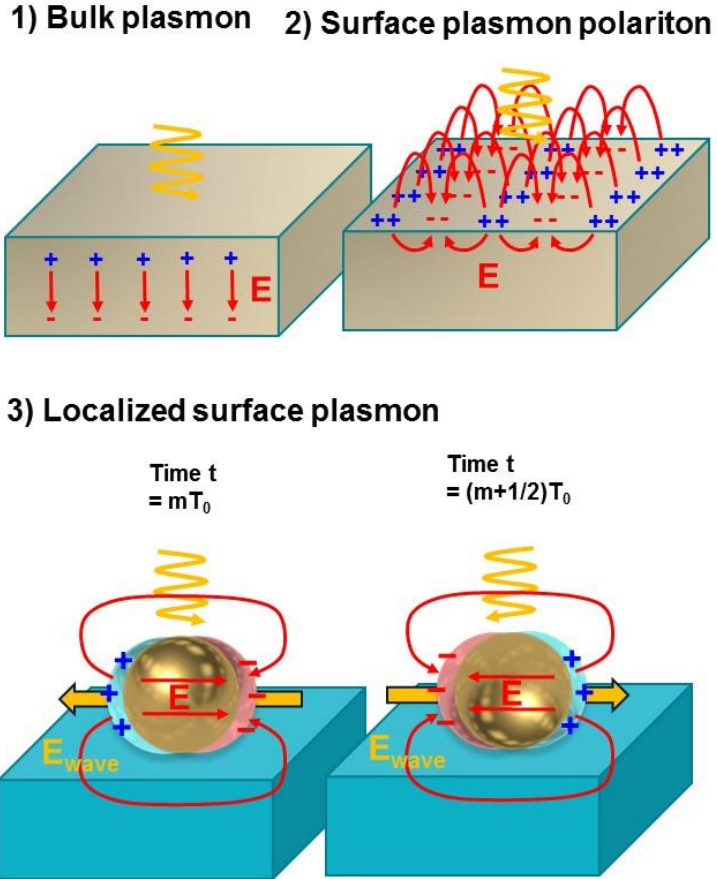


Figure 63 Graphical representation of resonance for summary of three plasmon modes.

Surface plasmon polariton propagation simulation by FDTD is shown in Figure 18. From the metal grating, the incident surface plasmon polariton propagates into  $x$  direction with evanescent field on vertical  $z$  direction.<sup>49</sup>

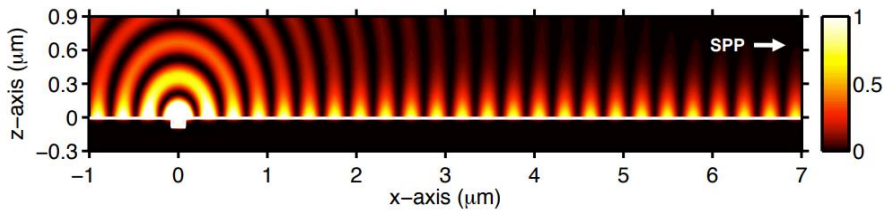


Figure 64 FDTD calculation of electric field around a single metal groove.

Even the size of gold nanoparticles is very small to see via optical microscope, due to the high scattering cross-section and diffraction we can observe the image in dark field from the Au nanoparticles.<sup>50</sup>

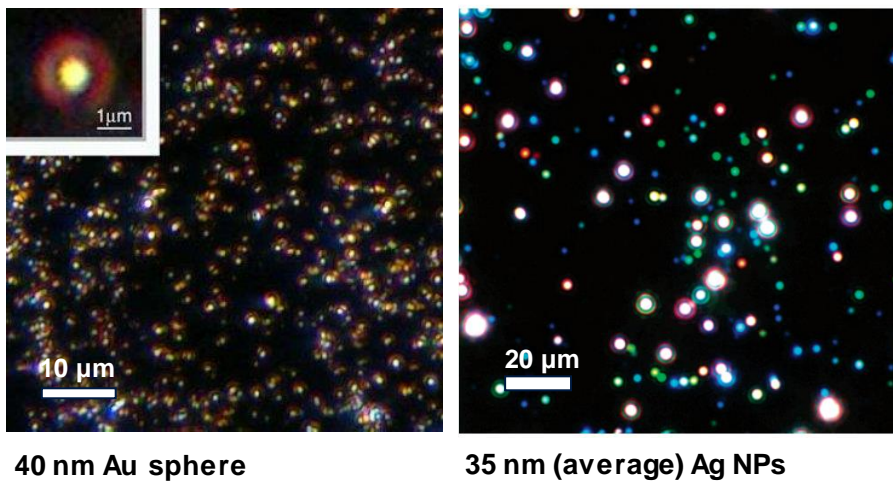


Figure 65 Dark field image of plasmonic nanoparticles.

### 3.8. Candidate Materials for Localized Surface Plasmon Resonances

Not only gold but also other metals can have localized surface plasmon resonance if they have high concentration of electrons. The localized plasmon resonance frequency should be  $3^{-0.5}$  times lower than the volume plasmon resonance frequency. The plasmon resonance frequency is expressed with electron density as below.

**Formula 3.24 LSPR frequency according to the electron concentration**

$$\omega_{\text{LSPR}} = \sqrt{\frac{n_e e^2}{3m^* \epsilon_0}}$$

Higher concentration of electron makes the increase of the localized surface plasmon resonance frequency. Metals have very narrow resonance spectra attributed to their small optical loss around resonance. On the contrary, the broad resonance spectra of conducting oxide is attributed to their high optical loss around resonance spectra.<sup>51</sup> The plasmon frequency can be tuned by controlling the composition of corresponding metals. Therefore, there is a high possibility of enhance the absorption property by introduction of plasmonic nanostructure for photonic applications. A gold, silver, and copper is usually chosen to harvest visible light spectra in the applications (Figure 20).<sup>52</sup> Especially, gold is chosen for its exceptional stability in harsh environments.

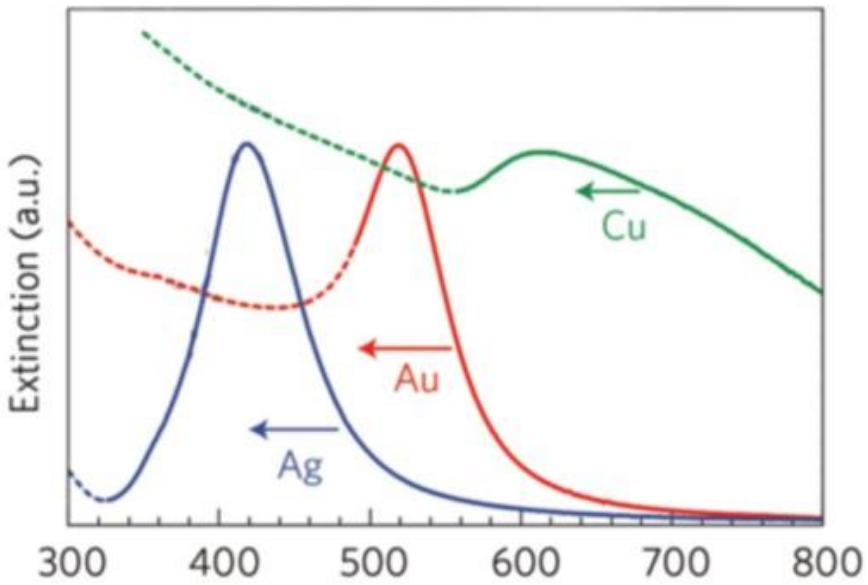
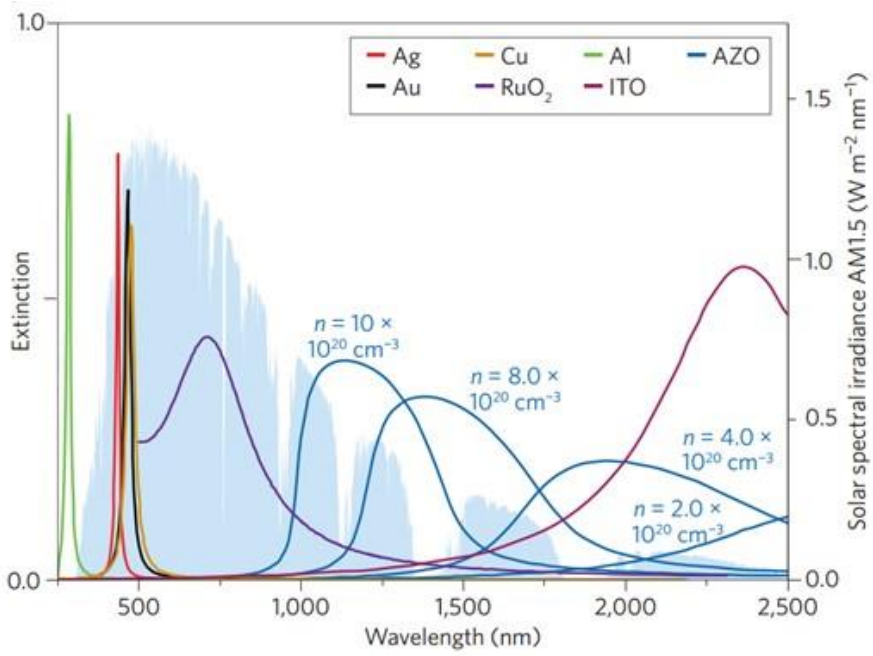


Figure 66 Optical extinction of metals and conducting oxide by LSPR.

### 3.9. Modulations of Extinction Spectra

In practical, the extinction spectra of metal nanoparticles are deeply related to with the size and surrounding medium. Extinction is consisted of absorption and scattering. Two properties decide the optical property of nanoparticle.<sup>53</sup> Extinction is increase upon increasing the size of metal nanoparticles as expected. When the size is sufficiently small (below 10 nm above 3 nm), scattering almost diminished. The scattering is effectively working above 50 nm. Absorption due to the intraband transition is attributed the absorption spectra of metal nanoparticles. If the size of nanoparticle is very large (~ a few hundred nm) the extinction spectra is unobservable due to the arise of surface plasmon polariton. The absorption always contributes to the extinction spectra of metal nanoparticles. In reality, the resonance of metal nanoparticle is redshift by increasing the size. This discussion is summarized in Figure 21.

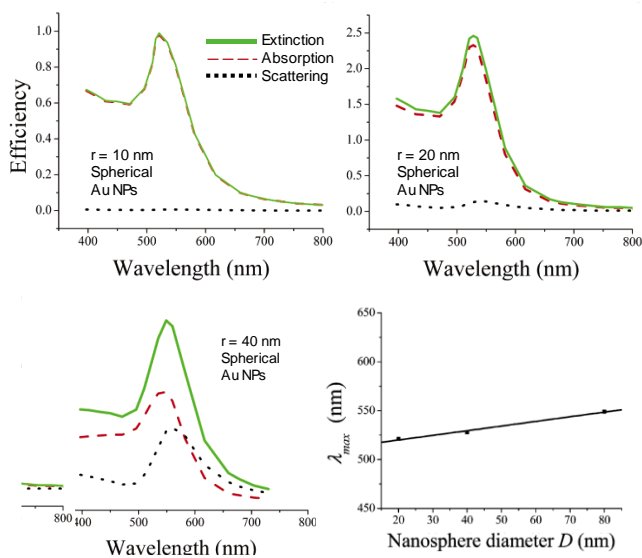


Figure 67 Extinction spectra of metal nanoparticles according to their size.

By decreasing of metal nanoparticle size below a few nanometer ( $> 3$  nm) the absorption by intraband transition almost diminishes due to the emergence of semiconducting property of metal nanoparticles by quantum confinement (Figure 22).<sup>54,55</sup>

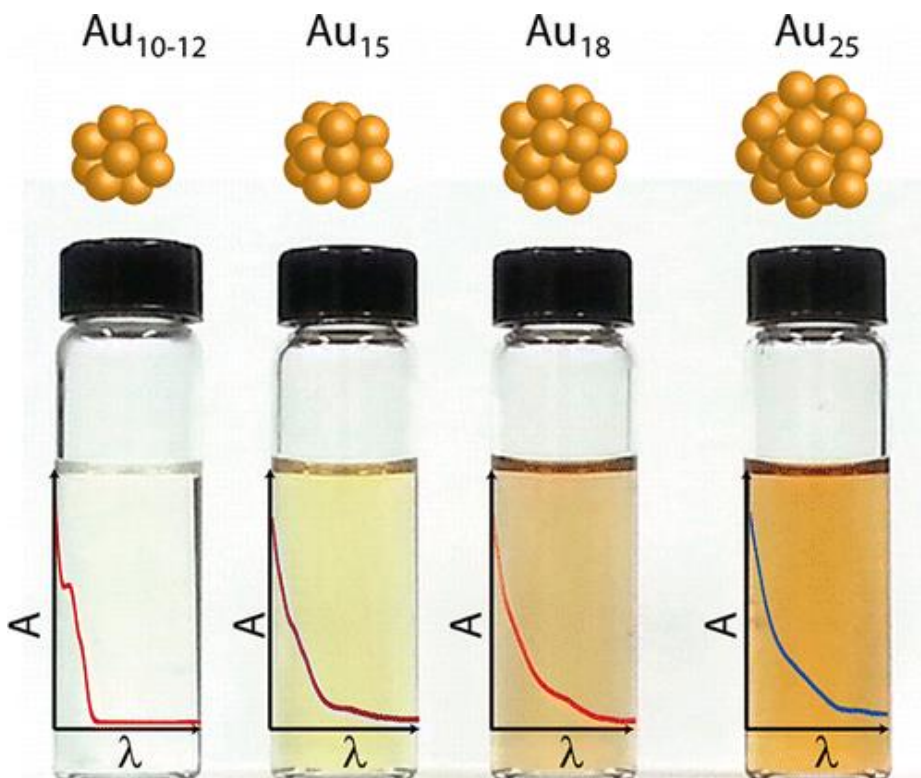


Figure 68. Glutathione-protected gold clusters exhibit size-dependent excited state and electron transfer properties.

Permittivity of surrounding medium definitely tunes the resonance frequency of metal nanoparticles. Below is FDTD simulated transmittance spectra of gold Plasmonic gold nanodisk on the dielectric substrate. Increasing the refractive index of substrate makes the redshift of the resonance frequency as shown in Figure 22(a). The displacement from a substrate also affects the resonance

spectra as shown in Figure 22(b). The longer interaction length makes the resonance spectra to be blueshifted.<sup>56</sup>

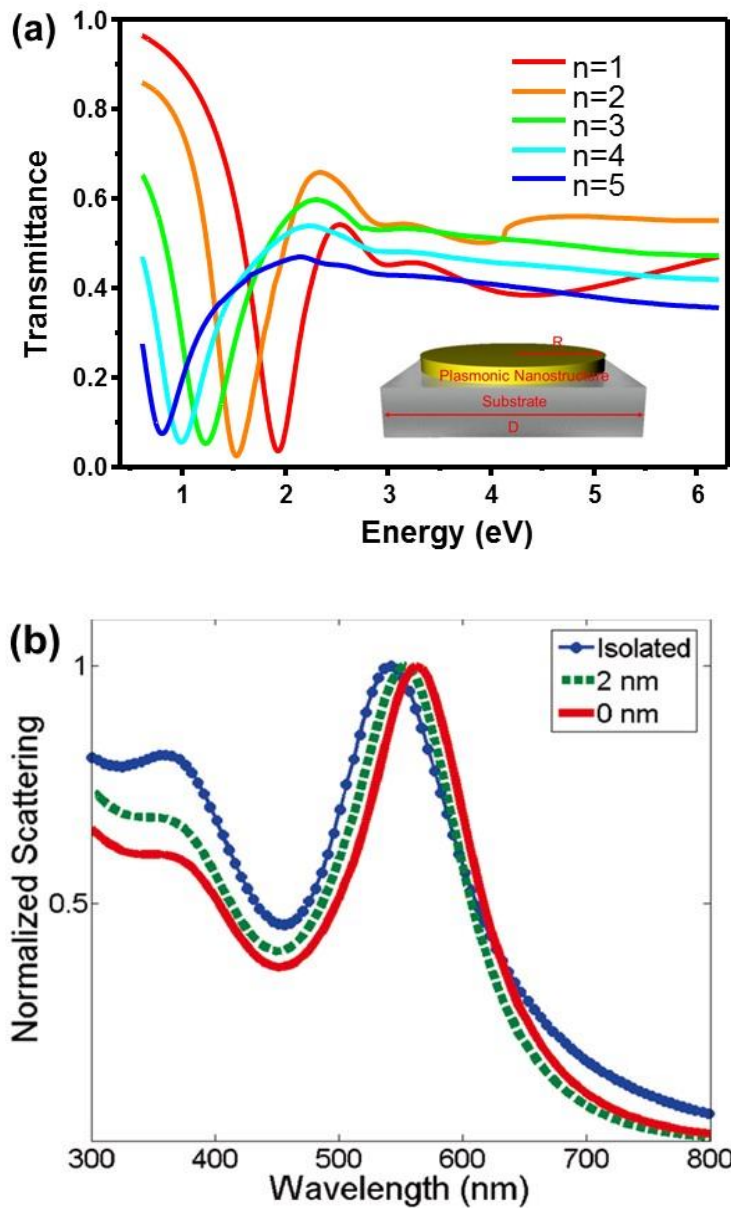


Figure 69 (a) Simulated dielectric constant (refractive index) dependence. (b) Resonance change upon metal nanostructure displacement with substrate

## Chapter 4

### Photoelectrochemical Water Splitting

#### Quote

**Akira Fujishima and Kenichi Honda**

“Because water is transparent to visible light it cannot be decomposed directly, but only by radiation with wavelengths shorter than 190 nm.”  
(1972, Nature)

## 4.1. Introduction

### 4.1.1 Configurations

To measure or drive electrochemical reaction, electrode connection with an external bias is required. Electrode should immerse into the electrolyte to measure a characteristic. The system contains electrical path and chemical path via electrolyte solution. To flow electrons in the circuit without conduction limitation, the sufficient electrolyte conductivity should be provided. To acquire the goal, ionic chemicals are added into the water. We need at least two electrodes to measure the performance of working in the cell. So conductive metallic electrode in the counter side is required to measure the performance correctly. Note that the counter electrode should not limit current flow in the cell.

Let us consider familiar two electrode configuration. The representative image is given in below Figure 70.

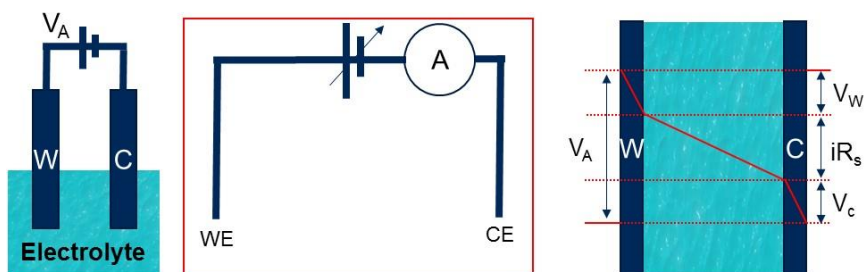


Figure 70. 2-electrode configuration of electrode.

In the 2-electrode configuration, working electrode (WE, the electrode that want to measure) and counter electrode (CE) is connected with cell via electrolyte rather than wire. The applied voltage ( $V_a$ ) is spreaded into the whole

system including the potential drop at the working electrode, counter electrode and electrolyte. The biggest problem in the configuration is potential drop at the electrolyte. As shown in Formula 4.1, the applied potential does not entirely through the electrode. If the small solution resistance so high that neglect of the potential drop is not available, this tendency become significant. Most of the system, we cannot measure the performance of the working electrode correctly with a 2-electrode configuration.

**Formula 4.1 Potential drop at 2-electrode configuration**

Potential drop in the system is given as below.

$$V_a = V_w + V_c + iR_s$$

If the solution resistance is negligible, then below relation is valid.

$$V_a \cong V_w + V_c$$

To overcome the situation, most electrochemical experiment adopts 3-electrode configuration in the performance measurement. The representative image is expressed in Figure 71.

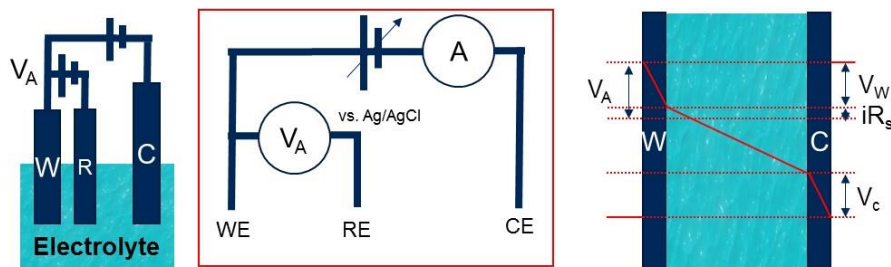


Figure 71. 3-electrode configuration of electrode.

In the 3-electrode configuration, potentiostat applies potential ( $V_a$ ) with respect to the reference electrode (RE) connected with WE. And the potential

difference with WE and CE is maintained by other bias element between WE and CE. As a result, the current is varied to maintain the potential applied between WE and RE. In the configuration, we can separately control the potential element and current element in the WE. In the configuration, the problem in the 2-electrode configuration is resolved. First of all, the applied potential is almost same as the potential applied in the WE. Small amount of potential drop from solution resistance ( $iR_s$ ) also can be neglected, when the solution resistance is negligible as written in Formula 4.2.

**Formula 4.2 Potential drop at 2-electrode configuration**

Potential drop in the system is given as below.

$$V_a = V_w + iR_s$$

The solution resistance is negligible for conducting electrolyte, Luggin capillary or  $iR$  corrector module.

$$V_a = V_w$$

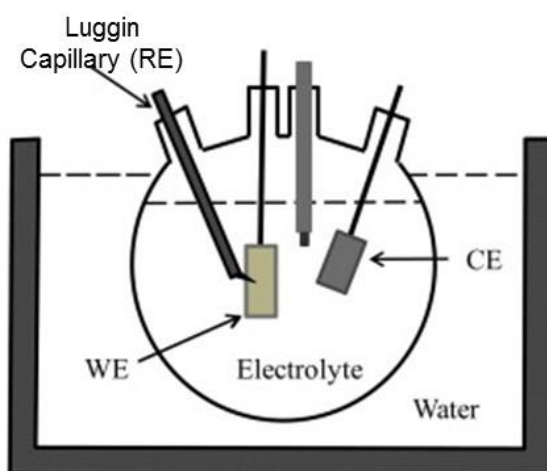


Figure 72. 3-electrode configuration with Ruggin capillary.

The resistance of the solution electrolyte resistance can be removed also via Luggin capillary. The Luggin capillary can reduce the distance between the WE surface and RE as small as possible as shown in Figure 72. In addition, the additional module can be used to remove the potential drop from solution resistance (iR corrector).

#### **4.1.2 The Potentiostat.**

A potentiostat is the electronic module required to control the cell in electrochemical situations. Actual potentiostat have more than 3 electrodes for specific purpose. Sensing and ground electrodes exist in the real potentiostat module. Sensing electrode is added to the working electrode in the 3-electrode configuration the purpose of the electrode is sense the potential at the terminal of WE to give a feedback at the circuit. Sometimes it is separated as a second reference electrode for the purpose of second reference electrode (RE2). This configuration is called as 4-electrode configuration which is frequently used in an electrochemical membrane. The potentiostat completes the circuit between WE and CE by ground. The potentiostat maker provides ground electrode (GE) for the specific condition balance for the reference. 3 units (voltage controller, signal controller and current measure resistor) are separated in the potentiostat. Signal of voltage is formed by the sum of the signal (for example, linear, sinusoidal and climbing). The current flowing the circuit ( $i_{CE}$ ) is not directly measured into circuit element. The current is measured by current measure resistor via amplifier (converter). Using several resistive units, the current can be read according to the scale. The whole explanation is included in Figure 73 (specific function and module controller is eliminated for the simplicity).

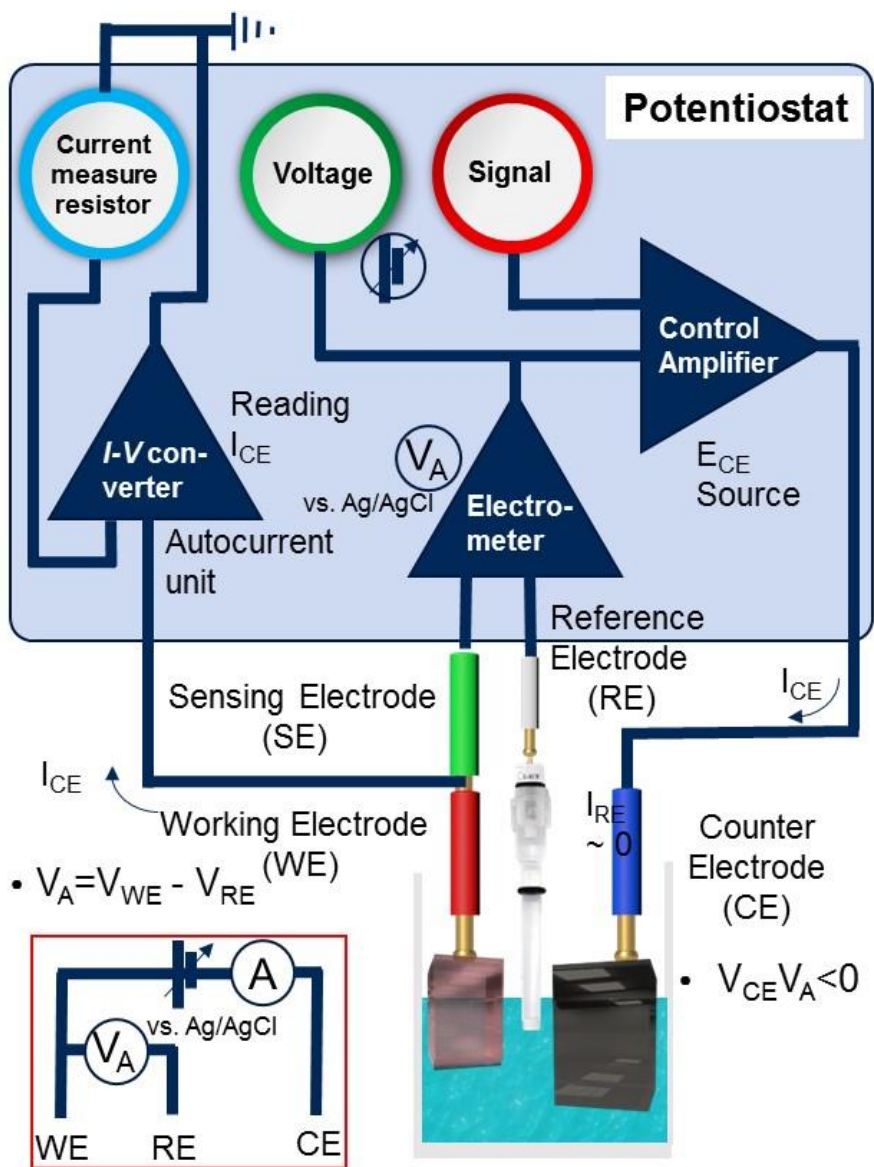


Figure 73. The simplified diagram of a potentiostat.

### 4.1.3 Reference Electrodes

The three types of standard potentials are defined by consideration of equilibrium from the Nernst equation. To deal with the potential at the electrode the Nernst equation is given in Formula 4.3.

### Formula 4.3 Nernst equation

Redox equation can be written as below.



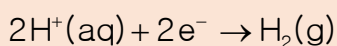
According to equilibrium theory, the potential can be written as below.

$$E = E^{\circ} - \frac{RT}{zF} \ln \frac{a_{\text{Red}}}{a_{\text{Ox}}} = E^{\circ} - \frac{0.05916}{z} \ln \frac{a_{\text{Red}}}{a_{\text{Ox}}}$$

According to the Nernst formula, the potential at the electrode can be analyzed. The hydrogen evolution potential near a Pt electrode in an ideal solution, we call it as standard hydrogen electrode (SHE) potential. Relation is given as below.

### Formula 4.4 SHE potential

Potential of Pt electrode in an ideal solution is deduced from the hydrogen evolution reaction.



By the Nernst equation, the equilibrium formula is given as below.

$$E = \frac{RT}{F} \ln \frac{a_{\text{H}^{+}}}{\sqrt{p_{\text{H}_2}/p^{\circ}}}$$

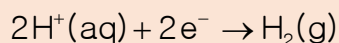
$$E = -\frac{2.303 RT}{F} \text{pH} - \frac{RT}{2F} \frac{p_{\text{H}_2}}{p^{\circ}}$$

With a consideration of non-real solution, the environment near the Pt electrode can be chosen as a 1N acid solution ( $\text{H}^{+}$  ions have no interaction) with hydrogen gas saturation. Potential from this type of Pt electrode is called as

normal hydrogen electrode (NHE). In addition, we can additionally consider the potential interaction with hydrogen ions. The reference condition is called as reference hydrogen electrode (RHE). So pH is critical factor for the standard potential of hydrogen reaction. The relation is given as below Formula 4.5.

#### **Formula 4.5 RHE potential**

Potential of Pt electrode in an ideal solution is deduced from the hydrogen evolution reaction.



By the Nernst equation, the equilibrium formula is given as below.

$$E = \frac{RT}{F} \ln \frac{a_{\text{H}^+}}{\sqrt{p_{\text{H}_2}/p^\circ}}$$

$$E = -\frac{2.303 RT}{F} \text{pH} - \frac{RT}{2F} \frac{p_{\text{H}_2}}{p^\circ}$$

According to the pH, above equation is arranged as below.

$$E_{\text{RHE}} = E_{\text{RHE}}^\circ - 0.0592 \text{ pH}$$

With applying voltage, above relation is rewritten as below.

$$E_{\text{RHE}} = (E_{\text{Electrode}}(\text{applied}) + E_{\text{Electrode}}^\circ) - 0.0592 \text{ pH}$$

#### **4.1.4 Conversion of Potentials**

The relation between absolute electrode potential and electrochemical potential with respect to the reference hydrogen electrode has been investigated by Trasatti (1986).<sup>57</sup> Using thermodynamic consideration and experimental

evidence, he succeed to drive the relation by consideration of Hg metal electrode. The detail is given in Formula 4.6.

**Formula 4.6 Relation between absolute hydrogen electrode potential and standard hydrogen electrode potential.**

Let's suppose SHE electrode potential with Hg junction.

The absolute potential of SHE electrode is calculated as follow.

$$E^{\circ}(\text{H}^+/\text{H}_2, \text{Abs}) = E^{\text{Hg}}(\text{Abs}) - E^{\text{Hg}}(\text{SHE})$$

The absolute potential of Hg with solution is the potential difference with Hg work function and contact potential. So below relation is achieved.

$$E^{\text{Hg}}(\text{Abs}) = \phi_{\text{Work}}^{\text{Hg}} + \Delta_{\text{contact}}^{\text{Hg}} \varphi$$

With combination of two equations, following equation is acquired.

$$E^{\circ}(\text{H}^+/\text{H}_2, \text{Abs}) = (\phi_{\text{Work}}^{\text{Hg}} + \Delta_{\text{contact}}^{\text{Hg}} \varphi) - E^{\text{Hg}}(\text{SHE})$$

Three value at the right side is measurable quantity and known as below.

$$\phi_{\text{Work}}^{\text{Hg}} = (4.50 \pm 0.02) \text{ eV}$$

$$\Delta_{\text{contact}}^{\text{Hg}} \varphi = -(0.248 \pm 0.001) \text{ V}$$

$$E^{\text{Hg}}(\text{SHE}) = -(0.192 \pm 0.001) \text{ V}$$

Above equation is arranged as following way.

$$\begin{aligned} E^{\circ}(\text{H}^+/\text{H}_2, \text{Abs}) &= (\phi_{\text{Work}}^{\text{Hg}} + \Delta_{\text{contact}}^{\text{Hg}} \varphi) - E^{\text{Hg}}(\text{SHE}) \\ &= ((4.50 - 0.248) + 0.192) \pm 0.02 \\ &= (4.44 \pm 0.02) \text{ V} \end{aligned}$$

$$E^{\circ}(\text{H}^+/\text{H}_2, \text{Abs}) - (4.44 \pm 0.02) \text{ V} = 0 \text{ V}$$

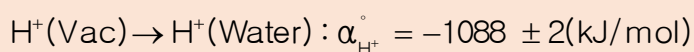
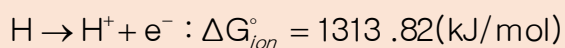
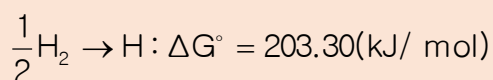
The  $H^+/H_2$  reaction at the SHE is 0 by definition.

$$E^\circ(H^+/H_2, SHE) = 0 V$$

Because above two equations are equivalent, it is arranged as below.

$$E^\circ(H^+/H_2, SHE)/V = E^\circ(H^+/H_2, Abs)/V - 4.44$$

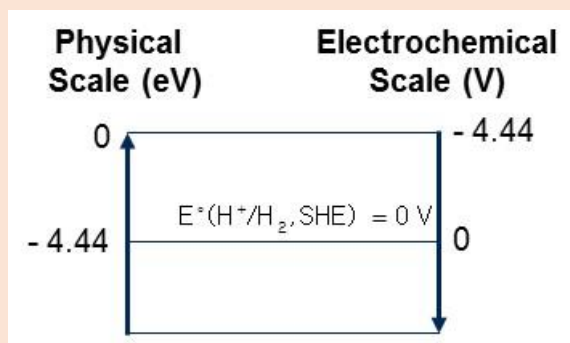
This calculation is matched with thermodynamic consideration. The Nernst equation for the hydrogen dissociation reaction to hydrogen ion is given as below.



(hydrogen ion solvation energy)

$$E^\circ(H^+/H_2, Abs) = \frac{\Delta G^\circ + \Delta G_{ion}^\circ + \alpha_{H^+}^\circ}{F} = (4.44) V$$

The value from two considerations is same. The relation is graphically shown below.



### 4.1.5 AM 1.5 G Standard

Even though the research for photoelectrochemical water splitting is focused on the utilization of sunlight, the sunlight is not available every day in stable. The intensity is changed according to the latitude, longitude, height and weather. So artificial sunlight is required. However, due to the difference of sunlight in the specific position on Earth, the standard condition for the sunlight is needed. AM 1.5 global (G) radiation condition indicates the sunlight from the 48.2 degree from zenith of north pole by passing the atmosphere. The sunlight is emitted from the sun by 5800 K blackbody radiation. Due to some absorption from the atmosphere, there are some spikes exist as shown in Figure 74.

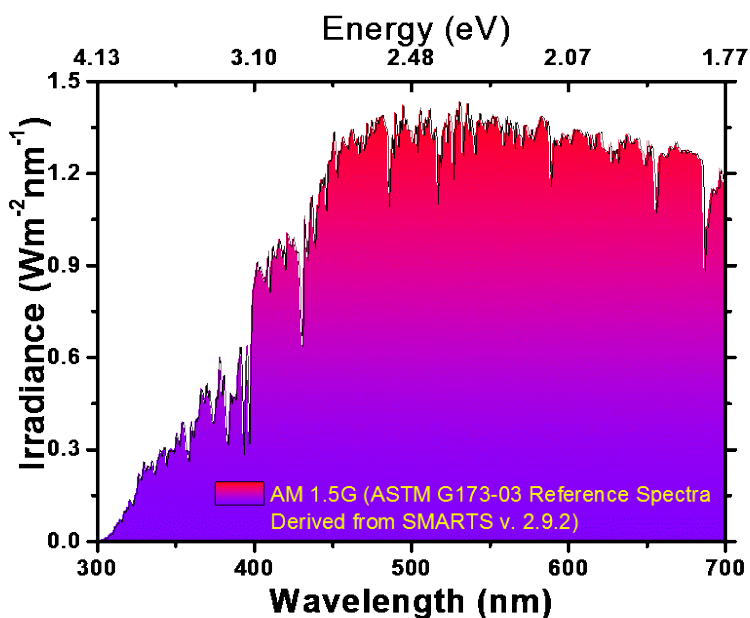


Figure 74. AM 1.5 G (global) spectra.

The suitable figure for the explanation of the standard is included in a Figure 75 and explanation is added in Table 2.

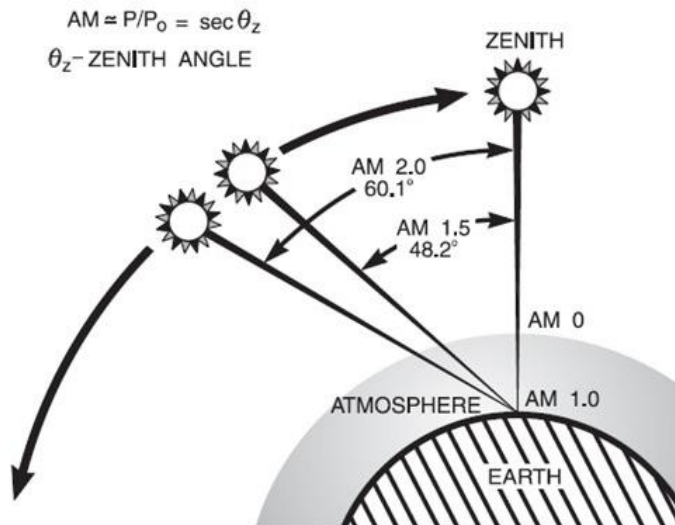


Figure 75. Explanation of Air Mass (AM) standard on Earth.

Table 2. Definition for the Air Mass (AM) global illumination.

<b>AM 0</b>
The spectrum outside the atmosphere, the 5,800 K black body, is referred to as "AM0".
<b>AM 1D</b>
Direct radiation that reaches the ground passes straight through all of the atmosphere, all of the air mass, overhead.
<b>AM 1G</b>
The global radiation with the sun overhead
<b>AM 1.5G</b>
Many of the world's major population centers angle of radiation

## 4.2. Principles of Solar Water Splitting

The concept of photoelectrochemical water splitting is firstly provided in nature by Fujishima and Honda (1972).<sup>58</sup> A numerous materials have been chosen for the purpose of photoelectrochemical water splitting and advance has been made. With a thermodynamic consideration, to split water, at least  $\Delta E^\circ = 1.23$  V thermodynamic voltage is required. The derivation is provided in Formula 4.7.

### Formula 4.7 Water reduction/oxidation (redox) voltage

For water splitting reaction, below reaction should be considered.



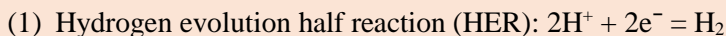
$\Delta G_f^\circ (\text{H}_2\text{O})$  indicates a formation energy of water.

$$2\Delta G_f^\circ (\text{H}_2\text{O}) = 2 \Delta G_f^\circ (\text{H}_2) + 2 \Delta G_f^\circ (\text{O}_2) + \Delta G_f^\circ (\text{H}_2\text{O}) - 4FE^\circ$$

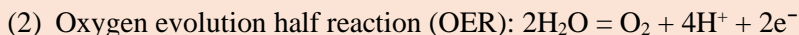
We can achieve thermodynamic voltage to split water by putting the formation energy above.

$$E^\circ = 1.229 \text{ (V)} \sim 1.23$$

The water splitting reaction is the sum of the two half reaction (oxidation and reduction). The reaction potential of hydrogen reaction is defined. So the oxygen evolution half reaction can be calculated from the water redox voltage.



The reaction occurs at 0 V vs. RHE.



The reaction occurs at 1.23 V vs. RHE.

## 4.2.1 Semiconductor-Liquid Junction

To understand the photoelectrochemical water splitting system, the energy diagram between semiconductor-liquid junction should be understood. Which is similar to the well-known p-n junction. In the case, the fermi level of the reaction is replaced with HOMO/LUMO level of water. So band bending in the water is not considered after equilibrium in basic consideration. The potential drop on the surface is presented well in the theory of electrical double layer. The diagram is shown in below Figure 76.

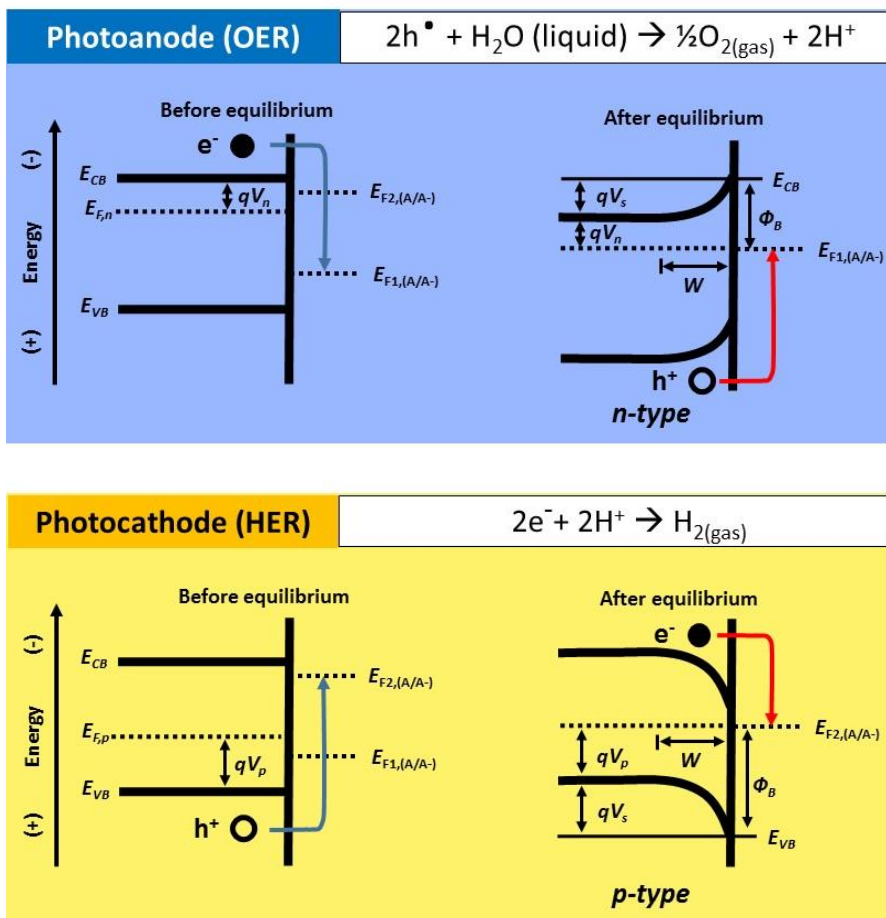


Figure 76 Semiconductor-liquid junction.

Before equilibrium, n-type semiconductor has electron as a majority carrier. The majority carriers (electrons) make an equilibrium for the redox potential of electrolyte at the possible highest electrochemical potential (lowest energy). After equilibrium, the band bending occur downward so that majority carrier (electron) cannot pass to the electrolyte due to the generation of depletion region at the semiconductor-electrolyte interface. The reaction is occurring by minority carrier (hole). In the n-type case, lowest reaction potential for electron reaction (or nearest reaction potential for hole) is oxygen evolution reaction potential of water. So with n-type semiconductor, oxygen is evolved. We call it as a photoanode.

Similarly, before equilibrium, p-type semiconductor has hole as a majority carrier. The majority carriers (holes) make an equilibrium for the redox potential of electrolyte at the possible lowest electrochemical potential (highest energy). After equilibrium, the band bending occur upward so that majority carrier (hole) cannot pass to the electrolyte due to the generation of depletion region at the semiconductor-electrolyte interface. The reaction is initiated from minority carrier (electron). In the p-type case, lowest reaction potential for hole reaction (or nearest reaction potential for electron) is hydrogen evolution reaction potential of water. So with p-type semiconductor, hydrogen is evolved. We call it as a photocathode.

Upon illumination the excess carriers on the semiconductor involves the water splitting reaction. So carrier dynamic on the photoelectrode is essential to get efficient reaction.

## 4.2.2 Electrical Double Layer Structures

Many model has been suggested in the history for potential distribution at the semiconductor-electrolyte interface. Among them, 4 model is chosen for the understanding. Below Figure 77 is attached for the graphical explanation.

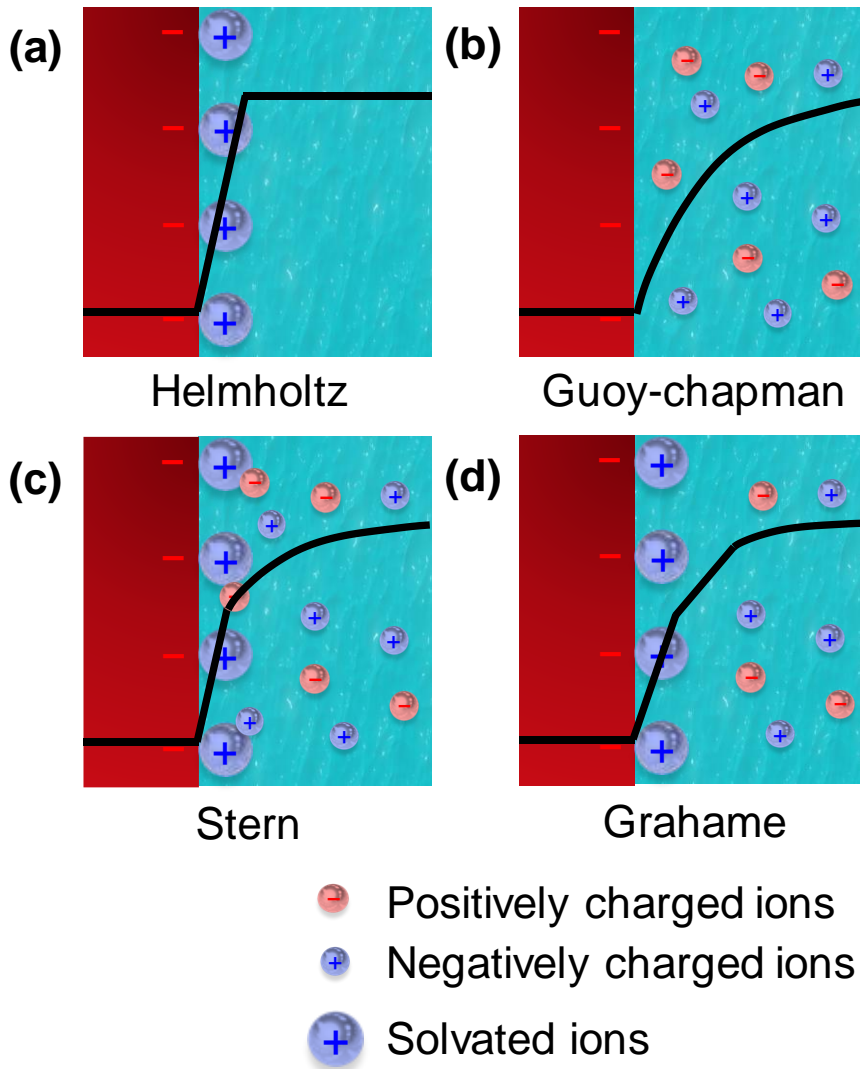


Figure 77 Electrical double layer structure suggested in history.

To explain the potential behavior at the interface, Helmholtz developed the model in 1853. He considered that all positive ions are attached to the metal interface as a monolayer due to the negative charges on the metal surface. He neglected ion diffusion at the interface. At 1913, Guoy-Chapman diffuse layer point charge model was suggested. They considered the diffusion of ions through the interface. They regarded ion as a point charge which is distributed from the surface similar to the Brownian motion. Far ahead, at 1924, Stern give a correction to the model. He considered ion solvation at the interface. The solvated ions are attracted to the surface of metal due to the charge. As a result, the monolayer and diffusion of ions can coexist. From the metal surface to a specific distance, the form of potential is linear. If the distance from the surface is larger than the solvated atom, diffusion of ion is activated. At 1940, Grahame separated the Stern layer into inner Helmholtz and outer Helmholtz layer. Due to the selective absorption of the solvated ions. The further understanding of the interface has achieved by Marcus. He developed the physical and mathematical fundamental of electron charge transfer at the interface. We call it as a 'electron transfer theory' or, simply, 'Marcus theory'. The theory will be discussed in the section in ahead.

### **4.2.3 Band Structure of Photoelectrochemical Water Splitting with n-type Photoanode**

By the understanding of the physics at an interface between semiconductor and electrolyte, the explanation of solar water splitting process is available. Though thermodynamic consideration suggests the thermodynamic voltage

with 1.23 V, that is not sufficient to deal the circumstances at the photoelectrode. More detailed figure is embodied as a schematic in Figure 78.

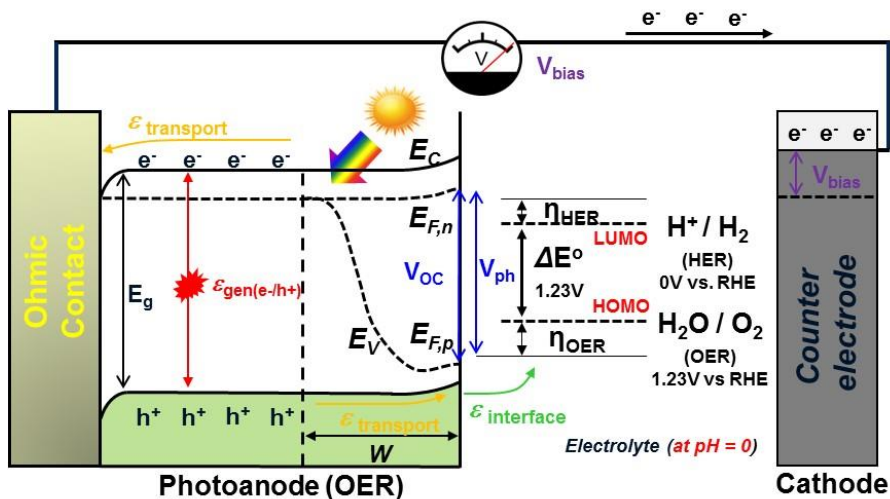


Figure 78. Band structure of photoanode with the illumination.

When the photoanode absorbs light, semiconductor generates excess carrier for the light-absorbing region. The excess carrier dissipates without band banding. They can be separated (activated) at the surface due to the electric field in depletion region (denoted as (W)). According to the basic semiconductor physics in below Formula 4.8, the generation of excess carrier at the interface results in the separation of the fermi level of majority carriers (electrons) and minority carriers (holes). The fermi level is slightly upward due to the excess carrier at the interface.

**Formula 4.7 Carrier concentration under illumination**

The equilibrium of carrier concentration is given as below by semiconductor physics.

$$(1) n_0^2 = np$$

Due to the generation of excess carrier from light, the carrier concentration can be written as below.

$$(2) n = n_0 + \Delta n \approx n_0$$

$$(3) p = p_0 + \Delta p \approx \Delta p$$

Under illumination, the electron concentration remains constant. But the hole concentration increases significantly.

The position of Fermi level is dependent on the carrier concentration by following below formula.

$$(4) E_{F,n} = E_i + kT \ln(n/n_i)$$

$$(5) E_{F,p} = E_i - kT \ln(p/n_i)$$

Therefore, band separation is maximized at the interface between semiconductor-electrolyte.

The potential difference between two quasi-Fermi level is the open circuit voltage ( $V_{oc}$ ) (maximum voltage that cell can exhibit).<sup>59</sup> The photovoltage ( $V_{ph}$ ) for OER reaction is the potential difference between the electron fermi level and OER reaction level. The relation is given in Formula 4.8.

#### **Formula 4.8 Driving force for OER in photoanode**

(1) Photovoltage

$$V_{ph} = E_{F,n} - E_{F,p}$$

(2) Driving force for OER reaction

$$V_{Dr.OER} = E_{F,p} - E^\circ(\text{H}_2\text{O}/\text{O}_2) (> 0 \text{ for spontaneous reaction})$$

(3) Driving force for HER reaction

$$V_{\text{Dr.HER}} = E_{F,n} - E^\circ(\text{H}^+/\text{H}_2) (> 0 \text{ for spontaneous reaction})$$

To activate the water splitting reaction at the photoanode, the photoanode photovoltage ( $V_{\text{ph}}$ ) should be larger than thermodynamic voltage (1.23 V). But there is more than the condition. To occur OER reaction, the quasi-fermi level of holes (simply, valence band position at the interface) should be negative than OER potential. And to activate HER reaction, the quasi-fermi level of electrons (simply, conduction band position at the interface) should be positive than HER potential. There is also kinetic barrier for the reaction (blocking reaction from a theoretical way). As a result, additional voltage is required to evoke reaction. The voltage for evoking reaction is called as overpotential ( $\eta$ ). Due to the thermalization loss and overpotential (kinetic barrier for water splitting reaction) practical water splitting voltage is quite larger than thermodynamic voltage (1.23 V). To evoke the OER reaction, the driving force for OER reaction should be larger than OER overpotential. And the principle is applied to the HER.

**Formula 4.9 Overpotential**

(1) OER overpotential

$$\eta_{\text{OER}} = E(\text{H}_2\text{O}/\text{O}_2) - E^\circ(\text{H}_2\text{O}/\text{O}_2)$$

(2) HER overpotential

$$\eta_{\text{HER}} = E^\circ(\text{H}^+/\text{H}_2) - E(\text{H}^+/\text{H}_2)$$

The potential-pH diagram for water splitting including overpotential is provided in the Figure 79. The thermodynamic potential suggested in previous section is the value at the pH = 0.

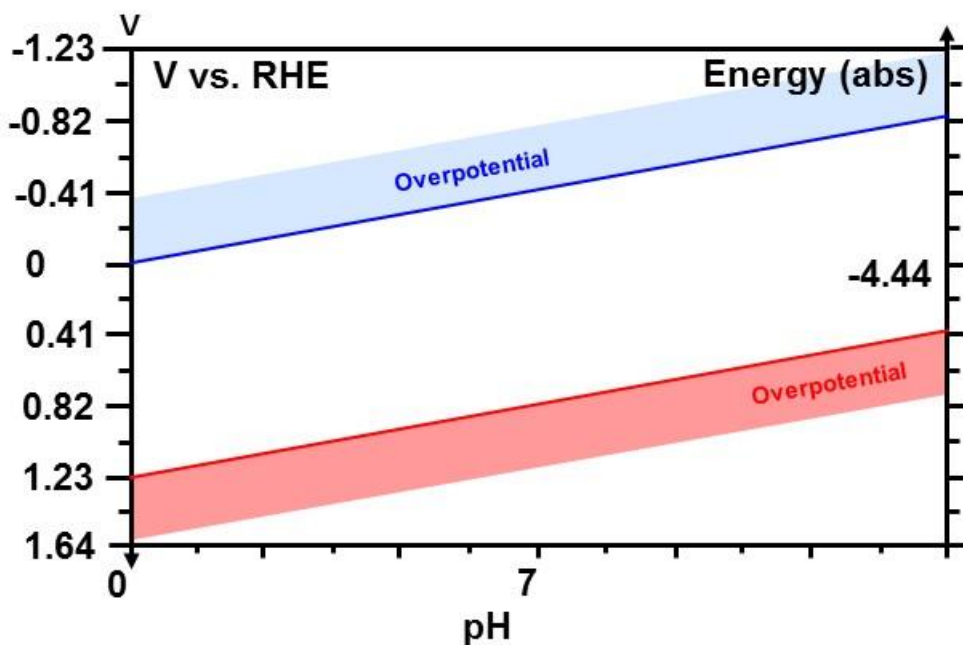


Figure 79. Water splitting potential including overpotential according to a pH.

Next we should consider the behavior of carrier, when the light illuminated into the semiconductor. Upon illumination, electron and hole pair is generated in the bulk region. After the charge generation, holes are transferred into the surface of semiconductor and electrons are transferred into the counter electrode. The transported charge should be transferred into the electrolyte via tunneling. Overall, three process is involved for solar water splitting process (charge generation, charge transport, charge transfer at the interface). Overall efficiency of the water splitting progress is decided by the efficiency of the three process. The overall efficiency from three process is called as quantum efficiency. More specific, the incident photon is converted to electron in the process. So, the external quantum efficiency (EQE) in the process is described as IPCE.

#### Formula 4.10 IPCE (incident photon to converted electron efficiency)

Three types of efficiency are considered for solar water splitting process.

$$\mathcal{E}_{\text{gen(e-/h+)}} , \mathcal{E}_{\text{transport}} , \mathcal{E}_{\text{interface}}$$

IPCE is the multiplied value of these three efficiency.

$$\text{IPCE} = \mathcal{E}_{\text{gen(e-/h+)}} \times \mathcal{E}_{\text{transport}} \times \mathcal{E}_{\text{interface}}$$

If the position of quasi Fermi level is not higher than the water splitting redox level (with overpotential), additional driving by external bias is required. For example, in the Figure 78, the HER is not occur without external bias due to the lack of the HER driving force to overcome HER overpotential. The reaction is going forward only with bias in the case. Practical condition for the water splitting is summarized.

(1) **Practical potential:  $E = 1.23 + \eta$  (V) > 1.6 (V)**

(2) **Band edge requirement:**

$$E_{F,n} \text{ (or CB edge)} < E(\text{H}^+/\text{H}_2) < E^\circ(\text{H}^+/\text{H}_2)$$

$$E_{F,p} \text{ (or VB edge)} > E(\text{O}_2/\text{H}_2\text{O}) > E^\circ(\text{O}_2/\text{H}_2\text{O})$$

(3) **Chemical stability in the electrolyte**

(4) **Efficient charge generation/transportation/transfer**

Chemical stability of the semiconductor will be discussed in next session.

### 4.3. Candidate Materials for Solar Water Splitting

#### 4.3.1 Considering Band-Edge Positions

As discussed in previous section, at least, band-edge of semiconductor should straddle the water redox level. As a result, according to the band

position, the ability of gas evolution is determined. For example, if the conduction band edge is negative than the HER level, HER reaction is possible. Similarly, if the valance band edge is positive than the OER level, OER reaction is possible. Band edge position is depicted in Figure 80, according to the conduction band positions. Band edge position is collected from the prominent recent review article.<sup>60</sup>

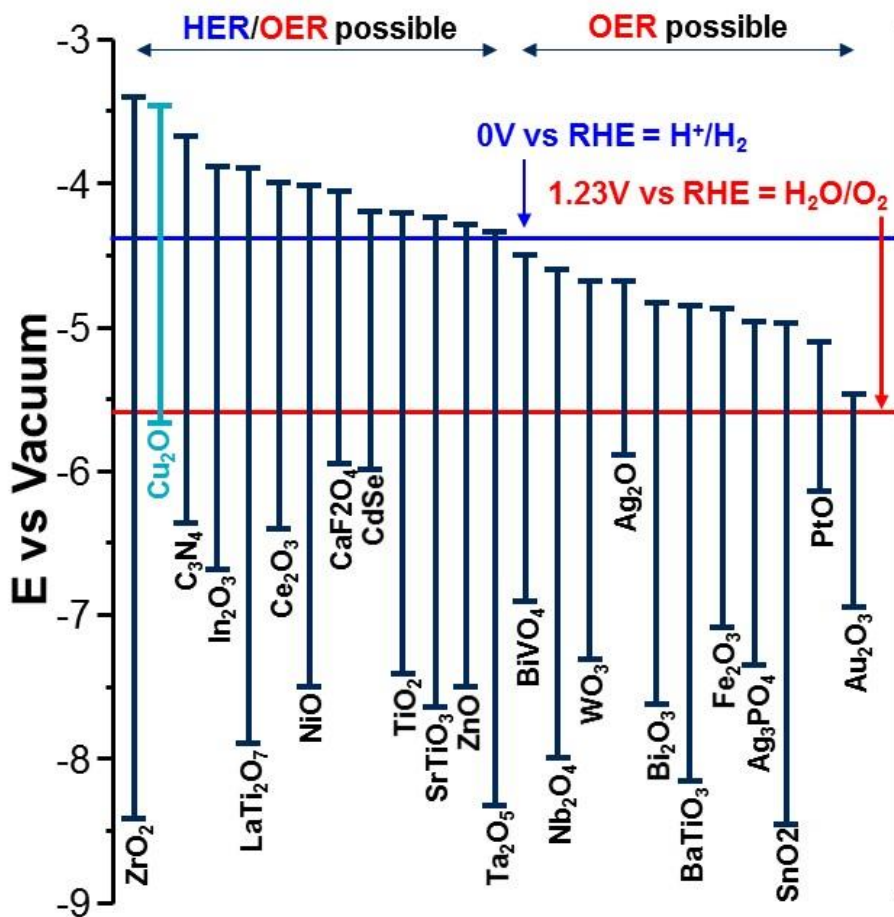


Figure 80. Possibility of water splitting reaction related to the band edge positions.

### 4.3.2 Corrosion Level

The selection of semiconductor materials for water splitting is more complicated due to the photocorrosion. There are several reactive redox level exists some type of semiconductors. This reactive redox level makes semiconductor to be decomposed rather than split water by charge generated from illumination.<sup>61</sup>

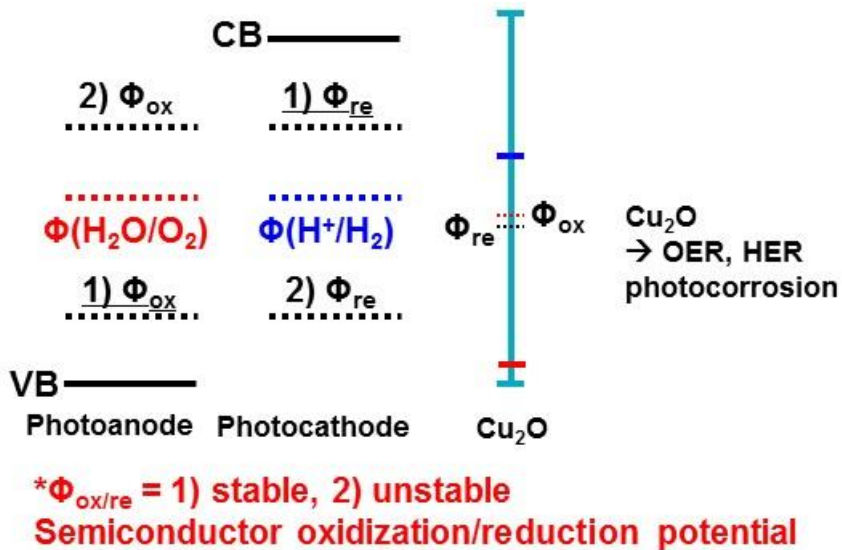


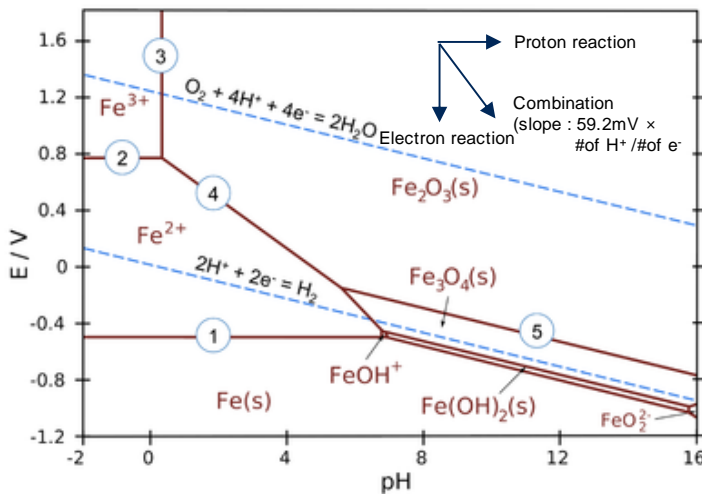
Figure 81. Explanation of a photocorrosion possibility from the semiconductor photoelectrode.

Detail is given in Figure 81. In the photoanode, if the photocorrosion level is below the OER level, the semiconductor photoanode have a resistant with photocorrosion due to the energy position with holes. While, if the photocorrosion level is above the OER level, the photocorrosion should be happen due to the thermodynamic principle. The situation is similar in the photocathode. If the photocorrosion level is above the HER level, the

semiconductor photocathode has a resistant with photocorrosion due to the energy position with electrons. While, if the photocorrosion level is below the HER level, the photocorrosion should be happen due to the thermodynamic principle. For an example,  $\text{Cu}_2\text{O}$  fulfills the photocorrosion condition as photoanode and photocathode.

### 4.3.3 Pourbaix Diagram

The stability with aqueous condition is also important. According to the pH and applied voltage, a thermodynamic stable phase is determined. The graph expresses the stability for these two condition is a Pourbaix diagram. Here, the famous semiconductor material hematite ( $\alpha\text{-Fe}_2\text{O}_3$ ) is adopted as an example in Figure 82.



**$\text{Fe}_2\text{O}_3 \rightarrow$  unstable at acidic media / cathodic potential**

Figure 82. Pourbaix diagram of hematite.

Without bias (0 E/V), in the low pH region,  $\text{Fe}^{2+}$  ion is dominating chemical form. On the other hand, in the high pH region,  $\text{Fe}_2\text{O}_3(\text{s})$  is dominating chemical

form. This implies that hematite ( $\alpha\text{-Fe}_2\text{O}_3$ ) is instable in the low-pH region. If we apply bias in pH 13 condition, the phase become reduced below negative bias (-0.4 E/V) and eventually become metal Fe(s) form. This indicates the usage of hematite as a photocathode is not proper.

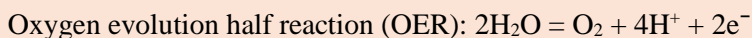
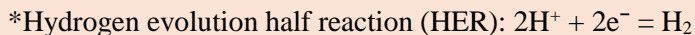
In addition, there are three types of lines (vertical, horizontal and declined) exist according to the slope. If the experimental condition moved vertical (apply bias), electrons is only involved. A vertical line between the phase implies that the reaction path is electron reaction. If the experimental condition moved horizontally (change pH), the number of proton ( $\text{H}^+$ ) is changed according to the condition. A horizontal line between the phase implies that the reaction path is proton reaction. If the experimental condition is moved with some slope, it means the electron-proton mixed reaction. The slope between the interface is calculated as Formula 4.11.

**Formula 4.11 Slope of interphase line in Pourbaix diagram**

Slope

$$= 59.2 \text{ mV} \times (\text{number of } \text{H}^+ \text{ in reaction}) / (\text{number of } \text{e}^- \text{ in reaction})$$

In case of water splitting reaction, 2 electrons and 4 hydrogens are involved. So the slope is 118.4 mV (/ dec)



#### 4.4. Pinning at the Semiconductor-Liquid Junction

There are two types of semiconductor-liquid junction according to the position of band edge when a bias is applied. If applied bias is activated on the semiconductor, the band bending occurs. While, if applied bias is working on the surface states, the band bending does not occur.<sup>62</sup> The two pinning conditions<sup>63</sup> are depicted on Figure 83.

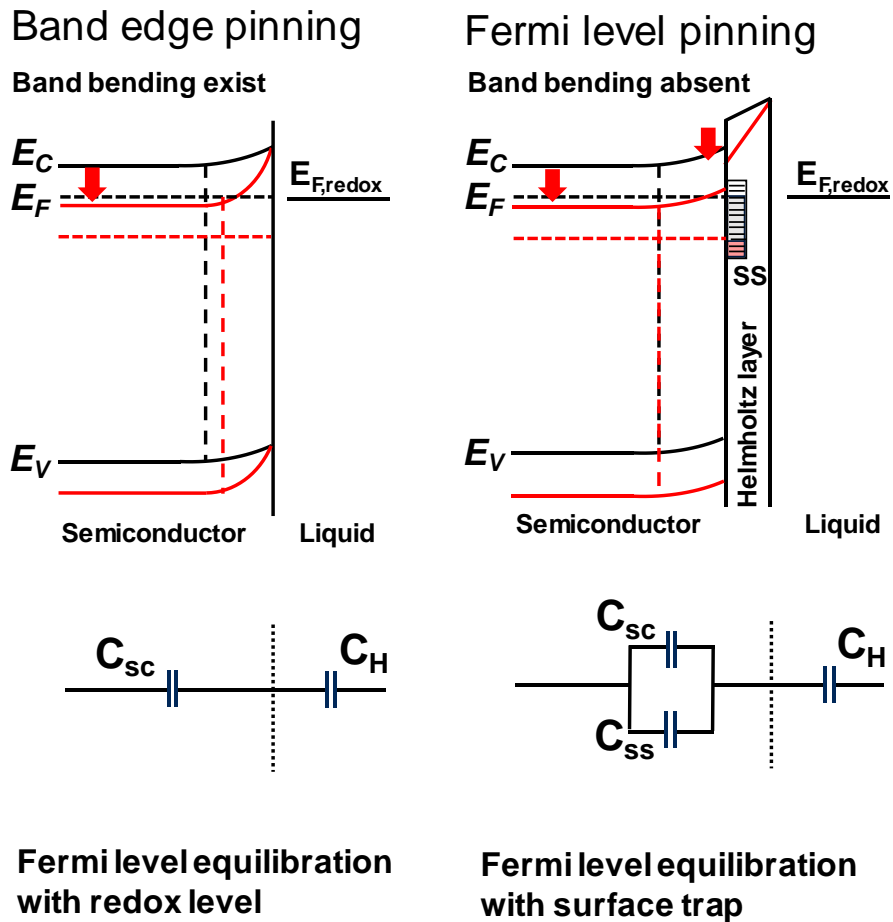


Figure 83. Two pinning condition under positive bias. Band edge pinning (left) and Fermi level pinning (right) is depicted.

Rather than the band bending in semiconductor, an abrupt potential drop at the interface exists. This behavior is related to the concentration of surface state. Normally, a number of surface states in semiconductor is negligible. However, in some circumstances, the number of surface states is comparable to the carrier concentration with a broad energy distribution in the semiconductor. They usually act as recombination center and increase the overpotential. From the difference between the pinning condition, the circuit element at the interface is considered in differ. The additional circuit element ( $C_{ss}$ ) is added to explain the charge carrier behavior at the interface of semiconductor.<sup>64</sup> The key fundamental reason for the behavior is the Fermi level equilibration mechanism. According to the concentration at the surface states and number of molecules in the surface, the equilibrium condition is modulated. A band structure after the high positive bias under Fermi level pinning condition is shown in Figure 84.

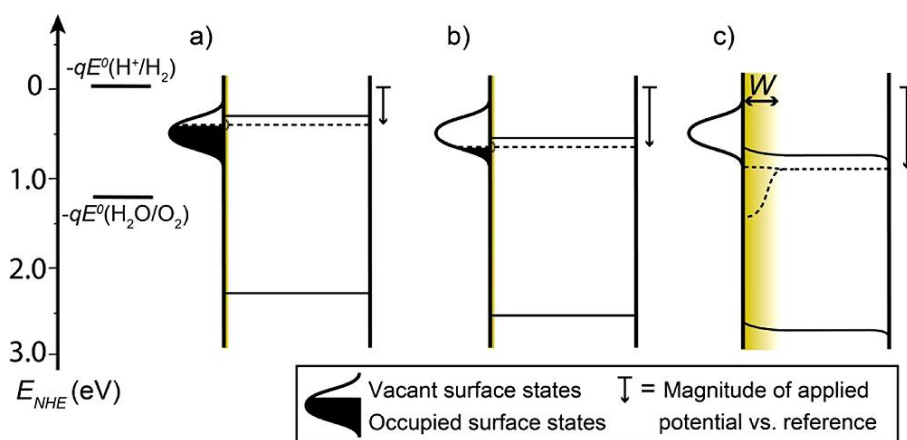


Figure 84. n-type semiconductor with Fermi level pinning. (a) Electrode at  $V_{FB}$ . (b) Weak anodic bias empties the surface state but band bending does not occur. (c) High anodic bias initiates the band bending of semiconductor.<sup>65</sup>

According to the discussion, the behavior of photovoltage with respect to the flat band potential can be recognized. With a band bending, the photovoltage is increase. So, observation of photovoltage increase by applied potential indicates the system is in the condition of band edge pinning. Due to the absence of band bending in Fermi level pinning condition, the photovoltage is constant with respect to applied voltage in the specific region. The behavior is depicted on the Figure 85.

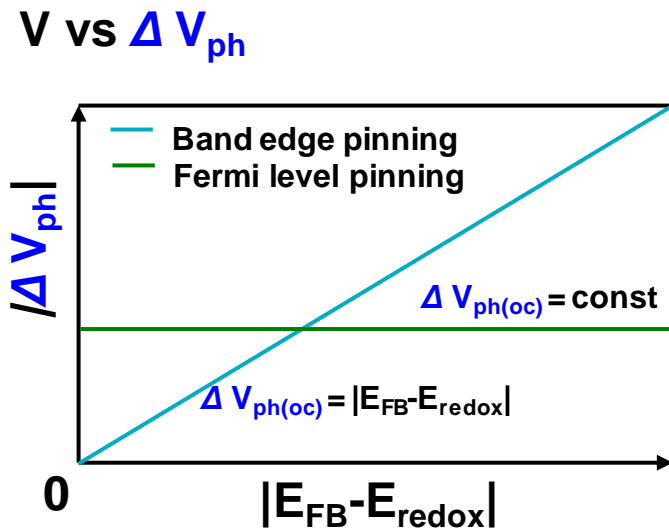


Figure 85. The photovoltage behavior according to the pinning conditions.

The behavior is highly dependent on the materials. Without the induce of defect on the surface, some of semiconductor materials inherently show the Fermi level pinning behavior under biasing. Specific materials for showing the behavior is known in the literature.<sup>64</sup> The known materials are arranged in the Figure 86.

- (1) Reduced photovoltage ( $\Delta V_{ph}$ )

- (2) Anodic onset potential shift (n-type)
- (3) More recombination of carriers.

No Fermi level pinning	Exhibit Fermi level pinning
<b>SrTiO<sub>3</sub></b> <b>ZnS</b> <b>SnO<sub>2</sub></b> <b>KTaO<sub>3</sub></b> <b>ZnO</b>	<b>Si/Ge</b> <b>InP</b> <b>GaAs</b> <b>InSb</b> <b>Mo-W/S-Se-Te</b>

Figure 86. Semiconductors do/do not exhibit Fermi level pinning.

For more detail. The band structure under the illumination<sup>66</sup> in two pinning condition is shown on Figure 87 for n-type and Figure 88 for p-type.

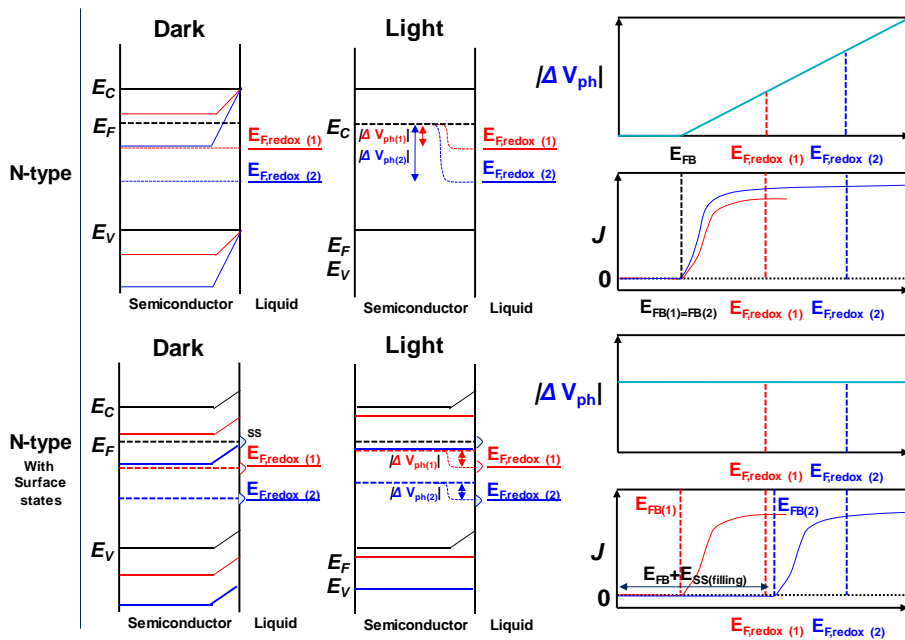


Figure 87. n-type Semiconductor illumination with bias for two pinning conditions.

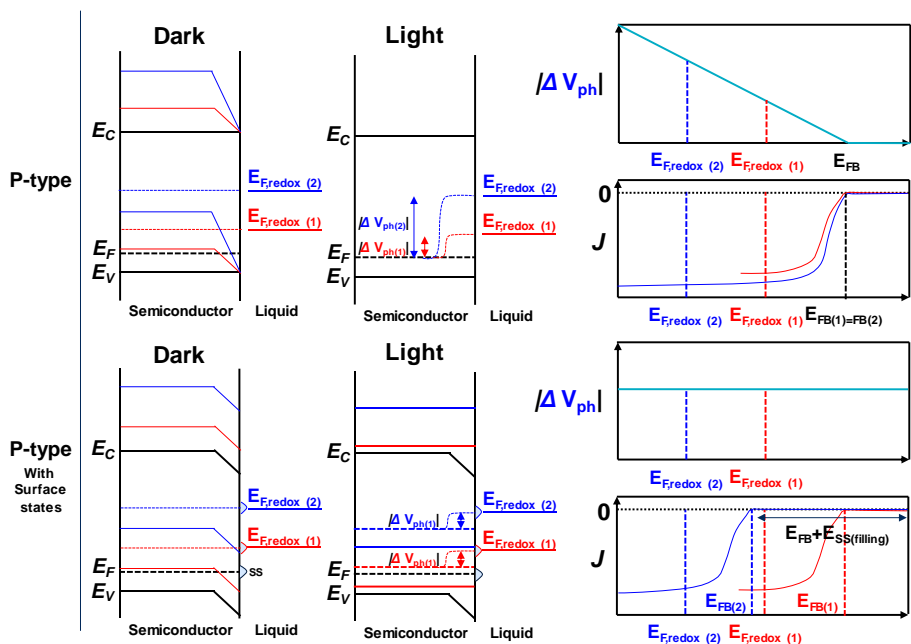


Figure 88. p-type Semiconductor illumination with bias for two pinning conditions.

Regardless of the semiconductor type with band edge pinning condition, a changing of redox potential of the system induce change of photovoltage. So resultant photocurrent is increase as the redox potential is far from the Fermi level of semiconductor. With Fermi level pinning condition, the photovoltage of the system is constant regardless of the redox potential change in the system. The flat band potential is shifted in the way of degeneration by increasing overpotential. The additional overpotential from the flat band shift is the result of surface state filling at semiconductor surface.

## 4.5. Polarization of Photoelectrode

### 4.5.1 Photoexcitation

To achieve water splitting, electrochemical voltage at least 1.23 V is required. Due to the absent of bandgap in metal, metal cannot generate electrons have high potential above 1.23 V vs. RHE. To achieve the goal, external bias is required to reduce Fermi level under OER potential. With aid of external bias, the holes in metal can transfer into OER potential as shown in Figure 89.

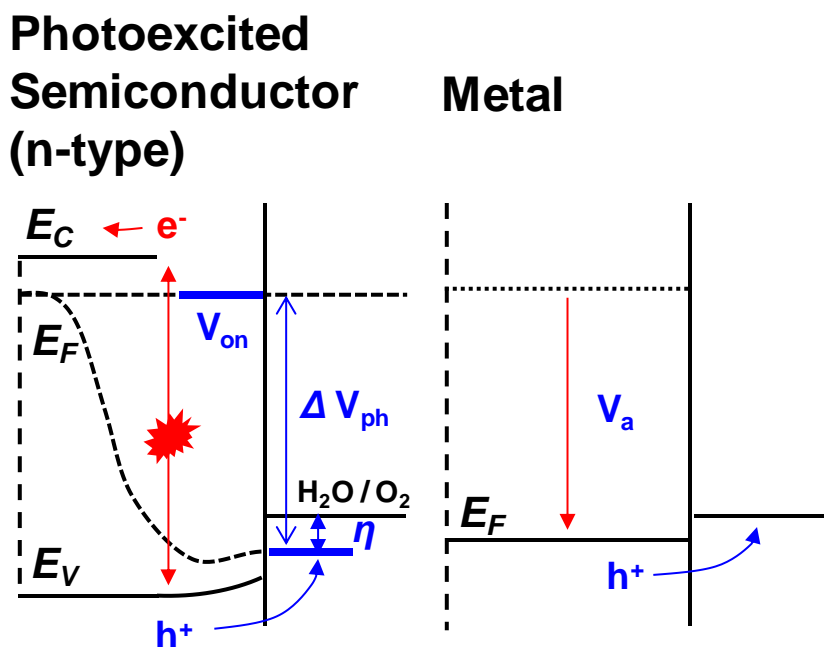


Figure 89. Excitation of carrier by external electrochemical potential. The electrochemical potential is achieved from the light (semiconductor) and bias (metal).

While, the situation in the semiconductor is quite different. From generation of photocarriers in semiconductor, hole at the semiconductor-liquid junction have

sufficient energy to surpass the water oxidation potential level (1.23 V vs. RHE). If the photovoltage is enough to high to overcome the oxidation potential level and OER overpotential, OER reaction can occur in photoanode. According to the graph, the relation is written as below Formula 4.12.

**Formula 4.12 Relationship between photovoltage and onset potential**

The symbols used in below formula is defined as following.

$\Delta V_{ph}$  (Photovoltage),  $\eta$  (OER overpotential),  $V^{\circ}$  (Thermodynamic OER potential; 1.23 V),  $V_{onset}$  (Onset potential of photocurrent) and  $V_{FB}$  (flat band potential)

$$(1) \Delta V_{ph} - \eta = V^{\circ} (1.23 \text{ V}) - V_{onset}$$

$$(2) \Delta V_{ph} = \eta + V^{\circ} (1.23 \text{ V}) - V_{onset}$$

$$< \eta + V^{\circ} (1.23 \text{ V}) - V_{FB} \text{ (note that; } V_{FB} < V_{onset} \text{)}$$

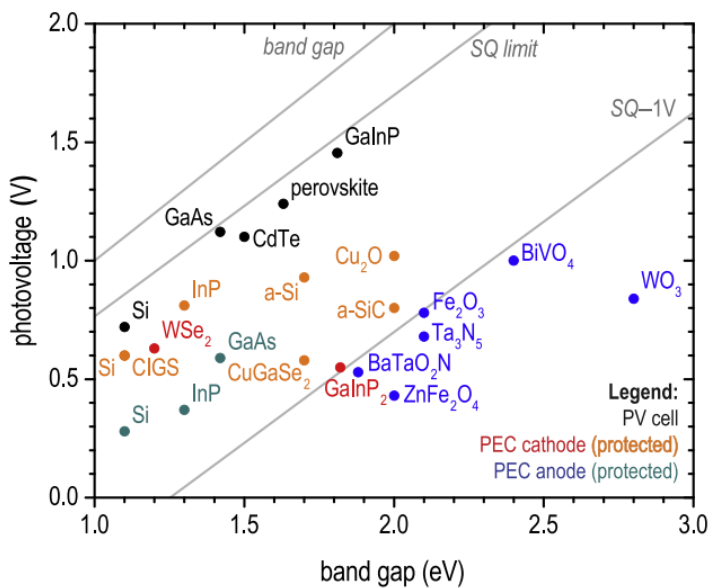


Figure 90. Photovoltage benchmarks.

The known photovoltage is quite low compared to the band gap of semiconductor. For example, the  $\Delta V_{\text{ph}}$  value for pristine hematite is lower than 0.4 V.<sup>67</sup> A benchmark for photovoltage is adopted from the review in Figure 90.<sup>68</sup>

### **4.5.2 Thermodynamic Consideration**

Now the question is arising, Why the water oxidation below 1.23 (V vs. RHE) is possible with light irradiation on semiconductor? Somebody would suspect that violation of the thermodynamic law. The answer is on the photovoltage of semiconductor. The photovoltage gives additional self-bias from photons. According to amount of bias from the illumination, bias need for OER is reduced. The more benefit is the generation of photoexcited excess carrier on semiconductor. Due to the photoexcited excess carrier, the reaction can proceed.

### **4.5.3 Polarization Curve (*I-V*)**

In an ideal situation, the photocurrent is become saturated due to the extraction photogenerated holes of a space charge layer by inherent electric field within an absorption length ( $\alpha$ ). In addition, the three process involved in solar water splitting process (charge generation, charge transport, charge transfer at the interface) can be 100 % efficient in a theoretical way. The condition is called a ‘idealized photoelectrode’. The three process is not efficient in a real situation and there is a photon loss from the surface due to the light-matter interaction (scattering, absorption, transmittance and reflectance). As a result, the performance of photoelectrode in a real situation is quite different. The performance can be measured by a measure of *I-V* characteristics. Usually,

according to the type of photoelectrode, the potential range is quite specified. For example, n-type photoanode is usually measured above 0 V vs. RHE potential and p-type photocathode is usually measured below 0 V vs. RHE. Anyway, the  $I$ - $V$  measure of photoelectrode is called as polarization. The corresponding curve is depicted in Figure 91.

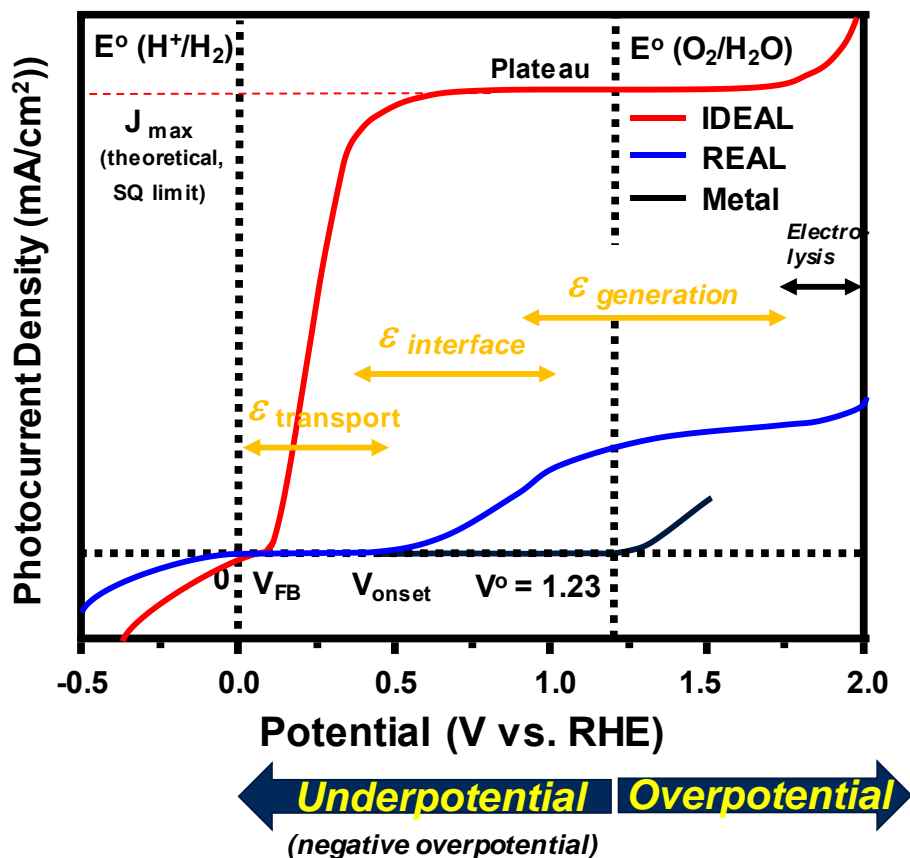


Figure 91. Polarization curve of photoanode.

Ideal onset potential ( $I > 0$ ) is a flat band potential ( $V_{FB}$ ). The holes can overcome the barrier for an idealized situation. But due to the kinetic/thermodynamic obstacles the potential become increase. In a realistic situation, the starting potential ( $I > 0$ ) is called as onset potential which is much

higher than the flat band potential and below 1.23 V vs. RHE. From the potential range from flat band and onset, the region is dominated by the efficiency of charge transfer at the interface. So, to reduce onset potential, catalysts for charge transfer at the interface is required. The current is become increase abrupt after the onset potential. The current behavior is dominated by charge transport to the semiconductor-liquid junction. The behavior is highly related to the recombination loss in semiconductor. In the saturation region around the plateau photocurrent, the current behavior is originated from the charge generation inside of semiconductor. To increase the saturated current, absorption of light by semiconductor should be enhanced by nanostructuring. In the quite high potential region, the all holes in the semiconductor have enough energy to overcome the reaction barrier. So the behavior is dominated by electrolysis rather than photoelectrolysis. Idealized photogenerated current behavior is described as an equation on below Formula 4.13.

#### **Formula 4.13 Idealized photocurrent**

The factors used in the equation is given as below.

$I_0$  = incident light intensity

$L_D$  = debye length

$L$  = diffusion distance of minority carriers

$\alpha$  = absorption coefficient

$I_{p,lim}$  = hole diffusion limit current

$$i_{\text{ph}} = eI_0 \left[ 1 - \exp \left( -2\alpha L_{\text{D,eff}} \sqrt{\frac{e(V - V_{\text{FB}})}{kT} + 1} \right) / (1 + \alpha L) \right]$$

$$\Delta V_{\text{ph}} = -\frac{\xi kT}{r} \ln \left( \frac{i_{\text{ph}}}{i_{\text{p,lim}}} + 1 \right)$$

#### 4.5.4 Light illumination directions

According to the charge transport capability of semiconductor, the photocurrent generation is controlled. More specific, there are two types of carriers in the semiconductor so called electrons and holes. Without nanostructuring and doping, the charge transport efficiency is inherent. For example,  $\text{Fe}_2\text{O}_3$  prefers electron transport and  $\text{BiVO}_4$  prefers hole transport (one carrier type conductivity is higher than the other). The situation is depicted in Figure 92.

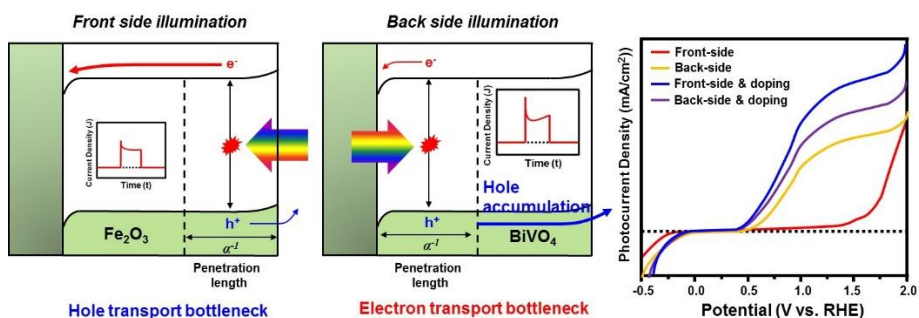


Figure 92. Photocurrent dependent on the illumination directions.

For example,  $\text{Fe}_2\text{O}_3$  have poor hole transport ability (on the other words; short hole diffusion length around  $\sim 2$  nm). So hole diffusion should be located near the semiconductor-electrolyte interface (front-side illumination). There is small amount of hole accumulation for the type of illumination state which resulted

in the photocurrent transient saturation (shoot is not seen and saturation current is observable). While,  $\text{BiVO}_4$  have poor electron transport ability. So electron diffusion should be located near the contact side (back-side illumination). There is high amount of hole accumulation for the type of illumination state which resulted in the photocurrent transient shooting (shoot is seen and saturation current is not observable). For the  $\text{BiVO}_4$  without doping and nanostructuring, back-side illumination leads to the enhanced photocurrent. However, with doping, front-side illumination leads to the enhanced photocurrent due to the retrieved electron transport bottleneck.

#### **4.6. Determination of Flat Band Potential**

Onset potential is directly measurable unit from the  $I$ - $V$  measurement. To recognize the flat band potential, impedance spectroscopy technique is chosen. The method is called as Mott-Schottky technique. By measuring the capacitance according to the potential, the flat band potential can be achieved as shown in Formula 4.14. Donor density can be calculated from the slope of  $1/(C_{sc})^2$  vs potential. And intercept with x-axis indicates the flat band potential.

#### Formula 4.14 Mott-Schottky equation

The factors used in the equation is given as below.

$C_{sc}$  = capacitance of the space charge layer

$\epsilon_r$  = relative permittivity

$\epsilon_0$  = permittivity in vacuum

$e$  = electric charge

$k$  = Boltzmann's constant

$T$  = temperature

$V_{appl}$  = applied bias

$V_{FB}$  = flat band potential

For N-type

$$\frac{1}{C_{SC}^2} = \left( \frac{2}{e\epsilon_r\epsilon_0N_d} \right) \left( (V_{Appl} - V_{FB}) - \frac{kT}{e} \right)$$

For P-type

$$\frac{1}{C_{SC}^2} = - \left( \frac{2}{e\epsilon_r\epsilon_0N_d} \right) \left( (V_{Appl} - V_{FB}) + \frac{kT}{e} \right)$$

## 4.7. Marcus Theory

To explain the electron transport at the semiconductor-liquid junction, Marcus theory is a proper choice. The imperfect explanation of electric double layer surface charge model is fulfilled with the theory. By Rudolph A. Marcus in 1956 explained the electron transfer reaction ratio from one chemical species to another. The proceed reaction of water splitting can be explained from the reaction coordinate as shown in Figure 93.

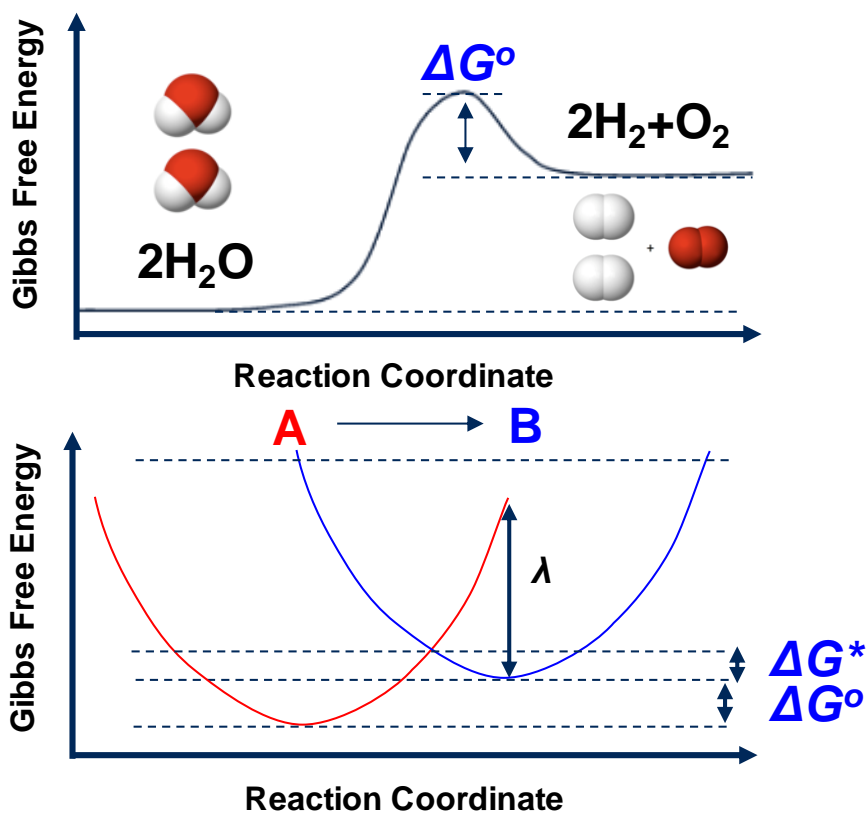


Figure 93. Reaction coordinate of water splitting.

In the process of water splitting, to split water into hydrogen and oxygen additional energy is needed. Molecules in the system have enough energy can

overcome the reaction barrier. The inherent energy barrier is denoting as  $\Delta G^\circ$ . Due to the kinetics, the additional energy  $\Delta G^*$  is required. The energy difference between two state at the reaction coordinate in B for equilibrium is called as reorganization energy ( $\lambda$ ). The energy is related to the quantity of energy for changing the nuclear configuration without electron transfer. Similar to the Arrhenius equation, using Eyring equation, the additional energy  $\Delta G^*$  is calculated as in Formula 4.15. The kinetic of the reaction by the Eyring equation is also attached.<sup>69</sup>

**Formula 4.15 Eyring equation**

The additional energy is calculated as below.

$$\Delta G^* = \frac{(\lambda + \Delta G^\circ)^2}{4\lambda}$$

Kinetic for the electron transfer is written as below.

$$k = A \frac{kT}{h} e^{-\frac{(\lambda + \Delta G^\circ)^2}{4\lambda RT}}$$

Interfacial electron transfer in water splitting is considered as the interaction of HER and OER reaction. Two is denoted as  $^\circ E_{Ox}$  and  $^\circ E_{Re}$  in Figure 94. The balance between the two potential is regarded as a Fermi level of electrolyte which is denoted as  $^\circ E_{F,Redox}$ . According to the Eyring equation, reorganization energy controls the energy distribution near the surface of semiconductor for the electron transfer. The disparity of overpotential by medium can be explained. Wider state distribution due to the high value of reorganization energy makes high over potential. The number range of reorganization energy

in material is known as 0.5 to 2.0. Water splitting reaction is proceeded from the electron transfer between semiconductor and probability density states (from the probability density function). The equation of function and corresponding current density by Eyring equation is give in the Formula 4.16.

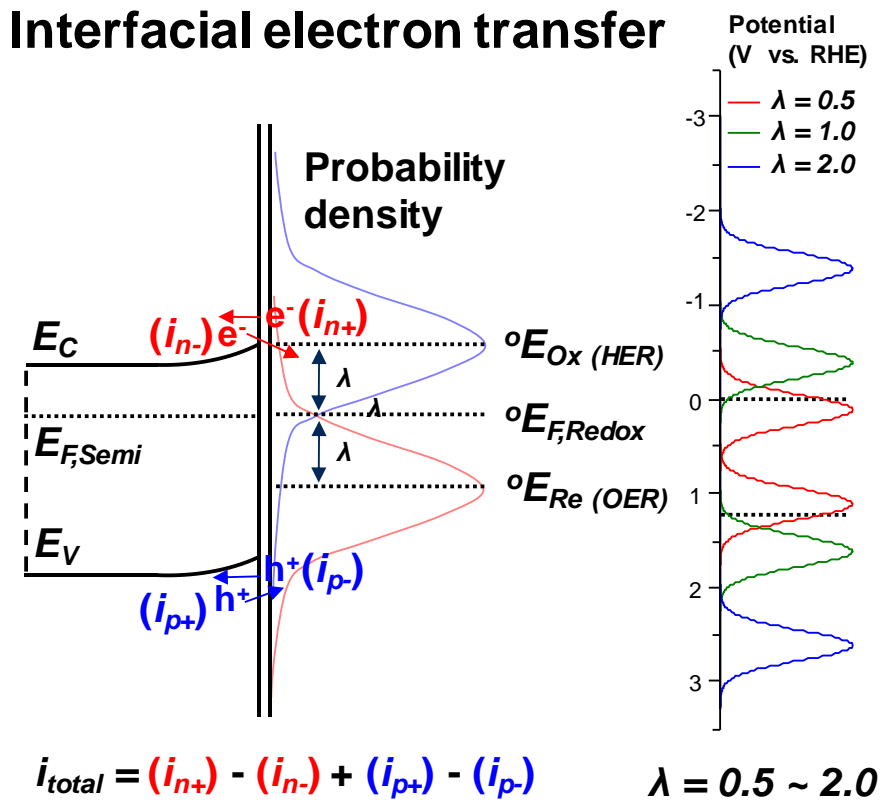


Figure 94. Interfacial electron transfer model by Marcus theory.

In addition, current due to the carrier flow at the semiconductor-liquid junction is analyzable. Distribution from probability density function from OER reaction makes electron flow from water to semiconductor ( $i_{n+}$ ) due to their high energy. Electrons in the semiconductor conduction band can flow into the probability density function from HER ( $i_{n-}$ ).

Similarly, Distribution from probability density function from HER reaction makes hole flow from semiconductor to water ( $i_{p+}$ ) due to their high energy. Holes in the semiconductor valence band can flow into the probability density function from OER ( $i_{p-}$ ). The four component contributes to the total current. The relation is summarized in Formula 4.16.<sup>70</sup>

**Formula 4.16 Probability density function at the semiconductor-liquid junction**

$$D_{Ox} = \exp\left[-\frac{(E - {}^{\circ}E_{F,Redox} - \lambda)^2}{4kT\lambda}\right]$$

$$D_{Re} = \exp\left[-\frac{(E - {}^{\circ}E_{F,Redox} + \lambda)^2}{4kT\lambda}\right]$$

$$j_{carrier} = qkN_{carrier}C_{redox} \frac{D_{redox}}{\sqrt{4\pi\lambda kT}}$$

### 4.8. Shockley and Queisser (SQ) Limit

Theoretical efficiency limit of photoconversion in photovoltaic (PV) was suggested by Shockley and Queisser at Journal of Applied Physics in 1961.<sup>71</sup> Theoretically, thermodynamic condition suggests the ultimate efficiency ( $T_s - T_c / T_c$ ). However, due to the physical processes involved in photoelectric conversion, the limitation is not achievable. They made the conclusion by systemizing the efficiency by p-n junction solar energy converters at 0 K. They assumed as a sun as a 6000 K black body photon radiator and 100 % efficient radiative recombination (thermal loss by recombination is ignored) or infinite

carrier multiplication.<sup>72</sup> The system converts all photons to electrons have energy having  $V_g = E_g/q$ . By the assumption, they suggested the semi-empirical limit of photoconversion in photovoltaic (PV) according to the bandgap by integrating energy of semiconductor by the bandgap in solar spectrum. As shown in Figure 95, above efficiency is degraded with low efficiency of radiative recombination factor. The graph is widely adopted to find ultimate current density of semiconductor material.

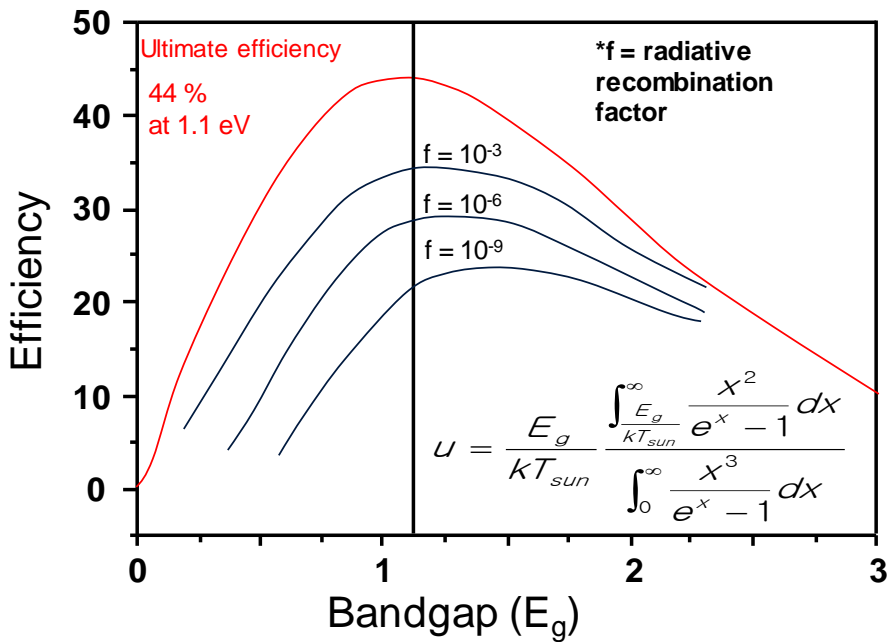


Figure 95. Theoretical efficiency limit in p-n junction solar cells.

One example of the bandgap-photocurrent relation is adopted from the review in Figure 96.

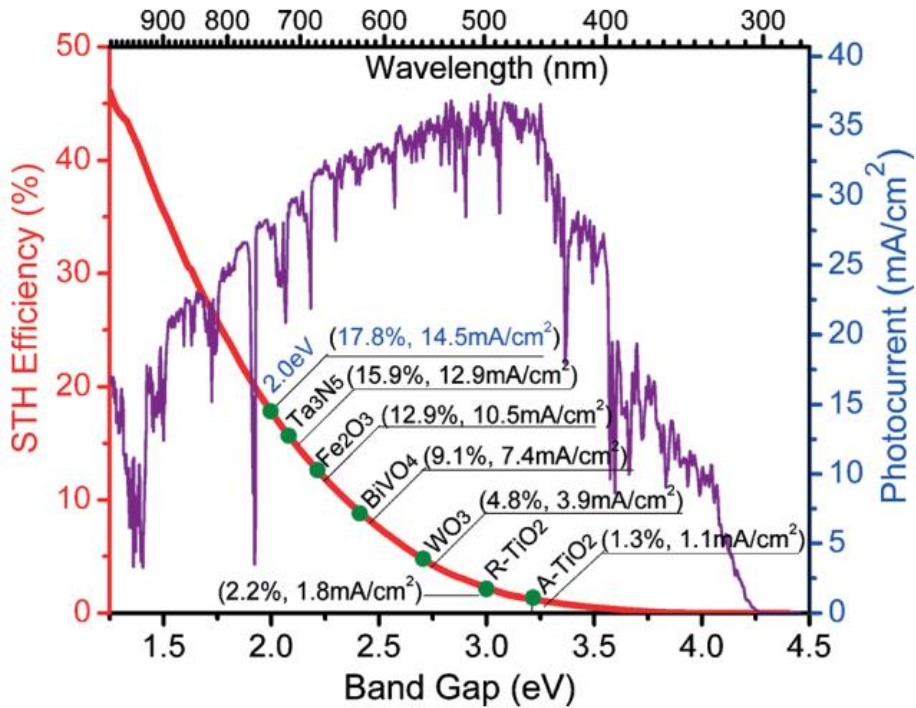


Figure 96. Dependence of the theoretical maximum solar-to-hydrogen efficiency and photocurrent density according to the bandgap in AM 1.5 G illumination.<sup>60</sup>

However, above discussion is imperfect. Because the system considers the PV system rather than photoelectrochemical conversion. So additional restriction exists for the calculation of theoretical efficiency.<sup>73</sup> The plot of SQ limit in the photoelectrochemical water splitting is shown in Figure 96. In addition, dual junction photoelectrode is expected have best efficiency for 40.0 % efficiency.

- (1) Illumination of AM 1.5G spectra rather than 6000 K black-body radiation.
- (2) Complete absorption of all photons above the bandgap of the semiconductor.

- (3) Only radiative recombination in the semiconductor exists (perfect anti-reflective coating and back reflector).
- (4) Diode ideality factor ( $n$ ) is equal to 1 (current is proportional to the  $\exp(eV/kT)$ ).
- (5) Catalytic overpotential is equal to 0 (exchange current density is infinite ( $\infty$ )).
- (6) Charge transfer coefficient ( $\alpha$ ) in Butler-Volmer relation is 0.5.
- (7) No series resistance (no degradation of short circuit current ( $I_{sc}$ )).
- (8) Electrochemical water splitting potential at standard condition,  $E_{redox} = 1.23$  V.
- (9) Perfect faradaic efficiency.

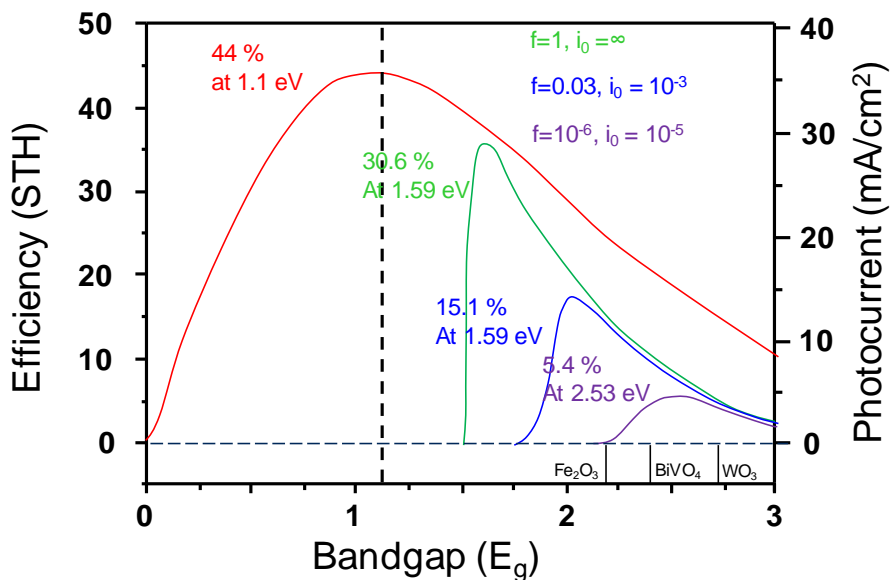


Figure 97. Theoretical efficiency of photoelectrochemical water splitting.

## Chapter 5

### Enlightening Solar Water Splitting with Plasmonic Gold Nanoparticles

#### Quote

**Scott C. Warren and Elijah Thimsen**

“The study of the optoelectronic effects of plasmonic metal nanoparticles on semiconductors has led to compelling evidence for plasmon-enhanced water splitting.” (2012, Energy and Environmental Science)

## 5.1. Plasmon Relaxation Process

### 5.1.1 Spontaneous and Stimulated Emission

If the energy is flowed into the atom, the electrons in the atom is become excited. The process is called as absorption. After absorption, electrons in the atom become stabilized by reducing the energy. There are two quantum mechanical way to reduce the energy of a system by emitting light. The first is spontaneous emission. In the process, the system emits photon as a spontaneous way (without the external stimulation). The second is a stimulated emission. The electron in the excited state become stabilized by stimuli of external photon. To achieve such a state, enough excited carrier lifetime (population inversion) is required. So, metastable state is required to achieve spontaneous emission. A schematic for the process is given in Figure 98.

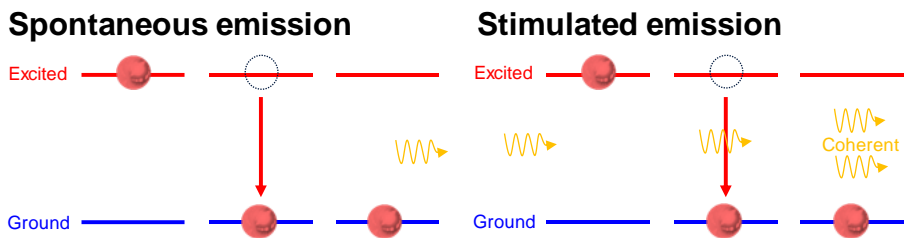


Figure 98. Schematic of photon emission mechanisms.

In other way, the energy from excited electron can be released as a form of phonon (or commonly in heat) by change of momentum in electron. A schematic for the process is given in Figure 99.

## Emission without photon (phonon)

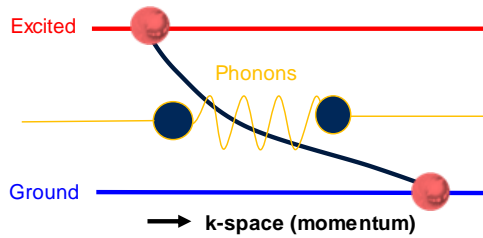


Figure 99. Schematic of phonon emission mechanism.

The possibility of the procedure is firstly investigated by A. Mooradian at 1968.<sup>74</sup> In the article, photoluminescence spectra of gold and copper due to the band transition is investigated as shown in Figure 100.

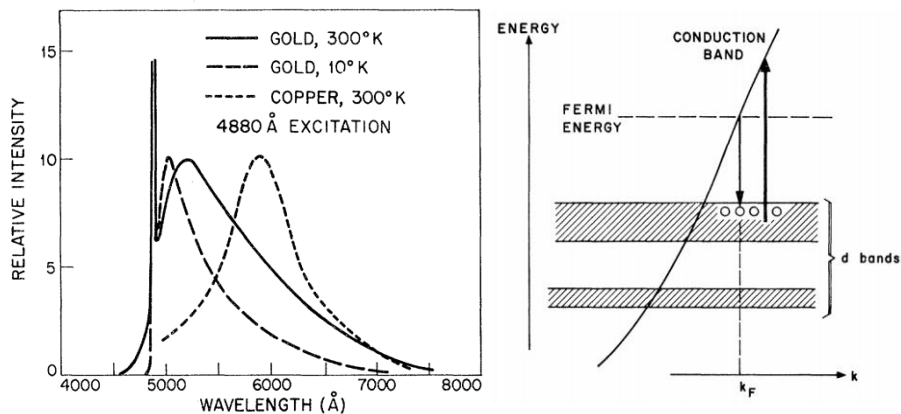


Figure 100. The incident light is grazed, and the emitted photon is collected normal to the surface.

For the various noble metals (gold, silver and copper), the photoluminescence spectra are addressed in more detail.<sup>75</sup> Due to the lack of possibility for metal population inversion, stimulated emission itself is not available. The PL property is attributed to the spontaneous emission from the band transition. The decay of the number of excited states is related to the radiative decay from

spontaneous emission and non-radiative decay from phonon generation. Those two decay factors are directly related to the quantum efficiency in the Formula 5.1. Interestingly, the surface plasmon polariton<sup>76</sup> induced stimulated emission and localized surface plasmon induced enhanced spontaneous emission has confirmed.<sup>77</sup>

**Formula 5.1 Decay of excited states**

Total decay rate is the sum of decay rate from radiative and nonradiative.

$$\Gamma_{tot} = \Gamma_{rad} + \Gamma_{nrad}$$

$$Q = \frac{\Gamma_{rad}}{\Gamma_{rad} + \Gamma_{nrad}}$$

**5.1.2 Radiative decay**

The radiative decay of localized surface plasmon in gold nanoparticles occurs from the two processes, namely, fluorescence and scattering. Even the fluorescence is described, the portion is negligible for the metal nanoparticles. Scattering (especially, Mie scattering) is dominant in radiative decay for metal nanoparticles.

**5.1.3 Non-Radiative Decay (Landau Damping)**

The non-radiative decay of localized surface plasmon in gold nanoparticle is initiated by Landau damping. Landau damping indicates the degradation of the longitudinal plasmon wave without the energy scattering. Due the plasmon wave energy transfer due to the plasmon-induced field to electron-hole pair excitation, electron can be excited. Between the plasmon excitation to excited carrier generation, the process is proceeded within 100 fs scale. After

generation of hot electron and holes, the distribution is become relaxed more evenly along the Fermi space. The process is called as carrier relaxation which occurs around 100 fs to 1 ps time scale. Eventually, the energetic carriers become stabilized by phonon generation (thermal dissipation) around 10 fs to 10 ns timescale. The timescale is quite long with respect to the bulk metal due to the confinement effect. The surface plasmon relaxation process via non-radiative decay is summarized as a picture in a Figure 101.

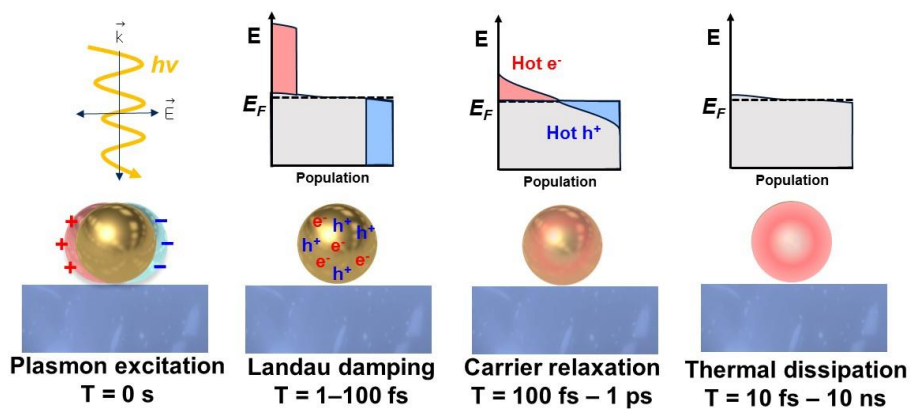


Figure 101. Plasmon relaxation via non-radiative decay.

### 5.1.4 Resonant Energy Transfer

Electron transfer by dipole (plasmon) – dipole (semiconductor) coupling is also possible. Different from the stand-alone state of gold nanoparticles, with the surrounding medium, different mechanism so called resonant energy transfer is also possible. Two type of energy transfer process is possible. If the dipole energy in semiconductor is transmitted to the plasmon, we call the process as förster resonance energy transfer (FRET). On the contrary, if the dipole energy of plasmon is transmitted to semiconductor via near-field

interaction, the process is called as plasmon induced resonance energy transfer (PIRET).

### 5.1.5 Modeling

For the interpretation of plasmon relaxation, two methods are frequently adopted. For experimental model and computational modeling. The first is the Phenomelological Plasmonic model shown in below Figure 102.

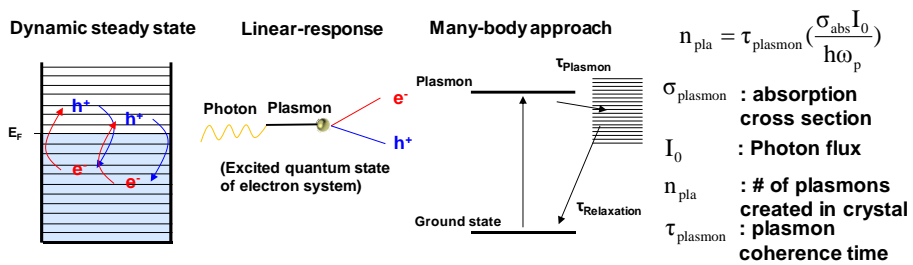


Figure 102. Phenomelological plasmonic model.<sup>78</sup>

Plasmon kinetics can be interpreted via phenomenological plasmonic model. When the metal is excited with external stimuli, electrons and hole pairs in metal is excited and grounded from dynamic steady state. The process is regarded the sum of the several process (linear response). At first, the photon generates plasmon by excitation. The second, the plasmon generated energetic electron and hole pairs. The last, the electron-hole pair is become relaxed. If we consider this linear-response in numerous number of atoms, energy level should be introduced. By consideration of the two process lifetime, the plasmon population in the equilibrium can be calculated. The calculation implies the plasmon population is highly dependent on the size, shape and photon flux of nanoparticles.

To deal plasmon in a computer, density matrix model is adopted as shown in Figure 103.

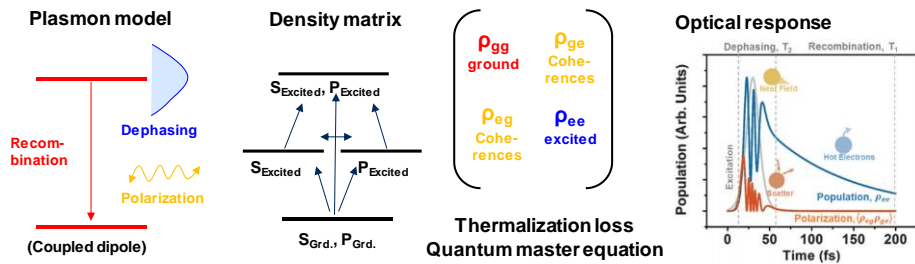


Figure 103. Density matrix model.<sup>79</sup>

Density matrix is needed to analyze the statistical ensemble of many quantum states. With a semiconductor, the energy state of a system can be considered as a result of combination of recombination, dephasing and polarization of material. The matrix can be solved as a linear response of system. The excitation of plasmon-semiconductor system is considered as coupling. So, ground state and excited state exist by hybridization. The consideration is arranged as a matrix element. And with a thermalization loss, optical response can be solved from the quantum master equation.

### 5.1.6 Summary of the Plasmon Relaxation

Above discussions are arranged in below Figure 104.

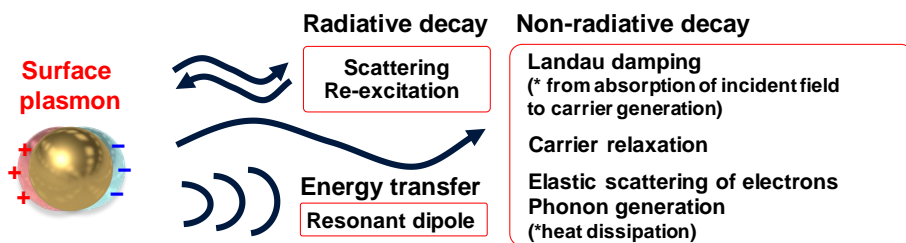


Figure 104. Plasmon relaxation process.

## 5.2. Plasmon Induced Charge Generation

A charge in the semiconductor can be formed from the plasmon induced charge generation process.<sup>80-83</sup> Five processes are generally involved as a plasmon induced charge generation. The process is depicted in Figure 105.

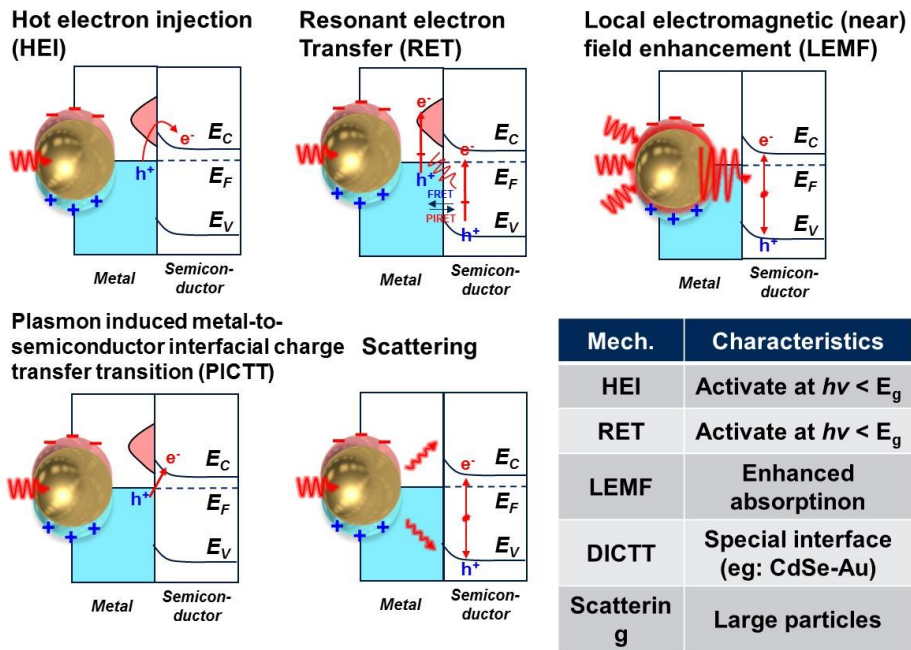


Figure 105. Plasmon induced charge generation process.

### (1) Hot electron injection (HEI)

: When the surface plasmon decay occurs in the plasmonic metal nanoparticle, hot electron and hole pairs are generated. The hot electrons can be transferred to the semiconductor conduction band by overcoming potential barrier. The requirement for the process is direct contact (or very close distance that tunneling occur) between plasmonic metal nanoparticle

and semiconductor. Spectral overlap between the surface plasmon and semiconductor is not required.

(2) (Plasmon induced) Resonant electron transfer (RET)

: When the coupling between photon, plasmons and electron-hole pairs is allowed, charge generation in semiconductor without charge (hot electron/hole) transfer from plasmon relaxation is possible. The energy is transferred by radiative interaction between plasmon dipole and semiconductor dipole. So, resonance spectra and bandgap overlap is required. Due to the dipole interaction, absorption of energy below the band gap of semiconductor is allowed.

(3) Local electromagnetic (near) field enhancement (LEMF)

: The plasmon can concentrate incident light at the desired position of semiconductor. Considering that the electron hole pair generation is proportional to the electric field density ( $|E|^2$ ), the concentration of light in the local region is beneficial. The mechanism enforces the light absorption, carrier generation (by interband transition of semiconductor) rate and carrier separation rate over a semiconductor. The mechanism cannot contribute to the semiconductor below the band gap.

(4) Plasmon induced metal-to-semiconductor interfacial charge transfer transition (PICTT)

: The mechanism is found very recently by K. Wu et al in 2015 (Science)<sup>84</sup>. Before the discovery, plasmon transition from electron-electron scattering

and interfacial electron transition is regarded as separated process. In the new discovery, the plasmon can activate electron hole pair at the separate material (i.e., electron in the semiconductor and hole in the metal). The phenomena are originated from the coupling and mixing of the metal and semiconductor energy levels. Due to the new plasmon coupling band formation, absorption band of the system can be extended. This is observed in the CdSe nanorods-gold nanoparticle hybrid.

#### (5) Scattering

: The scattering is well-known phenomena in the gold nanoparticles. The scattering extends the light-travel length in semiconductor. So absorption and charge carrier generation in semiconductor can be enhanced. This mechanism can be effectively working on the condition of photon with higher optical band gap energy than semiconductor.

Reaction can be enhanced with more mechanisms. For example, localized heating due to the plasmon relaxation, alignment of polarized molecules due to the plasmon, near-field induced electronic structure modification and modification of fermi level are possible candidate.

### **5.3. Excitation of Semiconductor by Localized Surface Plasmon Resonance of Gold Nanoparticles**

To achieve semiconductor photoelectrical performance enhancement, the charge transfer and flow at the metal nanoparticle-semiconductor interface should be considered.<sup>85</sup> When the contact between semiconductor-metal-liquid triple junction is formed, the Fermi level of the system is fitted to the redox

level of the system and the principle is applicable to the semiconductor liquid junction as shown in Figure 106 and 107.

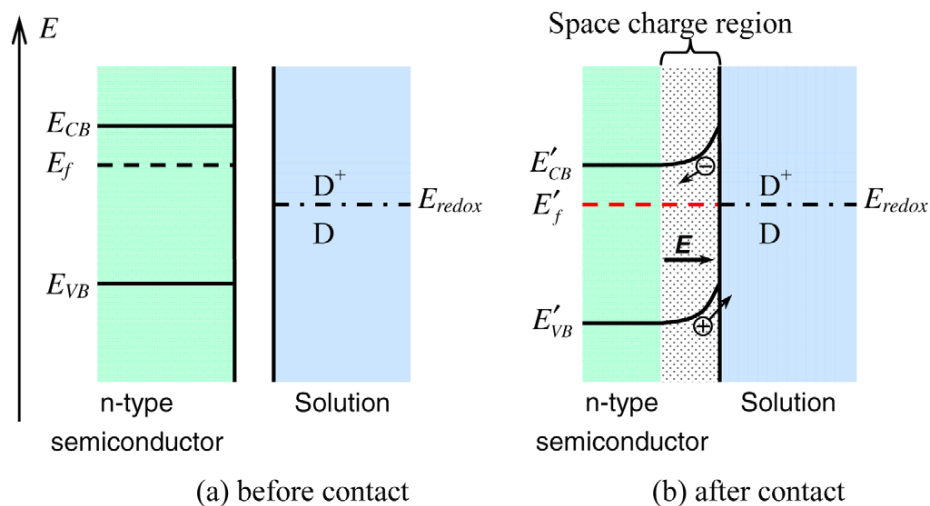


Figure 106. Band diagram for a n-type semiconductor-liquid junction.

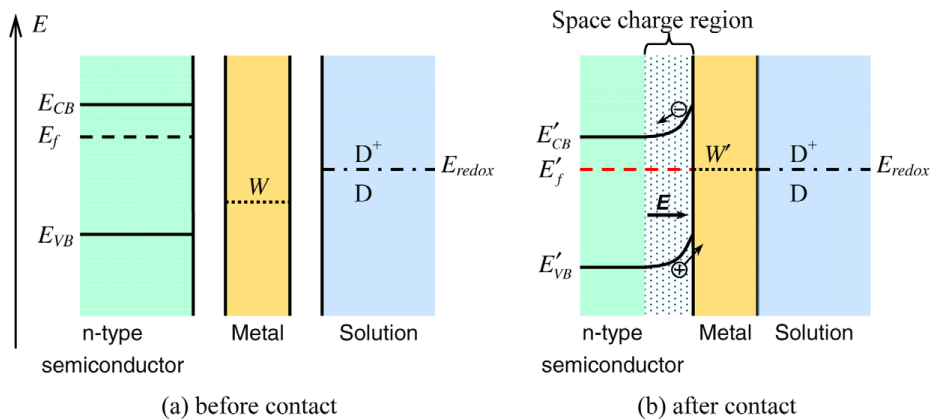


Figure 107. Band diagram for a n-type semiconductor-metal-liquid junction.

Let us rule out the solution part. Now, the position of Fermi level in a semiconductor and a metal is considered. Three kinds of Fermi level position alignments ( $E_{F,M} > E_{F,S}$ ,  $E_{F,M} = E_{F,S}$  and  $E_{F,M} < E_{F,S}$ ) are possible. The configuration before the contact is shown in the Figure 108.

## Before contact

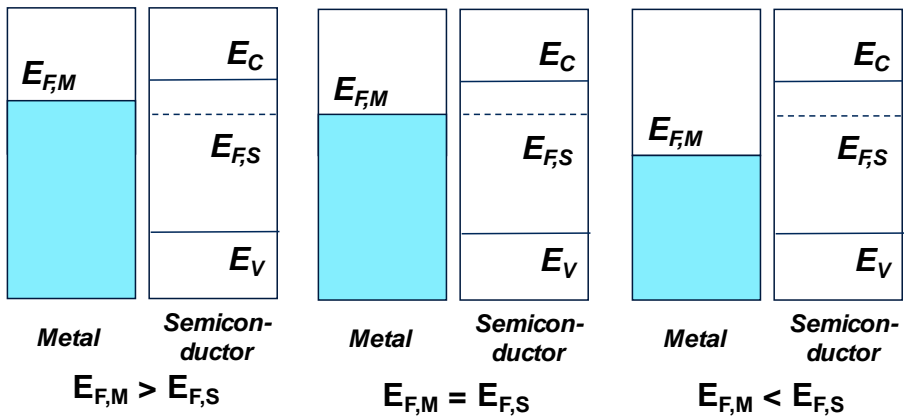


Figure 108. Possible band alignments of semiconductor-metal junction.

After the contact with excitation, a thermodynamically preferable charge (electron and hole pair) transfer by band position is progressed. Electrons prefer to move into the low energy level and holes prefer to move into the high energy level. Considering the criteria, preferred carrier move direction is drawn in Figure 109.

## Excitation with contact

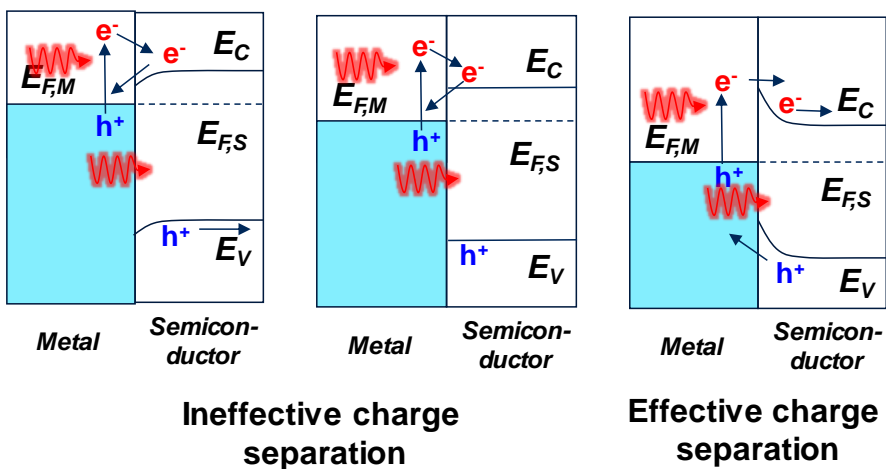


Figure 109. Preferred carrier move direction upon contact and illumination.

According to the diagram, the condition ( $E_{F,M} < E_{F,S}$ ) is only beneficial band alignment for plasmon induced charge generation in the semiconductor. Other two configuration involves the recombination of carriers at the interface.

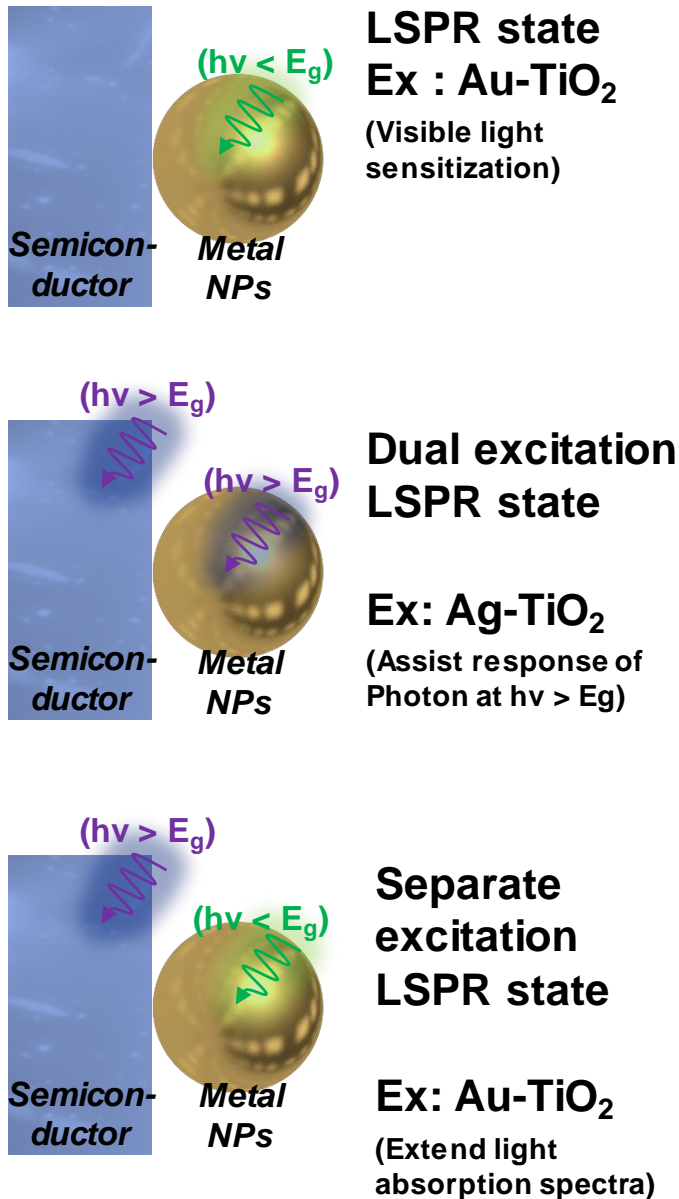


Figure 110. Excitation states of plasmonic metal nanoparticles and semiconductor junction.

In the solar water splitting operation, three types of enhancement (excitation states by light illumination) in metal-semiconductor junction is possible as shown in Figure 110. The first is light excitation in metal by visible light. The role of the plasmonic metal nanoparticle is visible light sensitization that semiconductor cannot absorb. The second is light excitation in metal by ultraviolet light. In the case, the metal assists photoresponse of semiconductor. The last one is called as separate excitation state. Semiconductor acts as a light absorber for over bandgap photon energy and metal nanoparticle acts as a light sensitizer. Above concept is adopted in plasmon enhanced photocatalysis on the recent researches.

## **5.4. Plasmon Enhanced Photocatalysis**

### **5.4.1 Photoactivity Enhancement from Light Intensity**

The activity of photocatalysis is dependent on the light intensity. Upon increasing light intensity, the photocatalytic activity is also enhanced. In a low intensity increase scale, the relation between photoactivity and light intensity is linear. The enhancement is much pronounced with plasmonic nanostructure as shown in Figure 111 (a).<sup>86</sup> The relation between photoactivity and light intensity is actually non-linear and fit in the power-law. For an plasmonic nanostructure, the behavior for enhancement is proportional to the value of power law in 3.5 ( $\propto \text{intensity}^{3.5}$ ) high as shown in Figure 111 (b).<sup>87</sup> The two behavior indicates the different mechanism activation according to the incident light intensity. In addition, the result indicates the possibility for highly-

efficient plasmon enhanced photocatalysis with high intensity local electromagnetic fields.

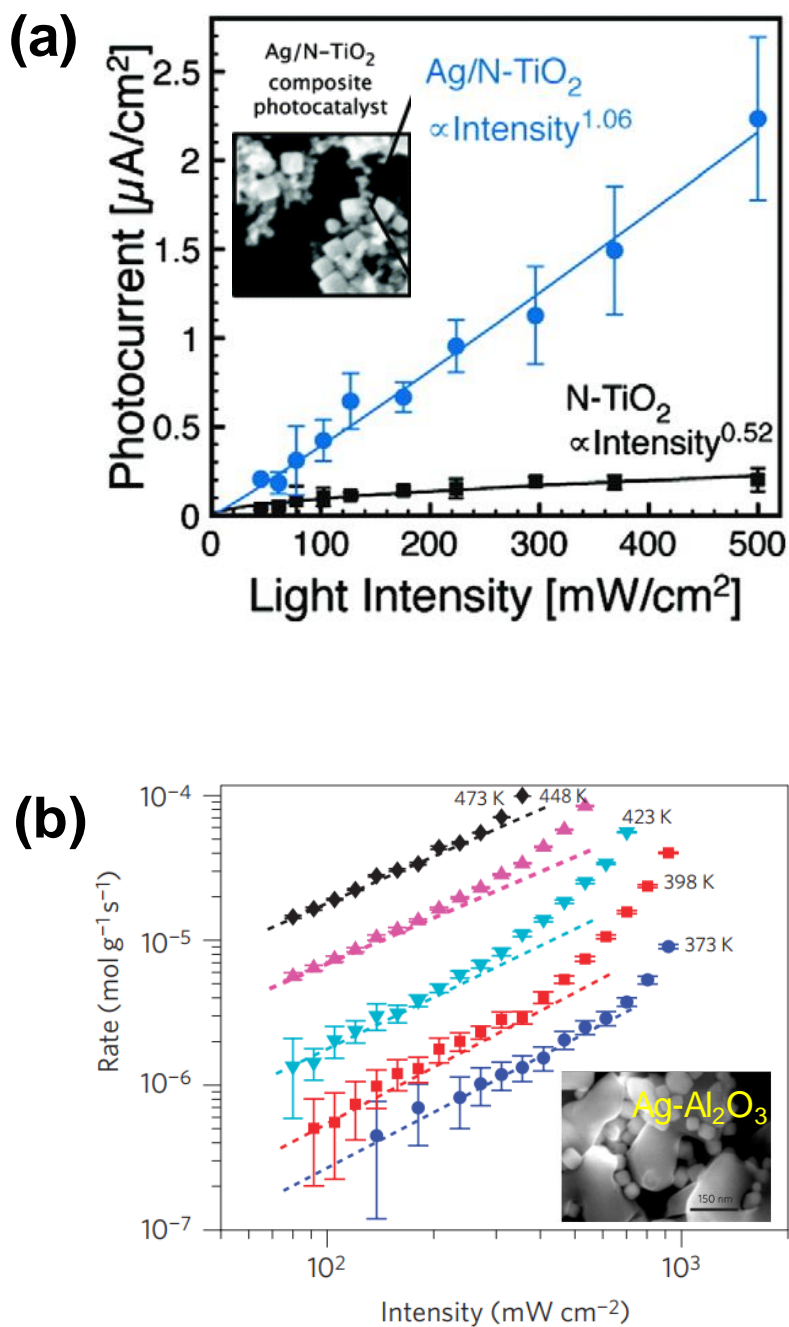


Figure 111. Photocatalytic activity enhancement from light intensity modulation.

## 5.4.2 Transient Negative Ion (TNI) States

The molecule interaction with plasmonic metal nanostructure can be investigated from previous results. Similar to the Marcus theory, the proceeding reaction can be depicted in reaction coordinate system as shown in Figure 112.<sup>88</sup>

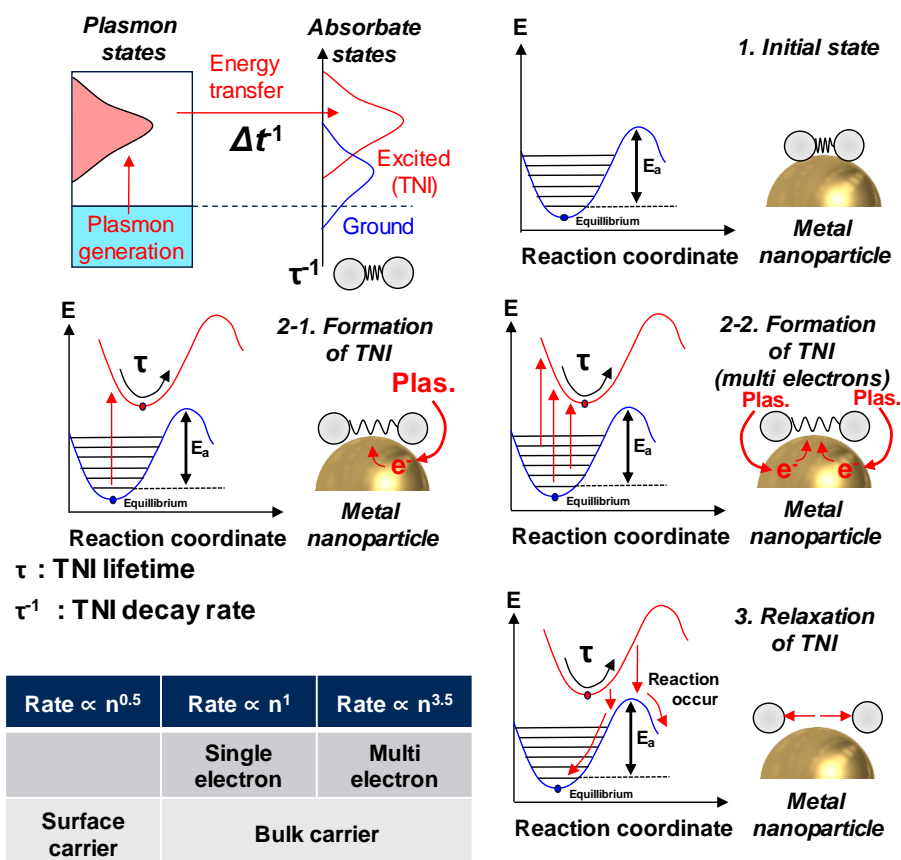


Figure 112. Absorption of transient negative ions on plasmonic metal nanoparticle (mechanism of plasmon photocatalysis).

For the oxygen evolution on the metal surface, the oxygen absorption is concomitant. The absorbed oxygen pair is a ground state. Oxygen evolution on metal surface is initiated as a form of negative ions. The energy is coming from

the energetic electron by excitation. The excited state from the ground state molecule is changed into the excited state as a form of transient negative ion (TNI) or dissipated as a phonon (heat). If the energy is sufficient to generate more than one electron, a multiple transition occurs. Scattering of electrons due to the vibration modes is necessary for the multi-electron transition. When the frequency of electron scattering is comparable to the energy transfer rate (plasmon lifetime), the multi-electron transition process is activated. Due to the multiple-scattering of electron, non-linear increase of the molecule evolution can be explained.

### 5.5. Exceeding Theoretical Efficiency (SQ Limit)

According to the solid state physics, excited state population in semiconductor is expected as below figure. With the small tail below the band gap, the absorption is gradually enhanced to specific saturation value due to the saturation of density of states. As shown in Figure 113.

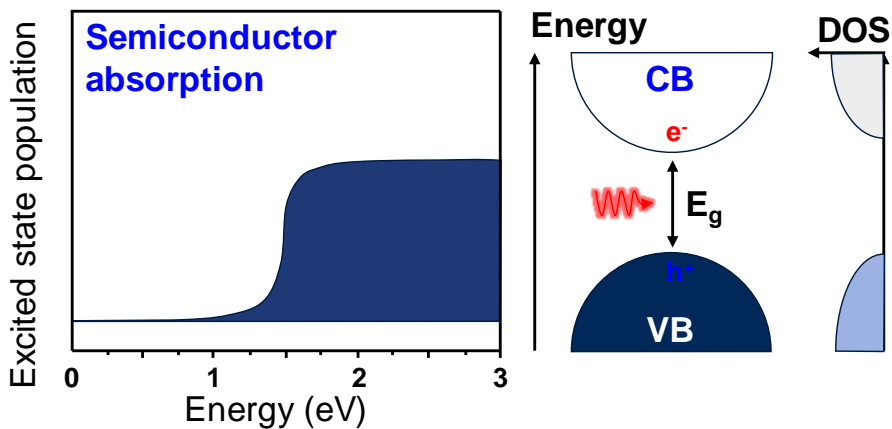


Figure 113. Optical absorption spectra of semiconductor.

According to the plasmon mechanism, the enhancement energy region is different as shown in Figure 114.

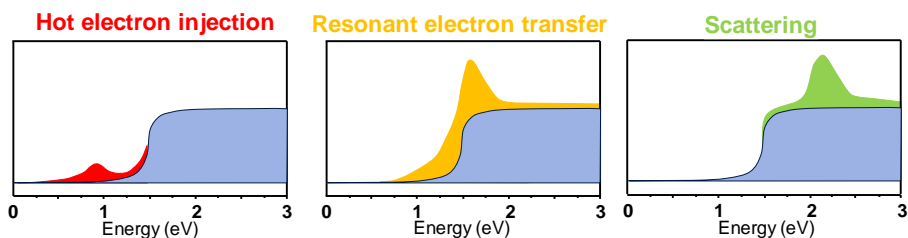


Figure 114. Plasmon induced absorption enhancement.<sup>79</sup>

The three mechanism is activated when the plasmonic metal nanoparticles are introduced on semiconductor. The efficiency of the mechanism is modulated according the plasmon energy, the band gap of semiconductor and plasmon relaxation time. The mechanism is activated differently due to the different limitation in photovoltaic (PV) and photoelectrochemical water splitting. The representative diagram for efficiency enhancement in water splitting is represented in Figure 115. The critical benefit of plasmon-induced solar water splitting is the possibility of high efficiency on the region over Shockley-Quessier limit. RET mechanism is dominant on the low band gap semiconductor and HEI mechanism is dominant on the high band gap semiconductor. Moreover, another plasmon-enhance charge generation mechanism has discovered recently, such as PICTT. The knowledge for mechanism of plasmon induced charge generation indicates that possibility of the more efficiency enhancement in the semiconductor-plasmonic metal composites.

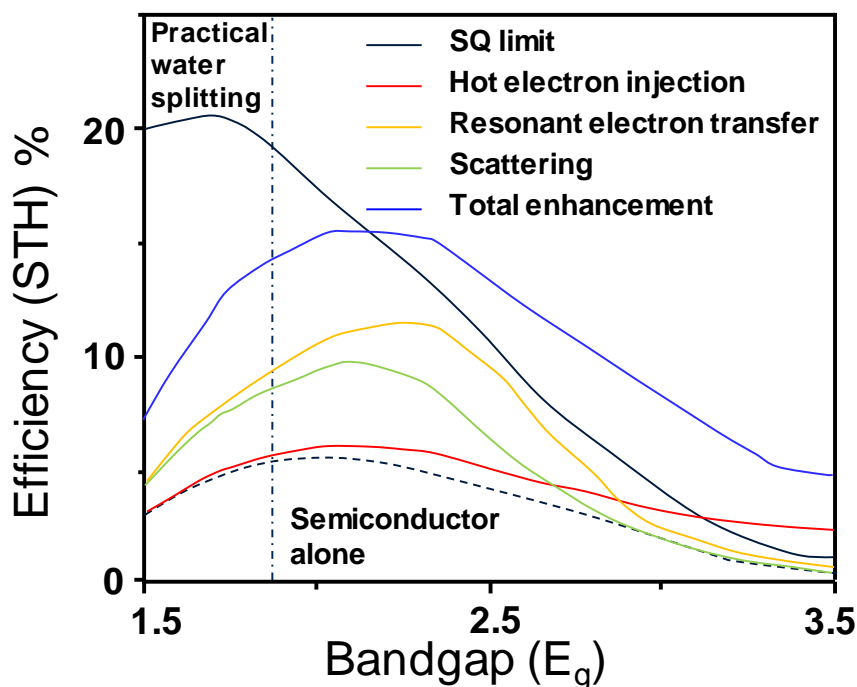


Figure 115. The theoretical efficiency (SQ limit) and plasmon induced efficiency enhancement.

## 5.6. Band Transitions in Conduction Band

Let us look around the electron configuration of gold. The ground state is written as  $[\text{Xe}]5d^{10}6s^1$ . The orbital is consisted with fully filled 5d orbital and partially filled 6s orbital. So, the hybridized 6sp band is exist near the Fermi level of gold in real band structure. When the electrons in gold is excited with external light, the electron transition between or inside orbital happens. If the transition is played in identical orbital (especially, 6sp), the transition is called as intraband transition. Whereas, if the transition is activated in different orbitals (especially, 6sp and 5d), the transition is called as interband transition. The band transitions (intraband and interband) are expressed in bandstructure

of gold as shown in Figure 116. Graphical representation of the band transition is given in Figure 117.

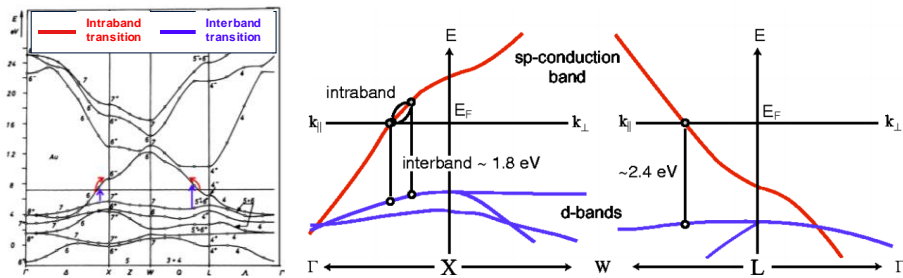


Figure 116. Bandstructure of gold<sup>78</sup> and corresponding electron transitions (interband and interband).<sup>89</sup>

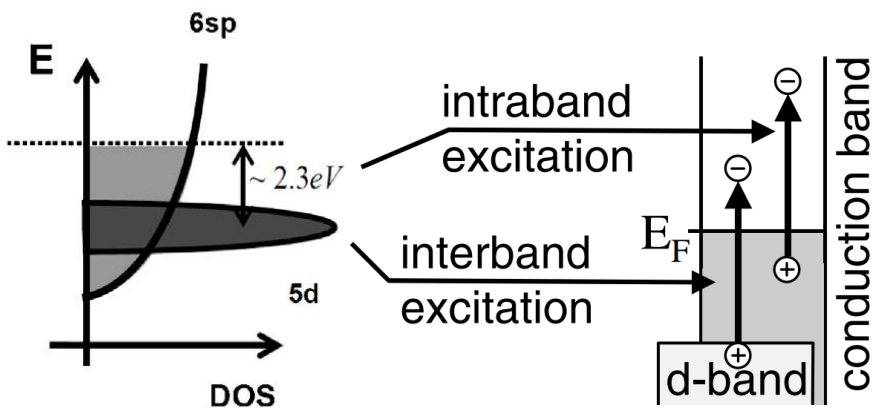


Figure 117. Schematic of band transitions in gold.<sup>90</sup>

The role of these excitation in absorption is quite different in gold nanoparticles. The intraband transition entails the absorption of visible light photons (or infrared light photons) due to relatively low intraband gap from 0 eV and localized surface plasmon resonance. While, the interband transition

carries the absorption for high energy photons over visible light wavelength range as shown in Figure 118.

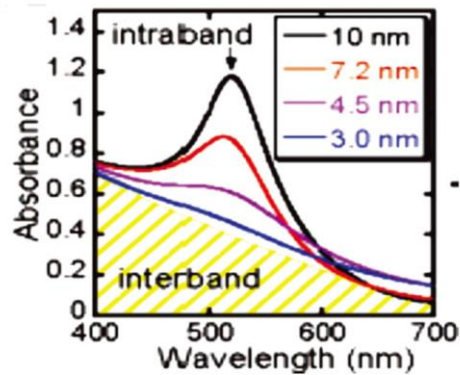


Figure 118. Absorption of light in gold according to the band transitions.<sup>52</sup>

With a resonance, the absorbed energy from intraband and interband transition can be emitted as a numerous form including generation of plasmons. As shown in Figure 119.

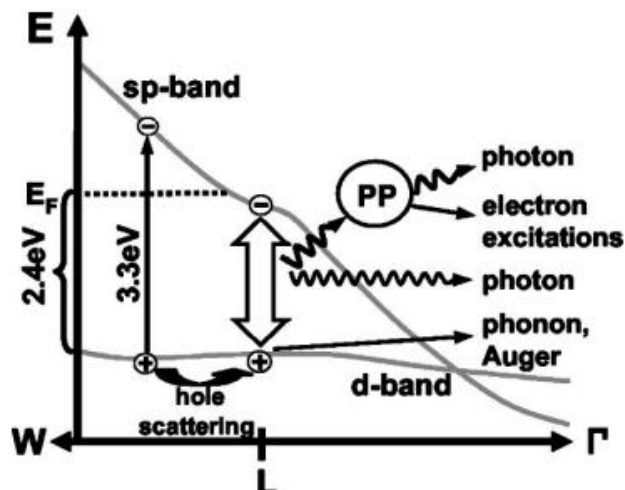


Figure 119. The energy relaxation process from interband transition in gold.<sup>91</sup>

The effect of interband transition in gold for plasmon enhanced solar water splitting is significant. Plasmon relaxation can increase the local thermal temperature for enhanced reaction kinetics, enlarges local light intensity for carrier generation rate, and extends the absorption of semiconductor for photon sensitization. Schematic is included in Figure 120.

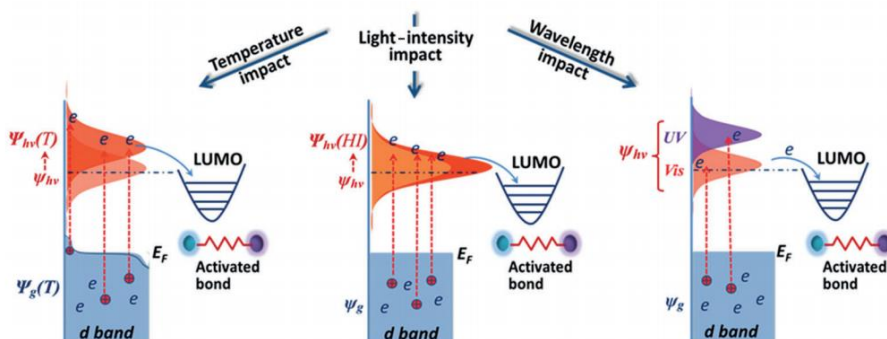


Figure 120. The effect of 5d to 6sp interband transition in gold nanoparticles.<sup>92</sup>

## 5.7. Utilization of Conduction Band Electrons in Au 5d Orbital

As described before, to enhance the efficiency of solar water splitting, utilization of interband transition is desired due to the many benefits. The utilization arises from the ultra-violet (UV) light activation of plasmonic gold nanoparticles. Here, several examples are attached as exemplary cases.

At 2009, Huaiyong Zhu et al. reported the gold nanoparticles as an oxidation photocatalyst of synthetic dyes.<sup>93</sup> They drive selective oxidation by composite with oxide. With a visible light, the composite oxidized SRB molecule. And with a UV light, the composite oxidized Phenol molecule. As shown in Figure 121.

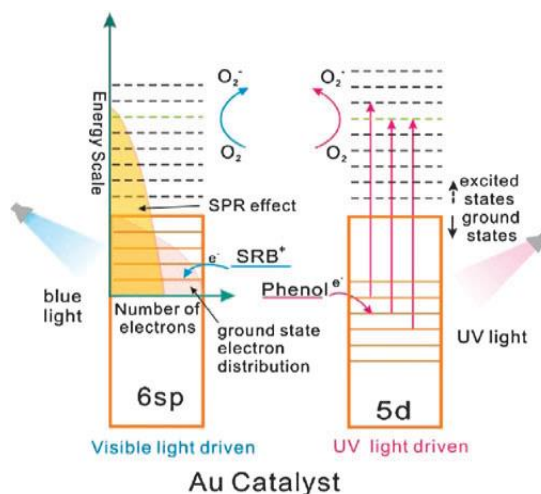


Figure 121. Selective oxidation of organic molecules by light irradiation in gold nanoparticle supported composites.

At 2013, Junquinang Yan et al. reported synergistic promotion of photocatalytic activity of TiO<sub>2</sub> particles for water redox reaction in Chemical Communications.<sup>94</sup> From the experiment, TiO<sub>2</sub> alone did not drive the hydrogen in visible light as expected. The efficiency of hydrogen evolution is degraded under UV-visible light illumination compared to the UV light. Interestingly, the efficiency is highly enhanced with composite phase with gold nanoparticles. Either the hydrogen evolution efficiency in UV light alone and UV-visible light illumination also enhanced. They defined the effect as a synergistic promotion effect. Due to their small particle size around 3 – 10 nm, they insisted that the catalytic activity of gold nanoparticles is shown in the experiment. The enhanced catalytic activity was ascribed to the trapping photo-excited electrons in the TiO<sub>2</sub> conduction band or enhancement of local field on TiO<sub>2</sub> nanoparticle surfaces. The detailed data is attached in Figure 122.

Sample	Hydrogen evolution rate/ $\mu\text{mol h}^{-1} \text{g}_{\text{cat}}^{-1}$			
	UV	Vis	UV-Vis	$\Delta^b$
TiO <sub>2</sub> -500	87.0	$\approx 0$	69.7	-17.3
Au/TiO <sub>2</sub> -500	10 726.6	9.1	14 658.2	3922.5

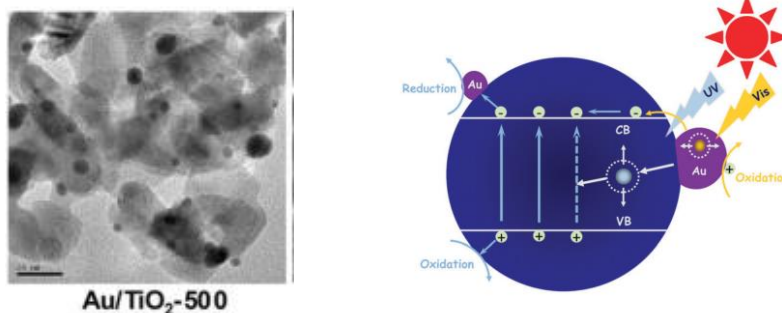


Figure 122. Synergetic promotion of hydrogen evolution in TiO<sub>2</sub>-gold nanoparticle composites.

In 2015, Zhongjin Lin et al. reported the photocatalysis enhancement in UV-visible light irradiation on Au/TiO<sub>2</sub> composite at Nanoscale.<sup>95</sup> The gold nanoparticle size used that experiment was 8 to 16 nm with averaged in 10 nm. They found optimal condition of enhancement by UV-visible dual light illumination on Au/TiO<sub>2</sub> composite. The degradation efficiency of methylene-blue (MB) has measured with varying the ratio of UV and visible light. Interestingly, the enhancement has straddle shape of enhancement with visible light. Efficiency become enhanced and degraded and enhanced again. They suggested that the dual-effect mechanism by localized surface plasmon resonance is activated. They attributed the phenomena as a result of reduced lifetime of the electrons by TiO<sub>2</sub> valence band under UV light excitations. Their result is summarized in Figure 123.

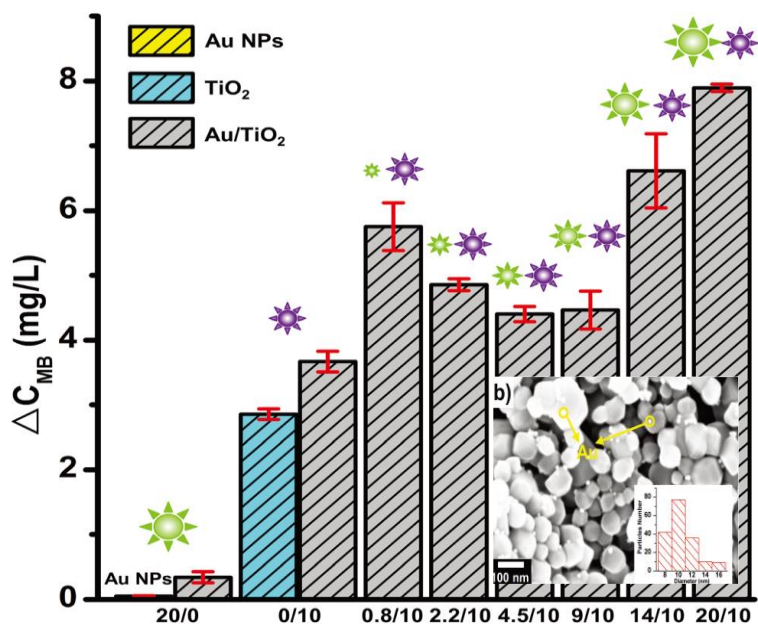


Figure 123. Dual-sided photocatalytic efficiency enhancement control by plasmonic gold nanoparticles for TiO<sub>2</sub> composite.

In 2016, Sung-Fu Hong et al. reported iridium oxide assisted plasmon induced photocatalysis enhancement at Advanced Energy Materials.<sup>96</sup> Using a co-catalyst deposition on gold nanoparticle deposited on TiO<sub>2</sub> nanowire array, electron lifetime extension is achieved. They expected that the hot electron injection from gold 5d orbital is efficient due to the largest contribution of density of states and a position of potential than water oxidation. At the article, they ascribed that the utilization of electrons in 5d orbital is restricted due to the low carrier lifetime of 5d orbital induced hot electrons. Their photocatalyst design was exemplary for the plasmonic water splitting, but the reaction that they showing was quiet poor. The result is arranged in Figure 124. So examination on the photoelectrochemical reaction for high-performance photoelectrode is required.

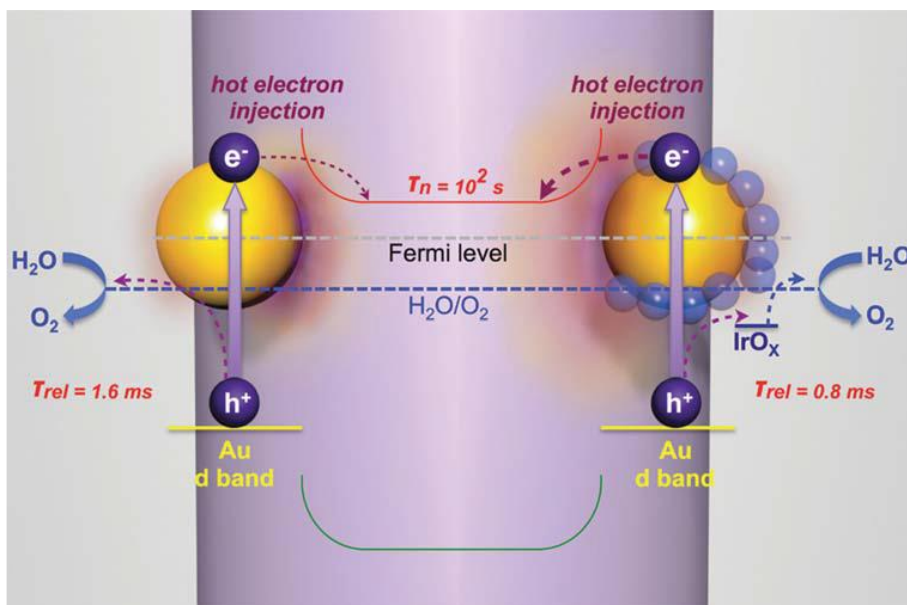


Figure 124. Utilization of holes in Au 5d orbital by iridium oxide co-catalysts.

## 5.8. Photocurrent Degradations in Plasmonic Photoanode

### 5.8.1 Photocurrent Degradation on Au-TiO<sub>2</sub>

In 2011, a legendary plasmon-enhanced photocatalytic water splitting research is reported in Nano Letters at First.<sup>97</sup> They observed 66 times great photocurrent enhancement than pristine TiO<sub>2</sub> photoelectrode with plasmonic Au nanoparticles. However, under UV light illumination, 4-fold photocatalytic activity reduction is observed. They described the photocatalytic enhancement in visible region is attributed to the local electromagnetic field enhancement near the TiO<sub>2</sub> surface. The reduction of photocatalytic activity under UV light illumination is attributed to the reduced photon flux on TiO<sub>2</sub> surface. Their result is arranged in Figure 125.

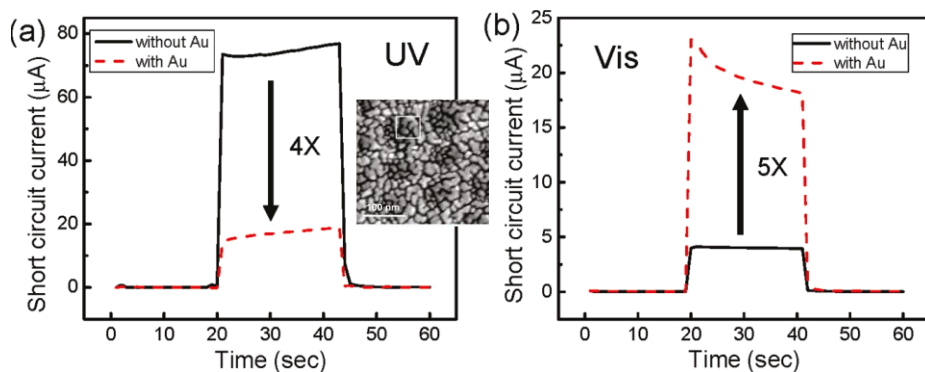


Figure 125. Photocurrent enhancement and degradation with irradiation of UV and visible light.

In 2015, LJ Breannan et al. analyzed the enhancement of IPCE on Au-TiO<sub>2</sub> system.<sup>98</sup> They showed that the photocurrent degradation on UV illumination is attributed to the IPCE degradation of TiO<sub>2</sub> (either electrons and holes) rather than gold nanoparticles. IPCE enhancement from gold nanoparticles are mainly ascribed by the holes on plasmonic gold nanoparticles.

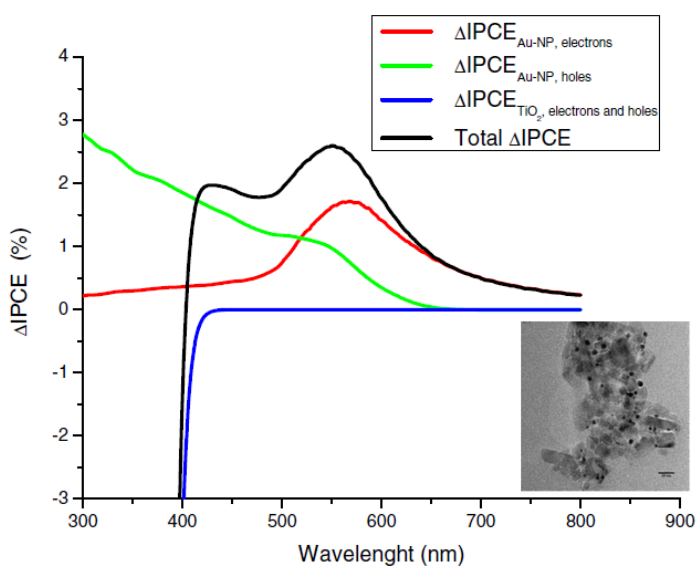


Figure 126. Analysis of IPCE enhancement on Au-TiO<sub>2</sub> composite.

## 5.8.2 Photocurrent Degradation on Au-Fe<sub>2</sub>O<sub>3</sub>

In 2011, Isabell Thomann et al. investigated plasmonic photocurrent enhancement for Au-Fe<sub>2</sub>O<sub>3</sub> composite system.<sup>99</sup> Various configuration was investigated by combination of surface/embedded configuration for nanoparticle, and stand-alone/core-shell structure of nanoparticle. Interestingly, at the surface configuration photocurrent degradation on UV range spectra was observed as we expected as shown in Figure 127.

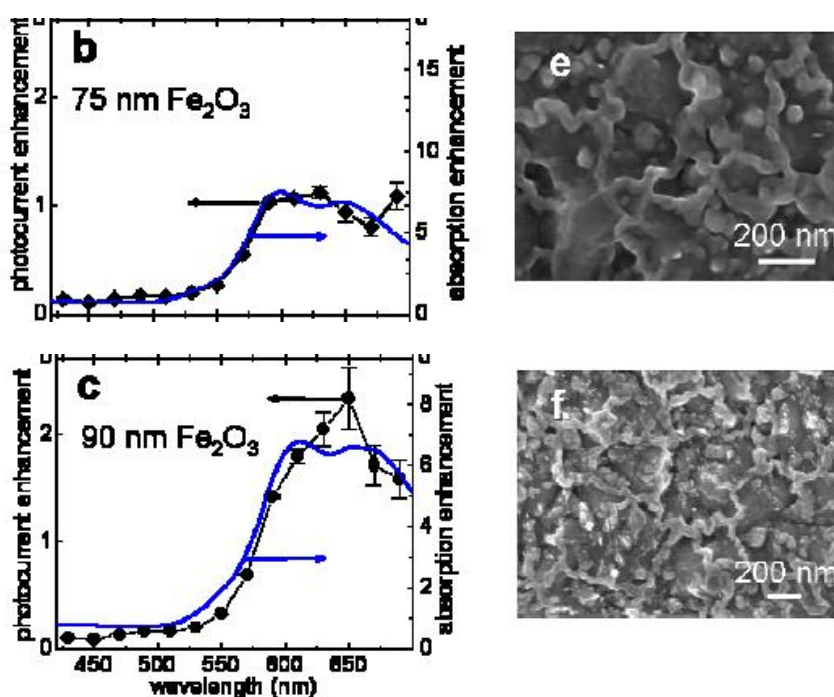


Figure 127. Photocurrent degradations in over-bandgap region of Fe<sub>2</sub>O<sub>3</sub> with surface configuration of gold nanoparticles.

Similarly, Elijah Thimsen (from the group of Scott C. Warren) tested the photocurrent enhancement at the Fe<sub>2</sub>O<sub>3</sub> nanorod for surface configuration and

Fe<sub>2</sub>O<sub>3</sub> film for embedded configurations. The overall photocurrent was lower than the Fe<sub>2</sub>O<sub>3</sub> nanorod with respect to the Fe<sub>2</sub>O<sub>3</sub> film. However, the enhancement was only achieved for embedded configuration on the Fe<sub>2</sub>O<sub>3</sub> film. They attributed the phenomena as a modulated carrier kinetic in the Fe<sub>2</sub>O<sub>3</sub> film according to the configurations as shown in Figure 128.

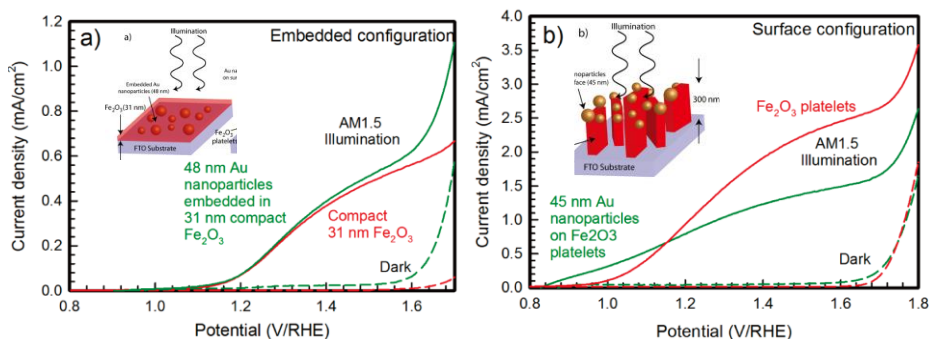


Figure 128. (a) Photocurrent enhancement from gold nanoparticles embedded in Fe<sub>2</sub>O<sub>3</sub> film. (b) Photocurrent degradation from gold nanoparticles on the surface of the Fe<sub>2</sub>O<sub>3</sub> nanorod.

To overcome the barriers observed in the literature, new concept and strategy will be suggested in the next chapter.

## Chapter 6

# Plasmonic Octahedral Gold Nanoparticles of Maximized Near Electromagnetic Fields for Enhancing Catalytic Hole Transfer in Solar Water Splitting

### Quote

**Mark L. Brongersma, Naomi J. Halas and Peter Nordlander**

“The discovery of the photoelectric effect by Heinrich Hertz in 1907 set the foundation for over 125 years of hot carrier science and technology. In the early 1990s it played a critical role in the development of quantum mechanics, but even today the unique properties of these energetic, hot carriers offer new and exciting opportunities for fundamental research and applications.” (2015, Nature Nanotechnology)

**Particle & Particle Systems Characterization 34**, 1600340 (2017)

**DOI:** 10.1002/ppsc.201600340

## 6.1. Motivation

To drive solar water splitting without degradation on the over-bandgap region of semiconductor, the shading effect from particle should be minimized and electric field should be maximized. From a shape control, the transition of interband (or intraband) efficiency should be enhanced. Here, plasmon enhanced solar water splitting based on the above discussion is proceeded using the shaped-controlled octahedral gold nanoparticles.

## 6.2. Introduction

Plasmonic solar water splitting is performed in plasmon-assisted water splitting systems based on the optoelectronic effects of plasmonic metal nanostructures.<sup>100</sup> Gold (Au) nanostructures are usually used in corrosive media due to their chemical stability and the strong response of their localized surface plasmon resonance (LSPR) in the visible (VIS) region. With plasmonic Au nanostructures, large bandgap semiconductors can utilize the sub-bandgap photon energy which cannot be absorbed by the semiconductor.<sup>101,102</sup> The enhancement of photoactivity in the VIS region by plasmonic Au nanostructures has mainly been attributed either to direct carrier injection<sup>85,88,103</sup> such as hot electrons injected into the semiconductor or to the increased carrier generation rate due to the near field electromagnetic coupling.<sup>104,105</sup> Electron excitation in a semiconductor through direct interfacial charge transfer mechanism has also discovered recently.<sup>106</sup> In contrast, some authors have reported Au nanoparticles (NPs) decoration could lead to degradation in the photoactivity of semiconductors.<sup>107-109</sup> While various plausible explanations

have been proposed, a rigorous model for plasmon-assisted photocatalysis has not yet been put forth.

Even though recent studies provide fascinating photoresponsivity by introducing plasmonic nanostructures in systems (including composite,<sup>110-112</sup> surface,<sup>107</sup> embedded,<sup>113</sup> and encapsulated<sup>114</sup> configurations), their results consistently reveal that photocatalytic reactions are dominant in the ultraviolet (UV) rather than VIS region. Notably, in the seminal work by the group of Moskovits in 2012, the plasmonic photoanode was first reported to show 20-fold efficiencies with VIS light compared to UV illumination.<sup>115</sup> The key of their success lies in the oxidation catalyst (cobalt-borate) which readily collects positive holes left behind in the aligned Au nanorods. The holes collected in the oxidation catalysts boost the oxygen evolving reaction (OER) and refill the lost electrons in the Au nanorods. From this, it was recognized that the hole transport process from LSPR was usually neglected. Hot hole transfer from the Au Fermi surface<sup>116</sup> to the OER level is likely to be hindered by the low energy of these holes. To prevent carrier recombination in solar water splitting, charge carriers (electrons and holes) in the semiconductor should be transferred to a semiconductor/liquid junction.<sup>117</sup> Likewise, both the hot electron and hole transport from LSPR should be considered due to the simultaneous characteristic of oxygen/hydrogen evolution half-reactions.

An appropriate approach for resolving this constraint is the morphological tailoring of Au nanostructures to readjust the hot carrier generation process from the LSPR. By considering the LSPR property in the Au nanoparticle is

well provided within the size range of from 20 to 50 nm,<sup>118</sup> a phenomenological plasmonic model predicts intense electric field in Au NPs inducing the increase of hot carriers.<sup>119</sup> Through the localized electromagnetic field enhancement mechanism for over-bandgap photon energies of the semiconductor, the charge carrier generation can happen efficiently.<sup>104</sup> Although optimization of correlated geometric factors for photoelectrochemical (PEC) applications has not yet been fully comprehended, it is experimentally known that the size,<sup>120</sup> shape<sup>121</sup> and configuration of a semiconductor matrix<sup>113,122,123</sup> of Au NP ensembles play a crucial role in the plasmonic carrier generation. Among these, shape is the least explored factor in PEC applications. Pu *et al.*<sup>121</sup> showed that the shape manipulation of Au NPs strongly affects the photoactivity of TiO<sub>2</sub> nanowires. However, photoactivity enhancements in the UV region are still more restricted than in the VIS region. Kazuma *et al.*<sup>124</sup> showed that higher LSPR-electromagnetic fields (EFs) in Ag nanorods generate more hot electrons. Moreover, surface-enhanced Raman scattering results of polyhedral and rounded Au NPs showed that sharp vertices and well-defined edges intensify LSPR-EFs.<sup>125</sup> We strongly believe that the shape factor could serve as a key towards fully uncovering the constraint of carrier injection in the plasmonic solar water splitting of wide bandgap semiconductors. A well-known TiO<sub>2</sub> wide band gap oxide semiconductor template was chosen in this study to investigate the hot carrier injection of Au NPs because TiO<sub>2</sub> theoretically absorbs only UV light.

Here, we report that shape-controlled octahedral Au NPs greatly promote the photoactivity (photocurrent, onset potential and incident photon-to-current

efficiency (IPCE)) of TiO<sub>2</sub> thin film with over-bandgap photon energy rather than sub-bandgap photon energy. Interestingly, the octahedral Au NPs also promote photoactivity from hematite film, WO<sub>3</sub> film and SrTiO<sub>3</sub> single crystal. Finite-Domain Time-Difference (FDTD) simulation demonstrates that octahedral Au NPs provide intensified LSPR-EFs in the entire UV-VIS region. This result can be explained by the presence of hot holes at the high energy, derived from the intensified LSPR-EFs at over-bandgap photon energy of the semiconductors. Due to the generality of photoactivity enhancements, hot hole injection is an essential process for efficient plasmonic solar water splitting.

### **6.3. Benefit of Au Interband Transition for Solar Water Splitting**

The photocatalytic behavior should be understood with the holes generated via band transitions in the octahedral Au NPs. Nonradiative damping of plasmon generates an electron-hole pair via intra/interband transitions, and the efficiency of these transitions can be tuned by modifying the shape of Au NPs.<sup>90</sup> The holes from the transition are distributed in the 6sp and 5d bands in accordance with the incident photon energy.<sup>78,116</sup> If the hot holes have adequate energy, the holes could participate in the redox reaction.<sup>126</sup> The physics of the interband transition in Au NPs is also well analyzed.<sup>127</sup> When the Au NPs are illuminated with light near the plasmon resonance frequency (VIS range), intraband transitions from the 6sp occupied states to the 6sp unoccupied states are dominant. Interband transitions between the 5d occupied states and the 6sp unoccupied states predominate when the Au NPs are illuminated with light far

from the plasmon resonance frequency (UV range). These transitions accompany hole generation in the valence bands (6sp and 5d), which is essential for OER reaction. Based on the frequency-dependent band transitions in the Au NPs, we provide a schematic hole reaction model to determine the difference in photocatalytic activity with respect to the frequency (UV-VIS) as shown in Figure 129. In the schematic, TiO<sub>2</sub> band edge positions were adopted from the prominent review.<sup>60</sup>

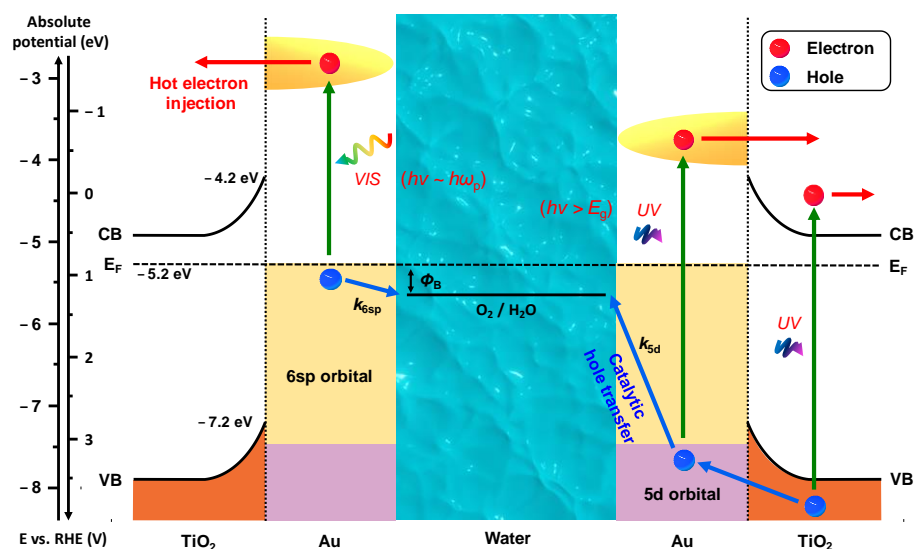


Figure 129. Hole reaction model for comprehensive descriptions of photocatalytic activity. Schematic illustration of photocatalytic activity enhancement mechanism in the TiO<sub>2</sub>/Au octahedral system where  $\Phi_B$  the is reaction potential barrier,  $k_{6sp}$  is the hole transfer constant for intraband transition,  $k_{5d}$  is the hole transfer constant for interband transition,  $h$  is the Flank's constant,  $\omega_p$  is localized surface plasmon resonance frequency of Au NPs and  $E_g$  is band gap energy of TiO<sub>2</sub>.

In VIS light illumination, electrons are transferred from the 6sp occupied states near the Au Fermi level ( $E_{F, Au}$ ) to the 6sp unoccupied states as a result of intraband transition. These electrons facilitate hot electron injection by overcoming the built-in Schottky barrier between the  $TiO_2$  and Au (for example, 550 nm light provides 2.26 eV to the electrons). Holes are generated in the 6sp occupied states near the  $E_{F, Au}$  as a consequence of the electron transition. However, the holes are barely transferred to the OER potential (1.23 V vs. RHE) due to the reaction potential barrier ( $\Phi_B$ ). Considering the two concurrent redox reactions (OER and HER) for water splitting, the hole transfer hindrance is detrimental for photoactivity. As a result, the hole transfer constant ( $k_{6sp}$ ) for the intraband transition remains almost the same, even with the intensified LSPR-EFs.

The electron transition from the 5d occupied states to 6sp unoccupied states occur at around 2.2 – 2.4 eV below the  $E_{F, Au}$ <sup>119</sup> with UV light illumination. These electrons have abundant energy to achieve hot electron injection (for example, 350 nm light provides 3.55 eV to the electrons). Compared to the holes in the 6sp occupied states, the hole transfer to the OER potential from the 5d occupied states is energetically favorable because the holes created in the interband transition do not have a reaction potential barrier. Such an amicable hole transfer is beneficial for enhancing photocatalytic activity and correlates the hole transfer constant ( $k_{5d}$ ) for the interband transition with LSPR-EFs. This hole reaction model does not indicate photocatalytic activity of semiconductor should follow the interband absorption of Au NPs. The critical point is the increased hole transfer constant ( $k_{5d}$ ) which efficiently promotes hole transfer

from the semiconductor to OER level. This lets us know that how the shape-tailored Au NPs can be act as a co-catalyst for over-bandgap photon energy of semiconductor and highlights the importance of hole transfer OER potential by Au NPs.

## 6.4. Optimization of Shape (Near Field Enhancements)

To quantify the LSPR-EF in the Au NPs, we performed FDTD simulation on the Au NP/TiO<sub>2</sub> systems at incident wavelengths of 550 nm (VIS range, near the LSPR frequencies of Au NPs) and 350 nm (UV range, far from the LSPR frequencies of Au NPs). To find out Au NPs shape, which generates intense LSPR-EFs, we performed FDTD simulations for six representative shapes (semicircle, triangle, circle, cube, hexagon and rhombus) (Figure 130).

Cross-sectional configuration						
Representative 3-dimensional shape	Hemisphere	Tetrahedron	Sphere	Cube	Rhombic dodecahedron	Octahedron
Position	①	①	①	①	①	①
Field enhancement at 550 nm	3.19	5.87	8.58	9.19	14.31	32.34
Field enhancement at 350 nm	1.23	1.33	1.943	1.88	2.22	3.15
Position	②	②	②	②	②	②
Field enhancement at 550 nm	Same with background	2.31	5.87	6.78	8.41	12.43
Field enhancement at 350 nm	Same with background	1.62	2.76	2.94	3.10	2.071
Position		③	③		③	③ / ④
Field enhancement at 550 nm		Same with background	Same with background		3.03	32.24 / 4.30
Field enhancement at 350 nm		Same with background	Same with background		2.05	2.44 / 2.13
Etc.	*Incident light direction to -z, maximum incident field amplitude at 550 & 350 nm are correspond to 1.495 & 1.852.					

Figure 130. Summary of the results of FDTD simulation performed on six representative shapes (semicircle, triangle, circle, cube, hexagon and rhombus).

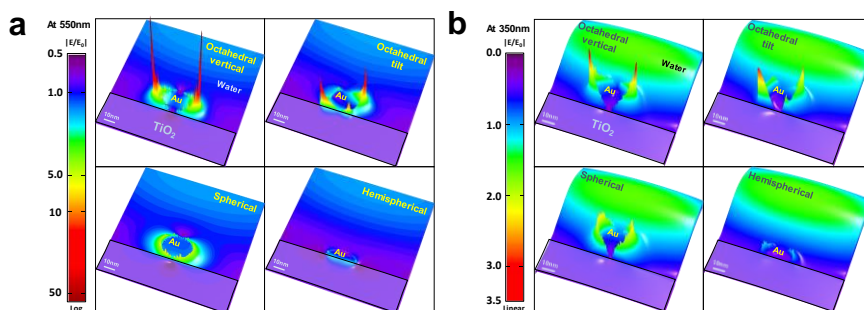


Figure 131. FDTD simulation results of near field enhancement for various shapes of Au NPs on the  $\text{TiO}_2$  flat film in water. (a) Field enhancement under 550 nm photons. (b) Field enhancement under 350 nm photons (octahedral vertical, octahedral tilt, sphere and hemisphere configurations are shown).

To drive plasmon enhanced solar water splitting, it is expected that the LSPR-EFs of Au NPs should be bigger than the maximum incident electromagnetic field amplitude at corresponding wavelengths. Considering the expectation, we found that the rhombus shape is the best candidate structure among the six representative shapes. As shown in Figure 131 (a), at an incident wavelength of 550 nm, the highest LSPR-EF was obtained with the octahedral Au NPs and lowest the LSPR-EF was obtained with the hemispherical Au NPs. Octahedral Au NPs in a vertical configuration yielded a maximum field enhancement ( $|E/E_0|$ ) of 62.26, which is approximately 19.5 times higher than that of hemispherical Au NPs. Spherical Au NPs showed a field enhancement of 8.58. Interestingly, as shown in Figure 131 (b), the order of the LSPR-EF intensity according to the Au NPs shapes at an incident wavelength of 350 nm was the same as that at an incident wavelength of 550 nm. The highest field enhancement region of octahedral Au NPs in vertical configuration was

calculated as 3.51, which is 2.85 times larger than that of the hemispherical Au NPs. Spherical Au NPs showed a field enhancement of 8.58. FDTD simulation results at 405 nm are attached to show the tendency for field enhancement between 350 nm and 550 nm wavelength (Figure 132).

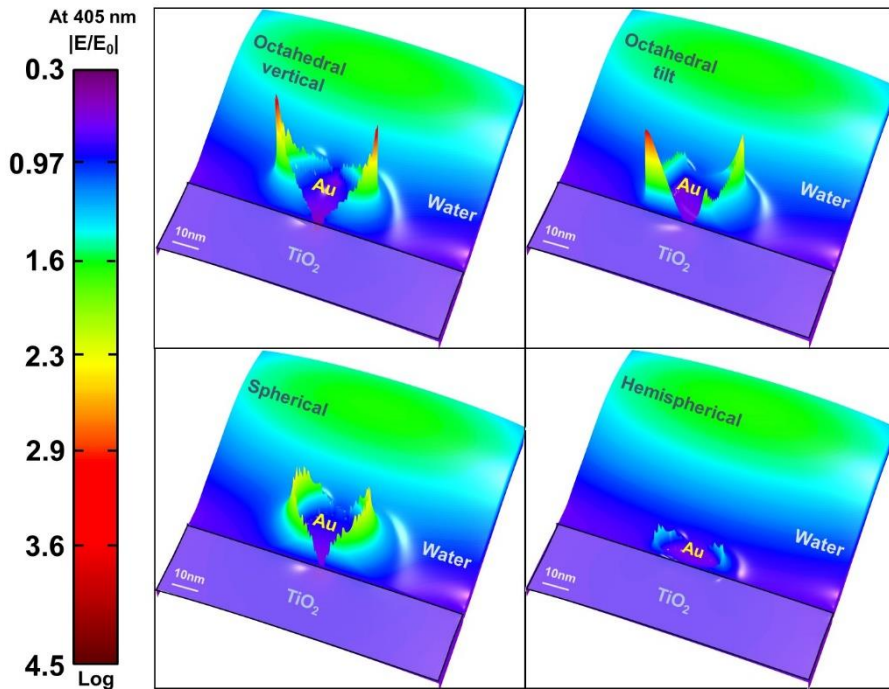


Figure 132. FDTD simulation results of near field enhancement for various shapes of Au NPs on the  $\text{TiO}_2$  flat film in water under 405 nm photons (octahedral vertical, octahedral tilt, sphere and hemisphere configurations are shown). The maximum field enhancements of corresponding shapes were recorded as 3.34, 3.17, 2.59 and 1.7.

Octahedral Au NPs recorded the largest field enhancement again. Without the Au NPs, electric field enhancement was not observed (Figure 133).

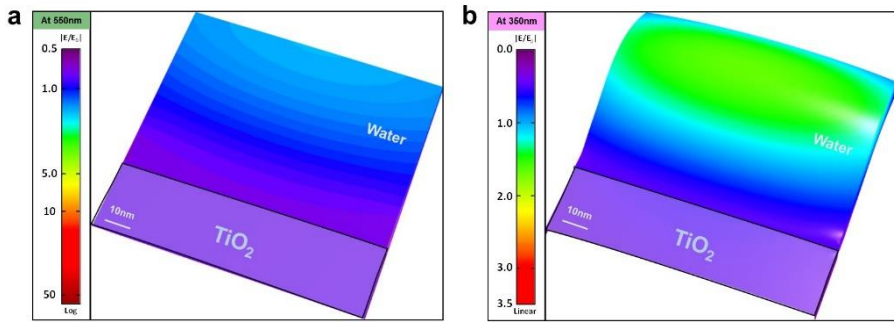


Figure 133. FDTD simulation results of near field in the absence of Au NPs. (a) Field enhancement under 550 nm wavelength. (b) Field enhancement under 350 nm wavelength.

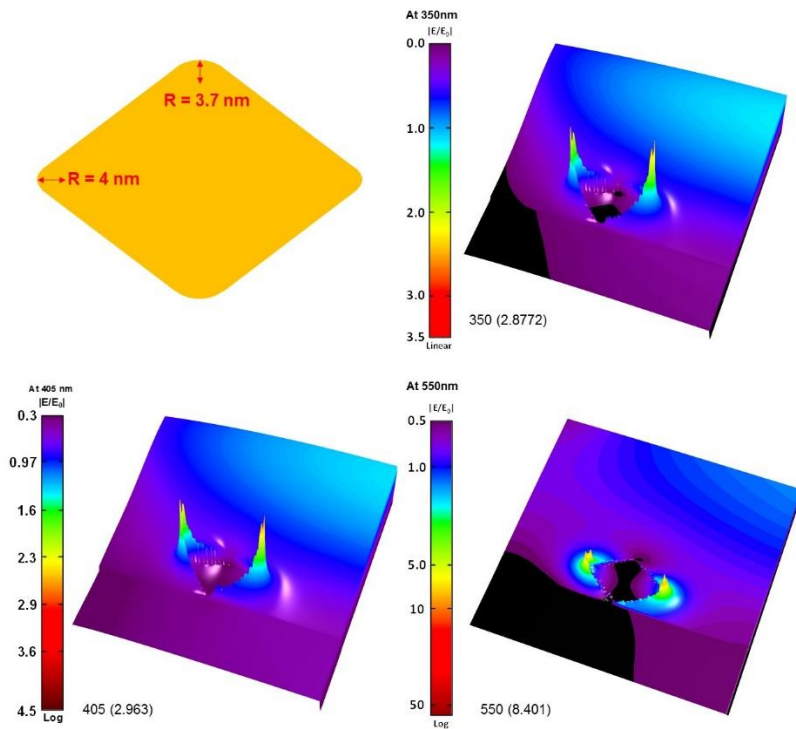


Figure 134. FDTD simulation results for realistic shape.

For the realistic value, I adopted rounded simulation with octahedral gold nanoparticles. The enhancement value is slightly reduced when the rounded shape is introduced, but the value is always higher than the spherical and hemispherical shapes. The tendency is depicted in Figure 134.

2-dimensional front-views for simulated configurations are illustrated in Figure 135.

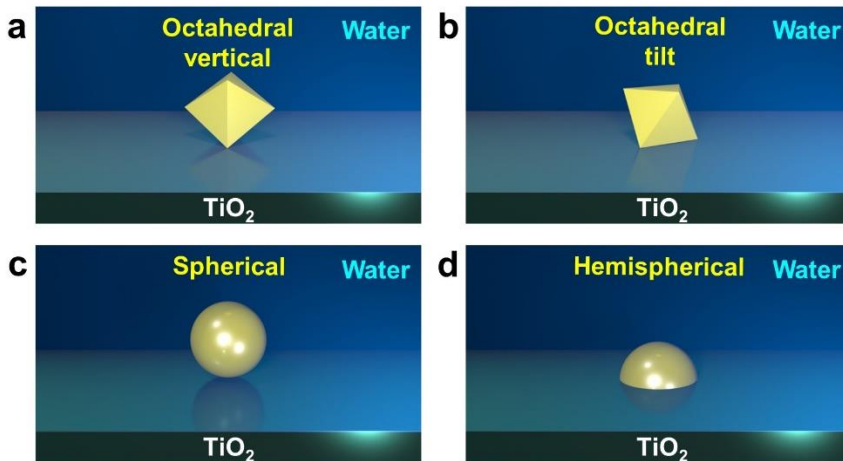


Figure 135. Schematic representation of Au nanoparticle FDTD configurations on TiO<sub>2</sub> thin film in Figure 2a,b is represented. (a) Octahedral Au nanoparticle vertical. (b) Octahedral Au nanoparticle tilt. (c) Sphere Au nanoparticle. (d) Hemisphere Au nanoparticle.

The FDTD results demonstrate that high LSPR-EFs are provided in the entire region of UV-VIS by the attachment of the octahedral Au NPs. In addition, the extinction cross-section was largest in the octahedral Au NP in FDTD

simulation compared with the other shapes as in Figure S5. The largest extinction cross-section supports the highest LSPR-EFs generation in octahedral Au NPs. Even scattering is one of the major mechanisms<sup>128</sup> for plasmonic enhancement, Mie scattering theory<sup>129</sup> and our FDTD simulation (Figure 136) indicate that substantive light scattering does not occur in the UV-VIS photon range.

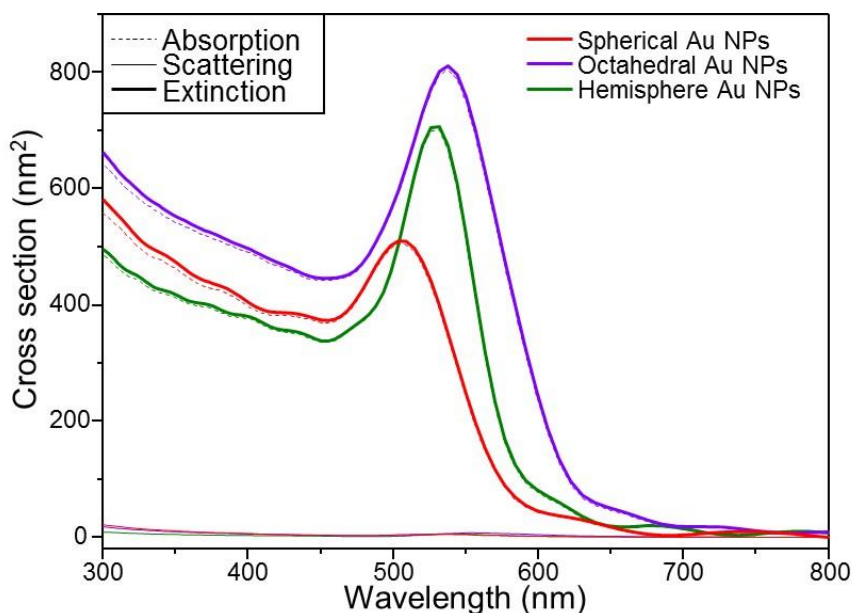


Figure 136. FDTD simulation results of absorption, scattering and extinction cross section of various Au NP shapes.

## 6.5. Gold Nanoparticle Decorated TiO<sub>2</sub> Films

Two different Au NP shapes (quasi-spherical and octahedral) are usually used to investigate the role of shape-controlled Au NPs on water-splitting photoactivity. The advantage of the octahedral Au NPs is that they can provide intensified LSPR-EFs compared with the quasi-spherical Au NPs due to their

sharp vertices and well-defined edges. As shown in Figure 137 (a)-(d) and Figure 138 (a)-(d), quasi-spherical and octahedral Au NPs were well synthesized using seed-mediated growth methods<sup>37,38</sup> and consisted of the lowest energy facets of (111) planes.<sup>39</sup> Au NPs synthesized from citrate stabilization were nearly spherical and their averaged size estimated to be 31.1 nm, whereas the octahedral Au NPs synthesized from cetyltrimethylammonium bromide/chloride (CTAB/C) stabilization were in a highly monodisperse manner and their averaged-size was around 33.5 nm (Figure 137 (e)). The UV-VIS absorption spectra of the synthesized Au nanoparticle solutions containing quasi-spherical and octahedral Au NPs exhibited a LSPR peak at 520 and 550 nm, respectively (Figure 137 (f)). The discrepancy with plasmon resonance wavelength between the shapes is mainly attributed to the sharp edges and vertices of shape in octahedral Au NPs.<sup>40</sup> These peaks were red-shifted on the surface of the TiO<sub>2</sub> films due to dielectric constant change.<sup>41</sup>

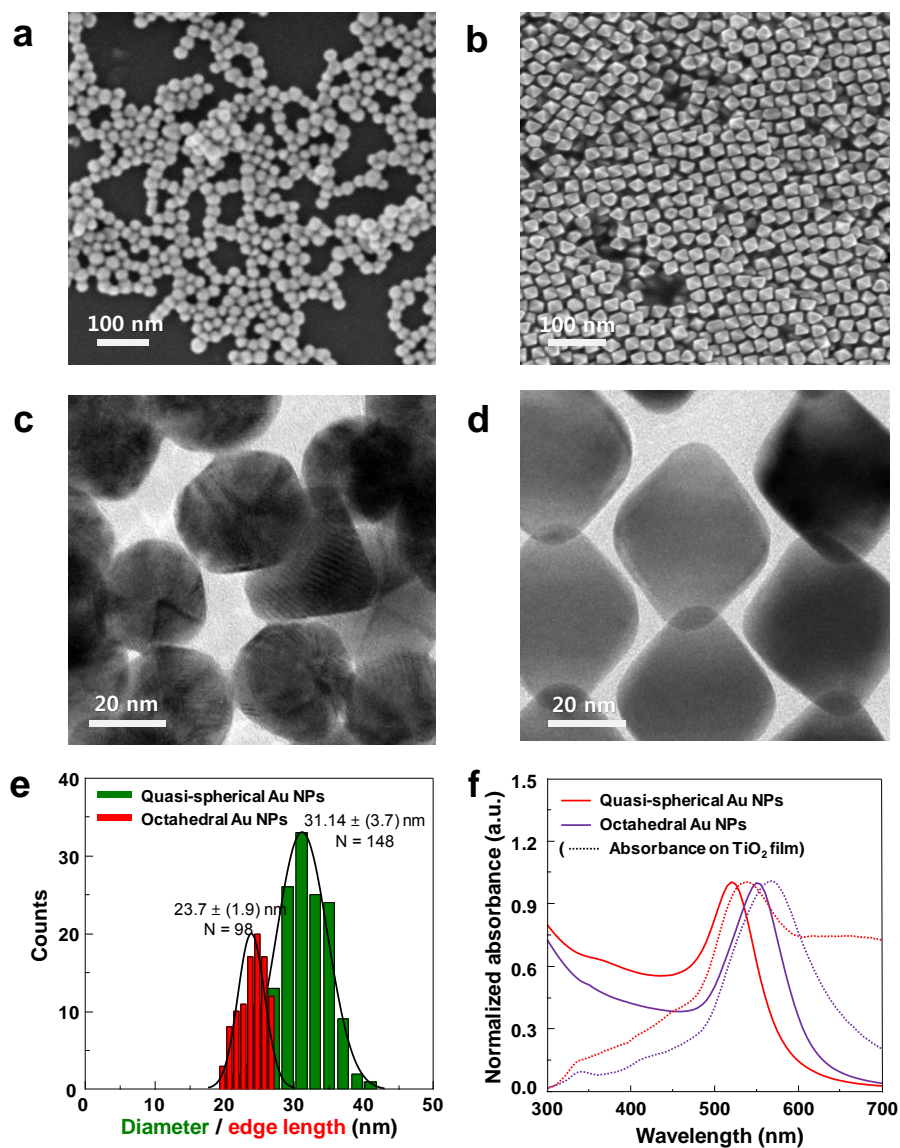


Figure 137. (a) SEM image of quasi-spherical Au NPs. (b) SEM image of self-assembled octahedral Au NPs. (c) TEM image of quasi-spherical Au NPs. (d) TEM image of octahedral Au NPs. (e) Diameter (for quasi-spherical) and edge length (for octahedral) distribution of Au NPs (please note that the diameter of a circumscribing sphere of octahedron is  $\sqrt{2}$  times greater than edge length). (f)

Normalized absorbance of synthesized solutions containing Au NPs. Dotted line (...) indicates corresponding absorbance on TiO<sub>2</sub> film.

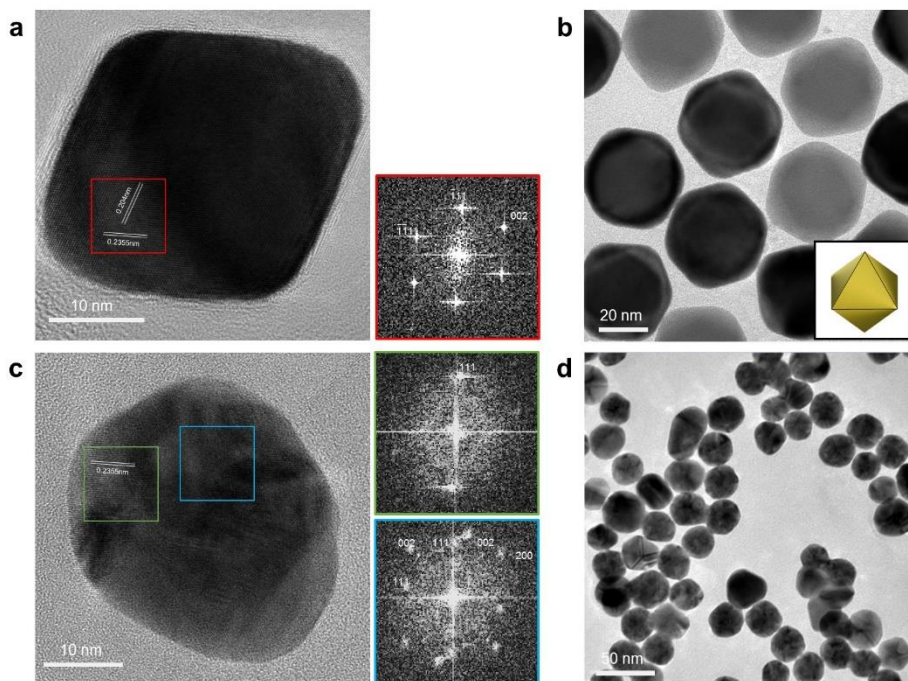


Figure 138. (a) TEM image of Au NPs together with a fast Fourier transform (FFT) pattern in selected area. (b) TEM image of octahedral Au NPs. Inset is provided to give readers better recognition of attachment configuration. (c) TEM image of quasi-spherical Au NPs together with a FFT pattern in selected area. (d) TEM image of quasi-spherical Au NPs.

## 6.6. Coverage Control of Gold Nanoparticles in TiO<sub>2</sub>/FTO film.

The linear sweep voltammetry measurements were carried out anodically above the hydrogen evolution potential and beyond 1.23 V vs. the reversible hydrogen electrode (RHE) potential under 1-sun condition. Note that the current level from our TiO<sub>2</sub> thin film photoanode was relatively lower than TiO<sub>2</sub>

NRs (Pu *et al.*<sup>121</sup>), due to the dissimilarities of the porosity and thickness between the photoanodes. Quasi-spherical and octahedral Au NPs were successfully attached on 80-nm-thick TiO<sub>2</sub> films through a deprotonation process (Figure 140).

The coverage control of Au NPs on the samples (Figure 141) was achieved by changing the volume of the precipitator solutions. X-ray diffraction (XRD) showed that the 80-nm-thick TiO<sub>2</sub> films were crystalline with anatase and rutile phases (Figure 142).

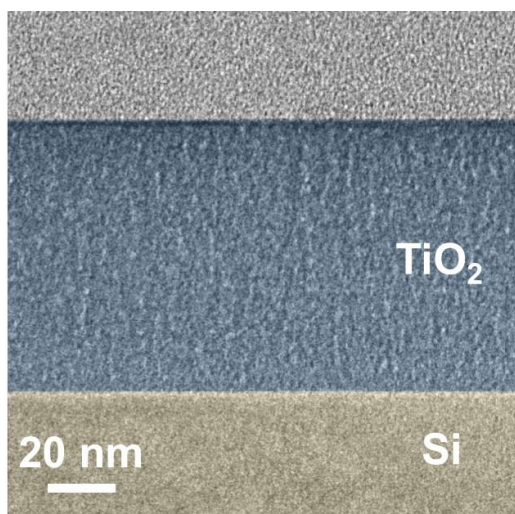


Figure 139. Cross-section TEM image of as-deposited 80-nm-thick TiO<sub>2</sub> film on silicon. Note that, TiO<sub>2</sub> film was deposited on Si to clearly show the thickness and uniformity. False colors (blue and yellow) were added in TEM image to enhance visibility.

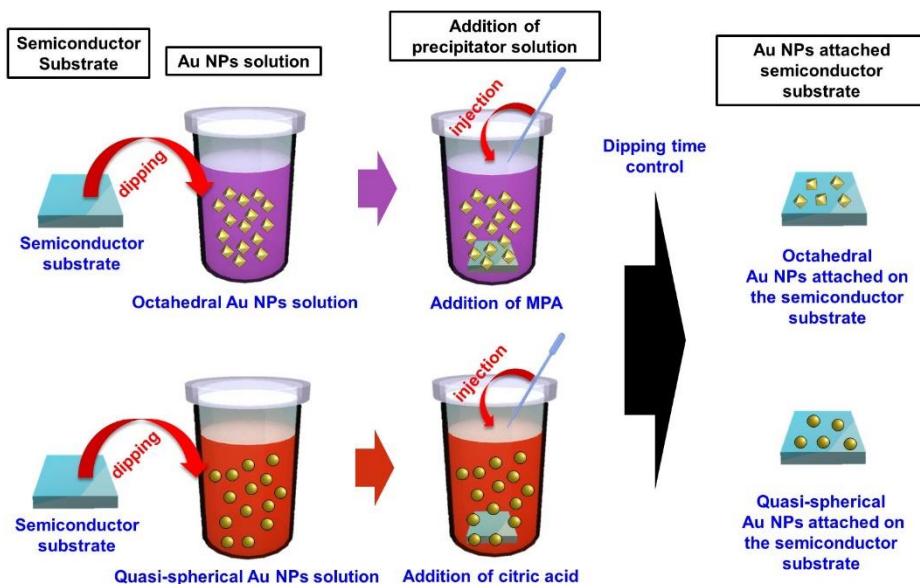


Figure 140. Schematic representation of deprotonation process.

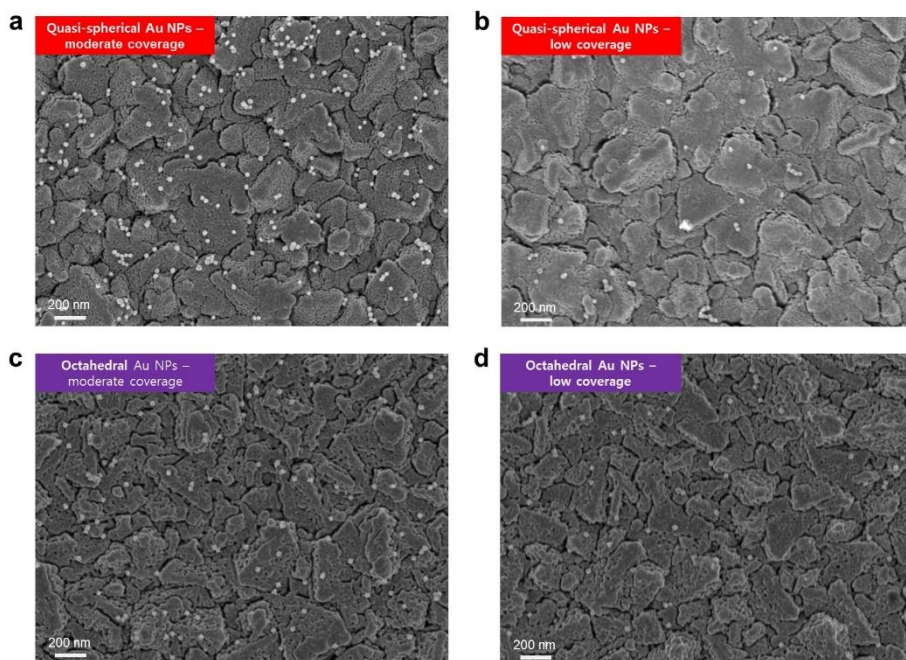


Figure 141. SEM image of coverage controlled Au NPs above 80-nm-thick TiO<sub>2</sub> film on FTO/Glass substrates. (a) quasi-spherical Au NPs with moderate coverage. (b) quasi-spherical Au NPs with low coverage. (c) Octahedral Au

NPs with moderate coverage. (d) Octahedral Au NPs with low coverage. The image is taken after measurement.

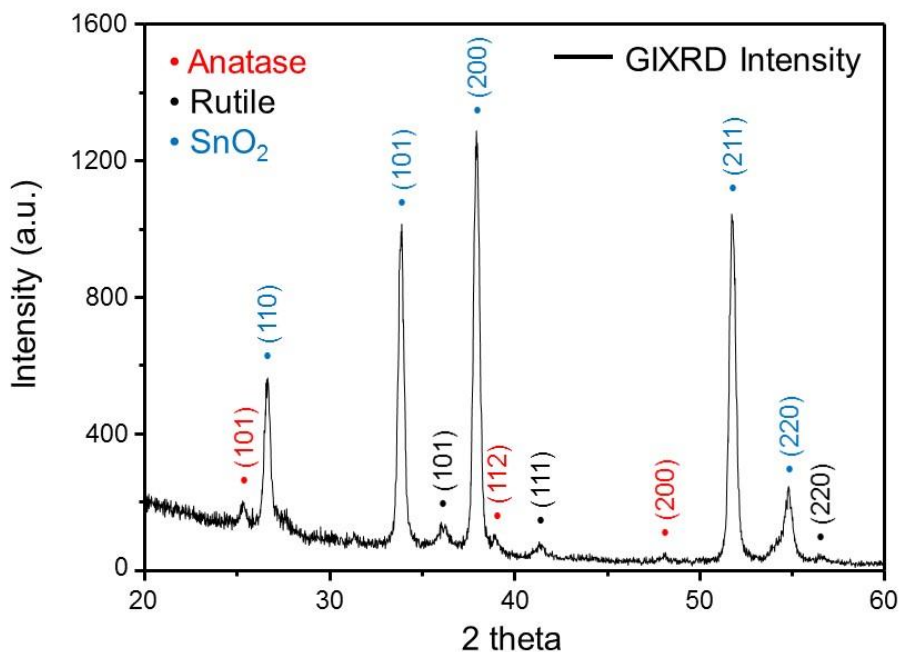


Figure 142. Grazing incidence X-ray diffraction (GIXRD) spectra of 80-nm-thick TiO<sub>2</sub> film on FTO/Glass substrate sample annealed at 700 °C.

## 6.7. Photocurrent Action Spectra

The attachment of quasi-spherical Au NPs (Figure 143 (a)) resulted in associated degradation of photocurrent, which deteriorated further with increased coverage of the quasi-spherical Au NPs (Figure 143 (b)). The degradation of photocurrent occurred regardless of the coverage. On the other hand, the attachment of octahedral Au NPs (Figure 143 (c)) leads to a substantial increase in the photocurrent, which reaches a maximum with the moderate coverage of octahedral Au NPs (Figure 143 (d)). The cathodic shift of the onset potential was also found with the attachment of the octahedral Au

NPs. It is expected that spherical Au NPs have citrate capping layer (around 0.7 nm)<sup>130,131</sup> and octahedral Au NPs have an MPA capping layer (around 0.68 nm).<sup>132</sup> Similar ligand lengths indicate the ligand difference is not the origin of the photocurrent dissimilarity. For reference, hemispherical Au NPs were formed through the annealing of electron-beam evaporated Au films (Figure 143 (e); Figure 144). The coverage of hemispherical Au NPs was managed by the modification of the Au film thickness. The photocurrents were degraded with regardless of the coverage (Figure 143 (f)). Eventually, no photocurrent was observed when the thickness of the deposited Au film reached 20 nm (Figure 145). The detailed information about coverage and the number of NPs is summarized in Figure 146. If the onset potential shift is triggered by passivation of surface states, the onset potential of TiO<sub>2</sub> film should decrease with increasing of the number of Au NPs. However, our experimental result indicate that the surface passivation is not the reason for onset potential shift. Overall results indicate that the differences in Au NPs contact modes (direct and indirect with TiO<sub>2</sub>) also would not be the origin of these photocurrent behaviors. If the role of Au NPs is just restricted to the field enhancement of near the surface of TiO<sub>2</sub> from Au NPs, the photocurrent should have arisen in all three cases (quasi-spherical, octahedral and hemispherical Au NPs). Moreover, the photocurrent behavior was also not proportional to the coverage of the samples (especially for moderate coverage of quasi-spherical and octahedral Au NPs). It is significant that the octahedral Au NPs enhance the photocurrent and lower the onset potential of the photoanodic TiO<sub>2</sub> films by enabling charge transfer around Au NPs, similar to co-catalysts such as noble-

metal catalysts ( $\text{RuO}_2$  and  $\text{IrO}_2$ )<sup>133</sup> and cobalt phosphate (Co-Pi),<sup>134</sup> implying that the Au NPs act as OER catalysts.

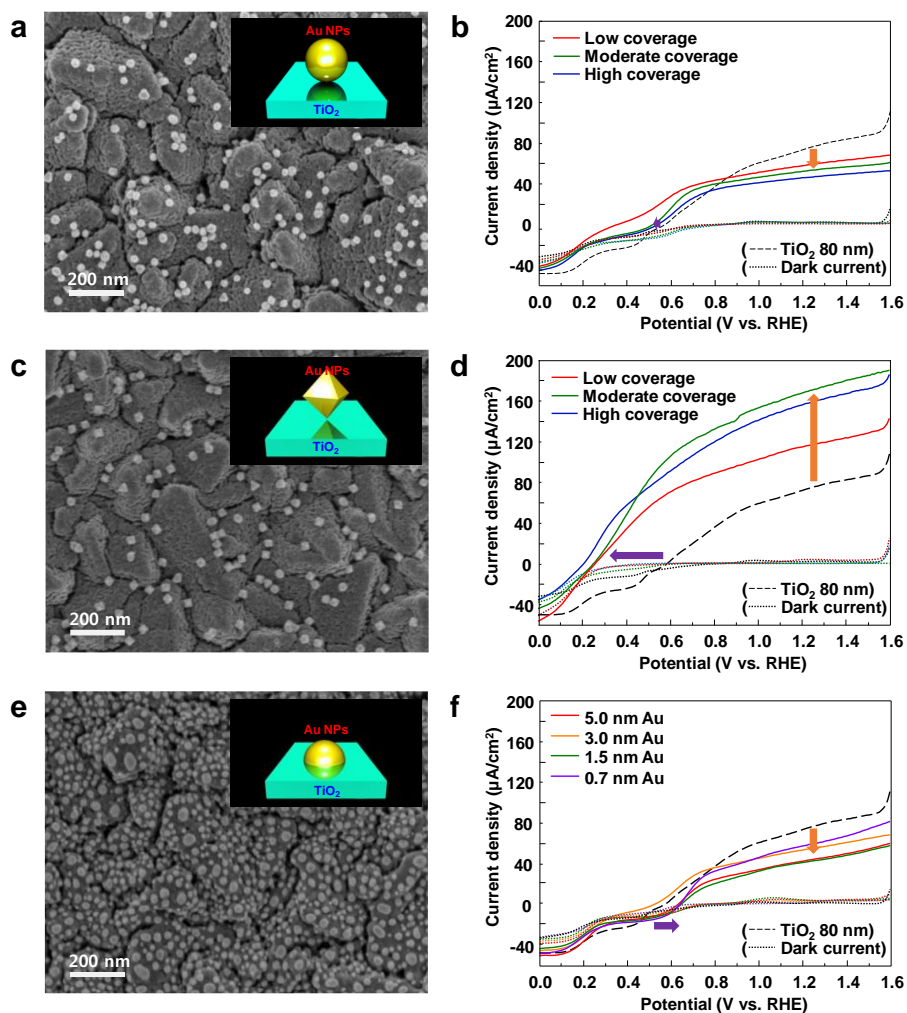


Figure 143. Linear sweep curves for Au attached to fluorine doped tin oxide (FTO)/TiO<sub>2</sub> 80 nm samples over various coverage (low, moderate and high). (a) SEM image of quasi-spherical Au NPs attached to FTO/TiO<sub>2</sub> 80 nm sample with high coverage. (b) Linear sweeps in dark/with photo for various coverage of quasi-spherical Au NPs. (c) SEM image of octahedral Au NPs attached to FTO/TiO<sub>2</sub> 80 nm sample with high coverage. (d) Linear sweeps in dark/with

photo for various coverage of octahedral Au NPs. (e) Hemispherical Au NPs from E-beam evaporator (3 nm Au) over FTO/TiO<sub>2</sub> 80 nm sample. (f) Linear sweep in dark/with photo for annealed Au NPs from E-beam evaporator (5.0, 3.0, 1.5 and 0.7 nm Au). In linear sweep data (b), (d) and (f), dashed line (- -) indicates linear sweep data of TiO<sub>2</sub> film without Au NPs, dotted line (...) indicates corresponding dark currents, orange arrow indicates the tendency of current behavior with Au NPs and purple arrow indicates the tendency of onset potential with Au NPs. Schematic of Au NPs configurations on TiO<sub>2</sub> are also drawn as inset in the SEM images.

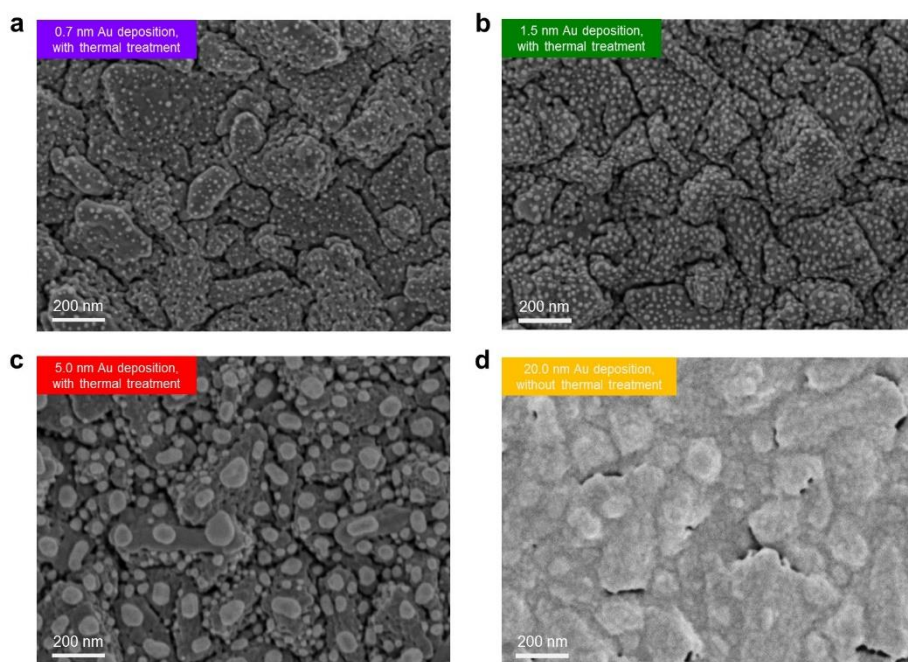


Figure 144. (a) SEM image of annealed e-beam deposited Au NPs (0.7 nm) over FTO / TiO<sub>2</sub> 80 nm sample. (b) SEM image of annealed e-beam deposited Au NPs (1.5 nm) over FTO / TiO<sub>2</sub> 80 nm sample. (c) SEM image of annealed

e-beam deposited Au NPs (5.0 nm) over FTO / TiO<sub>2</sub> 80 nm sample. (d) SEM image of e-beam deposited Au NPs (20.0 nm) over FTO / TiO<sub>2</sub> 80 nm sample.

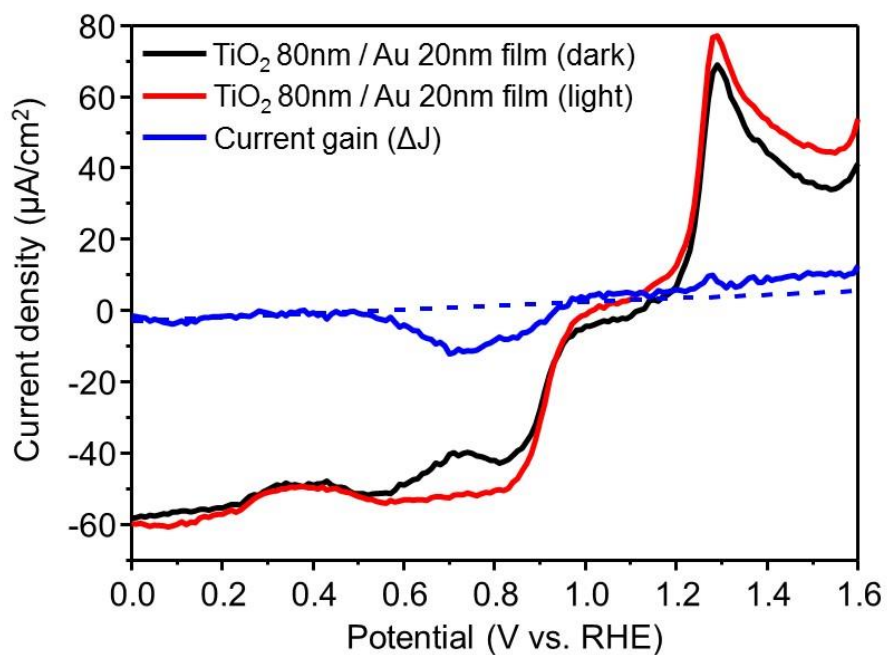


Figure 145. Linear sweep curves for 20 nm Au thin film 80-nm-thick TiO<sub>2</sub> film on FTO/Glass substrate. The sample does not show effective photocurrent under AM 1.5 G illumination (consider the current gain is almost zero).

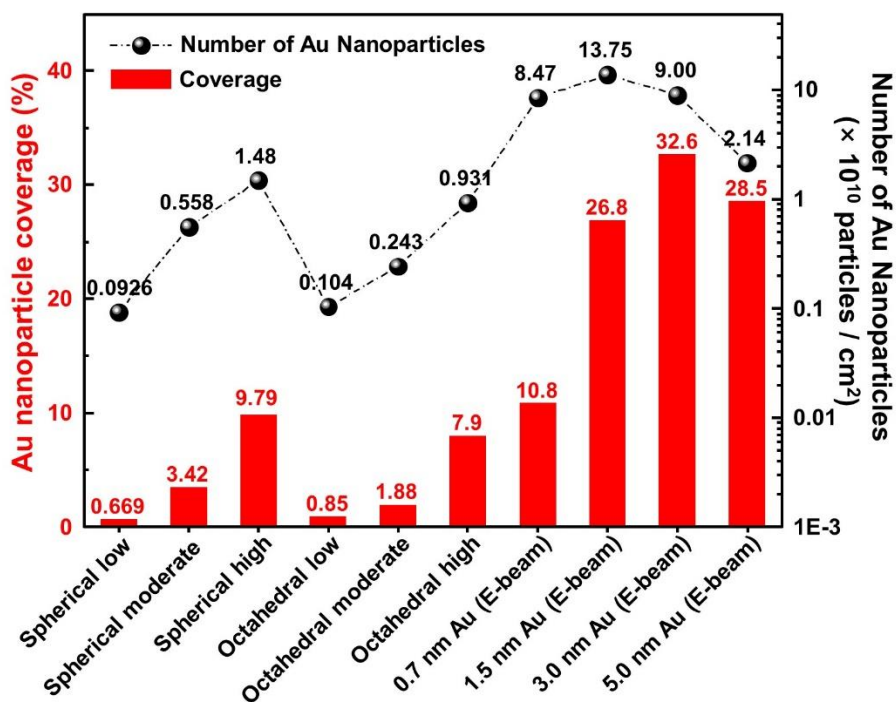


Figure 146. The detailed information about coverage and the number of Au NPs is summarized.

## 6.8. Wavelength Dependence of Photoactivity

As in Figure 147(a) and 147 (b), the monochromatic laser sources at 532 nm and 405 nm, respectively, that were used to investigate the photocurrent generation ability depending on the incident electromagnetic spectra (VIS and UV). Photocurrent transients were measured using a monochromatic laser with the fluence of  $10 \text{ mW}/\text{cm}^2$  at 1.23 V vs. RHE. At 532 nm, the transient photocurrent with shape-controlled octahedral Au NPs showed a smaller amount of photocurrent increase compared with that of the quasi-spherical Au NPs. On the other hand, the hemispherical Au NPs showed the highest transient photocurrent of almost five times greater than that of the 80-nm-thick  $\text{TiO}_2$  film.

With the 405 nm wavelength, the transient photocurrents with quasi-spherical and hemispherical Au NPs degraded below the photocurrent level of the 80-nm-thick TiO<sub>2</sub> film. Only octahedral Au NPs showed a superior photocurrent above that of the 80-nm-thick TiO<sub>2</sub> film.

The photocurrent from the 532 nm monochromatic laser remained in the range of nA/cm<sup>2</sup>, whereas the photocurrent from 405 nm remained in the range of μA/cm<sup>2</sup>. An essential point to note here is the photocurrent range disparity according to the incident wavelengths. The simultaneous increase in the photocurrent at both wavelengths (532 and 405 nm) was only achieved with the shape-controlled octahedral Au NPs. The photocurrent enhancement from the VIS range is significantly lower than the photocurrent degradation from UV range except for shape-controlled octahedral Au NPs. This result is analogous to the previously reported results in which it was confirmed that, even with the considerable photocurrent enhancement in the VIS region achieved with the plasmonic nanostructure, the photocurrent contribution of the VIS region is usually much less than that of the UV region.<sup>107,114,121</sup> This strongly indicates that photoactivity enhancement from the UV region is critical for the overall photoactivity of semiconductor photoanodes.

To clarify the results from the photocurrent transients, we measured the photovoltage and IPCE of the Au NPs decorated 80-nm-thick TiO<sub>2</sub> films. As arranged in Figure 147 (c), octahedral Au NPs showed the largest photovoltages at 405 nm. However, at 532 nm, the photovoltage from the octahedral Au NPs was similar to that from the hemispherical Au NPs. Photovoltages were

recorded under open circuit condition as shown in Figure 148. From the IPCE measurement (Figure 147 (d)), we can verify that the photoactivity of the over-bandgap photon energy region was enhanced with octahedral shaped Au NPs. Unfortunately, the IPCE near the LSPR frequency region is barely recognizable due to electrical noise, but we could indirectly determine the IPCE property from previous photovoltage-current measurements (Figure 147(a)-(c)).

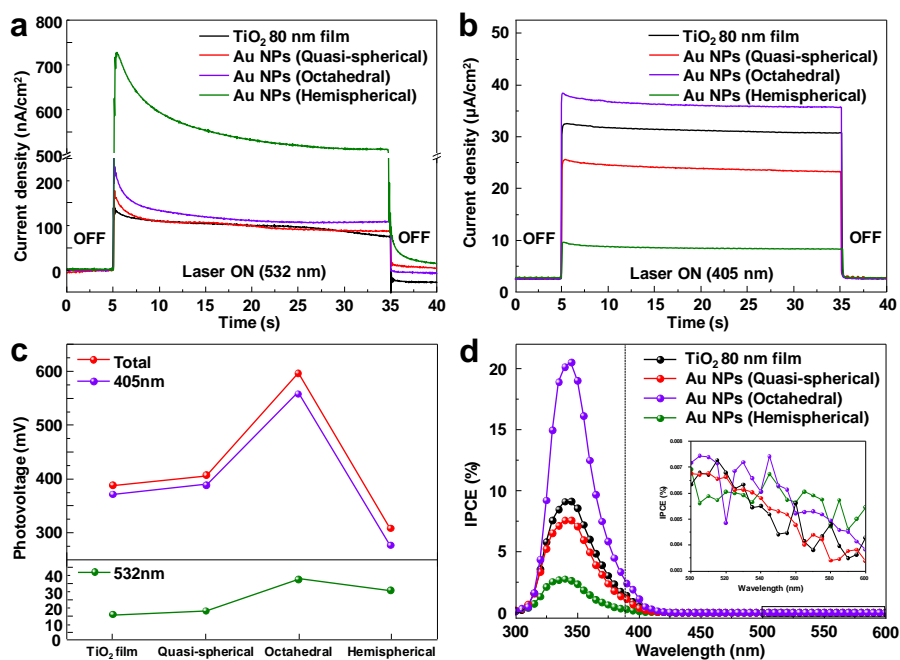


Figure 147. (a) Photocurrent transient at 1.23 V vs. RHE with monochromatic 10 mW/cm<sup>2</sup> fluence at 532 nm. (b) Photocurrent transient at 1.23 V vs. RHE with monochromatic 10 mW/cm<sup>2</sup> fluence at 405 nm. (c) Photovoltage gains of samples at open circuit potential. (d) IPCE spectra of above mentioned samples at 1.23 V vs. RHE. Moderate coverage of quasi-spherical Au NPs, moderate coverage of octahedral Au NPs and 3.0 nm E-beam evaporated Au on 80-nm-thick TiO<sub>2</sub> samples were used for the measurements. The vertical dotted line

(...) indicates the band gap energy of TiO<sub>2</sub>. Inset is also shown to clarify the photocurrents in the visible light are within the noise level.

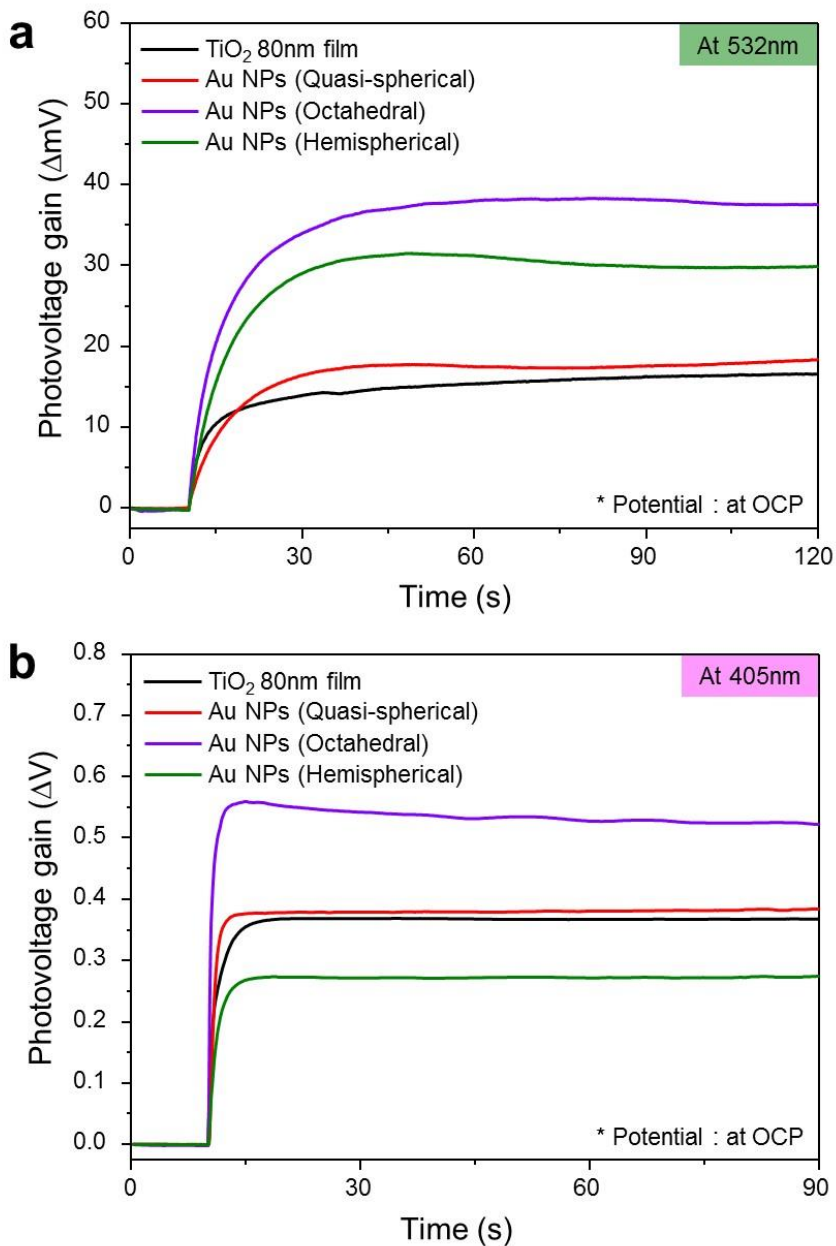
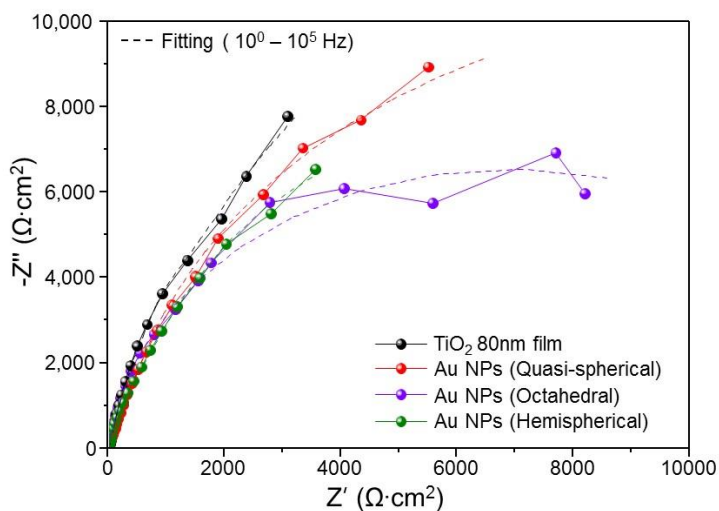


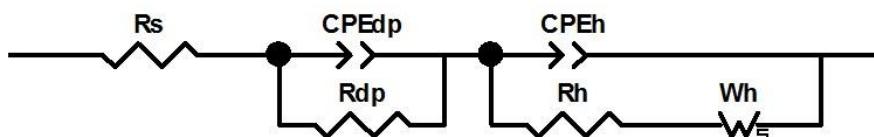
Figure 148. Photovoltage gain profiles of samples (quasi-spherical Au NPs attached FTO/TiO<sub>2</sub> 80 nm with moderate coverage sample, octahedral Au NPs, hemispherical Au NPs)

attached to FTO/TiO<sub>2</sub> 80 nm with moderate coverage sample and annealed e-beam deposited Au NPs (3nm) over FTO/TiO<sub>2</sub> 80 nm sample. (a) Photovoltage gain at OCP with the fluence of 10 mW/cm<sup>2</sup> at 405 nm. (b) Photovoltage gain at OCP with the fluence of 10 mW/cm<sup>2</sup> at 532 nm.

## 6.9. Impedance Analysis

The improved charge generation of octahedral Au NPs is experimentally demonstrated with Nyquist impedance measurements while 1-sun illumination (Figure 149). Warburg impedance ( $W_h$ ) is added to circuit element for fitting the impedance well. The capacitance in semiconductor region ( $CPE_{dp}$ ) among the samples are analogous. While the capacitance at the interface ( $CPE_h$ ) with octahedral Au NPs is maximized. This result shows enhanced charge generation from shape-controlled octahedral Au NPs in TiO<sub>2</sub> surface as expected in the FDTD simulations. The improvement of photocatalytic activity with the over-bandgap photon energy gives a clue that the shape-controlled octahedral Au NPs behave as oxygen evolution catalysts.





$(R/10^4 \Omega \cdot \text{cm}^2)$ $(\text{CPE}/10^{-6} \text{ F})$	$R_{dp}$ (semiconductor)	$\text{CPE}_{dp}$ (semiconductor)	$R_h$ (interface)	$\text{CPE}_h$ (interface)
TiO <sub>2</sub> 80nm film	3.55	2.43	20.77	5.21
Au nanoparticles (Quasi-spherical)	2.27	1.01	118.91	1.27
Au nanoparticles (Octahedral)	1.73	1.27	120.87	13.9
Au nanoparticles (Hemispherical)	2.93	3.11	108.56	6.32

\*dp : (depletion region), h : (helmholtz diffusion layer)

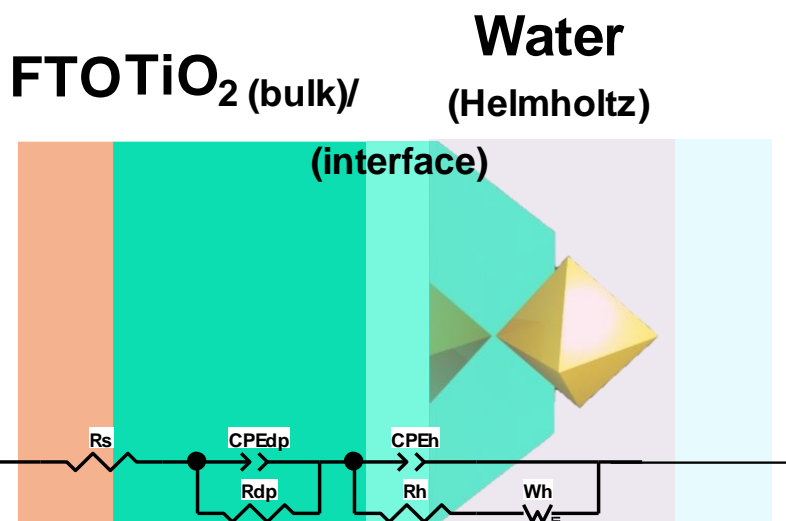


Figure 149. Nyquist plots at 1.23 V vs. RHE under AM 1.5G illumination. Equivalent circuit analyses are summarized in the table where  $R_{dp}$  is the resistance of depletion region in semiconductor,  $\text{CPE}_{dp}$  is the capacitance of

depletion region in semiconductor,  $R_h$  is the resistance of Helmholtz diffusion layer and  $CPE_h$  is the capacitance of Helmholtz diffusion layer.

## **6.10. Qualitative Modeling of Plasmon Enhanced Solar Water Splitting**

As previously explained, photocatalytic activity enhancement with intensified LSPR-EFs is effective in the interband transitions rather than in the intraband transitions in Au NPs. The shape-control of Au NPs barely affects to the hole transfer constant ( $k_{6sp}$ ) in VIS light illumination, while the shape-control of Au NPs strongly affects to the hole transfer constant ( $k_{5d}$ ) in UV light illumination. The shading effect is arising via bulk-like properties from over-attachment and aggregation of Au NPs, interband absorption of Au NPs, and backward scattering of small-sized Au NPs because of Mie scattering. Taking into account the shading effect on Au NPs, we drew a qualitative diagram of the photocatalytic activity enhancements by shape-controlled Au NPs. The interrelationship among the photocatalytic activity, the intensified LSPR-EF and coverage is shown in Figure 148. Three criteria are adopted for the graph. First, an infinite number of Au NPs cannot accommodate photocatalytic activity (as shown in Figure 143). Second, moderate coverage is needed for maximizing the photocatalytic activity. Third, the shading effect should be considered. While it appears that the photocatalytic activity would be enhanced by increasing the surface coverage of the Au NPs on the semiconductor, in reality, any approaching light is partially lost with a semiconductor photoanode due to the shading effect of the Au NPs. Therefore, a moderate coverage is needed to achieve the maximum photocatalytic activity. Our results can be

understood with the qualitative diagram of the photocatalytic activity enhancement provided in Figure 150.

In VIS light, the amount of photocatalytic activity degradation from the shading effect of Au NPs is less than the amount of photocatalytic activity enhancement from Au NPs because TiO<sub>2</sub> does not absorb VIS light. Thus, the shading effect of Au NPs in VIS light is negligible unless bulk-like properties occur. The photocatalytic activity with the octahedral Au NPs is not maximized in the VIS light, because the hole transfer constant ( $k_{6sp}$ ) almost remains unchanged. Therefore, whether we provide high electric field from octahedral Au NPs or low electric field from quasi-spherical Au NPs, photocurrent does not change much with respect to shape. High photocurrent in VIS light in from many hemispherical Au NPs supports this phenomenon. On the other hand, in UV light, the tendency of photocatalytic activity enhancement is more complex due to the correlation of the hole transfer constant ( $k_{5d}$ ) with LSPR-EF. Even though shading effect on TiO<sub>2</sub> increases, because TiO<sub>2</sub> absorbs light in the UV region, the increased hole transfer constant ( $k_{5d}$ ) led to high photocatalytic activity which could overcome the shading effect. From these analyses, we can conclude that the overall photocatalytic activity from the plasmonic Au NPs is the sum of photocatalytic activity enhancement from LSPR-EF and photocatalytic activity deterioration from shading effect. There would be a saturation of the PEC property enhancement with increasing of surface coverage of Au NPs on semiconductor due to the extinction cross-section interference between NPs. Considering our linear sweep voltammetry data with spherical Au NPs and previously reported literatures,<sup>135-137</sup> shading effect would

be linearly proportional to the surface coverage of Au NPs. Taking of photocatalytic activity enhancement and degradation from the above considerations into account, there should be an optimum surface coverage value of Au NPs on semiconductor to achieve the maximum photocatalytic activity enhancement.

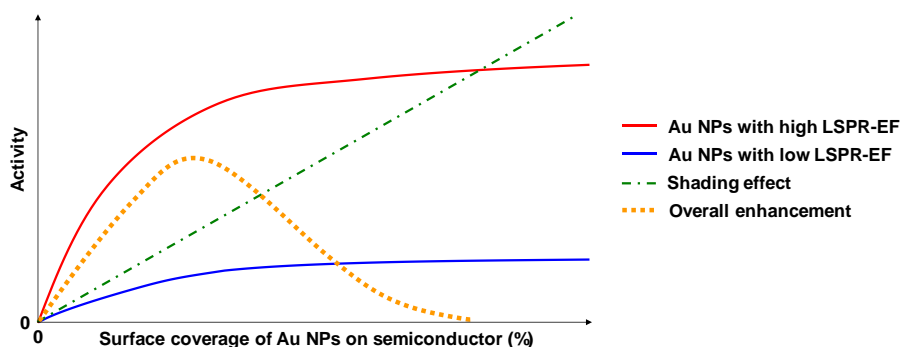


Figure 150. Qualitative diagram of the photocatalytic activity enhancement by shape-controlled Au NPs. The overall enhancement is calculated by subtraction for the activity of Au NPs with high LSPR-EF and activity of shading effect from Au NPs. Each component enhances and deteriorates photocatalytic activity subsequently.

## 6.11. Detection of Oxygen Evolution Reaction with Gold Nanoparticle Decorated TiO<sub>2</sub> Nanorod

It was impossible to compare the gas evolution and efficiency of with a thin film TiO<sub>2</sub> photoanode due to the very small amount of O<sub>2</sub> evolution. Through the employing of TiO<sub>2</sub> nanorods (NRs)<sup>138</sup> (Figure 149 (a)), we have achieved almost 10 times higher photocurrent density (Figure 149 (b)). The photocurrent density at 1.23 V vs. RHE was almost 20 % enhanced by attaching a small

number of octahedral Au NPs (a projected coverage is less than 0.7 %). Following OER reactions are done after Ar purging.

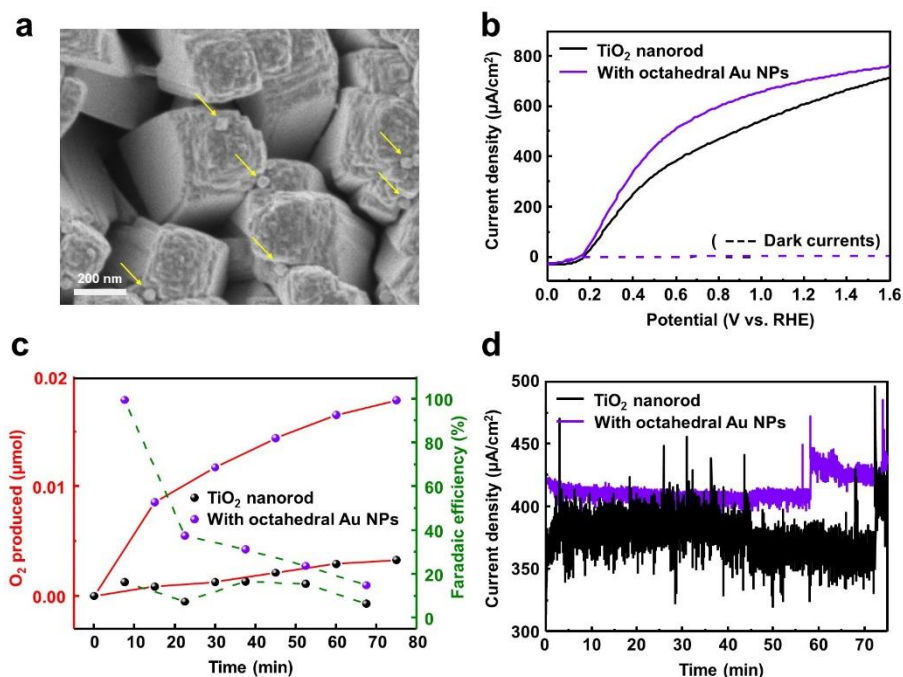


Figure 151. Gas chromatography measurements for TiO<sub>2</sub> NRs. (a) Low coverage of octahedral Au NPs on the TiO<sub>2</sub> NRs. Yellow arrow indicates octahedral Au NPs. (b) Linear sweep of corresponding samples. (c) The amount of oxygen produced and faradaic efficiencies with respect to time. (d) Photocurrent transient at 1.4 V vs. RHE in AM 1.5G illumination.

Interestingly, gas chromatography measurements that were carried out in 1.4 V vs. RHE within 75 min shows that much larger amount of O<sub>2</sub> was evolved in octahedral Au NPs decorated TiO<sub>2</sub> NRs than without decoration case (Figure 151 (c)). In addition, a Faradaic efficiency was calculated based on the photocurrent transient data in Figure 151 (d). Generally, if the metal photo-

corrosion were occurring, the hydrogen/oxygen gas evolution and should be deteriorated.<sup>100</sup> Our results with TiO<sub>2</sub> NRs did not show such a deterioration. Moreover, the shape change of octahedral Au NPs was negligible with a 3-hour irradiation with 1.4 V vs. RHE in thin film (Figure S17). It is also known that metal NPs photo-corrosion is only significant in long-term irradiation,<sup>139</sup> and our result confirms the octahedral Au NPs hardly suffer from photooxidation in this operation. This result provides the clear evidence for reaction acceleration by octahedral Au NPs and signifies the role of octahedral Au NPs as oxygen evolution catalyst.

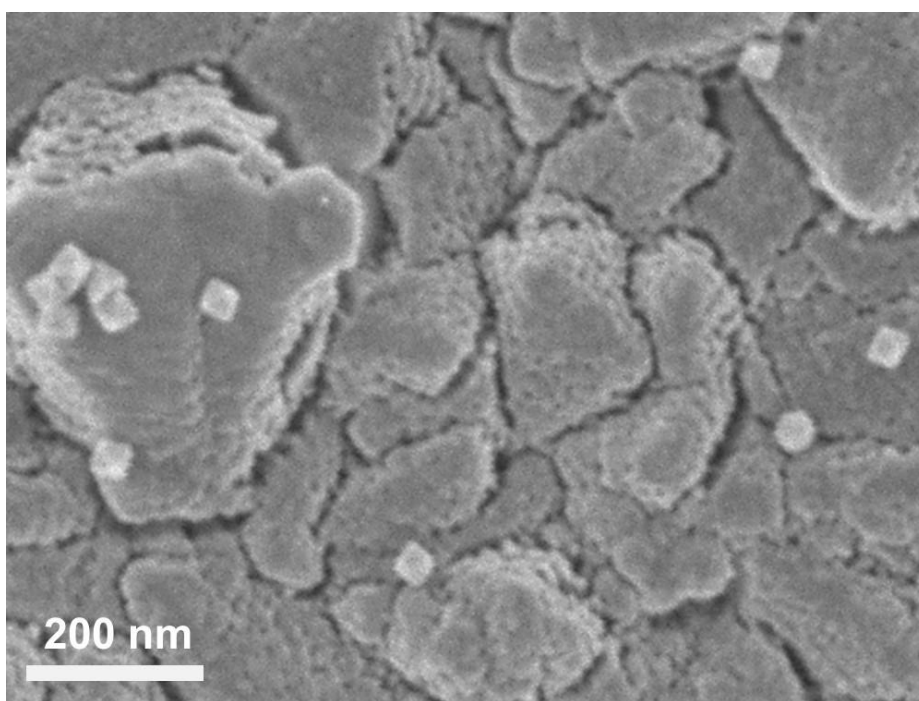


Figure 152. SEM image of octahedral Au NPs on TiO<sub>2</sub> film after 3-hour illumination (AM 1.5 G) at 1.4 V vs. RHE.

## 6.12. Conclusion

We have experimentally demonstrated that octahedral Au NPs can enhance the efficiency of plasmonic solar water splitting. Our band-transition model removes ambiguity of plasmon-mediated photocatalytic activity enhancement. For efficient plasmonic solar water splitting based on oxide semiconductors, we should consider not only LSPR induced absorption but also the hole transfer to the OER level. Au NPs having sharp vertices provide intensification of the local field, which enables forceful hole transfer to the oxygen evolution level. Even though there are lot of things to consider (crystallinity, symmetry and contact mode of Au NPs) for further improvement, the Au NPs shape containing fine or many sharp vertices (for example, Janus type nanostar<sup>140</sup>) could enhance the efficiency of plasmonic solar water splitting through the intensification of incident UV light. We believe that shape-controlled NPs will revolutionize plasmonic solar water splitting, and guarantees highly effective photoelectrode activates in the entire UV-VIS range.

## 6.13. Experimental Characterizations

FDTD simulation: The FDTD simulations were performed with a program FDTD solution (Lumerical solutions). The near field simulation was conducted with a 1.78 fs pulse length. The simulation condition was a perfectly matched layer (PML) boundary conditions. The meshing condition was set to automatic non-uniform mode, and the refinement was set to conformal variant 1. The calculation region was  $125 \times 150 \text{ nm}^2$  and the mesh size was  $0.5 \times 0.5 \text{ nm}^2$ .

Physical properties characterization: To ensure the crystalline nature of the annealed TiO<sub>2</sub> film, grazing incidence X-ray diffraction (XRD) analysis (X'pert PRO, PANalytical with Cu K $\alpha$  ( $\lambda = 1.54056 \text{ \AA}$ ) radiation) was performed. Field emission scanning electron microscopy (FE-SEM, MERLIN compact, Zeiss) and high-resolution transmission electron microscopy (TEM, JEM-2100F, JEOL) were also used. Instruments were accessed from Research Institute of Advanced Materials (RIAM, Seoul National University). Absorption spectra were recorded using a UV-vis-NIR system (Cary 500, Agilent Technologies) with a spectral range from 400 to 700 with a resolution of 1nm.

Photoelectrochemical characterization: All photoelectrochemical measurements were taken using a potentiometer (IviumStat, Ivium Technologies). Semiconductor thin film photoanodes from the E-beam evaporator, Pt wire and Ag/AgCl electrode (saturated KCl) were utilized as the working electrode, counter electrode, and reference electrode, respectively, in a three-electrode configuration. 1M NaOH solution (pH 13.6) was used as the electrolyte in the cell. The potential was converted with the Nernst equation against the reversible hydrogen electrode ( $E_{\text{RHE}} = E_{\text{Ag/AgCl}} + 0.0592 \text{ pH} + E^{\circ}_{\text{Ag/AgCl}}$  with  $E^{\circ}_{\text{Ag/AgCl}} = 0.205\text{V}$  at 25 °C). A 150 W Xenon lamp (model 10500, ABET technology) and a laser (Ozoptics; 405 nm and 532 nm) were used as light source. Photovoltage gains are calculated using a subtraction of photovoltage maximum point

with baseline at dark during the measurement time (120 s) ( $\Delta V = V_{\text{photo, max}} - V_{\text{dark, OCP}}$ ; OCP, open circuit potential) with an AM 1.5G sunlight ( $100 \text{ mW/cm}^2$ ) illumination. A monochromator (Mmac 200, Dongwoo OPTRON) from 300 to 600 nm was used in the IPCE measurement at 1.23 V vs. RHE. A 150 W xenon lamp (Model 10500, ABET Technology) was used as a light source. The light intensity was calibrated from a photodiode (Bunkokeiki). For the linear sweep measurement, a 20 mV/s scan rate was used and the range was 0 V vs. RHE to 1.6 V vs. RHE. AM 1.5G sunlight ( $100 \text{ mW/cm}^2$ ) was illuminated on the samples for the photocurrent measurements. The IPCE and Photocurrent transient were measured at 1.23 V vs. RHE potential. The Nyquist plot was recorded at the DC potential of 1.23 V vs. RHE and an AC potential frequency range of 100000 – 0.1 Hz with an amplitude of 10 mV under light irradiation. In addition, impedance fitting software (ZView, Scribner Associates) was used to analyze the experimental EIS data for the equivalent circuit model. Gas chromatography (Agilent GC 7890B) measurements are done in the closed gas system with Ar purging.

## Chapter 7

### **Dominance of Plasmonic Resonant Energy Transfer over Direct Electron Transfer in Substantially Enhanced Water Oxidation Activity of BiVO<sub>4</sub> by Shape-Controlled Au Nanoparticles**

#### Quote

**Scott C. Warren and Elijah Thimsen**

“The study of the optoelectronic effects of plasmonic metal nanoparticles on semiconductors has led to compelling evidence for plasmon-enhanced water splitting.” (2012, Energy and Environmental Science)

**Small 13**, 1701644 (2017)

**DOI:** 10.1002/sml.201701644

## 7.1. Motivation

Previous plasmon enhanced water splitting result is driven with the over-bandgap photon energy. In the condition, hot electron injection is main enhancement mechanism. If the bandgap energy straddle with the plasmon resonance frequency, another mechanism so called resonant electron transfer is possible. The previous work is restricted on the half part of plasmon-enhanced solar water splitting.

At the previous work, the versatility of photocurrent enhancement with plasmonic octahedral gold nanoparticles is investigated as shown in Figure 153.

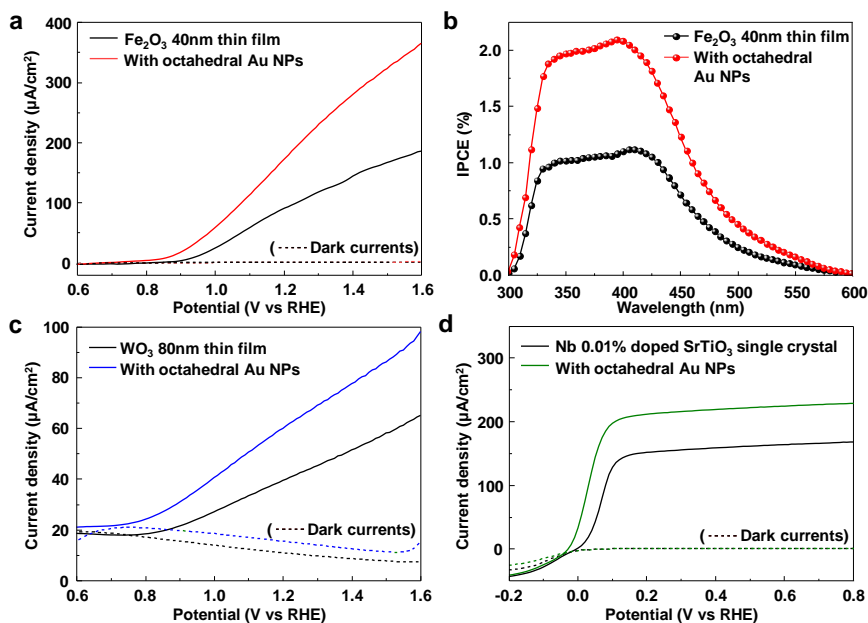
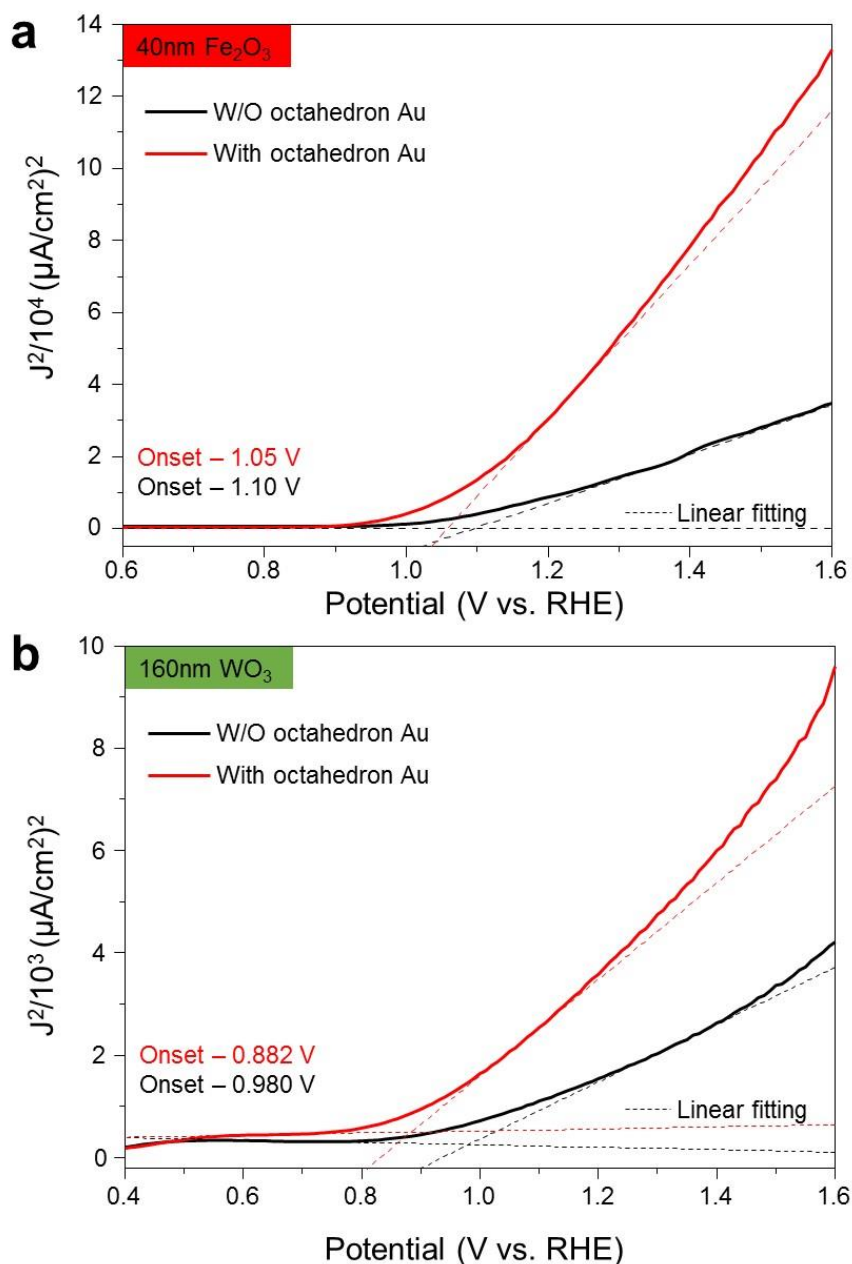


Figure 153. Photoactivity curves for other oxide n-type photoelectrode materials with or without octahedral Au NPs under 1-sun illumination. (a) For Fe<sub>2</sub>O<sub>3</sub> 40 nm. (b) Corresponding IPCE spectra for Fe<sub>2</sub>O<sub>3</sub> 40 nm with or without

octahedral Au NPs. (c) For  $\text{WO}_3$  80 nm. (d) For Nb 0.01 % doped  $\text{SrTiO}_3$  single crystal. Dashed line (- -) corresponds to dark currents.

To verify the validity and versatility of our concept, we tested whether the enhancement of photocatalytic activity using shape-controlled octahedral Au NPs is limited to the Au NPs/ $\text{TiO}_2$  system. Apart from  $\text{TiO}_2$  (3.2 eV), various representative wide bandgap photoanode materials such as hematite ( $\alpha\text{-Fe}_2\text{O}_3$ ; 2.2 eV),  $\text{WO}_3$  (2.6 eV), and  $\text{SrTiO}_3$  (3.3 eV) were decorated with octahedral Au NPs. The decoration of octahedral Au NPs on various semiconductors was achieved using the deprotonation process. Their PEC properties were examined to determine the plasmonic photocatalytic activity enhancement of the octahedral Au NPs as shown in Figure 151. For a  $\text{Fe}_2\text{O}_3$  thin film, the photocurrent increased by two times and the onset potential was cathodically shifted (Figure 151 (a)). The IPCE was doubled at over-bandgap photon energies (Figure 151 (b)). Photocatalytic activity enhancement with octahedral Au NPs was also observed with the  $\text{WO}_3$  film and with the Nb doped (0.01 %)  $\text{SrTiO}_3$  single crystal (Figure 151 (c) and (d)). The photocurrents and onset potentials for the  $\text{WO}_3$  film and  $\text{SrTiO}_3$  single crystal were similarly promoted as those in the  $\text{Fe}_2\text{O}_3$  thin film. The onset potential shifts of the three oxide semiconductors are analyzed in Figure 154. According to the Butler-Volmer model,<sup>141</sup> increase of the photocurrent with octahedral Au NPs means more photogenerated holes are approaching the interface which indicates enhanced heterogeneous reaction (water oxidation). The plateau photocurrent in  $\text{SrTiO}_3$  implies the reaction suffers mass transfer limitation in the anodic potential region due to the low carrier mobility of  $\text{SrTiO}_3$  single crystal. Overall, our

result clearly shows the decorated octahedral Au NPs mainly behaved better than as catalysts in over-bandgap photon energy of semiconductor rather than as plasmonic visible light sensitizers. This experimental versatility provides validity of photocatalytic activity enhancement by intensified LSPR-EFs.



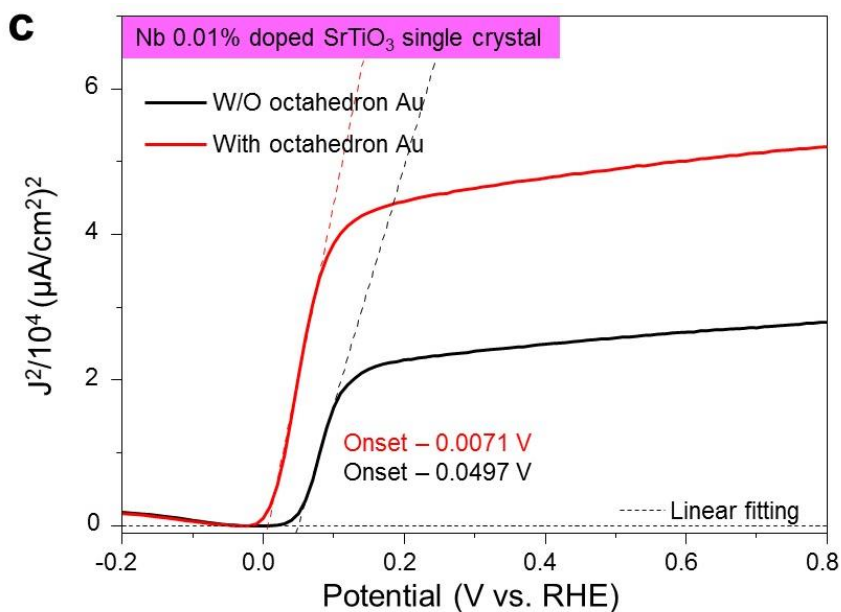


Figure 154. The shown  $J^2$ -V analysis is drawn from data from Fig. 151 to analyze onset potential. (a) For Fe<sub>2</sub>O<sub>3</sub> 40 nm thin film. (b) For WO<sub>3</sub> 80 nm thin film. (c) For Nb 0.01 % doped SrTiO<sub>3</sub> single crystal.

## 7.2. Introduction

Artificial photosynthesis, using solar energy to produce hydrogen, is a very attractive route to reduce the environmental impact of energy production and address the increasing global energy demands.<sup>142-146</sup> Hydrogen production from photoelectrochemical (PEC) water splitting is a promising pathway for solar energy conversion. Metal oxides are frequently studied as photoelectrode materials due to their advantages, such as price and stability in the solution.<sup>147-154</sup> The theoretical photocurrent is not yet explored from metal oxides due to the low solar to hydrogen conversion efficiency, although extensive researches exist. Hence, there is still large potential to develop efficient PEC materials for

solar water splitting. Desirable metal oxides should have a small bandgap to utilize a significant portion of visible light, and a valence band edge that is positive enough to drive PEC water oxidation efficiently. A promising metal oxide photoelectrode material for efficient water oxidation is bismuth vanadate ( $\text{BiVO}_4$ ), which can absorb a substantial portion of the visible spectrum due to its relatively narrow bandgap energy ( $\approx 2.4$  eV) and suitable valence band position for water oxidation.<sup>154-158</sup> Nevertheless, the photocurrent density of  $\text{BiVO}_4$  based photoanodes is considerably less than the theoretical value, since the inherent charge carrier recombination in the bulk of  $\text{BiVO}_4$  suffers from inefficient charge separation and photoexcited charge carriers with a short diffusion length.<sup>155-157</sup> In this regard, elemental doping, pairing with various oxygen evolution catalysts (OECs),<sup>154,157,159</sup> and heterojunctions,<sup>142,158,160-167</sup> have been suggested to improve the photoactivity of  $\text{BiVO}_4$ .

Plasmonic gold and silver nanostructures have attracted extensive attention in overcoming the limitations such as serious charge recombination of photoanodes,<sup>168,169</sup> due to their ability to confine light in the vicinity of their surface and strong surface plasmon resonance (SPR).<sup>88,168,170-174</sup> Especially, gold nanoparticles (Au NPs) are preferred in plasmonic solar water splitting due to their chemical stability in a harsh environment, and intensified localized surface plasmon resonance (LSPR) in the visible (vis) spectrum. Also, a Schottky junction is naturally formed as long as the noble metal and the semiconductor have different work functions and are in contact with each other. The Schottky junction may promote charge separation, enhance charge transfer, and modify the electronic band structure.<sup>175</sup> Thus, it can enhance PEC

performance of photoanode materials such as BiVO<sub>4</sub>. The LSPR in the vis spectrum enables the utilization of sub-bandgap energy which cannot be absorbed by large bandgap semiconductors. The energy contained in the oscillating electrons or local electromagnetic fields, generated by LSPR, can be transferred from the metal to semiconductor via direct electron transfer (DET) or plasmon resonant energy transfer (PRET).<sup>80,168,169,172</sup> As for the DET mechanism, the light-induced plasmon in the metal NPs produce hot electrons, which are injected into the conduction bands of the semiconductor over the metal/semiconductor barrier, contributing to the photocurrent for water splitting. In the PRET mechanism, the plasmonic metal NPs enhance the electric field intensity on the surface of the semiconductors, thereby increasing the photon absorption near the surface, in other words, they allow for the formation of electron–hole pairs in the near-surface region of the semiconductor. The surface localized enhancements in light absorption greatly increase the diffusion length of electrons or holes to the semiconductor surface, and thus improve the photoactivity of the semiconductors by minimizing electron–hole recombination.<sup>169,176</sup>

The significance of optimized geometric factors such as size, shape, and composition of Au NPs for plasmonic solar water splitting has been experimentally confirmed in photoanodes with wide bandgap.<sup>173,177,178</sup> Several recent studies about BiVO<sub>4</sub> with plasmonic Au NPs have been reported recently. BiVO<sub>4</sub> films with Au NPs of diameters changing from 10 to 80 nm showed the size effect of Au NPs on photocurrent density. Maximum PEC enhancement was found for plasmonic Au NPs with a diameter of 30 nm due

to the pronounced overlap of the LSPR resonance spectrum with the interband excitation spectrum in BiVO<sub>4</sub>.<sup>168,173,179</sup>[28, 34, 40] Controlling the size of Au NPs is recognized to be essential for efficient hot electron injection via interband excitation in plasmonic Au NPs, and plays a critical role in decreasing the overpotential of BiVO<sub>4</sub> films.<sup>83,173</sup> Although the shape of Au NPs affects LSPR electric fields (LSPR-EFs) and has a decisive effect on charge injection and transfer, the shape effect of Au NPs on BiVO<sub>4</sub> was not reported yet. Also, there is no in-depth study to bring out the underlined mechanism of the improvement to PEC properties of BiVO<sub>4</sub> by shape-controlled plasmonic Au NPs.

Herein, we report the shape-controlled Au NPs with optimum coverage that greatly promote the photoactivity of BiVO<sub>4</sub> (photocurrent and incident photon-to-current efficiency (IPCE)) in over-bandgap photon energy, rather than sub-bandgap photon energy. Well-defined octahedral Au NPs significantly increase the photocurrent of BiVO<sub>4</sub>, while hemispherical Au NPs degrade it, since largely enhanced LSPR-EFs are only observed with the shape-controlled octahedral Au NPs. Finite-domain time-difference (FDTD) simulation also validates intensified LSPR-EFs in the entire UV–vis region from the octahedral Au NPs compared to hemispherical Au NPs, indicating that the control of the shape of plasmonic Au NPs is the key to achieving high PEC efficiency. Interestingly, the value of IPCE unconventionally improved at 430 nm unlike wide bandgap semiconductors such as TiO<sub>2</sub> that can be understood by the presence of PRET over DET. The unconventionally promoted PEC performance of octahedral Au NPs/BiVO<sub>4</sub> film is attributed to the synergetic

effect of the similar light absorption bands of BiVO<sub>4</sub> and the shape-controlled Au NPs. It is strongly believed that the surface decoration of Au NPs on BiVO<sub>4</sub> films largely suppresses the photogenerated electron–hole recombination near the solid/electrolyte interface. These results highlight the critical importance of shape-controlled plasmonic Au NPs in enhancing PEC properties of moderate bandgap semiconductors with severe charge recombination.

SPR is an intrinsic property of Au NPs, in which the oscillation frequency is highly sensitive to size and shape of the metal.<sup>80,177,180</sup> Previous studies have been primarily focused on the enhancement of the photoactivity of plasmonic Au NPs/BiVO<sub>4</sub> according to the change of the size, and composition of Au NPs, while the photoactivity enhancement induced by morphological shape-controlled Au NPs was not fully demonstrated. To quantify the shape effect including the electric field amplification upon SPR, and the photoactivity enhancement of Au NPs, we choose two different shapes of Au NPs such as octahedral and hemispherical with similar diameter around 20–30 nm. The LSPR peak position and linewidth is highly dependent on their size and shape.<sup>53</sup> The plasmonic resonance peak positions of octahedral Au NPs lie around 550 nm, as shown in Figure 155. Moreover, the plasmonic resonance peak position of hemispherical Au NPs is expected to lie around 520–540 nm,<sup>168</sup> which we cannot measure because they should be constrained on the substrate due to the deposition method. The discrepancy of peak positions is less than 30 nm. Hemispherical Au NPs deposited from e-beam evaporator are formed randomly, while octahedral Au NPs with sharp vertices having equilibrium shape of face-centered cubic are primarily synthesized by seed-growth method. The most

stable shape of Au NPs with sharp edges that can be composed of (111) plane is octahedron.<sup>125</sup> It was reported that octahedral Au NPs have higher enhancement in LSPR electric fields than other shapes.<sup>176</sup>

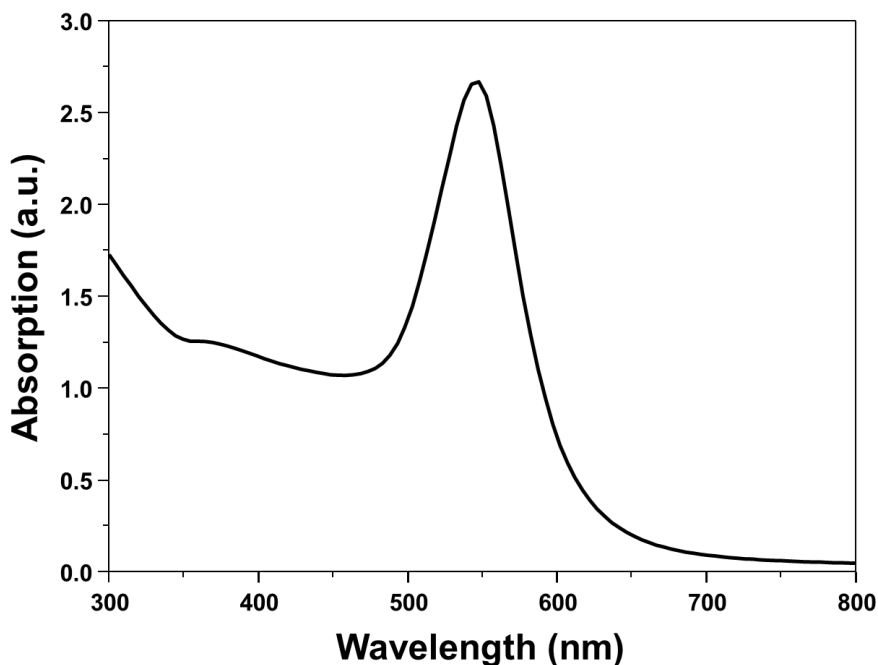


Figure 155. The absorption spectrum of octahedral Au NPs.

### 7.3. Near-Field Enhancements

We performed FDTD simulation to calculate the spatial distribution of electric field intensity near the interface of Au NPs/BiVO<sub>4</sub> as a function of the incident light wavelength. Figure 156 (a) and (b), Figures 157., and Figure 158 shows the model for FDTD simulation, which contains hemispherical and octahedral Au NP domain with a diameter of 25 nm and edge length of 30 nm, respectively. The FDTD results demonstrate the high LSPR-EFs in the entire region of UV–vis by attachment of the octahedral Au NPs on BiVO<sub>4</sub> film. The fields at the Au/BiVO<sub>4</sub> interface is significantly increased with shape-controlled Au NPs.

Such a near-field enhancement is highly interconnected with PRET.<sup>80</sup> LSPR-EFs in the Au NPs propagate into BiVO<sub>4</sub> near the interface. Such resonance suggests that certain amount of dipoles can be induced in BiVO<sub>4</sub> as consequence of strong dipole–dipole interactions at the interface. The phenomenological plasmonic model expected that charge separation in semiconductor is more pronounced with intensified near-electric fields induced by plasmonic NPs.<sup>32</sup> Overall, these simulation results indicate that charge separation in BiVO<sub>4</sub> can be vividly enhanced by the octahedral Au NPs. We selected the position of octahedral Au NPs on BiVO<sub>4</sub> film with the highest electric field among various configurations of octahedral Au NPs; and then compared the hemispherical and octahedral Au NPs at incident wavelengths of 550, 430, and 350 nm. Figure 154 (c) and (d) shows that higher LSPR-EFs were obtained with the octahedral Au NPs than with the hemispherical Au NPs at an incident wavelength of 550 nm. Octahedral Au NPs in a vertical vertices configuration on BiVO<sub>4</sub> yielded a maximum electric field enhancement ( $|E/E_0|$ ) of 20.53, which is  $\approx 5.78$  times higher than that of hemispherical Au NPs. Figure 154 (e) and (h) shows that the LSPR-EF intensity according to the Au NP shapes (hemispherical, octahedral) at incident wavelengths of 430 and 350 nm displayed the same tendency as an incident wavelength of 550 nm. Table 3 shows that the highest electric field enhancement of octahedral Au NPs with the vertical configuration at incident wavelengths of 430 and 350 nm emerged as 2.87 and 2.55, which are 1.46 and 1.49 times larger than those of the hemispherical Au NPs, respectively. The FDTD results demonstrate the high LSPR-EFs in the entire region of UV–vis by attachment of the octahedral Au

NPs on BiVO<sub>4</sub> film. Two different Au NP shapes (hemispherical and octahedral) have been applied to prove the role of shape control of Au NPs for enhancing water-splitting efficiency. The octahedral Au NPs can provide the highest intensified LSPR-EFs compared to the hemispherical Au NPs, since they have sharp vertices and well-defined edges.<sup>80,125,177,180</sup>

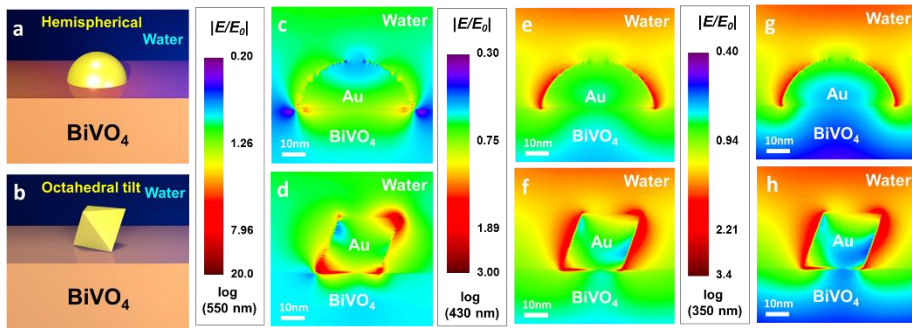


Figure 156. Schematic representation of Au Nanoparticle Finite-difference time-domain (FDTD) configurations on BiVO<sub>4</sub> film. (a) Hemispherical Au nanoparticle. (b) Octahedral Au nanoparticle. FDTD simulation results of near field enhancement for hemispherical and octahedral Au NPs on the flat BiVO<sub>4</sub> film in water. (c) Field enhancement for hemispherical Au NPs under 550 nm photons. (d) Field enhancement for octahedral Au NPs under 550 nm photons. (e) Field enhancement for hemispherical Au NPs under 430 nm photons. (f) Field enhancement for octahedron Au NPs under 430 nm photons. (g) Field enhancement for hemispherical Au NPs under 350 nm photons. (h) Field enhancement for octahedral Au NPs under 350 nm photons.

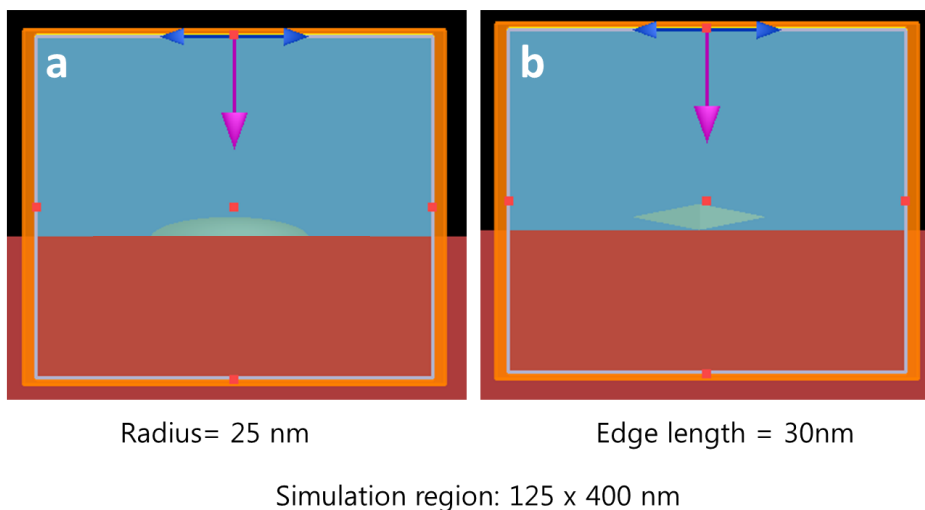


Figure 157. Model used in finite-difference time-domain (FDTD) for the simulation. (a) Hemispherical Au NPs. (b) Octahedral Au NPs

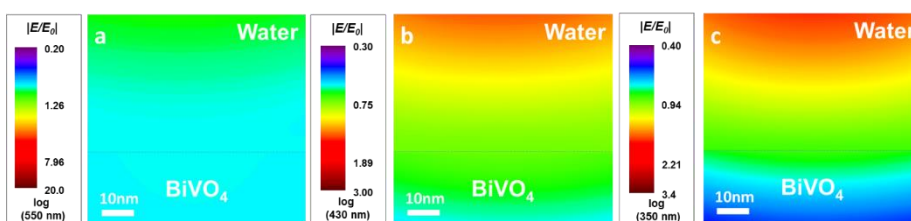


Figure 158. FDTD simulation results of near field enhancement for flat BiVO<sub>4</sub> film in water. (a) Field distribution of BiVO<sub>4</sub> under 550 nm photons. (b) Field distribution of BiVO<sub>4</sub> under 430 nm photons. (c) Field distribution of BiVO<sub>4</sub> under 530 nm photons.

Table 3. Field enhancement of hemispherical Au NPs and octahedral Au NPs under 350 nm, 430 nm and 550 nm.

Field enhancement (max)	Hemisphere Au NPs	Octahedral Au NPs

<b>350 nm</b>	1.97	2.87
<b>430 nm</b>	1.71	2.55
<b>550 nm</b>	3.55	20.53

## 7.4. Gold Nanoparticle Decorated BiVO<sub>4</sub> Films

Figure 159 (a)-(f), Figure 158 and Figure 159 show that hemispherical and octahedral Au NPs are well formed using e-beam evaporation deposition and seed-mediated growth methods, respectively.<sup>32,125</sup> BiVO<sub>4</sub> film with thickness about 200 nm was synthesized by pulsed electrodeposition, which enables the formation of more uniform films than continuous electrodeposition since the pulse-off time ( $t_{\text{off}}$ ) allows the diffusion of ions from the solution to the surface of the working electrode, thus lowering the concentration gradient during the next pulse-on time ( $t_{\text{on}}$ ).<sup>181,182</sup> Figure 160 shows the X-ray diffraction (XRD) data, which indicate that the BiVO<sub>4</sub> films consist of a monoclinic phase. Figure 158 indicates that the octahedral Au NPs synthesized from cetyltrimethylammonium bromide/chloride stabilization are highly monodispersed. The attachment of octahedral Au NP process was inspired by recent paper.<sup>183</sup> pH of the citric acid solution was a critical factor to control the surface adsorption to TiO<sub>2</sub>. We used mercaptopropionic acid (MPA) molecule which has thiol and carboxylic acid group to provide the specific adsorption to Au (thiol group) and control the adsorption to TiO<sub>2</sub> (carboxylic acid group).<sup>184</sup> Due to the low pH of the Au NP solution from the HAuCl<sub>4</sub> precursor, we expected that MPA molecule is easily adsorbed onto the BiVO<sub>4</sub> by making surface bonding from oxygen (-O-). To prevent agglomeration, due to the

lowering of zeta potential from MPA adsorption to Au NPs surface, intermediate condition of MPA concentration between stabilization and agglomeration was used to attach Au NPs homogeneously. And average size of octahedral Au NPs is about 30 nm. The size is a very appropriate size for plasmon resonance, since it is well known that the Au NPs within 20–50 nm enhanced the LSPR property.<sup>80,83,168,173,177</sup> Figure 159 (b) and (c) shows high resolution transmission electron microscopy images and X-ray diffraction patterns of octahedral Au NPs, which consist of the lowest energy facets of planes. The cross-sectional transmission electron microscopy (TEM) image in Figure 159 (d) indicates that octahedral Au NPs are well positioned on the BiVO<sub>4</sub> films. Figure 159 (e) and (f) shows that most of Au NPs locate on the top surface of BiVO<sub>4</sub> film, and Au NPs are homogeneously distributed across the BiVO<sub>4</sub> films, which is confirmed by the field emission scanning electron microscopy. Figure 159 (g) shows photographs of FTO, BiVO<sub>4</sub> film, octahedral Au NPs/BiVO<sub>4</sub>, and hemispherical Au NPs/BiVO<sub>4</sub>. After attaching octahedral Au NPs, the color of BiVO<sub>4</sub> is little changed, however the color of hemispherical attached BiVO<sub>4</sub> is changed to green. The active area of octahedral Au NPs/BiVO<sub>4</sub> to measure PEC properties is shown in Figure 159 (h).

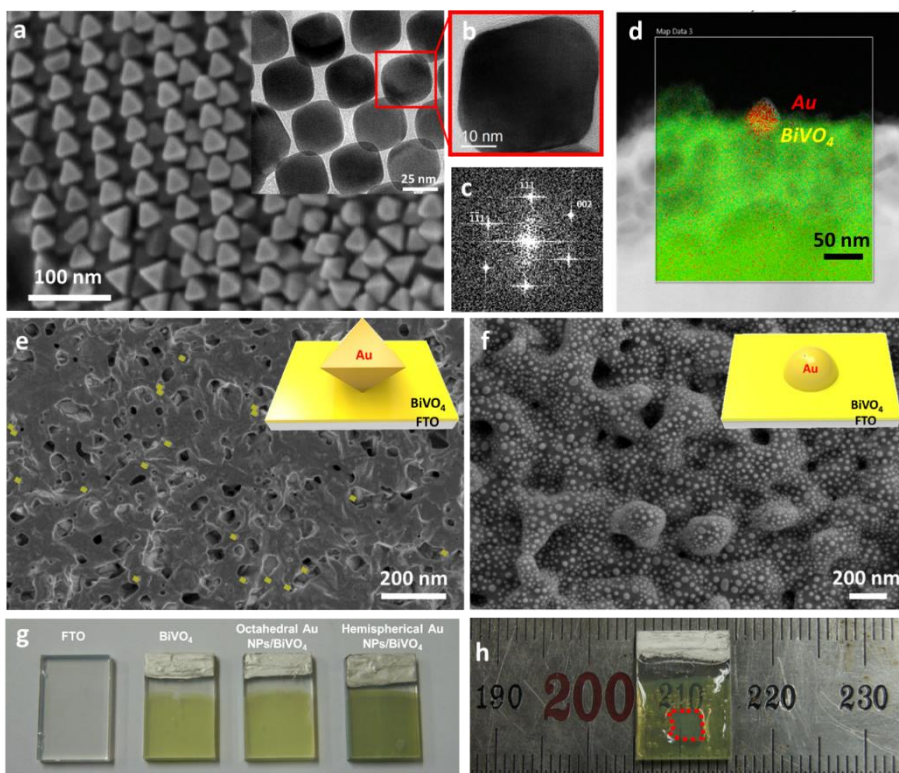


Figure 159. (a) SEM and TEM (inset) images of octahedral Au NPs. (b) Enlarged TEM images of octahedral Au NPs. (c) Fast Fourier transform (FFT) pattern of octahedral Au NP. (d) Cross sectional EDS image of the octahedral Au NPs attached to BiVO<sub>4</sub> film. (e) False-colour scanning electron microscopy (SEM) image of octahedral Au NPs attached to BiVO<sub>4</sub> films with optimum coverage. (f) SEM image of the hemispherical Au NPs from E-beam evaporator (1.5 nm) attached to BiVO<sub>4</sub> film. (g) Photographic images of FTO, BiVO<sub>4</sub>,

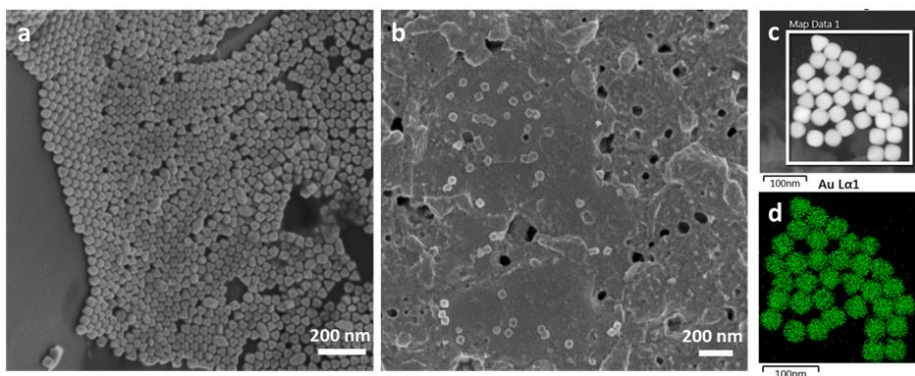


Figure 160. (a) SEM image of octahedral Au NPs. (b) SEM image of octahedral Au NPs attached to BiVO<sub>4</sub> with optimum coverage. (c),(d) EDS images of octahedral Au NPs.

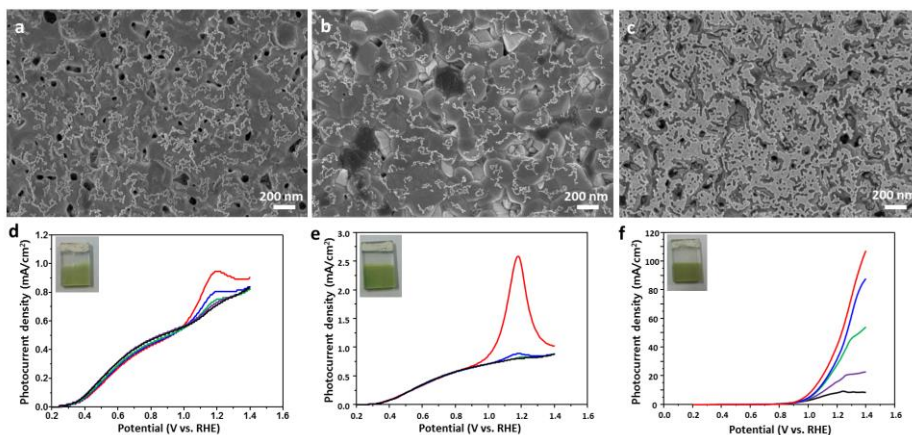


Figure 161. SEM image of the hemispherical Au NPs from E-beam evaporator attached to BiVO<sub>4</sub> film. (a) 0.7 nm, (b) 1.5 nm and (c) 5 nm thickness. Photocurrent density of hemispherical Au NPs/BiVO<sub>4</sub> with (d) 0.7nm, (e) 1.5 nm and (f) 5 nm.

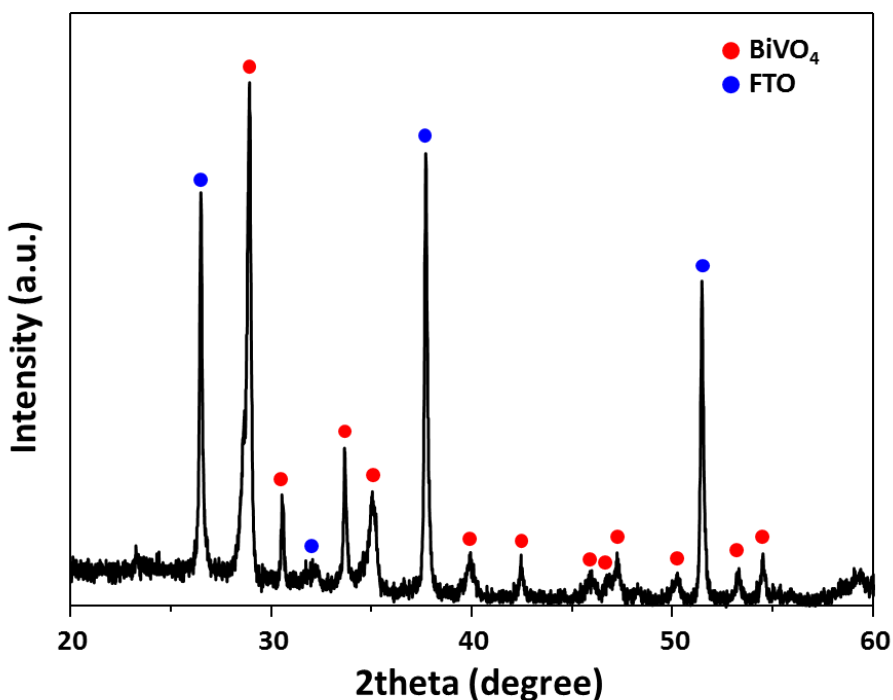


Figure 162. X-ray diffraction (XRD) pattern of BiVO<sub>4</sub> film.

## 7.5. Photocurrent Action Spectra

We compared the photocurrent densities of octahedral and hemispherical Au NP/BiVO<sub>4</sub> systems, as displayed in Figure 163. We changed the coverage of the Au NPs to find the optimum coverage for each NPs. The photocurrent density with the octahedral Au NPs/BiVO<sub>4</sub> is significantly enhanced about threefold at the 1.23 V versus reversible hydrogen electrode (RHE). However, the photoactivity of hemispherical Au NPs/BiVO<sub>4</sub> is slightly decreased, compared to the BiVO<sub>4</sub> films. Our results indicate that if the shape of Au NPs is not controlled, it is hard to observe the PEC enhancement of BiVO<sub>4</sub> anode. Although LSPR-EF enhancement is observed in presence of the hemispherical and octahedral Au NPs, the octahedral Au NPs can provide intensified LSPR-EFs compared with the hemispherical Au NPs due to their sharp vertices and

well-defined edges.<sup>176</sup> Also, the reduced enhancement with hemispherical Au NPs is the reduction of exposed area of BiVO<sub>4</sub> to electrolyte, which can influence the water oxidation efficiency on the BiVO<sub>4</sub> surface. Therefore, less exposed surface of BiVO<sub>4</sub> due to the increased coverage with hemispherical Au NPs can be another reason for the decreased photocurrent. Figure 160 shows the relation between the coverage of the hemispherical Au NPs and photocurrent density, we adjusted the amount of the hemispherical Au NPs by controlling the deposition time of e-beam evaporation. In all cases, the photocurrent density of hemispherical Au NPs attached on BiVO<sub>4</sub> film has rapidly decreased, and that of the finally measured value has recorded the lower photocurrent than the BiVO<sub>4</sub> film. The peak at 1.2–1.3 V versus RHE, as shown in Figure 161 indicates the oxidation of Au NPs. We also confirmed that the morphology of octahedral Au NPs did not change after PEC measurement, as displayed in Figure 164. The tendency of photocurrent density is well matched with the FDTD simulation results. From these results, it is clear that the octahedral Au NPs with sharp vertices show remarkably higher enhancement in the photocurrent density than the hemispherical Au NPs with relatively smooth surface. Plasmonic NPs with sharp vertices facilitate charge separation in the semiconductor more easily via reducing the restoring force for electron oscillation than NPs of rounded structure during coherent electron oscillation,<sup>176,185</sup> which could be expected from the FDTD simulation results. Therefore, the enhancement of photocatalytic activity with the over-bandgap photon energy gives a clear clue that the shape-controlled octahedral Au NPs behave as an OEC.

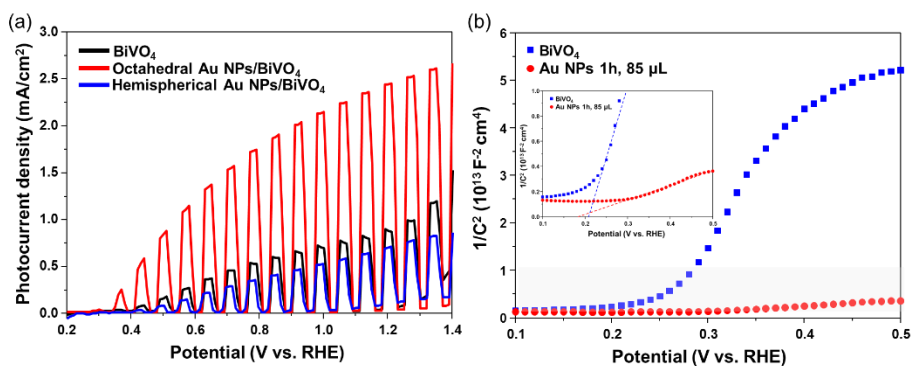


Figure 163. (a) Linear sweep voltammograms for BiVO<sub>4</sub> film, hemispherical Au NPs/BiVO<sub>4</sub> and octahedral Au NPs/BiVO<sub>4</sub> photoelectrodes measured in 0.5 M phosphate buffer with 1 M Na<sub>2</sub>SO<sub>3</sub> at a scan rate of 10mV/s under 1.5 G solar light under the chopped light condition. (b) Mott-Schottky plot of bare BiVO<sub>4</sub> and octahedral Au NPs/BiVO<sub>4</sub> photoelectrode measured under light off. The inset is enlarged Mott-Schottky plot of bare BiVO<sub>4</sub> and octahedral Au NPs/BiVO<sub>4</sub> in the grey region. \* Frequency: 1 kHz, Amplitude : 10 mV.

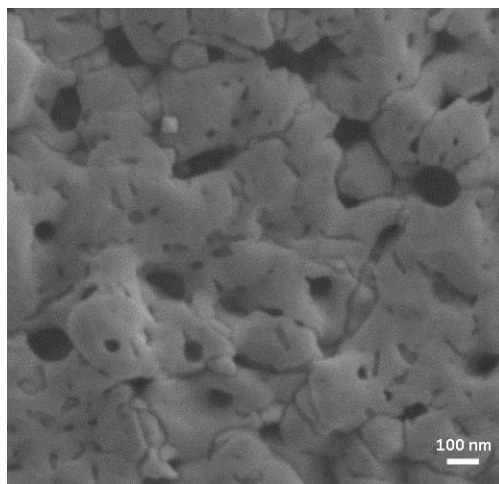


Figure 164. SEM image of octahedral Au NPs/BiVO<sub>4</sub> photoelectrode after photoelectrochemical measurement.

Figure 163 (b) shows that we also measured the donor concentration, capacitance of the double layer, and flat band potential of the octahedral Au NP/BiVO<sub>4</sub> and BiVO<sub>4</sub> film using the Mott–Schottky relation. The carrier concentration can be calculated by the slope of the Mott–Schottky curves. The lower the slope of a Mott–Schottky plot, the higher the carrier concentration. The carrier concentration significantly increased after attachment of octahedral Au NPs. And the general increment of  $C$  indicated that the double layer formed on the surface has a large capacitance.<sup>100</sup> The observed result (for  $1/C^2$  value, BiVO<sub>4</sub> > octahedral Au NPs/BiVO<sub>4</sub>) was measured at the same frequency of 1 kHz, which means that octahedral Au NP attached BiVO<sub>4</sub> has more charge carriers than that of BiVO<sub>4</sub> film. The flat band potential ( $E_{fb}$ ) of BiVO<sub>4</sub> film is determined to be about 0.21 V versus RHE. After attaching of octahedral Au NPs, the  $E_{fb}$  shifts negatively by 30 mV, which is favorable for the electrons to pass through the circuit to the counter electrode. This is also a possible reason for the cathodic shift of the onset potential of photocurrent.

## **7.6. Coverage Control of Octahedral Gold Nanoparticles in BiVO<sub>4</sub>/FTO film.**

To compare the plasmonic effect of octahedral Au NP/BiVO<sub>4</sub> films according to various coverages of octahedral Au NPs, we controlled the amount of MPA precipitation solution and dipping time to attach octahedral Au NPs on the BiVO<sub>4</sub> films. Figure 165 shows scanning electron microscopy (SEM) images of octahedral Au NPs/BiVO<sub>4</sub> by changing the dipping time from 0 to 6 h, and fixing the amount of MPA solution at 85  $\mu$ L. When the coating time of Au

precursor is over 1 h, small quantities of Au NPs aggregate into clusters; in particular, an excessive agglomeration is shown for a dipping time of 6 h.

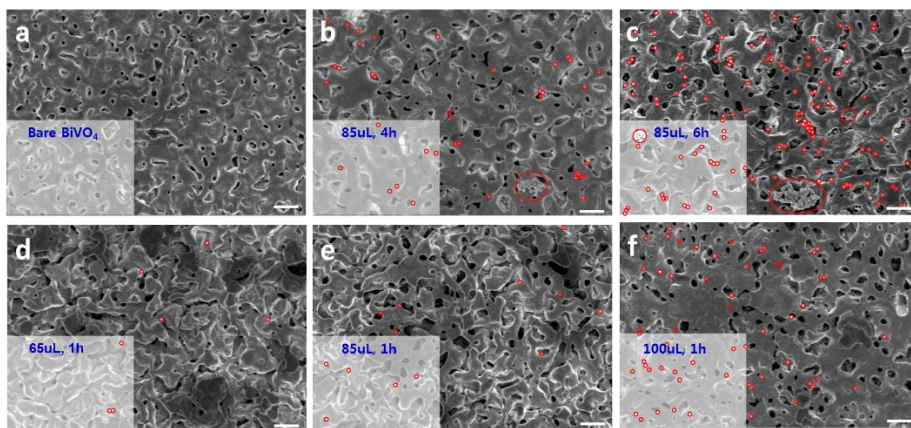


Figure 165. (a)-(c) SEM images of the octahedral Au NPs changing coverage according to dipping time, 0h, 4h and 6h, respectively. (d)-(f) SEM images of the octahedral Au NPs changing coverage according to amount of the MPA precipitation solution. Scale bar is 200 nm.

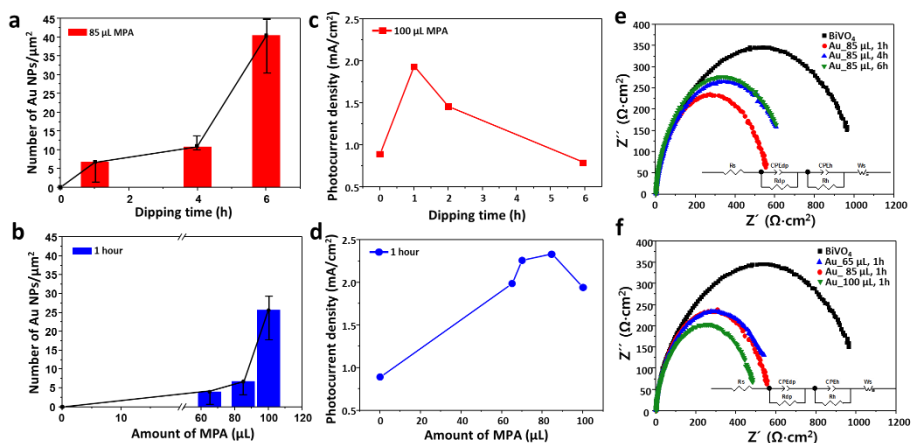


Figure 166. (a) Number of octahedral Au NPs in the selected area (grey region, shown in the Supplementary figure S8. (a)-(c) (see Fig. S8, ESI†)) according to the dipping time. (b) Number of octahedral Au NPs in the selected area (grey

region, shown in the Figure 166. (d)-(f) according to amount of the MPA precipitation solution. (c), (d) Photocurrent density of Au NPs/BiVO<sub>4</sub> photoelectrodes controlled the dipping time and amount of the MPA precipitation solution at 1.23 V vs. RHE, respectively. (e), (f) Electrochemical impedance spectra (EIS) for various Au NPs/BiVO<sub>4</sub> photoelectrodes. The solid line was fitted by the ZSimpWin software using the proposed equivalent circuit model. The EIS was measured at 1.23 V vs. RHE under simulated solar illumination in 0.5 M phosphate buffer with 1 M Na<sub>2</sub>SO<sub>3</sub>. Inset shows equivalent circuits for various Au NPs/BiVO<sub>4</sub> photoelectrodes.

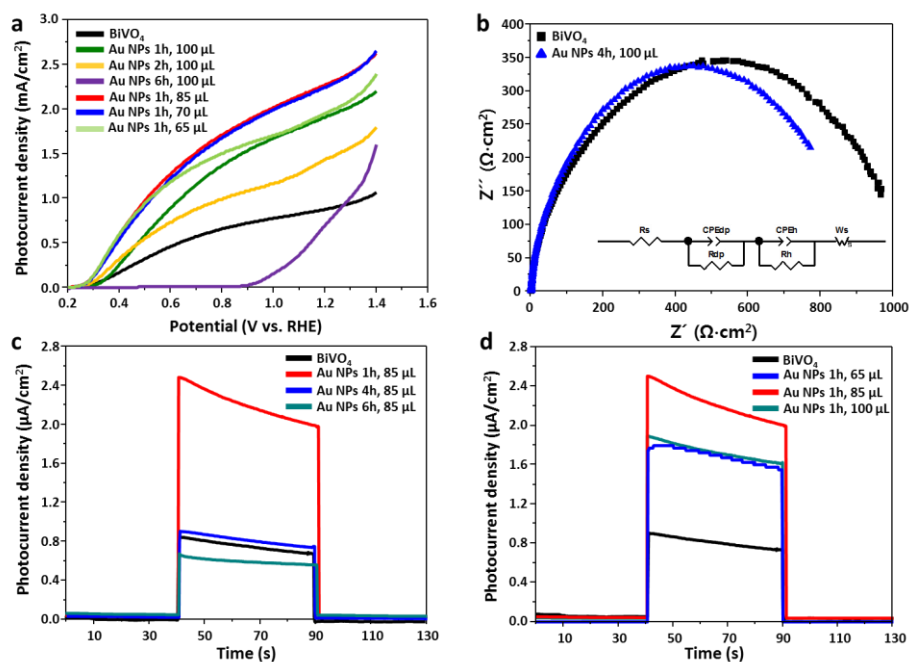


Figure 167. Figure S9. (a) Linear sweep voltammograms (LSVs) data of octahedral Au NPs/BiVO<sub>4</sub> photoelectrodes with different dipping time and amount of MPA solution. (b) Electrochemical impedance spectra (EIS) for comparing BiVO<sub>4</sub> film and Au NPs/BiVO<sub>4</sub> photoelectrode with extreme

conditions. The solid line was fitted by the ZSimpWin software using the proposed equivalent circuit model. The inset shows equivalent circuits for various Au NPs/BiVO<sub>4</sub> photoelectrodes. (c) Amperometric current density-time profiles for BiVO<sub>4</sub> film and octahedral Au NPs/BiVO<sub>4</sub> photoelectrodes according to change of the dipping time. (d) Amperometric current density-time profiles for bare BiVO<sub>4</sub> and octahedral Au NPs/BiVO<sub>4</sub> photoelectrodes according to change of the amount of the MPA solution. The EIS and J-t curves were measured at 0.63 V (vs. Ag/AgCl) under simulated solar illumination in 0.5 M phosphate buffer with 1 M Na<sub>2</sub>SO<sub>3</sub>.

Figure 166 (a) shows the change of numbers of octahedral Au NPs in the specific area of BiVO<sub>4</sub> films according to dipping time. We measured the PEC properties of Au NP/BiVO<sub>4</sub> anodes with different coverage of octahedral Au NPs. The increased coverage of Au NPs boosts light absorption and charge transfer, and thus improves the photocurrent. However, when dipping time is more than 1 h, the photocurrent density of octahedral Au NPs/BiVO<sub>4</sub> decreases gradually with the increase in dipping time. Figure 166 (b) and Figure 167 (a) show that the photocurrent density of octahedral Au NPs/BiVO<sub>4</sub> having a dipping time of 6 h recorded a lower value than that of BiVO<sub>4</sub> films. Also, the onset potential of Au NPs with a dipping time of 6 h is positively shifted compared to BiVO<sub>4</sub> films. The interspacing of plasmonic Au NPs is an important parameter to affect photoactivities of Au NPs. The moderate distance between Au NPs is needed since the spacing of Au NPs exceeds beyond a certain distance, diminishing of the near-field plasmon coupling between two Au NPs occurs. A strong dependence of the PRET on the diameter of the Au

NPs and reduction in the spectral overlap between the  $\text{BiVO}_4$  light absorption band and the redshifting plasmonic absorption of Au NPs with increasing size is revealed, which hampers the effectivity of PRET.<sup>169</sup> Also, the plasmonic absorption shorter than the  $\text{BiVO}_4$  absorption edge about 510 nm can enhance the photoactivities through PRET. Therefore, a further increase in the coverage reduced the effect of PRET.<sup>169</sup> Figure 167 (a) and Figure 168, on the other hand, show that the octahedral Au NPs/ $\text{BiVO}_4$  with optimum coverage revealed negatively shifted onset potential. This result confirms that the attachment of Au NPs with proper coverage leads to the catalytic enhancement (reduction of overpotential), since an electrochemical cocatalyst could significantly facilitate the transfer of photogenerated holes from the semiconductors to water at a lower bias.

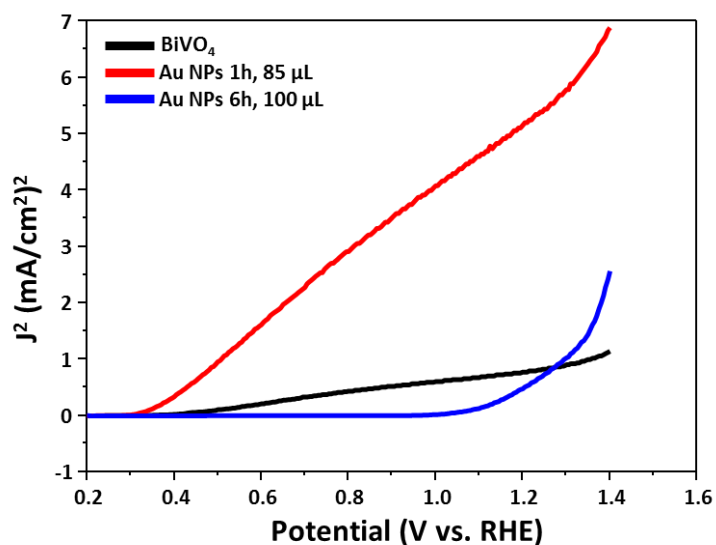


Figure 168. The shown  $J^2$ -V analysis is drawn from data from Fig. 165 to analyze onset potential.

The amount of MPA solution to attach the octahedral Au NPs on the BiVO<sub>4</sub> films was changed from 0 to 100 μL. Figure 166 (b) and Figure 165 (a), (d), (e), (f) show the change of the number of particles, unlike controlling the dipping time, agglomeration was not observed on the BiVO<sub>4</sub> films. The amount of MPA precipitation solution is closely related to PEC properties of octahedral Au NPs/BiVO<sub>4</sub>. Figure 166 (d) shows the photocurrent behaviour of the octahedral Au NPs/BiVO<sub>4</sub> at 1.23 V versus RHE. The photoactivity of the octahedral Au NPs/BiVO<sub>4</sub> increases gradually until the amount of MPA solution increases to 85 μL, but a further increase in the amount of MPA precipitation solution resulted in degradation of the photocurrent density. This photocurrent degradation could be due to two possible reasons. First, the large number of Au NPs grown at the increasing dipping time and amounts of MPA solution may cover a large portion of the BiVO<sub>4</sub> surface, which retard the access of light to the BiVO<sub>4</sub> surface to reduce the photocurrent generation. Second, the high coverage of the Au NPs may reduce the surface area of BiVO<sub>4</sub> films in direct contact with the electrolyte and thereby hinders the water oxidation performance.<sup>172,180</sup> Figure 167 (c) and (d) shows the amperometric photocurrent versus time (*t*) curves under a bias voltage of 1.23 V versus RHE. In all cases, we observed a photocurrent spike upon initial illumination, which relaxed to a steady state, indicating the stability of the octahedral Au NPs/BiVO<sub>4</sub>. The highest photocurrent of 2.4 mA cm<sup>-2</sup> was obtained at 1.23 V versus RHE for octahedral Au NPs/BiVO<sub>4</sub> synthesized by an MPA precipitation solution of 85 μL and dipping time of 1 h. From these results, we believe that the amounts of the attached Au NPs must be properly controlled,

since a high coverage of Au NPs on the semiconductor will reduce the light exposure of the semiconductor, as well as hinder the reactant access of the semiconductor, while low coverage will lead to poor light utilization efficiency during photocatalysis.<sup>177</sup> We emphasize that the photocurrent of our octahedral Au NPs attached on BiVO<sub>4</sub> films is the highest for previously reported plasmonic Au NP/BiVO<sub>4</sub> photoanodes without additional treatment such as nanostructuring, heterojunction, or doping measured with hole scavenger for solar water splitting.<sup>100,168,173,174,179</sup>

To understand the effect of the coverage of the octahedral Au NPs on BiVO<sub>4</sub>, electrochemical impedance spectroscopy (EIS) was also conducted to evaluate the kinetics of charge generation and transfer during oxygen evolution reaction (OER) reaction. The impedance spectra of octahedral Au NPs/BiVO<sub>4</sub> was measured by applying 1.23 V versus RHE under simulated solar light illumination, and is presented as a Nyquist diagram in the frequency range 100 kHz–100 mHz. The high photoactivity is reflected by a small semicircle in the Nyquist plots. For the better fitting of the Nyquist plot, Warburg impedance ( $W_h$ ) is included in the circuit elements. Figure 166 (e) and (f) and Table 4. show that the largest  $R_{dp}$  (resistivity in the depletion region) and  $R_h$  (resistivity in the Helmholtz region) for BiVO<sub>4</sub> film indicate that the charge transfer characteristics of BiVO<sub>4</sub> are very poor; on the other hand, all cases of the octahedral Au NPs attached on BiVO<sub>4</sub> film show a good charge transfer efficiency, exhibiting a low  $R_{dp}$  and  $R_h$ . The capacitance at the interface (constant phase element ( $CPE_{dp}$ ,  $CPE_h$ )) with optimum coverage of octahedral Au NPs on BiVO<sub>4</sub> is maximized. Among them, octahedral Au NPs having the

attachment condition of MPA precipitation solution of 85  $\mu\text{L}$  and dipping time of 1 h recorded the lowest value of the diameter of the semicircle and the highest value of CPE. This result shows enhanced charge generation and transfer from shape-controlled octahedral Au NPs with moderate coverage on  $\text{BiVO}_4$  surface.

Table 4. Circuit analysis of the EIS spectra for various octahedral Au NPs/ $\text{BiVO}_4$  photoelectrodes.

$(R/\Omega\cdot\text{cm}^2)$ $(\text{CPE}/10^{-8} \text{ F})$	$R_s$	$R_{dp}$ (semi)	$\text{CPE}_{dp}$ (semi)	$R_h$ (interface)	$\text{CPE}_h$ (interface)
$\text{BiVO}_4$	1.68	196.18	0.99	768.84	3.73
AuNPs/ $\text{BiVO}_4$ (65 $\mu\text{L}$ , 1h)	1.12	75.97	4.37	447.18	3.78
AuNPs/ $\text{BiVO}_4$ (85 $\mu\text{L}$ , 1h)	1.72	64.54	12.45	486.21	10.10
AuNPs/ $\text{BiVO}_4$ (100 $\mu\text{L}$ , 1h)	1.73	110.47	3.99	591.71	5.78
AuNPs/ $\text{BiVO}_4$ (85 $\mu\text{L}$ , 4h)	1.61	69.52	12.12	558.01	7.54
AuNPs/ $\text{BiVO}_4$	1.47	79.92	5.65	526.27	3.50

(85 $\mu$ L, 6h)					
AuNPs/BiVO <sub>4</sub>	1.78	154.93	5.59	676.84	8.53
(100 $\mu$ L, 4h)					

## 7.7. Stability Test

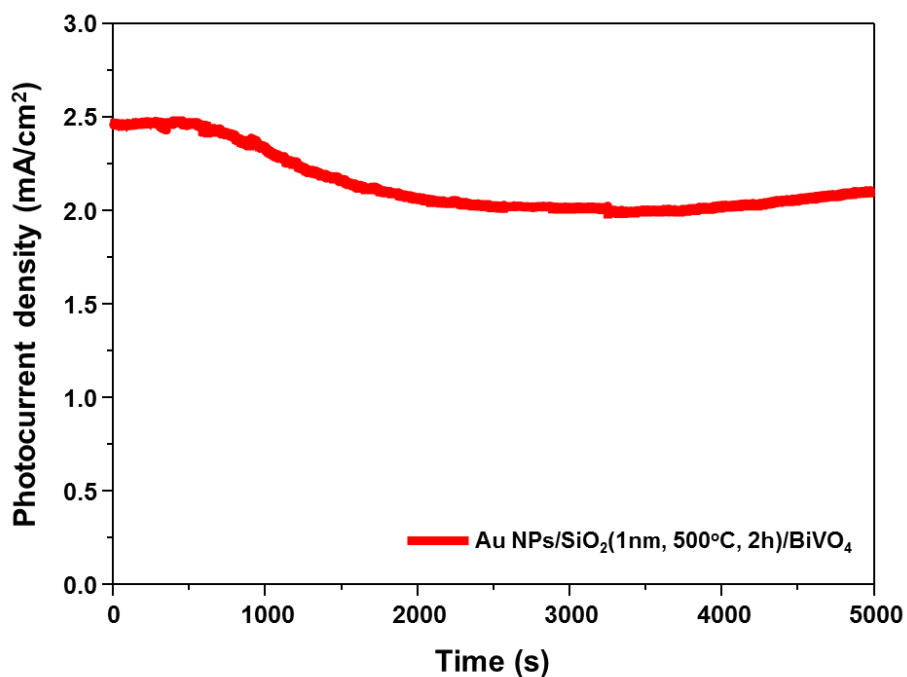


Figure 169. Stability test of octahedral Au NPs/SiO<sub>2</sub>(1nm)/BiVO<sub>4</sub> measured in 0.5 M phosphate buffer solution with 1M Na<sub>2</sub>O<sub>3</sub> at 1.10 V vs. RHE.

Figure 169 shows that the photocurrent was measured at 1.1 V versus RHE continuously for 5000 s under AM 1.5 G condition to determine the stability of the octahedral Au NPs/BiVO<sub>4</sub> with optimum coverage. The photocurrent density of  $2.3 \pm 0.1 \text{ mA cm}^{-2}$  was consistent for 5000 s, demonstrating the

potential of octahedral Au NPs/BiVO<sub>4</sub> as photoanodes for practical applications. In particular, we used very thin film of SiO<sub>2</sub> (about ≈1 nm) as an insulating layer, since the very thin thickness of SiO<sub>2</sub> films under 5 nm thickness is generally used to enhance the plasmonic solar water splitting efficiency.<sup>169,174,185</sup> After the deposition of SiO<sub>2</sub>, the photocurrent density increased slightly due to the PRET effect and the decreased photogenerated electron–hole recombination originated from the surface passivation of defect sites and improved interfacial charge separation.<sup>169,174,185</sup>

## 7.8. Photoactivity

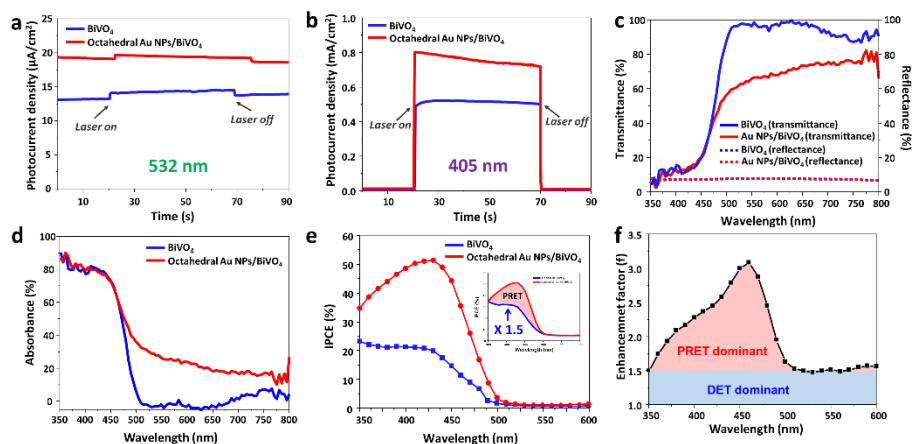


Figure 170. (a) and (b) Amperometric current density-time profiles for bare BiVO<sub>4</sub> and octahedral Au NPs/BiVO<sub>4</sub> photoelectrodes at 1.23 V vs. RHE with the fluence of 10 mW/cm<sup>2</sup> at 532 nm and 405 nm, respectively. (c) and (d) Absorption of the bare BiVO<sub>4</sub> and octahedral Au NPs/BiVO<sub>4</sub> films by estimating the transmission and reflection spectra using an integrating sphere (Absorbance = 1 – Transmittance – Reflectance) (e) IPCE spectra of bare BiVO<sub>4</sub> and octahedral Au NPs/BiVO<sub>4</sub> photoelectrodes at 1.23 V vs. RHE. (f) IPCE Enhancement of octahedral Au NPs/BiVO<sub>4</sub> photoelectrodes.

Figure 170 (a) and (b) shows the monochromatic laser sources at 532 and 405 nm, respectively, that were used to identify the generation of photoactivity depending on the incident electromagnetic spectra (vis and UV). Photocurrent transients were measured using a monochromatic laser with a fluence of  $10 \text{ mW cm}^{-2}$  at 1.23 V versus RHE. At 532 nm, the amount of photocurrent density seems to slightly increase compared with that of the  $\text{BiVO}_4$  films; however, this value is very negligible. The photocurrent from the 532 nm monochromatic laser remained in the range of  $\mu\text{A cm}^{-2}$ ; while the photocurrent from 405 nm remained in the range of  $\text{mA cm}^{-2}$ . With the 405 nm wavelength, the photocurrent density of the octahedral Au NPs/ $\text{BiVO}_4$  showed about 40% enhancement. An important point to note here is the photocurrent range disparity according to the incident wavelengths. Figures 171 and 172 show the gains of the photovoltage at 405 and 532 nm, respectively, recorded under constant current and open circuit condition. The photovoltage gains are derived from the enlarged surface areas after the attachment of octahedral Au NPs, since the increased surface area dilutes the concentration of minority carriers in the near-surface region, thus altering the Fermi level of minority carriers.<sup>185</sup> Figure 170 (c) and (d) shows the absorption spectra of octahedral Au NP/ $\text{BiVO}_4$  and  $\text{BiVO}_4$  film by estimating the transmission and reflection spectra using an integrating sphere (absorbance =  $1 - \text{transmittance} - \text{reflectance}$ ). The light absorption of  $\text{BiVO}_4$  film in the region from 500 to 800 nm is negligible, while attachment of octahedral Au NPs significantly enhanced the absorption. The enhancement of the absorption in the range from 500 to 800 nm is due to the LSPR effect occurred by introducing an octahedral Au NP. Figure 170 (e) and

(f) shows the results of the IPCE that we measured in order to clarify the mechanism of plasmonic solar water splitting in octahedral Au NPs/BiVO<sub>4</sub>. The IPCE of octahedral Au NPs/BiVO<sub>4</sub> demonstrated high values approaching 50% in the wavelength of 450 nm wavelength. At this point, the IPCE value recorded threefold enhancement compared to the BiVO<sub>4</sub> films. The IPCE values of the octahedral Au NPs/BiVO<sub>4</sub> above 500 nm approach zero like the bare BiVO<sub>4</sub> film. It indicates that hot electron injection is relatively difficult to occur in the visible wavelength region. Hot electron injection can occur when the induced energy is corresponding to the bandgap energies of materials or more. Since the catalytic hole transfer constant almost remains unchanged, the photocatalytic activity with the octahedral Au NPs is not maximized in the visible light range.<sup>176</sup> Figure 173 shows a primary recorded PEC enhancement at the UV–vis region reported in wide bandgap TiO<sub>2</sub>.<sup>176,177</sup> The PEC enhancement at the visible light range (about 500–600 nm) is also negligible corresponding to our results.

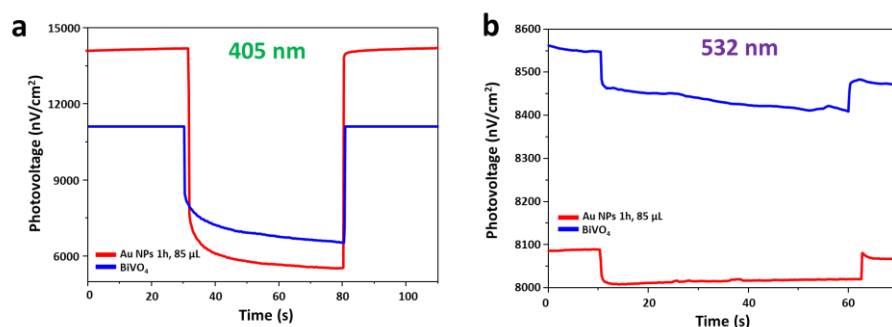


Figure 171. Photovoltage gains of octahedral Au NPs/BiVO<sub>4</sub> at (a) constant current of 500  $\mu$ A under 405 nm, (b) constant current of 10  $\mu$ A 405 nm under 532 nm.

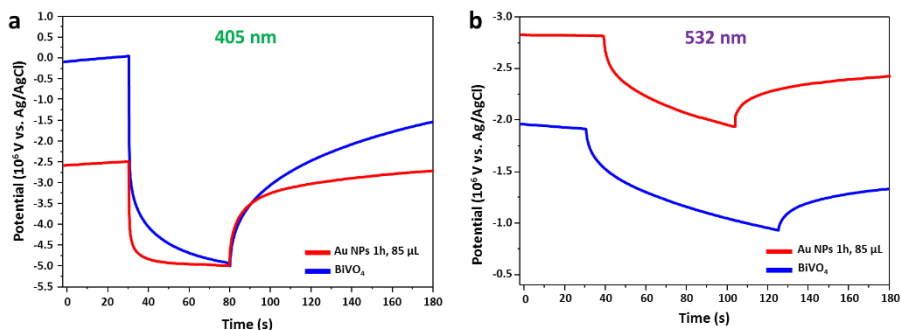


Figure 172. Photovoltage gains of octahedral Au NPs/BiVO<sub>4</sub> at open circuit potential (a) 405 nm, (b) 532 nm.

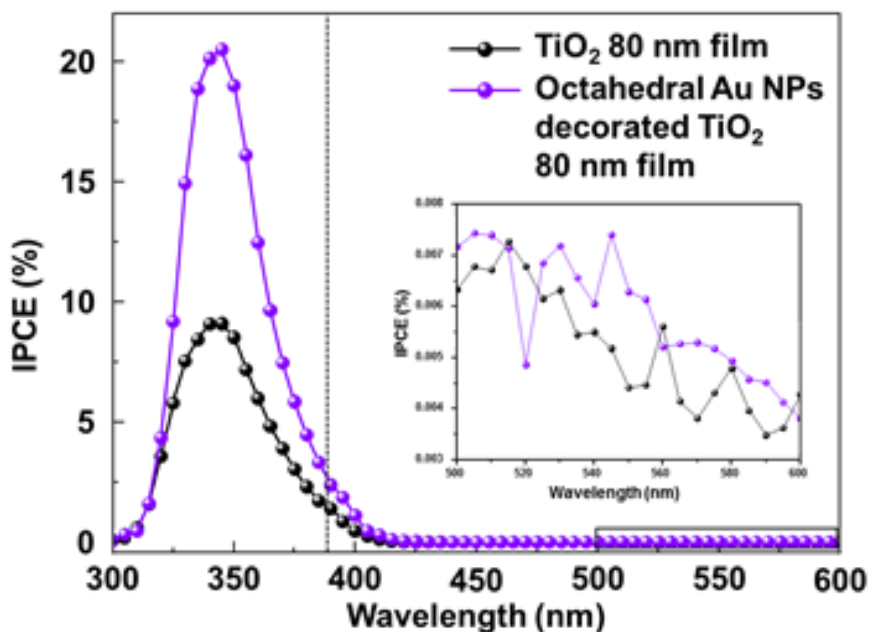


Figure 173. (a) IPCE spectra at 1.23 V vs. RHE. Octahedral Au NPs were decorated on 80-nm-thick TiO<sub>2</sub> film. The vertical dotted line (--) indicates the band gap energy of TiO<sub>2</sub>. Inset indicates that the photocurrent enhancement for the visible light is below the noise level.

## 7.9. Energy Band Diagram for Plasmon Enhanced Solar Water Splitting in BiVO<sub>4</sub>

We believe that the improved photoactivity of the octahedral Au NPs/BiVO<sub>4</sub> is primary due to the well-defined shape of Au NPs, since Au NPs with sharp vertices and edges can intensify LSPR-EFs and generate hot carriers.<sup>80,125</sup> There are three main mechanisms of plasmonic Au NPs that contribute to the solar water splitting process, that is, a light-trapping enhancement, DET, and PRET.<sup>83,180,185</sup> Light trapping validates when the size of the plasmonic metal NPs is larger than 100 nm. Particle sizes larger than 100 nm cause a broadening and damping of the plasmon resonance due to electromagnetic retardation effects.<sup>100</sup> The average size of our octahedral Au NP is only about 30 nm, thus making the light-trapping effect negligible. Both the DET and the PRET mechanisms may have significant effects on the enhancement of OER activity of the octahedral Au/BiVO<sub>4</sub>. Because of the SPR effect, octahedral Au NPs can absorb light with energy smaller than the bandgap energy of BiVO<sub>4</sub>, and the hot electrons excited to the SPR states of Au NPs can be injected into the conduction band of BiVO<sub>4</sub>, as displayed in Figure 174. The IPCE graph of the previously reported wide bandgap semiconductor such as TiO<sub>2</sub> shows the same tendency after attaching plasmonic Au NPs, as shown in Figure 173. Otherwise, our octahedral Au NP/BiVO<sub>4</sub> shows a unique feature of IPCE at 430 nm. Thus, we strongly propose that another mechanism, in addition to DET, is needed to interpret the PEC enhancement of our octahedral Au NP/BiVO<sub>4</sub> system. Above the 1.5-fold enhancement of IPCE, the PRET can act as a main mechanism for improving

the PEC properties, as shown in the inset of Figure 168 (e) and (f), since the absorption band of the BiVO<sub>4</sub> film is similar to the resonance wavelength of octahedral Au NPs and thus the two material systems can resonate optically each other. For hot electron injection process to occur, plasmonic Au NPs and n-type semiconductor should form a Schottky contact.<sup>85</sup> However, this restriction is removed when PRET mechanism is introduced. If spectral overlap with semiconductor and LSPR peak position is satisfied, PRET process is always activated regardless of the contact with semiconductor.<sup>186</sup> The previous study showed that PRET is dominant even at the outside range of LSPR peak at the sandwich structure (Au@SiO<sub>2</sub>@Cu<sub>2</sub>O). In the PRET mechanism, the energy of plasmonic oscillation is transferred from a plasmonic material to the semiconductor through an enhanced electromagnetic field. The presence of octahedral Au NPs increases the electromagnetic field close to the surface of BiVO<sub>4</sub> due to plasmon resonance, as predicted in the FDTD simulations in Figure 156. Thus, dipoles are induced in the BiVO<sub>4</sub> near the interface. This dipole–dipole interaction of the PRET significantly increases the generation rate of electron–hole pairs near the BiVO<sub>4</sub> surface.<sup>80,169,172,185</sup> The UV–vis spectra of octahedral Au NPs/BiVO<sub>4</sub> and octahedral Au NPs are compared to support evidence of the PRET mechanism, as shown in Figure 170 (d) and Figure 155. The UV–vis absorption spectrum of the octahedral Au NPs shows the plasmonic resonance peak at ≈550 nm. It should be noted that the NPs exhibit the plasmonic absorption plateau of considerable light absorption in the wavelength range from 350 to 500 nm. The absorption edge of BiVO<sub>4</sub> lies in the plasmonic absorption of the Au NPs, implying that the PRET mechanism

can dominate the PEC enhancement of the Au NPs/BiVO<sub>4</sub>. In other words, octahedral Au NPs on the BiVO<sub>4</sub> films play a role in surface passivation that is beneficial to decrease the inherent surface recombination of photogenerated electron–hole pairs, leading to the significantly enhanced PEC performance. It was hard to observe the PRET when the incident wavelength is longer than 500 nm. For efficient dipole–dipole interaction between Au NPs and BiVO<sub>4</sub>, the wavelength of the incident light is critical. Since the bandgap energy of BiVO<sub>4</sub> is 2.4 eV, the over-bandgap transition (wavelength shorter than ≈510 nm) is only allowed in bulk BiVO<sub>4</sub>, as depicted in Figure 175. We believe that dipole–dipole interaction at sub-bandgap energy region becomes effective for PEC if the dimension of BiVO<sub>4</sub> is as small as the Au NPs.<sup>187</sup> Therefore, we can strongly insist that PRET is the critical effect in enhancing the plasmonic water splitting efficiency of the octahedral Au NPs/BiVO<sub>4</sub> over DET, as highlighted in the Figures 170 (f) and 174.

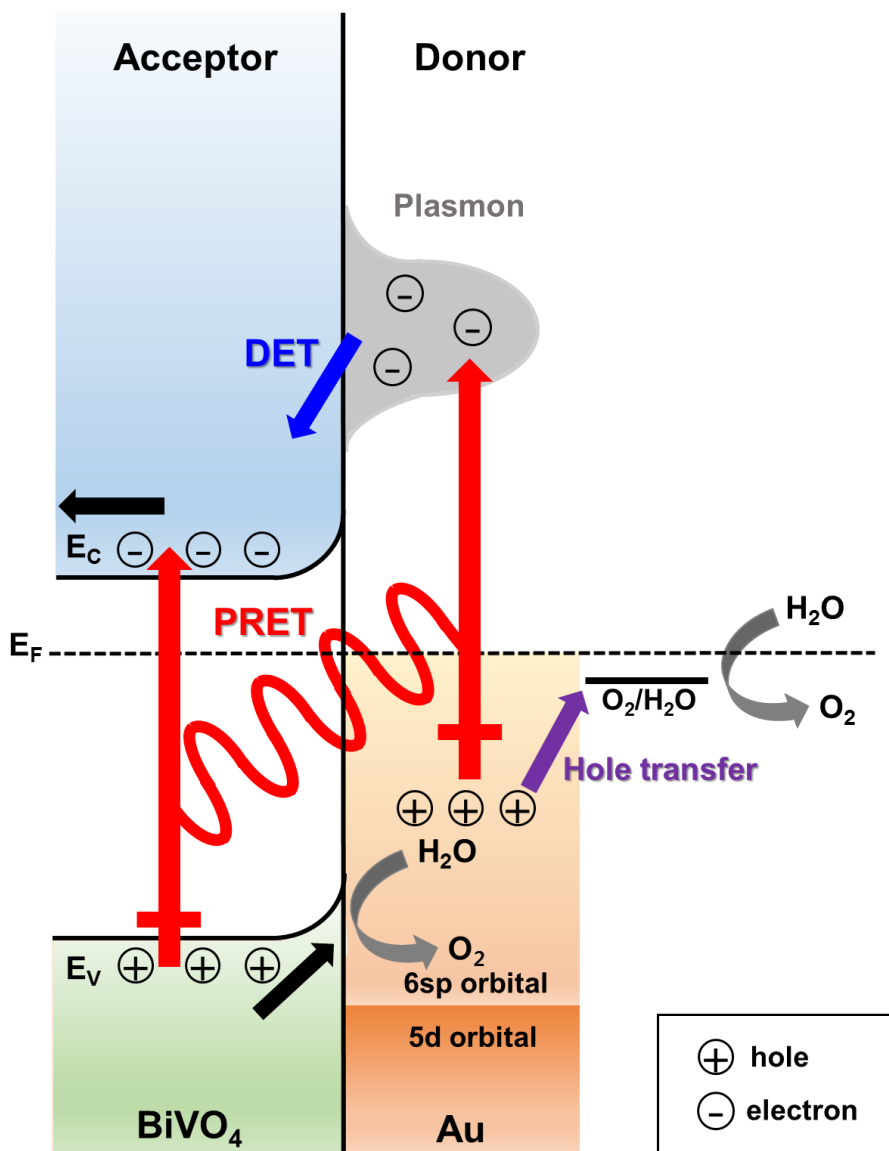


Figure 174. Schematic for the energy band diagram of the octahedral Au NPs/BiVO<sub>4</sub> system to show that both DET and PRET mechanisms work in the system.

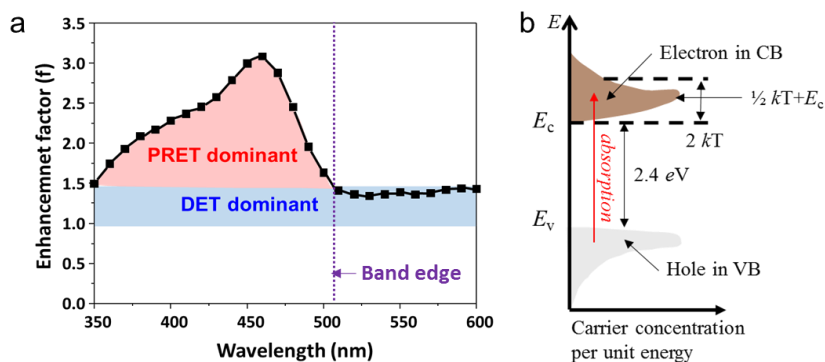


Figure 175. (a) IPCE enhancement in the octahedral Au NPs/BiVO<sub>4</sub> photoelectrode. (b) Energy distribution of electrons and holes in the conduction and valence bands of BiVO<sub>4</sub>. The highest electron and hole concentrations are  $1/2 kT$  away from  $E_c$  and  $E_v$ .

## 7.10. Conclusion

The plasmonic octahedral Au NPs also act as electrochemical cocatalyst for OER. Without Au NPs, the photogenerated hole transfer kinetics across the BiVO<sub>4</sub>/electrolyte interface is slow, and leads to the recombination of electron–hole pairs.<sup>172,188</sup> Since octahedral Au NPs serve as OEC, they can mediate the hole transfer rate from BiVO<sub>4</sub> to water and greatly increase the charge transfer rate, resulting in the enhanced photoactivity. The improved charge transfer rate highly suppresses hole accumulation at the BiVO<sub>4</sub>/solution interface. Our experimental results clearly show the validity of photocatalytic activity enhancement of BiVO<sub>4</sub> film by intensified LSPR-EFs originating from the shape-controlled octahedral Au NPs.

We studied shape-controlled plasmonic Au NPs to enhance the photoactivity of BiVO<sub>4</sub>, and found that octahedral Au NPs/BiVO<sub>4</sub> has superior PEC properties

compared to hemispherical Au NPs/BiVO<sub>4</sub>, since the sharp vertices and well-defined edges of the octahedral Au NPs provide more intensification of the local field than the hemispherical Au NPs, which enables forceful OER. The octahedral Au NPs/BiVO<sub>4</sub> with the optimized coverage by controlling the amount of MPA precipitation solution and dipping time showed a markedly enhanced photocurrent density of 2.4 mA cm<sup>-2</sup> at 1.23 V versus RHE. The improved performance of these photoelectrodes is due to their higher absorption, charge generation, and separation through the introduction of the LSPR-induced effects (DET and PRET). In particular, we highlight that the absorption band edge of BiVO<sub>4</sub> properly matches with the resonant wavelength for the field enhancement by the shape-controlled plasmonic Au NPs. Thus, the synergetic promotion effects occur compared to previously reported studies about wide bandgap semiconductors. Our approach with the shape-controlled Au NPs provides great potential in plasmonic solar water splitting and paves the way for developing highly efficient photoelectrodes of shape-controlled plasmonic metal NPs/BiVO<sub>4</sub> with moderate coverage in the overall UV–vis range.

## 7.11. Experimental Characterizations

Synthesis of Octahedral Au Nanoparticles: Seed-mediated growth method was used for the synthesis of octahedral shaped Au nanoparticles.<sup>80,125</sup> First, cetyltrimethylammonium bromide (CTAB, ≥99.9%, Sigma-Aldrich)-capped Au seeds were synthesized from the strong reduction agent (NaBH<sub>4</sub> ≥99%). 10 × 10<sup>-3</sup> M ice-cold NaBH<sub>4</sub>, aqueous solution (0.6 mL) was added to a 10.0 mL aqueous solution (incorporating 0.25 × 10<sup>-3</sup> M, gold chloride hydrate

( $\text{HAuCl}_4 \cdot x\text{H}_2\text{O}$ , 99.999%, Sigma-Aldrich) and  $100 \times 10^{-3}$  M CTAB. The brownish seed solution was stirred for 2 h at 30 °C to decompose the remaining  $\text{NaBH}_4$ . Next, cetyltrimethylammonium chloride (CTAC,  $\geq 98\%$ , Wako) capped Au seeds were synthesized from the CTAB-capped Au seeds. Then,  $100 \times 10^{-3}$  M (1.5 mL) ascorbic acid (AA, 100%) was added to another aqueous mixture solution (incorporating  $5 \times 10^{-3}$  M  $\text{HAuCl}_4$  (0.2 mL),  $200 \times 10^{-3}$  M CTAC (2 mL), and water (1.8 mL)). After the color of the mixture solution changed from yellow to transparent, 100  $\mu\text{L}$  CTAB-capped Au seed solution was promptly injected. The solution was left at room temperature, until a red-wine color was seen. The as-synthesized Au seeds were concentrated by centrifugation, and redispersed in 1 mL of  $20 \times 10^{-3}$  M aqueous CTAC solution. Finally, 100  $\mu\text{L}$  of the redispersed CTAC seed solution was rapidly injected into the transparent aqueous growth solution (incorporating  $5 \times 10^{-3}$  M  $\text{HAuCl}_4$  (0.4 mL),  $200 \times 10^{-3}$  M CTAB (0.5 mL),  $200 \times 10^{-3}$  M CTAC (4.5 mL),  $100 \times 10^{-3}$  M AA (60  $\mu\text{L}$ ), and water (4.3 mL)).

**Attachment of Au Nanoparticles:** The process was inspired by the sodium citrate absorption process reported by Mudunkotuwa and Grassian.<sup>183</sup> 1 mL octahedral shaped Au nanoparticle solution was added to a scintillation vial that contained the substrates. Then, a precipitator solution (containing 0.5 M MPA ( $\geq 99\%$ , Alfa Aesar) and 0.5 M sodium hydroxide (NaOH, 1 M, Daejung)) was added to the octahedral shaped Au nanoparticle solution. The coverage of the octahedral shaped Au nanoparticle on the samples was controlled by dipping time and volume change of the precipitator solution.

Synthesis of Hemispherical Au Nanoparticles: Au deposited BiVO<sub>4</sub> was synthesized by electron beam evaporator (Korea Vacuum Technology). Au pellets of 99.99% purity were used for the thin film deposition. The deposition rate was 0.03 Å s<sup>-1</sup>, and the correct Au film thicknesses of 0.7, 1.5, and 5 nm were controlled by a thickness monitor.

Synthesis of BiVO<sub>4</sub> Films: Precursor was prepared by dissolving bismuth nitrate pentahydrate (BiN<sub>3</sub>O<sub>9</sub>·5H<sub>2</sub>O, 98%, JUN) in a solution of vanadium oxide sulfate hydrate (VOSO<sub>4</sub>·5H<sub>2</sub>O, 99.99%, Aldrich) at pH <0.5 with the addition of nitric acid (HNO<sub>3</sub>, 67%, JUN). Then, 2 M sodium acetate (CH<sub>3</sub>COONa, Aldrich) was added, raising the pH to ≈5.1, which was then adjusted to pH 4.7 using a few drops of concentrated HNO<sub>3</sub>. This mildly acidic pH condition is necessary, because at pH values >5, V (IV) precipitates form in the solution.<sup>157,158</sup> Pulsed anodic electrodeposition was conducted in a standard three-electrode system with a working electrode of F:SnO<sub>2</sub>, an Ag/AgCl reference at 1.95 V versus Ag/AgCl for 10 min at 80 °C (≈2–3 mA cm<sup>-2</sup>). The duration time of the voltage pulse for synthesizing the BiVO<sub>4</sub> films used in this study was on time of 10 s, and off time of 30 s. All freshly prepared samples were then rinsed and annealed at 500 °C for 6 h in air, at a heating rate of 2 °C min<sup>-1</sup>. After annealing, as-deposited films were converted to a crystalline monoclinic phase of BiVO<sub>4</sub>.

*FDTD Simulation:* The simulations were achieved from the FDTD solutions program (Lumerical Solutions). The dielectric function of BiVO<sub>4</sub> was adopted from a prominent report.<sup>189</sup> The near field simulation was conducted with a 1.78

fs pulse length. The simulation condition was a perfectly matched layer boundary condition, automatic nonuniform mode, and the refinement was set to conformal variant 1. The calculation region was set to  $125 \times 400 \text{ nm}^2$ , and the corresponding mesh size was  $0.5 \times 0.5 \text{ nm}^2$ .

*Characterization:* The morphologies of Au NPs/BiVO<sub>4</sub> were characterized by field-emission scanning electron microscopy (MERLIN Compact, JEOL). Bright-field and high-resolution transmission electron microscopy (JEM-2100F, JEOL) with 200 kV field-emission images were obtained to investigate the microstructure of the Au NPs/BiVO<sub>4</sub>. XRD characterization was performed to confirm the crystalline phase of BiVO<sub>4</sub>.

*PEC Measurements:* The photoelectrochemical properties of BiVO<sub>4</sub>-based photoelectrodes were measured in phosphate buffer solution with the presence of 0.1 M sodium sulfite (Na<sub>2</sub>SO<sub>3</sub>), which served as an efficient hole scavenger. The oxidation of sulfite is thermodynamically and kinetically more facile than the oxidation of water, since the photogenerated holes are rapidly consumed for the oxidation of sulfite, thus measuring photocurrent in the sulfite oxidation enables investigation of the photoelectrochemical properties of BiVO<sub>4</sub>-based electrodes independently of its poor water oxidation kinetics. The photocurrent versus potential curve was recorded while sweeping the potential in the positive direction with a scan rate of  $10 \text{ mV s}^{-1}$  under a solar simulator with an AM 1.5 G filter; the light intensity of the solar simulator was calibrated to 1 sun ( $100 \text{ mW cm}^{-2}$ ), using a reference cell. The IPCE was measured using a light source and monochromator at 1.23 V versus RHE. The EIS was conducted by applying

0.63 V versus Ag/AgCl. The sweeping frequency was from 100 kHz to 100 mHz, with an AC amplitude of 10 mV. The measured spectra were fitted by using the ZSimpWin software.

## Chapter 8

### Siege of Metal Oxide Surface with {111} form Au Nanoparticles Using PEGylation

#### Quote

**Erik C. Dreaden. et al.**

“Over the past two decades, beautiful colors and unique electronic properties of gold nanoparticles have also attracted tremendous attention due to their historical applications in art and ancient medicine and current applications in enhanced optoelectronics and photovoltaics. In spite of their modest alchemical beginnings, gold nanoparticles exhibit physical properties that are truly different from both small molecules and bulk materials, as well as from other nanoscale particles.” (2012, Chemical Society Reviews)

Submitted to elsewhere (ACS Nano) (2017).

## 8.1. Motivation

The previous result is very restricted due to the generation of high-coverage without agglomeration. With a deprotonation method, the gold nanoparticles become aggregated either MPA and citric acid due to the lowering of zeta potential. Especially, a restriction of high coverage octahedral gold nanoparticle decoration hinders for achieving theoretical efficiency. To prevent the phenomena, the surface ligand exchange from CTAB to stable and adhesive for semiconductor is required. So a functionalized molecule with high affinity to gold is requisite. Here, a new process is devised for the purpose.

## 8.2. Introduction

Plasmonic nanoparticles (NPs) have opened a wide range of applications that include nano-sized medicines,<sup>190,191</sup> hydrothermal nanostructure growth,<sup>192,193</sup> optical and chemical sensors,<sup>194,195</sup> and water splitting catalysts<sup>196,197</sup> due to their exceptional optical response from plasmon. Gold (Au) has been regarded as the best candidate<sup>51</sup> material in the concept of plasmonic applications due to their stability in harsh environments and tunable plasmon resonance in the visible-to-infrared light region.<sup>198</sup> Incoming light energy can be efficiently transferred and converted to nearby medium from the plasmon relaxation process. The process involves with an effect on localized heating, incident near-field enhancement, hot-electron injection, and resonant electron transfer to an adjacent semiconductor.<sup>80,199</sup> The efficiencies of these relaxation processes are highly dependent on the shape and size of Au NPs.<sup>79</sup> In particular, they are strengthened at size-controlled Au NPs having sharp vertices or edges.<sup>125,200,201</sup>

According to the phenomenological plasmonic model, an efficient plasmon relaxation process is expected with shape-controlled Au NPs.<sup>78</sup> In previous research, we intensively investigated shape dependence of the plasmon relaxation processes for shape-controlled Au NPs<sup>176,202</sup>. We found in plasmonic solar water splitting, that octahedral Au NPs are much more active than quasi-spherical and hemispherical Au NPs, whose diameters are similar to those of the octahedral ones. As far as we know, from the theoretical simulations and experimental results,<sup>176,202</sup> among various shapes of Au NPs, the octahedral shape has the best ability to enhance incident near-fields on semiconductor nanostructures.

For further applications, attachment of octahedral Au NPs on a semiconductor with high coverage is required. Currently, high coverage Au NPs decorations are achieved from physical vapor deposition processes,<sup>203</sup> and precursor reductions<sup>201</sup> (thermal or photo). However, their methods yield shape-uncontrolled Au NPs. High coverage decoration of shape-controlled Au NPs on semiconductor has not yet been achieved. The following two methods are widely utilized to synthesize shape-controlled Au NPs. The first is the citrate reduction method, and the second is a seed-mediated growth method using a cetyltrimethylammonium bromide/chloride (CTAB/C) capping agent. Although the citrate reduction method can provide homogenous quasi-spherical Au NPs over 10 nm,<sup>16</sup> the synthesis of non-quasi-spherical Au NPs from citrate reduction is not possible. However, the shape-controlled octahedral Au NPs is achievable via a seed-mediated growth process. In this method, CTAB/C chemicals decide the morphology of Au NPs and act as a capping agent to

prevent agglomeration. Even though the characteristic is beneficial for the synthesis of Au NPs, the CTAB/C molecules hinder Au NPs from the practical applications. The attachment of Au NPs to semiconductor from seed-mediated growth method is restricted due to the charge from  $\text{CTA}^+$ . Besides, the complete removal of CTAB/C chemical agents is impossible because the removal of CTAB/C below critical micelle concentration<sup>204</sup> induces agglomeration of the Au NPs and/or collapse of the bilayer structure on Au NPs surface.<sup>35</sup> Even though it is intricate, a method is required for attaching shape-controlled Au NPs synthesized from seed-mediated growth.

Ligand exchange reactions over the surface of Au NPs are currently preferred method of attaching shape-controlled Au NPs attachment onto a semiconductor. Ligand exchange reactions to attach Au NPs are usually initiated with a molecule having a thiol (-SH) functional group, due to the high electron affinity of sulfur (S) to Au.<sup>184</sup> To attach Au NPs on semiconductor in aqueous phase, thiolated-acids (for example, mercaptopropionic acid (MPA);  $\text{HS}(\text{CH}_2)_2\text{COOH}$ ) are usually adsorbed into targeted semiconductor surface by dipping,<sup>180</sup> or dropping.<sup>176</sup> But the result is very restricted due to the relatively low coverage,<sup>180,205</sup> and the agglomeration problem (Figure 176) on the semiconductor surface. This bottleneck comes from the positive ionic nature of exchanged thiolated-acid ligand which reduces the zeta potential of Au NPs. To overcome such a barrier, we expect that non-ionic (covalent) ligand is required to reserve the stability of Au NPs, to achieve high coverage Au NPs decoration of targeted semiconductor nanostructures. Among the possible candidates, thiolated polyethylene glycol (PEG-SH) is adequate for the

functionalization of Au NPs due to their stability, solubility to water/organic solvents, commercial availability, bio-compatibility, and high probability for attachment of semiconductor due to the hydroxide (-OH) function group.<sup>206</sup> Even though facile ligand exchange reaction with PEG-SH for phase transfer were reported of citrate-capped Au NPs and CTAB/C capped Au NPs,<sup>207,208</sup> octahedral Au NPs originating from the ligand exchange reaction has not yet been reported.

Here, we show an efficient method for high-coverage attachment of octahedral Au NPs onto a targeted semiconductor nanostructure by ligand-exchange reaction with PEG-SH via ethanol-dichloromethane mixture (EtOH-DCM). The importance of the octahedral Au NPs in the concept of near-field enhancement is shown from finite-difference time-domain (FDTD) simulation compared with truncated octahedral Au NPs and cuboctahedral Au NPs. To attach electric-field amplifying octahedral Au NPs onto a targeted semiconductor surface, the surface functionalization of Au NPs by PEG-SH is required. However, the ligand exchange reaction to PEG-SH in aqueous solution does not proceed well enough into the Au (111) to evoke octahedral Au NPs attachment onto the semiconductor surface. To solve the problem, we introduced phase transfer through the addition of EtOH-DCM with a phase transfer agent (PEG-SH). PEG-SH functionalizes the octahedral Au NPs by removing the CTAB/C capping agent. A number density of about  $1.65 \times 10^{14}$  ea/cm<sup>2</sup> (about 31.6 % coverage) of particle on Si surface concentration is achieved, which is analogous to coverage for Au NPs generated by physical

vapor deposition.<sup>176,203</sup> The transparent color of the transferred solution after a few hour indicates that the octahedral Au NPs in solution are physically attached to the targeted semiconductor nanostructure through a process with uniform distribution. Through the spectroscopic analysis (Raman and Fourier transform infrared spectroscopy (FTIR)), we schematically visualized the surface CTA<sup>+</sup> bilayer structure and PEG-SH activation mechanism at the (100) and (111) surface of Au NPs.

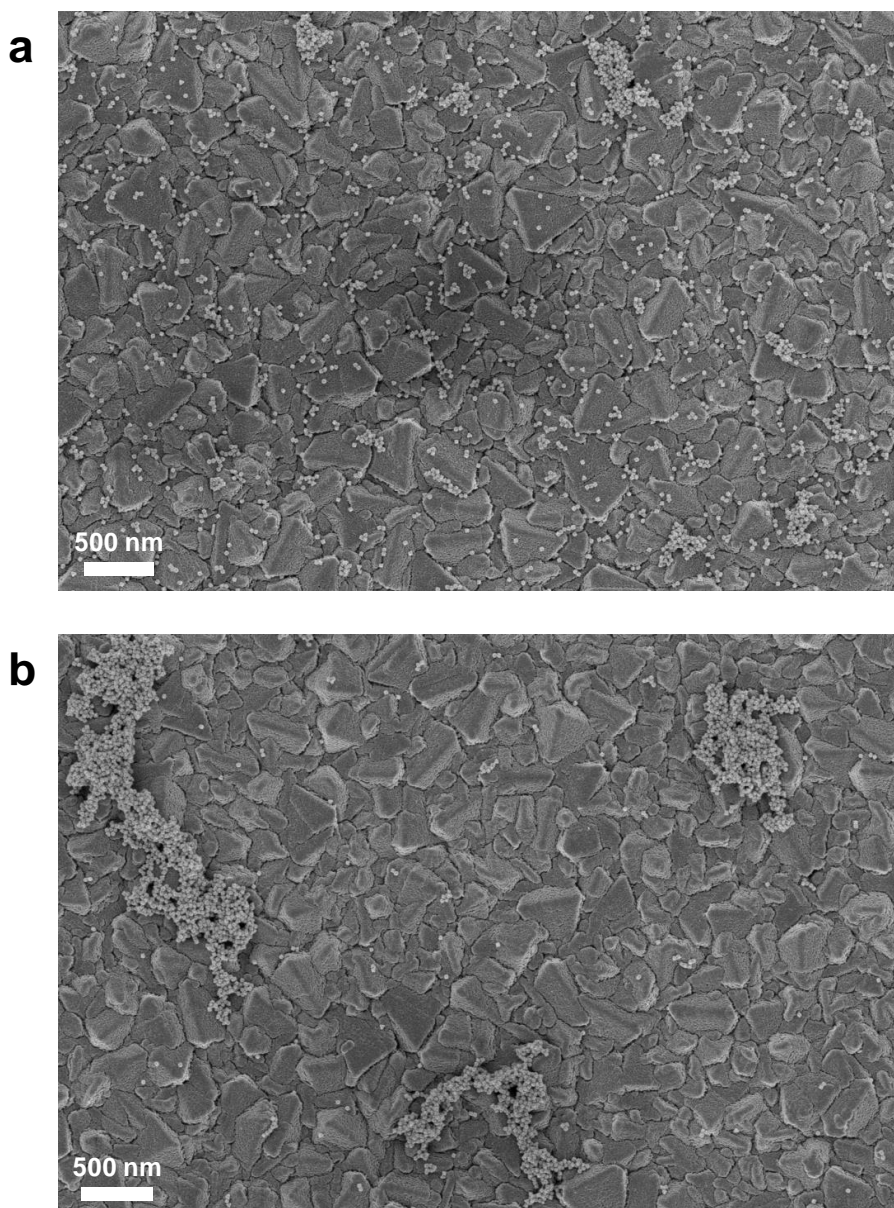


Figure 176. Agglomeration of octahedral Au nanoparticles on  $\text{TiO}_2/\text{FTO}$  on glass substrate. (a) Moderately agglomerated Au nanoparticles ( $\sim 50\%$ ). (b) Heavily agglomerated Au nanoparticles ( $\sim 100\%$ ).

## 8.2. Near-Field Enhancements

The finite-difference time-domain (FDTD) method is employed to show the electric-field amplifying ability of shape-controlled octahedral Au NPs. Three kinds of morphology (octahedral, truncated octahedral and cuboctahedral) are adopted in the simulation. To fit the size of these Au NPs, the height is adjusted to 30 nm. The simulation configurations of the three kinds of Au NPs are shown in Figure 175 (a). To clearly differentiate the facets of these Au NPs visually, two distinct colors are used according to the facets. The (100) and (111) facets are colored as blue and yellow, respectively, in the Figure 1a. To compare the electric-field amplifying ability of three-kind Au NPs, the FDTD simulations that were executed at incident wavelength of (350, 450, 550 and 650) nm, at Figure 175(b)-e. The field intensities for each of the Au NPs are highest near the plasmon resonance frequency (around 550 nm). The overall results show that the incident electric field is significantly pronounced with octahedral Au NPs than with truncated octahedral or cuboctahedral shapes, regardless of the incident light wavelength. The maximum electric field enhancement ratios ( $|E/E_0|$ ) for twelve outputs for Figures 177(b)-(e) are arranged in Figure 178. This FDTD simulation results indicate that octahedral Au NPs have most excellent ability to amplifying incident electric-field among three shapes. We found by experiment and simulation that the octahedral Au NPs is the best choice to enhance incident near field in single-crystalline stand-alone Au NPs.<sup>176</sup>

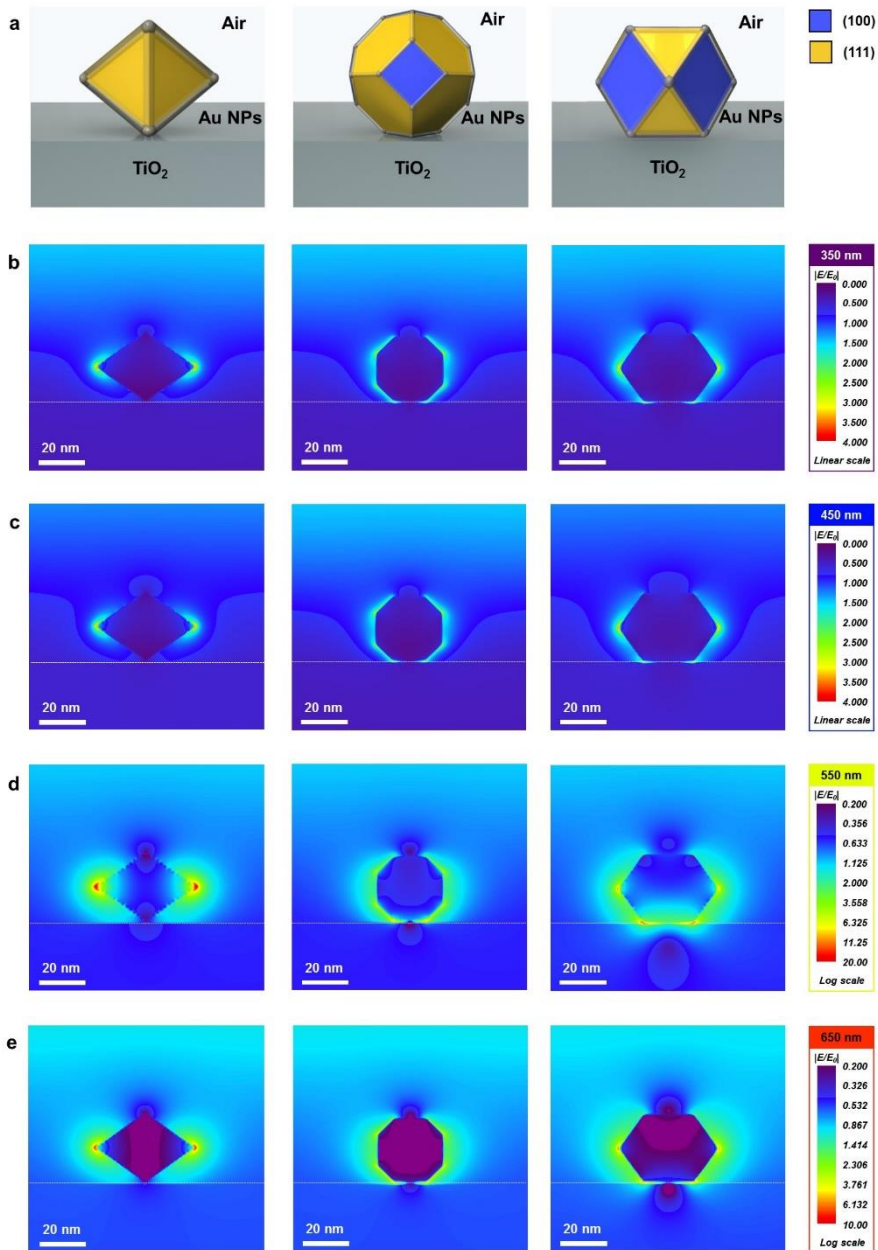
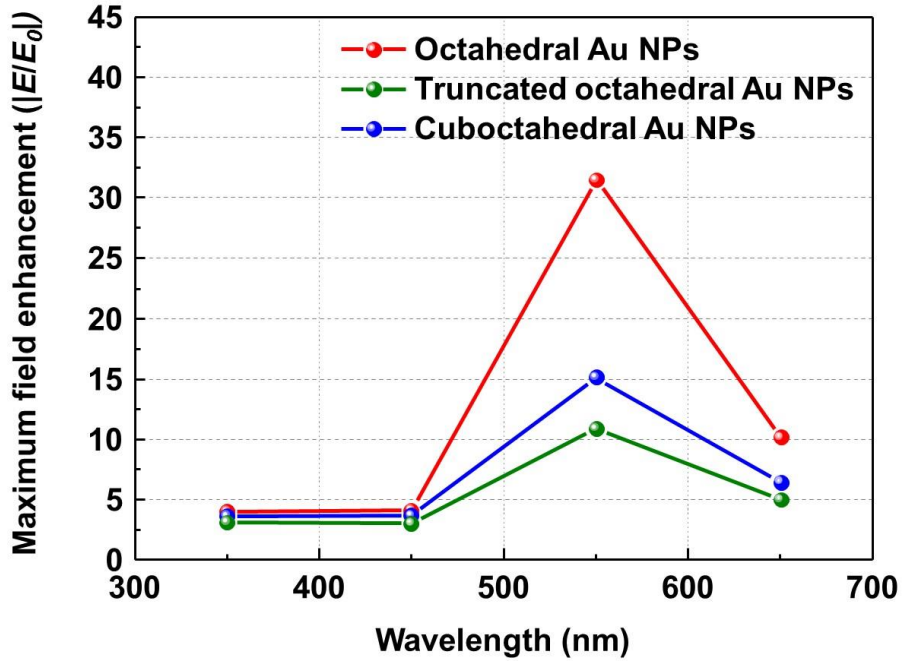


Figure 177. FDTD simulation results ( $|E/E_0|$ ) of the three kinds of Au nanoparticles (octahedral, truncated octahedral and cuboctahedral) at various incident wavelengths. (100) and (111) facets are denoted as yellow and blue, respectively. (a) Schematic configurations of Au nanoparticles. (b) Field

enhancement at 350 nm photons. (c) Field enhancement at 450 nm photons. (c) Field enhancement at 550 nm photons. (b) Field enhancement at 650 nm photons.



Wavelength (nm)	350	450	550	650
Octahedral Au NPs	3.995	4.015	31.50	10.135
Truncated octahedral Au NPs	3.107	3.003	10.856	4.978
Cuboctahedral Au NPs	3.62	3.65	15.12	6.43

Figure 178. The maximum electric field enhancement ( $E/E_0$ ) from twelve finite-difference time-domain (FDTD) simulations. The value is arranged in either grape and table.

### 8.3. Agglomeration of Gold Nanoparticles

## 8.4. Gold Nanoparticle Attachment by PEGylation

Figures 179 (a)-(c) show the morphology of the three types of Au NPs (octahedral, truncated octahedral and cuboctahedral) aggregated on 40 nm TiO<sub>2</sub>/Si substrate. The images are achieved through field-effect scanning electron microscopy (FE-SEM). The transmission electron microscopy (TEM) images of these Au NPs are attached as insets. The 3-dimensional configurations of Au NPs that were reconstructed from the TEM images are also included as an inset. The edge sizes of the three types of Au NPs are estimated to be around (20 - 25) nm. Figure 180 shows the proportions of (111) and (100) facets according to their shapes as reported,<sup>32</sup> and as calculated. The schematic of Au NPs attachment procedure based on phase transfer via PEGylation<sup>207,208</sup> is shown in the Figure 179 (d). The process consists of two streams according to their medium (in aqueous and organic phase). First, 0.02 mL of PEG-SH aqueous solution (1 mg / 1 mL) is added into a glass vial containing aqueous solution Au NPs (10 mL). After a while (more than 30 min), an organic mixture of ethanol (EtOH) and dichloromethane (DCM) (1:1 volume ratio) is added to the aqueous solution containing Au NPs. Phase transfer automatically proceeds upon adding the organic medium (DCM-EtOH). After collecting Au NPs sediments via centrifugation, the concentration of a solution containing the Au NPs is appropriately adjusted to control the coverage of Au NPs on a targeted semiconductor,

by adding an organic medium. Au NPs can be simply attached to the substrate via dipping. Finally, after dipping, the targeted substrate is washed with EtOH to remove residues. Figure 179 (e) shows the attachment of Au NPs inside of a transparent vial due to the PEGylation (PEG-SH attachment on Au NPs surface). PEGylated Au NPs solution for 24 h shows that the attachment of Au NPs proceeds most with truncated cube Au NPs, and proceeds least (is almost transparent) with octahedral Au NPs. This result implies that due to the lack of activity on (111) facets, PEGylation does not sufficiently proceed on the octahedral Au NPs on a targeted semiconductor in aqueous phase. Figure 179 (f) shows that without PEG-SH, the phase transfer of octahedral Au NPs from aqueous to DCM-EtOH medium is not facilitated. Due to the micelle collapse of Au NPs with the addition of EtOH, the color of the solution is highly diluted. The phase transfer of Au NPs is possible after addition of PEG-SH. With a short time (less than 30 min) of PEGylation, the phase transfer does not proceeded efficiently. A long PEGylation time (over 3 h) is required for sufficient ligand exchange reaction in the aqueous phase. The role of the EtOH-DCM medium is the removal of CTA<sup>+</sup> bilayer structure to facilitate PEG-SH attachment on the Au surface, which is similar to the result from phospholipid bilayer structure.<sup>209</sup> To show complete ligand exchange, we taken imagery of the octahedral Au NPs after phase transfer by TEM with negative staining

technique<sup>210</sup> (Figure 181). High coverage octahedral Au NPs output visualized with glass vial is added in the Figure 179 (g).

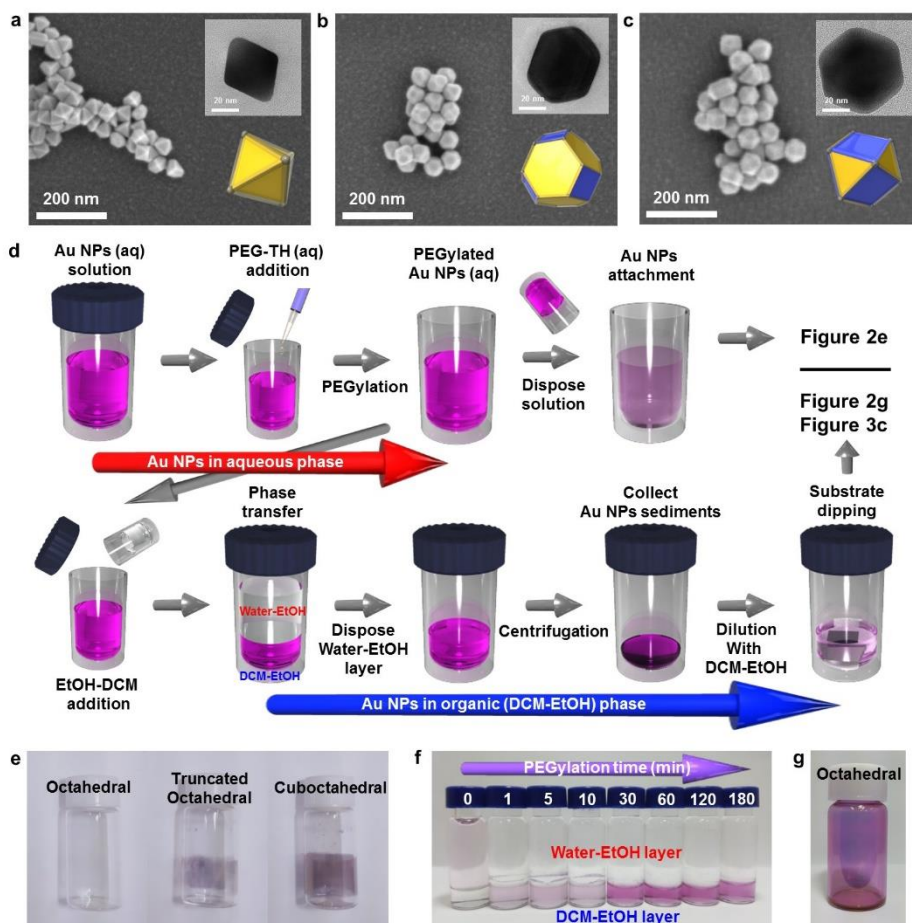


Figure 179. Agglomerated (a) octahedral, (b) truncated octahedral and (c) cuboctahedral Au nanoparticles on TiO<sub>2</sub> thin films. (d) A schematic of the Au NPs attachment procedure based on phase transfer to organic medium via PEGylation. (e) A schematic for the process of anchoring Au nanoparticles for the semiconductor nanostructure attachment using PEGylation in aqueous phase and phase transfer to organic medium. (f) Phase transfer to organic

medium according to the PEGylation time. (g) Image of octahedral Au nanoparticle attached vial.

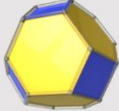
	Octahedral Au NPs	Truncated octahedral Au NPs	Cuboctahedral Au NPs
Shape			
(100) portion	0 %	22.4 %	63.4 %
(111) portion	100 %	77.6 %	36.6 %

Figure 180. Calculated coverage of three equilateral shaped Au NPs (octahedral, truncated octahedral and truncated cube) for (100) and (111) facets. (Equilateral is assumed.)

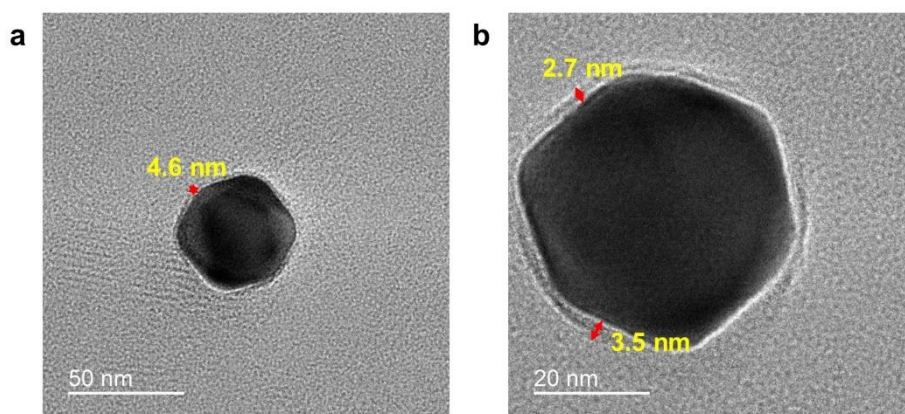


Figure 181. PEGylated octahedral Au NPs taken by negative staining technique.

(a) Low magnification. (b) High magnification.

## 8.5. Gold Nanoparticle Attachment by phase Transfer

Figure 180 (a) presents the absorption spectra for the three kinds of Au NPs solution as measured and normalized to their resonance peak from (300 to 800) nm. The resonance peaks for octahedral, truncated octahedral and cuboctahedral Au NPs in aqueous solution were (541, 538, and 559) nm respectively. The resonance peaks for truncated octahedral Au NPs and truncated cube Au NPs in aqueous solution were blue-shifted (2 and 3) nm in sequence after PEGylation due to the dielectric constant change of the surroundings from the absorption of PEG-SH into the Au NPs surface.<sup>56</sup> Interestingly, the resonance peak shift for octahedral Au NPs solution is not observable from the absorbance measurements. This result suggests PEGylation has not proceeded to the Au NPs surface. For the attachment process, 10 ml as-synthesized octahedral Au NPs were concentrated to 0.5 ml via centrifugation after phase transfer. We controlled the dipping time and solution concentration to control the nanoparticle coverage on Si substrate during the attachment process. Corresponding results are arranged on Figure 182 (b) (as-centrifuged concentration of Au NPs solution is indicated as C). With increasing of concentration and extending dipping time, the number of Au NPs on Si surface is increased. After 1-day, the octahedral Au NPs organic solution is becoming transparent (Figure 183 (a)) in comparison with the pristine Au NPs in aqueous solution (Figure 183 (b)). This result shows that PEGylation of the octahedral Au NPs in aqueous solution is achieved via phase transfer process to organic medium (EtOH-DCM). A SEM image of silicon surface with the highest coverage is shown in Figure 183 (c). To show the

versatility of the method, the octahedral Au NPs are decorated into the TiO<sub>2</sub> nanorods (NRs) (Figure 182 (d), Figure 184) and various semiconductor films (Fe<sub>2</sub>O<sub>3</sub>, SnO<sub>2</sub>, WO<sub>3</sub>, and SiO<sub>2</sub>; Figure 185 (a)-(d)). In addition, the image of octahedral Au NPs decorated TiO<sub>2</sub> NR/FTO is attached as an inset image.

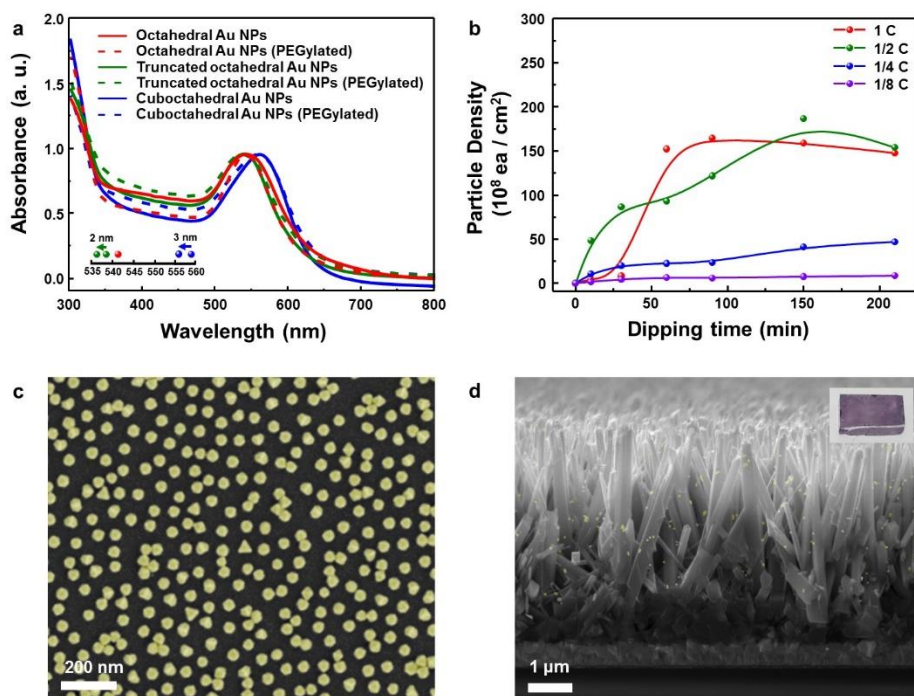


Figure 182. (a) Normalized absorbance of synthesized solutions containing three shape-controlled Au NPs (octahedral, truncated octahedral and cuboctahedral). Dotted lines indicate the absorbance of solutions after PEGylation. Peak positions are also included as inset. (b) Attached octahedral Au NPs density on Si by the process by dipping time and concentration. (c) SEM image of highest coverage of octahedral Au NPs from the conditions. (d) Octahedral Au NPs decoration on Au nanorod by phase transfer to organic medium via PEGylation. (Octahedral Au NPs in the SEM images are depicted as false yellow color.)

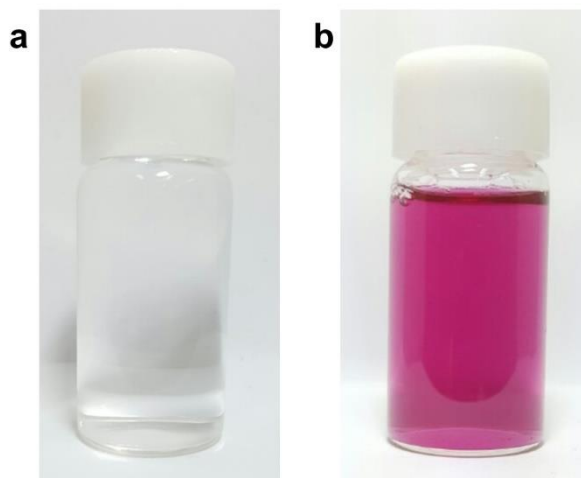


Figure 183. (a) The Au NPs solution (organic phase, EtOH-DCM) after Au octahedral NPs attachment (transparent). (b) The original (aqueous phase) as-synthesized Au octahedral NPs solution (purple).

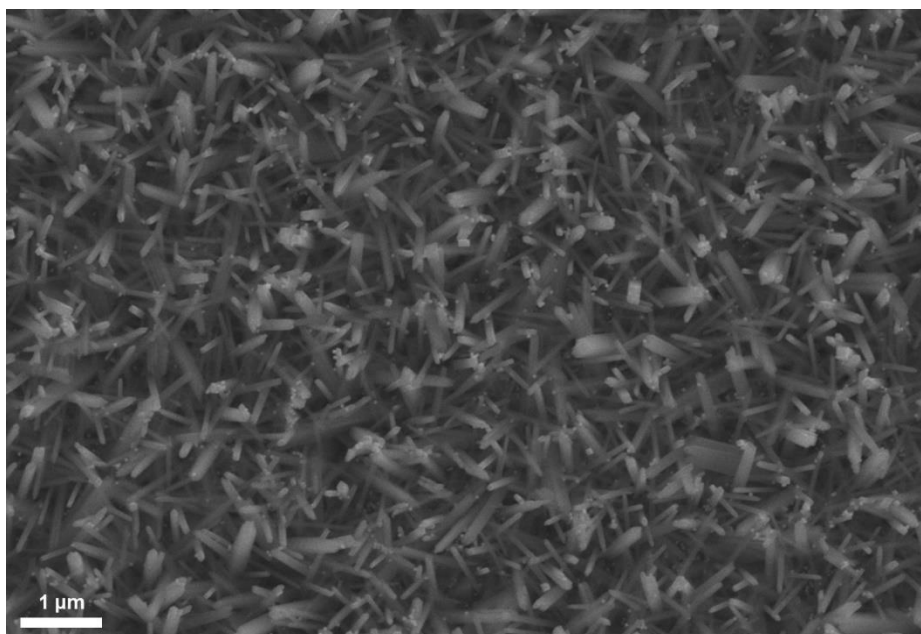


Figure 184. Octahedral Au NPs decorated TiO<sub>2</sub> nanorods on planar view.

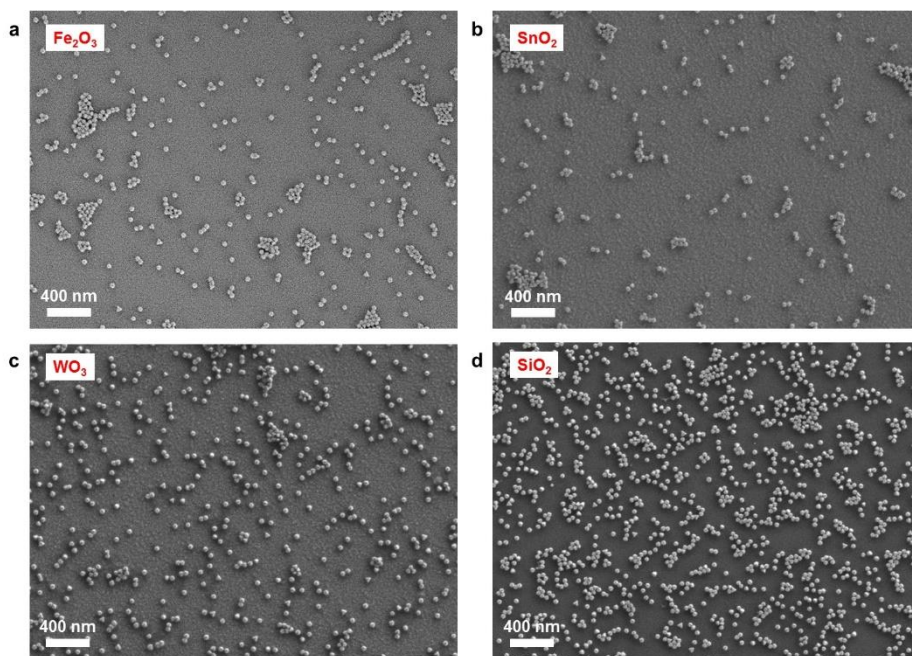


Figure 185. Octahedral Au NPs attachment on various semiconductors. (a) octahedral Au NPs decorated Fe<sub>2</sub>O<sub>3</sub> film (40-nm-thick) on Si substrate. (b) octahedral Au NPs decorated SnO<sub>2</sub> (40-nm-thick) film on Si substrate. (c) octahedral Au NPs decorated WO<sub>3</sub> film (40-nm-thick) on Si substrate. (d) octahedral Au NPs decorated SiO<sub>2</sub>/Si substrate.

## 8.6. Raman Spectra Analysis

To analyze the results originating from the shapes of Au nanoparticle, we investigated the CTA<sup>+</sup> molecular vibration mode through Raman and FTIR spectroscopy. Figure 4a shows the main Raman spectra of CTA<sup>+</sup> molecule from (600 to 3,000) cm<sup>-1</sup> wavenumbers. For comparison, the Raman signal of CTAB 200 mM aqueous solution is also attached in Figure 187. The first domain in Figure 184 (720 to 800) cm<sup>-1</sup> is attributed to stretching ( $\nu$ ) vibration of the CTA<sup>+</sup> headgroup (trimethylammonium). The vibrational signal at 760 cm<sup>-1</sup> is

attributed to CN<sup>+</sup> headgroup symmetrical stretching.<sup>211</sup> Even though the detail has not yet been reported, the signal around 730 cm<sup>-1</sup> can be attributed to the another head group vibrational mode.<sup>212</sup> The vibrational mode at 730 cm<sup>-1</sup> is usually unobservable in CTA<sup>+</sup> capped Au NPs in a Raman excitation<sup>212,213</sup>, and it only recorded in previous literature with Au nanosphere which is synthesized from CTA<sup>+</sup> growth solution with citrate-reduced seed.<sup>214</sup> The phenomenon would be attributed to the facet of the spherical particle that is mainly composed of (111) and a small portion of (100) facets.<sup>215,216</sup> Our result strongly indicates that the bilayer structure of CTA<sup>+</sup> in octahedral Au NPs is different from that in the other shaped Au NPs.

The second domain in Figure 186 (1,000 to 1,600) cm<sup>-1</sup> originate from skeletal vibration in the carbon backbone chain of CTA<sup>+</sup>. The signal at 1,085 cm<sup>-1</sup> indicates carbon-carbon (CC) stretching ( $\nu$ ) vibration of CTA<sup>+</sup> alkyl-chains.<sup>214</sup> We can figure out the headgroup vibrational activity compared with a backbone from the peak intensity ratio ( $I_{1085} / (I_{760} + I_{730})$ ) of Raman spectroscopy. Table 1 shows that the value is lowest in octahedral Au NPs. The analysis indicates suppressed backbone vibration and promoted headgroup vibration in CTA<sup>+</sup> on the (111) facet. The peaks at (1,300 and 1,610) cm<sup>-1</sup> mean CH<sub>2</sub> twisting ( $t$ ) and wagging ( $w$ ) vibration mode sequentially (out-of-plane vibration) in hydrocarbon backbone. If the hydrogen moves in the same (or different) vertical direction, it would be wagging (or twisting). The ratio ( $I_{1300} / I_{1510}$ ) shows the vibrational tendency of the backbone chain.

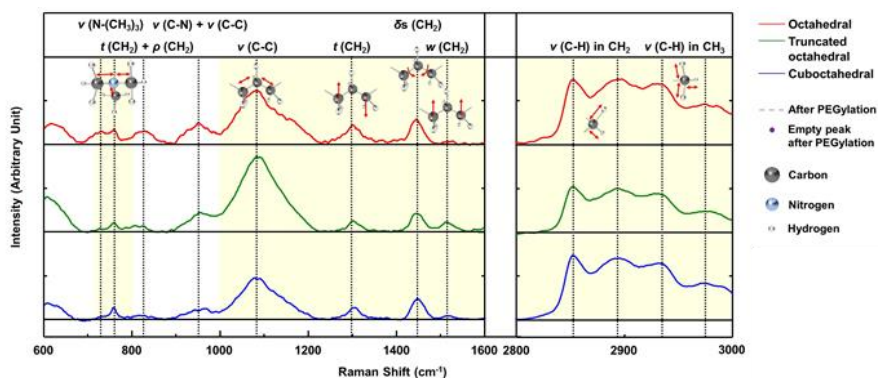


Figure 186. Normalized Raman spectroscopic analysis of the three shape-controlled Au NPs solutions from (600 to 3,000)  $\text{cm}^{-1}$ . Smoothed data is also included (numbers indicate peak positions).

Table 5. Vibrational activity of the CTA<sup>+</sup> molecule in Au NPs solution.

Intensity ratio		$I_{1085} / (I_{760} + I_{730})$	$I_{1300} / I_{1510}$	$I_{1445} / I_{1300}$	$I_{2880} / I_{2930}$	$I_{2892} / I_{2973}$	$(I_{2892} + I_{2890}) / (I_{2973} + I_{2930})$
Description		Backbone vibrational activity	Out-of-plane vibrational activity (same directional movement)	In-plane mode activity	C-H stretching activity in backbone (symmetrical)	C-H stretching activity in backbone (antisymmetrical)	C-H stretching activity in backbone (total)
Shape	Octahedral	1.94	7.86	1.27	1.05	1.598	1.18
	Truncated octahedral	6.42	1.25	1.72	1.16	2.095	1.29
	Cuboctahedral	2.56	2.98	1.76	1.10	1.669	1.22

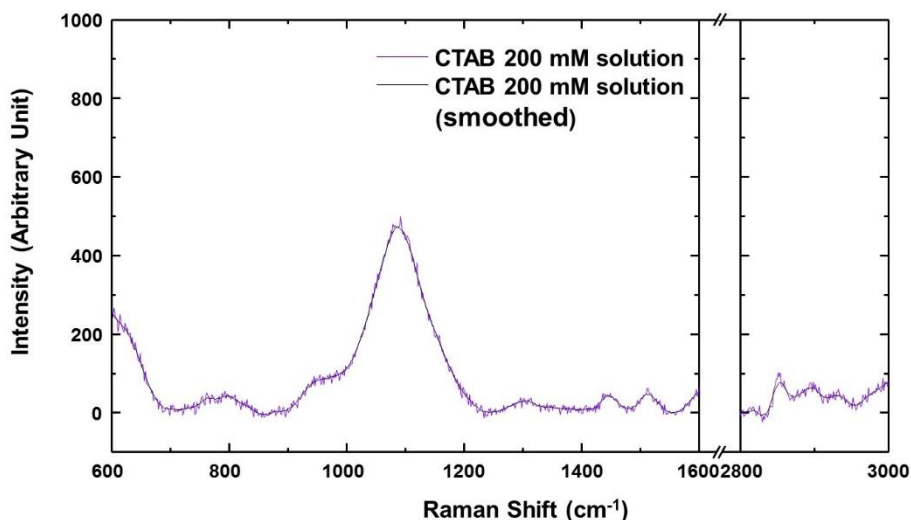


Figure 187. RAMAN spectra of CTAB 200 mM solution.

As shown in Table 5, hydrogen favors a different vertical directional movement in octahedral Au NPs. The result indicates strong strain in the CTA<sup>+</sup> bilayer structure due to the suppressed atomic vibration of hydrogen. The peak at 1,445 cm<sup>-1</sup> means CH<sub>2</sub> scissoring ( $\delta_s$ ) vibrational mode (in-plane vibration).

The lowest peak intensity ratio ( $I_{1445} / I_{1300}$ ) of octahedral Au NPs among the three Au NPs means suppressed in-plane vibration which supports strong strain in the CTA<sup>+</sup> bilayer structure in octahedral Au NPs. The last domain in Figure 186 (2,800 to 3,000) cm<sup>-1</sup> is attributed to stretching ( $\nu$ ) vibrational modes of hydrocarbons (CH<sub>x</sub>).<sup>212</sup> The signals at (2,850 and 2,892) cm<sup>-1</sup> indicates stretching ( $\nu$ ) vibrational modes of hydrocarbon in the backbone (CH<sub>2</sub>) in symmetrical and anti-symmetrical mode. The two last signals at (2930 and 2973) cm<sup>-1</sup> means stretching ( $\nu$ ) vibrational modes hydrocarbon in headgroup (CH<sub>3</sub>) in symmetrical and anti-symmetrical mode. Overall comparison of the three intensity ratio results ( $I_{2850} / I_{2930}$ ,  $I_{2892} / I_{2973}$  and  $(I_{2892} + I_{2890}) / (I_{2973} + I_{2930})$ ) from

Table 1 indicates suppressed CTA<sup>+</sup> carbon chain vibration in octahedral Au NPs.

## 8.7. FT-IR Spectra Analysis

For more detail, we investigated the FTIR absorption spectra of Au NPs solution from (2,000 cm<sup>-1</sup> to 4,000) cm<sup>-1</sup> in Figure 188. These data were measured from dropping of a small amount of solution onto the glass substrate and normalized according to their peak value (2,915 cm<sup>-1</sup>). For reference, FTIR absorption spectra of CTAB 200 mM solution and PEG-SH aqueous solution (Figure 189 (a)) and the designation of the peaks (Figure 189 (b)) are included. Several uncommon phenomena are observed in FTIR. The unreported peak is observed at 3,004 cm<sup>-1</sup>. The peak would be attributed to a partial redshift of the peak at 3,015 cm<sup>-1</sup> (CH<sub>3</sub> stretching ( $\nu$ ) vibration), owing to the strain of CTA<sup>+</sup> bilayer structure. In the literature, the signal around 3,239 cm<sup>-1</sup> is reported as hydroxyl vibration of a surface-absorbed water molecule.<sup>217,218</sup> Though the truncated octahedral and cuboctahedral Au NPs show the FTIR signals from the water molecule absorption on Au NPs surface, octahedral Au NPs do not show the signal which means restricted water molecule adsorption on the octahedral Au NPs surface. Therefore to have enhanced hydrophobicity, CTA<sup>+</sup> bilayer in octahedral Au NPs should be more densely-packed than those in the truncated octahedral and cuboctahedral Au NPs.<sup>219</sup> Interestingly, the octahedral Au NPs does not show a peak at (3,390 and 3,440) cm<sup>-1</sup> and a new signal at 3,474 cm<sup>-1</sup> is observed. It is known that this region indicates the stretching vibration due to the absorption of CTA<sup>+</sup> headgroup<sup>125</sup>. The unreported peak at

3,474  $\text{cm}^{-1}$  can be regarded as the blue shifted signal from (3,390 and 3,440)  $\text{cm}^{-1}$  signals owing to the strong binding of the  $\text{CTA}^+$  headgroup compared to that of the other shapes. Also, strong binding of the molecule on the Au (111) surface is also expected from computational calculations.<sup>220,221</sup> The water solvation frequency of  $\text{CTA}^+$  ( $\sim 3,600 \text{ cm}^{-1}$ ) indicates the formation of  $\text{CTA}^+$  bilayer structure on Au NPs surface.<sup>125</sup> The FTIR signal after PEGylation shows extinction of the  $\text{CTA}^+$  headgroup absorption signal (3,390 and 3,440)  $\text{cm}^{-1}$  for truncated octahedral and cuboctahedral Au NPs, while the signal at 3,474  $\text{cm}^{-1}$  from octahedral Au NPs is not. The overall spectroscopic data suggest that PEGylation on octahedral Au NPs is difficult due to the unique  $\text{CTA}^+$  bilayer structure (strong binding of  $\text{CTA}^+$  headgroup and densely-packing) on the (111) facet.

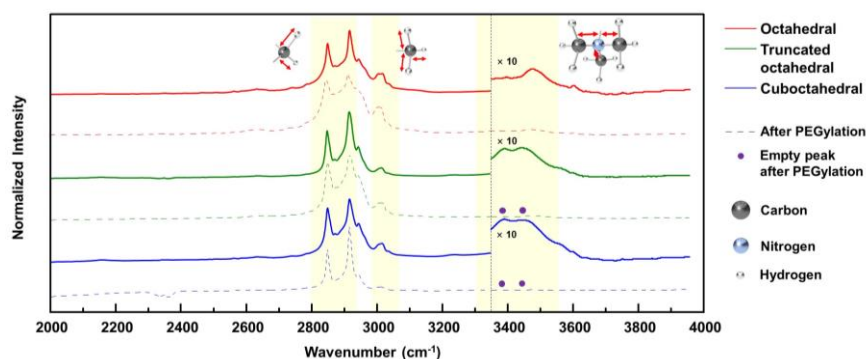


Figure 188. Normalized FTIR spectroscopic analysis of the three shape-controlled Au NPs solutions before and after the PEGylation from (2,000 to 3,950)  $\text{cm}^{-1}$ . The intensity from FTIR at specific region around 3,400  $\text{cm}^{-1}$  is enlarged 10 times for visual assistance. The empty peak after PEGylation is denoted as gray dots (numbers indicate peak positions).

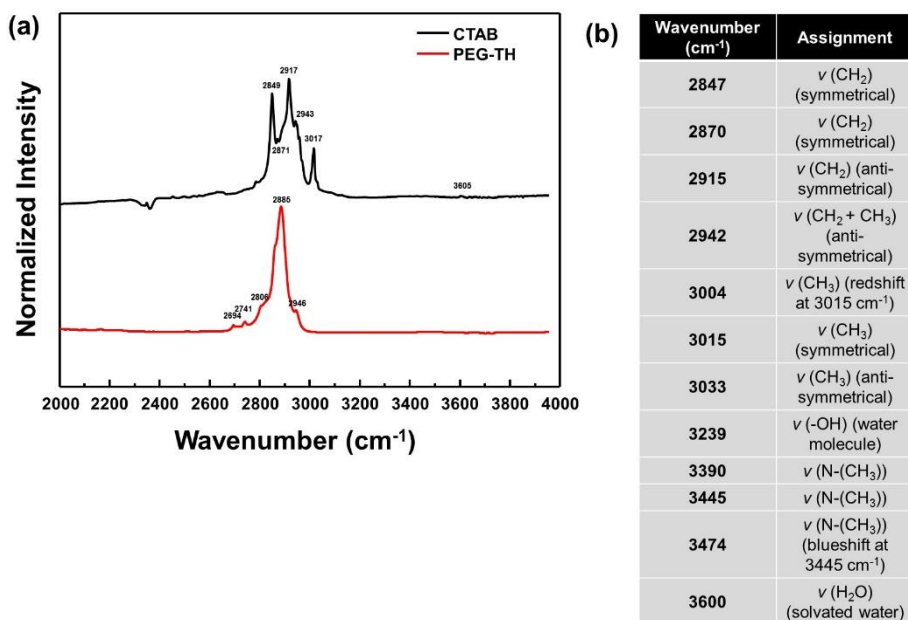


Figure 189. (a) FTIR spectra of dried CTAB (black) and PEG-TH solution on glass substrate. (b) Peak designation of CTA<sup>+</sup> molecule in FTIR spectra.

## 8.8. Attachment Mechanism

To explain the attachment results according to the Au NPs shape, the facets of Au NPs should be considered. The surface bonding is detrimental to explaining the above selectivity for PEGylation in the aqueous phase. As shown in Figure 190 (a), Au (100) surface atom has 8 neighboring atoms, and 4 additional surface bonds are available. Considering the CTA<sup>+</sup> headgroup binding on (100) the Au vacant site and the spectroscopic analysis in Figure 190, CTA<sup>+</sup> headgroup bindings are loose on the (100) surface and bilayer density should not be dense. The sufficient space between the headgroup binding sites can make the CTA<sup>+</sup> molecules intersect. The CTA<sup>+</sup> bilayer structure on the (100) surface is inferred to be an inter-digitated structure (Figure 190 (b)) according to our spectroscopic condition and previous report.<sup>36</sup> The sparse and thin CTA<sup>+</sup>

hydrophobic bilayer, in addition to the loose binding of the CTA<sup>+</sup> headgroup, allows the PEG-SH molecule to be successfully attached onto Au (100) surface (in the truncated octahedral and cuboctahedral Au NPs cases). Meanwhile, the Au (111) surface atom has 9 neighboring atoms, and 3 additional surface bonds are available as shown in Figure 190 (c). The CTA<sup>+</sup> headgroup binding on the (111) Au vacant site and the spectroscopic analysis in Figure 190 show dense CTA<sup>+</sup> bilayer structure and strong CTA<sup>+</sup> headgroup bindings on the (111) surface. The adjacent headgroup binding sites block the intersection of CTA<sup>+</sup> molecules. As a result, the CTA<sup>+</sup> bilayer structure on the (111) surface is deduced from our spectroscopic result and the Au (111) facet structure to be a densely-packing structure. The thick and dense CTA<sup>+</sup> hydrophobic bilayer in addition to the strong binding of the CTA<sup>+</sup> headgroup results in prohibition of PEG-SH binding onto the (111) surface.

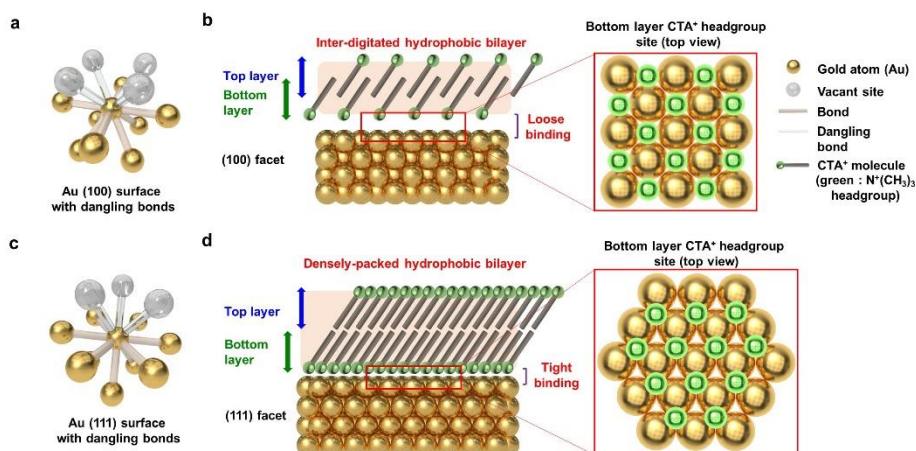


Figure 190. Schematic of the CTA<sup>+</sup> bilayer structure according to the facet of Au NPs. (a) One Au (100) surface atom with dangling bonds. (b) Inter-digitated

hydrophobic CTA<sup>+</sup> bilayer structure on (100) facet. (c) One Au (111) surface atom with dangling bonds. (d) Densely-packed hydrophobic CTA<sup>+</sup> bilayer structure on (111) facet. The CTA<sup>+</sup> molecule headgroup adhesion site is denoted in the schematic as green balls.

## 8.9. Exceeding the Theoretical SQ Limit

Photocurrent enhancement with the method is tested on BiVO<sub>4</sub> film. With a quite dilatation (1:5), the maximized photocurrent is achieved as shown below Figure 191.

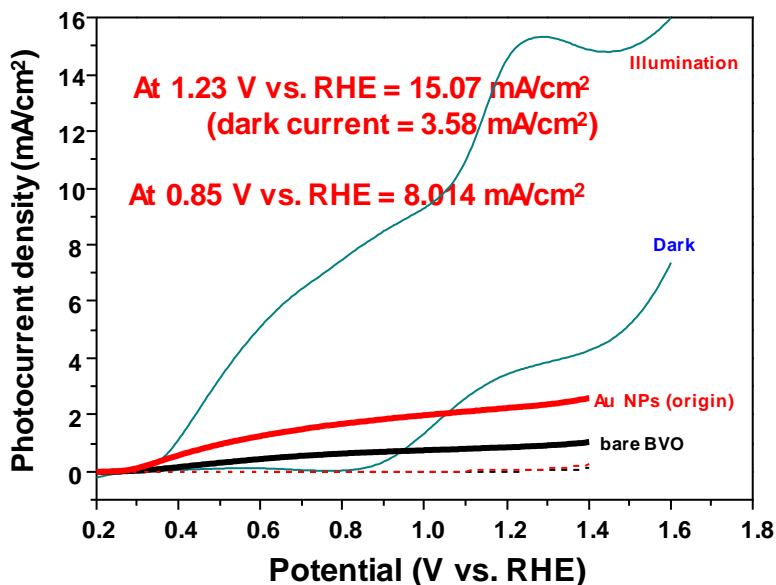


Figure 191. Photocurrent enhancement with high-coverage of octahedral gold nanoparticles formed by ligand exchange method with PEG-TH. The result is shown with the previous result.

Around the potential at 0.8 V vs. RHE, no dark current arises and photocurrent is highly enhanced. Above the potential, the redox peak is shown from 0.8 V

vs. RHE to 1.4 V vs. RHE. Also electrolysis starting from 0.8 V vs. RHE has observed. The peak is attributed to the oxidation of gold nanoparticles to  $\text{Au}(\text{OH})_3$  phase. Repeated measurement showed current degradation and hide of peak. Note that The recorded photocurrent is higher than the theoretical limit of  $\text{BiVO}_4$  as shown in Figure 192.

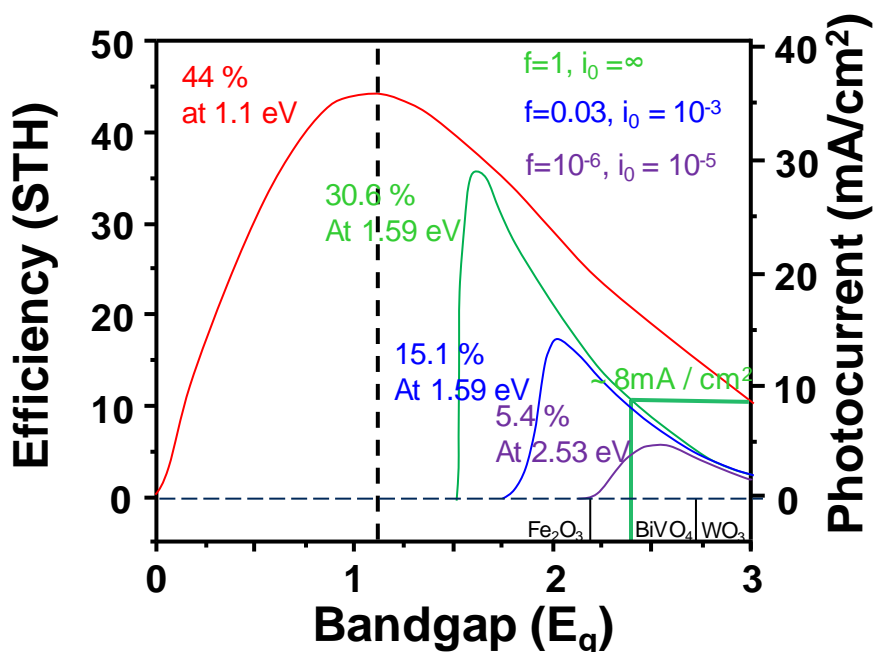


Figure 192. Theoretical photocurrent of  $\text{BiVO}_4$ .

## 8.10. Conclusion

Through examination of Au NPs ligand exchange reaction of PEG-SH in water via absorption measurement, Raman spectroscopy, FTIR spectroscopy and visual observation of glass vial, we have confirmed that PEGylation is much depressed with octahedral Au NPs in the aqueous phase, in comparison with truncated octahedral and cuboctahedral NPs. The PEGylation results for

the three shapes of Au NPs indicate that PEG-SH adhesion to the Au surface is more reliable at the Au (100) surface rather than the Au (111) surface. We succeeded in high coverage decoration of octahedral Au NPs on semiconductor surface via removal of the CTAB/C ligand for PEG-SH activation of inactive Au (111) surface with the EtOH-DCM medium. The controlled attachment of octahedral Au NPs via PEGylation in an organic medium (EtOH-DCM) to the semiconductor with sufficient coverage proves the potential of the proposed method for further plasmonic applications of shape-controlled Au NPs. The covalent bonding property of PEG-SH profoundly reduced the agglomeration of Au NPs. Due to the highly efficient plasmon decay process (including hot electron/heat generation, near-field concentration and resonant energy transmission) by shape-controlled Au NPs, we expect that this procedure will facilitate the application of the LSPR property of Au NPs from high coverage attachment.

## 8.11. Experimental Details

Materials: Cetyltrimethylammonium bromide (CTAB,  $\geq 99.9\%$ ), L-ascorbic acid (AA, 100%), sodium borohydride ( $\text{NaBH}_4$ ,  $\geq 99\%$ ), trisodium citrate dihydrate ( $\text{Na}_3\text{C}_6\text{H}_5\text{O}_7 \cdot 2\text{H}_2\text{O}$ ,  $\text{Na}_3\text{Cit}$ ), gold chloride hydrate ( $\text{HAuCl}_4 \cdot x\text{H}_2\text{O}$ , 99.999%) and poly(ethylene glycol) methyl ether thiol (thiolated polyethylene glycol, PEG-TH, average  $M_n = 2000$ ) were obtained from Sigma-Aldrich. Cetyltrimethylammonium chloride (CTAC,  $\geq 98\%$ ) was obtained from Wako. Sodium hydroxide (NaOH, 1 M), anhydrous ethanol ( $\text{C}_2\text{H}_5\text{OH}$   $\geq 99.9\%$ ) and dichloromethane ( $\text{CH}_2\text{Cl}_2$   $\geq 99.5\%$ ) were obtained from Daejung. 3-

Mercaptopropionic acid (MPA) ( $\geq 99\%$ ) was purchased from Alfa Aesar. Si wafers and wet oxidized (300 nm) SiO<sub>2</sub>/Si wafers were purchased from DASOM RMS. Those chemicals were used without further purification with deionized water (Pure Water Corporation). Fluorine doped tin oxide (FTO,  $8\Omega/\square$ ) was purchased from Wooyang GMS. Titanium dioxide (TiO<sub>2</sub>), tungsten oxide (WO<sub>3</sub>) and hematite ( $\alpha$ -Fe<sub>2</sub>O<sub>3</sub>) were purchased from Kojundo Chemical (grain shape, 99.9%).

Semiconductor thin film preparation from Electron beam evaporator (E-beam): Titanium dioxide (TiO<sub>2</sub>), tungsten oxide (WO<sub>3</sub>) and hematite thin film ( $\alpha$ -Fe<sub>2</sub>O<sub>3</sub>) were deposited on Si wafer (100). Film thicknesses were obtained from the thickness monitor. To crystallize an as-deposited film, thermal annealing was performed in ambient air condition in a box furnace (FB 1310M, Thermo Scientific).

Au nanoparticle attachment with MPA: We have this revised method in previous research<sup>176,202</sup>. Briefly, 1 mL octahedral-shaped Au nanoparticle solution was added to a scintillation vial. The objective samples were immersed into the octahedral-shaped Au nanoparticle solution. Then, a precipitator solution containing MPA (0.5 M) and NaOH (0.5 M) was added to the octahedral-shaped Au nanoparticle solution. The coverage of the octahedral-shaped Au nanoparticle on the samples is controlled by changing the volume of the precipitator solution. The SEM images in Figure 2 were achieved via this procedure.

Synthesis of CTAC-capped Au seeds: A seed-mediated growth method is used for the synthesis of shape-controlled Au nanoparticles. First, CTAB-capped Au seeds were synthesized from a strong reduction agent ( $\text{NaBH}_4$ ). 10 mM ice-cold  $\text{NaBH}_4$  aqueous solution (0.6 mL) was added to a 10.0 mL aqueous solution (incorporating 0.25 mM  $\text{HAuCl}_4$  and 100 mM CTAB). The brownish seed solution was stirred for 2 hours at 30 °C to decompose the remaining  $\text{NaBH}_4$ . Next, CTAC-capped Au seeds were synthesized from the CTAB-capped Au seeds. Then, 100 mM (1.5 mL) AA was added to another aqueous mixture solution (incorporating 5 mM  $\text{HAuCl}_4$  (0.2 mL), 200 mM CTAC (2 mL) and water (1.8 mL)). After the color change of the mixture solution from yellow to transparent, 100  $\mu\text{L}$  CTAB-capped Au seed solution was promptly injected. The solution was left in room temperature until a red-wine color was seen. The as-synthesized Au seeds were concentrated by centrifugation and redispersed in 1 mL of 20 mM aqueous CTAC solution.

Growth of octahedral Au nanoparticles: 100  $\mu\text{L}$  of the redispersed CTAC seed solution was rapidly injected into the transparent aqueous growth solution (incorporating 5 mM  $\text{HAuCl}_4$  (0.4 mL), 200 mM CTAB (0.5 mL), 200 mM CTAC (4.5 mL), 100 mM AA (60  $\mu\text{L}$ ) and water (4.3 mL)). Stirring was vigorously performed during the growth process.

Synthesis of truncated octahedral Au nanoparticles: 100  $\mu\text{L}$  of the redispersed CTAC seed solution was rapidly injected into the transparent aqueous growth solution (incorporating 5 mM  $\text{HAuCl}_4$  (0.4 mL), 200 mM CTAB (0.5 mL), 200

mM CTAC (4.5 mL), 100 mM AA (30  $\mu$ L) and water (4.3 mL)). Stirring was vigorously performed during the growth process.

Synthesis of truncated cube Au nanoparticles: 100  $\mu$ L of the redispersed CTAC seed solution was rapidly injected into the transparent aqueous growth solution (incorporating 5 mM HAuCl<sub>4</sub> (0.4 mL), 200 mM CTAB (0.5 mL), 200 mM CTAC (4.48 mL), 100 mM AA (60  $\mu$ L) and water (4.5 mL)). Stirring was vigorously performed during the growth process.

FDTD simulations: The FDTD simulations were performed with a program FDTD solution (Lumerical solutions). The near field simulation was conducted with 1.78 fs pulse length. The simulation condition was a perfectly matched layer (PML) boundary condition. The meshing condition was set to automatic non-uniform mode, and the refinement was set to conformal variant 1. The calculation region was 100 nm  $\times$  100 nm and the mesh size was 0.5 nm  $\times$  0.5 nm. The simulation was conducted with titanium dioxide (TiO<sub>2</sub>) thin film at air environment.

Characterizations: Field emission scanning electron microscopy (FE-SEM, MERLIN compact, Zeiss), high-resolution transmission electron microscopy (TEM, JEM-2100F, JEOL), UV/VIS spectroscopy (V-770, JASCO) and Fourier transform infrared spectroscopy (FT-IR, Nicolet iN10, Thermo Fisher Scientific) were also used. For the Raman analysis, 532 nm laser source was utilized on glass capillary tube containing Au NPs solution. Instruments were accessed from the Research Institute of Advanced Materials (RIAM, Seoul National University).

## Chapter 9

### Summary

#### Quote

**C. W. Moon (the Author)**

“I am confident that this work provides a cornerstone for utilize high energy hole generation/injection at plasmonic solar water splitting. I believe that shape-controlled nanoparticle would make a great contribution to the plasmonic solar water splitting systems and guarantees highly effective photoelectrode.” (2017)

This work provides a cornerstone for utilize high energy hole generation/injection at plasmonic solar water splitting. I believe that shape-controlled nanoparticle would make a great contribution to the plasmonic solar water splitting systems and guarantees highly effective photoelectrode. To explain the final result, I described from beginning to end from plasmon enhanced solar water splitting.

Through the Chapter 1, historical base of plasmon is described. The use of gold nanoparticles in history is shown. Also, at the end, modern technology for the plasmon is introduced (FDTD and shape controlled gold nanoparticle synthesis).

Through the Chapter 2, gold nanoparticle synthesis methods until modern day are described. In summary, citrate reduction and seed-mediated growth method is widely adopted. Nanoparticle attachment strategy based on the chemical physics around the nanoparticles is explained.

Though the Chapter 3, interaction of light and electrons in metal is explained in detail. In the process, reader can understand that the formation of localized surface plasmon resonance in the nano-sized gold nanoparticles. Also the physical property of LSPR is highly dependent on the size and shape.

Though the Chapter 4, the fundamental of photoelectrochemical water splitting is explained in detail. Based on the understanding of semiconductor-liquid interface, the understanding of semiconductor-Au nanoparticle-liquid interface interface is driven.

Though the Chapter 5, various mechanism of localized surface plasmon based solar water splitting is addressed. Overcoming of theoretical efficiency (Shockley-Queisser limit) is theoretically possible. At last, the observed photocurrent degradations in plasmonic photoanode is shown.

Though the Chapter 6, plasmonic photoanode (Au-TiO<sub>2</sub>) works for over-bandgap photon wavelength is achieved from the application of octahedral gold nanoparticles. The reason for the phenomena is described with catalytic hole activation from 5d orbital by intense local electromagnetic field.

Though the Chapter 7, the versatility and usefulness of octahedral gold nanoparticle is proven with BiVO<sub>4</sub>. The photocurrent enhancement mechanism in this case is attributed to the bandgap energy overlap with plasmon resonance energy (resonant electron transfer) which is different from Chapter 6.

Though the Chapter 8, high-coverage gold nanoparticle attachable method is shown via ligand exchange and phase transfer. The method application to the solar water splitting induced theoretical efficiency overcome of BiVO<sub>4</sub> photoanode.

Even though gold nanoparticle has interesting property of electron-light collective interaction (which is called as plasmon resonance), in the concept of application, that is not applicable alone. The value is excavated via the interaction with surrounding system by transmission of energy. The role of plasmon resonance is very similar to the salt (NaCl) which is added in our daily food. The energy from the plasmon can be emitted via three processes (radiative emission, non-radiative emission and resonant energy transfer by dipoles). Due

to the diverse mechanism of plasmon relaxation and abnormal extinction property with light enables highly efficient energy transfer into surrounding medium. The discussion is restricted to the solar water splitting from now on, however, the idea can be extended to the electron-electron and electron-light interaction property in material system. Anomalous property can be driven and observed from the process of interaction. The plasmonic metal nanostructures have been received great attention from the past due to their exceptional property. Similarly, they have a great potential for future investigation.

## References

- 1 Freestone, I., Meeks, N., Sax, M. & Higgitt, C. The Lycurgus cup—a roman nanotechnology. *Gold Bulletin* **40**, 270-277 (2007).
- 2 Barber, D. & Freestone, I. C. An investigation of the origin of the colour of the Lycurgus Cup by analytical transmission electron microscopy. *Archaeometry* **32**, 33-45 (1990).
- 3 Jin, R. *et al.* Photoinduced conversion of silver nanospheres to nanoprisms. *Science* **294**, 1901-1903 (2001).
- 4 Faraday, M. The Bakerian lecture: experimental relations of gold (and other metals) to light. *Philosophical Transactions of the Royal Society of London* **147**, 145-181 (1857).
- 5 Turkevich, J. Colloidal gold. Part II. *Gold Bulletin* **18**, 125-131 (1985).
- 6 Faraday, M. LIX. Experimental relations of gold (and other metals) to light.—The bakerian lecture. *The London, Edinburgh, and Dublin Philosophical Magazine and Journal of Science* **14**, 512-539 (1857).
- 7 Tyndall effect, <<https://www.thoughtco.com/definition-of-tyndall-effect-605756>> (
- 8 Berenger, J.-P. A perfectly matched layer for the absorption of electromagnetic waves. *Journal of computational physics* **114**, 185-200 (1994).
- 9 Dreaden, E. C., Alkilany, A. M., Huang, X., Murphy, C. J. & El-Sayed, M. A. The golden age: gold nanoparticles for biomedicine. *Chemical Society Reviews* **41**, 2740-2779 (2012).
- 10 Turkevich, J., Stevenson, P. C. & Hillier, J. A study of the nucleation and growth processes in the synthesis of colloidal gold. *Discussions of the Faraday Society* **11**, 55-75 (1951).
- 11 Frens, G. Particle size and sol stability in metal colloids. *Colloid & Polymer Science* **250**, 736-741 (1972).
- 12 Frens, G. Controlled nucleation for the regulation of the particle size in monodisperse gold suspensions. *Nature* **241**, 20-22 (1973).
- 13 Ji, X. *et al.* Size control of gold nanocrystals in citrate reduction: the third role of citrate. *Journal of the American Chemical Society* **129**, 13939-13948 (2007).
- 14 LaMer, V. K. & Dinegar, R. H. Theory, production and mechanism of formation of monodispersed hydrosols. *Journal of the American Chemical Society* **72**, 4847-4854 (1950).
- 15 Dunne, P. W., Munn, A. S., Starkey, C. L., Huddle, T. A. & Lester, E. H. Continuous-flow hydrothermal synthesis for the

- production of inorganic nanomaterials. *Phil. Trans. R. Soc. A* **373**, 20150015 (2015).
- 16 Bastús, N. G., Comenge, J. & Puentes, V. Kinetically controlled seeded growth synthesis of citrate-stabilized gold nanoparticles of up to 200 nm: size focusing versus Ostwald ripening. *Langmuir* **27**, 11098-11105 (2011).
- 17 Polte, J. r. *et al.* Mechanism of gold nanoparticle formation in the classical citrate synthesis method derived from coupled in situ XANES and SAXS evaluation. *Journal of the American Chemical Society* **132**, 1296-1301 (2010).
- 18 Yu, Y.-Y., Chang, S.-S., Lee, C.-L. & Wang, C. C. Gold nanorods: electrochemical synthesis and optical properties. *The Journal of Physical Chemistry B* **101**, 6661-6664 (1997).
- 19 Jana, N. R., Gearheart, L. & Murphy, C. J. Seed-mediated growth approach for shape-controlled synthesis of spheroidal and rod-like gold nanoparticles using a surfactant template. *Advanced Materials* **13**, 1389 (2001).
- 20 Nikoobakht, B. & El-Sayed, M. A. Preparation and growth mechanism of gold nanorods (NRs) using seed-mediated growth method. *Chem. Mater* **15**, 1957-1962 (2003).
- 21 Ali, M. R., Snyder, B. & El-Sayed, M. A. Synthesis and optical properties of small Au nanorods using a seedless growth technique. *Langmuir* **28**, 9807-9815 (2012).
- 22 Xu, X. *et al.* Seedless synthesis of high aspect ratio gold nanorods with high yield. *Journal of Materials Chemistry A* **2**, 3528-3535 (2014).
- 23 Wilcoxon, J. & Abrams, B. Synthesis, structure and properties of metal nanoclusters. *Chemical Society Reviews* **35**, 1162-1194 (2006).
- 24 Burrows, N. D. *et al.* Anisotropic nanoparticles and anisotropic surface chemistry. *The journal of physical chemistry letters* **7**, 632-641 (2016).
- 25 Tian, N., Zhou, Z.-Y. & Sun, S.-G. Platinum metal catalysts of high-index surfaces: from single-crystal planes to electrochemically shape-controlled nanoparticles. *The Journal of Physical Chemistry C* **112**, 19801-19817 (2008).
- 26 Yu, N. F. *et al.* Electrochemical synthesis of tetrahedral rhodium nanocrystals with extraordinarily high surface energy and high electrocatalytic activity. *Angewandte Chemie International Edition* **53**, 5097-5101 (2014).
- 27 Macia, M., Campina, J., Herrero, E. & Feliu, J. On the kinetics of oxygen reduction on platinum stepped surfaces in acidic media. *Journal of Electroanalytical Chemistry* **564**, 141-150 (2004).

- 28 Xiong, Y. & Xia, Y. Shape-controlled synthesis of metal nanostructures: the case of palladium. *Advanced Materials* **19**, 3385-3391 (2007).
- 29 Magnussen, O. Ordered anion adlayers on metal electrode surfaces. *Chemical reviews* **102**, 679-726 (2002).
- 30 Meena, S. K. *et al.* The role of halide ions in the anisotropic growth of gold nanoparticles: a microscopic, atomistic perspective. *Physical Chemistry Chemical Physics* **18**, 13246-13254 (2016).
- 31 Millstone, J. E., Wei, W., Jones, M. R., Yoo, H. & Mirkin, C. A. Iodide ions control seed-mediated growth of anisotropic gold nanoparticles. *Nano letters* **8**, 2526-2529 (2008).
- 32 Eguchi, M., Mitsui, D., Wu, H.-L., Sato, R. & Teranishi, T. Simple reductant concentration-dependent shape control of polyhedral gold nanoparticles and their plasmonic properties. *Langmuir* **28**, 9021-9026 (2012).
- 33 Wu, H.-L., Kuo, C.-H. & Huang, M. H. Seed-mediated synthesis of gold nanocrystals with systematic shape evolution from cubic to trisoctahedral and rhombic dodecahedral structures. *Langmuir* **26**, 12307-12313 (2010).
- 34 Ahn, H.-Y., Lee, H.-E., Jin, K. & Nam, K. T. Extended gold nano-morphology diagram: synthesis of rhombic dodecahedra using CTAB and ascorbic acid. *Journal of Materials Chemistry C* **1**, 6861-6868 (2013).
- 35 Park, K., Koerner, H. & Vaia, R. A. Depletion-induced shape and size selection of gold nanoparticles. *Nano letters* **10**, 1433-1439 (2010).
- 36 Yang, P.-W. *et al.* Tracing the Surfactant-Mediated Nucleation, Growth, and Superpacking of Gold Supercrystals Using Time and Spatially Resolved X-ray Scattering. *Langmuir* **33**, 3253-3261 (2017).
- 37 Bastus, N. G., Comenge, J. & Puntès, V. Kinetically Controlled Seeded Growth Synthesis of Citrate-Stabilized Gold Nanoparticles of up to 200 nm: Size Focusing versus Ostwald Ripening. *Langmuir* **27**, 11098-11105, doi:10.1021/la201938u (2011).
- 38 Eguchi, M., Mitsui, D., Wu, H. L., Sato, R. & Teranishi, T. Simple Reductant Concentration-Dependent Shape Control of Polyhedral Gold Nanoparticles and Their Plasmonic Properties. *Langmuir* **28**, 9021-9026, doi:10.1021/la3002114 (2012).
- 39 Wang, Z. L. Transmission electron microscopy of shape-controlled nanocrystals and their assemblies. *J Phys Chem B* **104**, 1153-1175, doi:Doi 10.1021/Jp993593c (2000).

- 40 Li, C. *et al.* High-Yield Synthesis of Single-Crystalline Gold  
Nano-octahedra. *Angewandte Chemie* **119**, 3328-3332 (2007).
- 41 Ringe, E. *et al.* Unraveling the Effects of Size, Composition, and  
Substrate on the Localized Surface Plasmon Resonance  
Frequencies of Gold and Silver Nanocubes: A Systematic Single-  
Particle Approach. *Journal of Physical Chemistry C* **114**, 12511-  
12516, doi:10.1021/jp104366r (2010).
- 42 Mudunkotuwa, I. A. & Grassian, V. H. Citric Acid Adsorption  
on TiO<sub>2</sub> Nanoparticles in Aqueous Suspensions at Acidic and  
Circumneutral pH: Surface Coverage, Surface Speciation, and Its  
Impact on Nanoparticle-Nanoparticle Interactions. *Journal of the  
American Chemical Society* **132**, 14986-14994,  
doi:10.1021/ja106091q (2010).
- 43 *Laser & Diffraction Grating*,  
<[http://physicsopenlab.org/2017/08/29/laser-diffraction-  
grating/](http://physicsopenlab.org/2017/08/29/laser-diffraction-grating/)>
- 44 Wood, R. W. XLII. On a remarkable case of uneven distribution  
of light in a diffraction grating spectrum. *The London, Edinburgh,  
and Dublin Philosophical Magazine and Journal of Science* **4**,  
396-402 (1902).
- 45 Wood, R. W. Anomalous diffraction gratings. *Physical Review*  
**48**, 928 (1935).
- 46 Fano, U. Effects of configuration interaction on intensities and  
phase shifts. *Physical Review* **124**, 1866 (1961).
- 47 Miroshnichenko, A. E., Flach, S. & Kivshar, Y. S. Fano  
resonances in nanoscale structures. *Reviews of Modern Physics*  
**82**, 2257 (2010).
- 48 Luk'yanchuk, B. *et al.* The Fano resonance in plasmonic  
nanostructures and metamaterials. *Nature materials* **9**, 707-715  
(2010).
- 49 Lindquist, N. C., Nagpal, P., McPeak, K. M., Norris, D. J. & Oh,  
S.-H. Engineering metallic nanostructures for plasmonics and  
nanophotonics. *Reports on Progress in Physics* **75**, 036501  
(2012).
- 50 McFarland, A. D. & Van Duyne, R. P. Single silver nanoparticles  
as real-time optical sensors with zeptomole sensitivity. *Nano  
letters* **3**, 1057-1062 (2003).
- 51 Clavero, C. Plasmon-induced hot-electron generation at  
nanoparticle/metal-oxide interfaces for photovoltaic and  
photocatalytic devices. *Nature Photonics* **8**, 95-103 (2014).
- 52 Yamada, K., Miyajima, K. & Mafuné, F. Thermionic emission of  
electrons from gold nanoparticles by nanosecond pulse-laser  
excitation of interband. *The Journal of Physical Chemistry C* **111**,  
11246-11251 (2007).

- 53 Jain, P. K., Lee, K. S., El-Sayed, I. H. & El-Sayed, M. A. Calculated absorption and scattering properties of gold nanoparticles of different size, shape, and composition: applications in biological imaging and biomedicine. *J. Phys. Chem. B* **110**, 7238-7248 (2006).
- 54 Stampelcoskie, K. G. & Kamat, P. V. Size-dependent excited state behavior of glutathione-capped gold clusters and their light-harvesting capacity. *Journal of the American Chemical Society* **136**, 11093-11099 (2014).
- 55 Koppen, J. V., Hapka, M., Szczeńsiak, M. M. & Chałasiński, G. Optical absorption spectra of gold clusters Au<sub>n</sub> (n= 4, 6, 8, 12, 20) from long-range corrected functionals with optimal tuning. *The Journal of chemical physics* **137**, 114302 (2012).
- 56 Ringe, E. *et al.* Unraveling the effects of size, composition, and substrate on the localized surface plasmon resonance frequencies of gold and silver nanocubes: a systematic single-particle approach. *The Journal of Physical Chemistry C* **114**, 12511-12516 (2010).
- 57 Trasatti, S. The absolute electrode potential: an explanatory note (Recommendations 1986). *Pure and Applied Chemistry* **58**, 955-966 (1986).
- 58 Fujishima, A. & Honda, K. Electrochemical photolysis of water at a semiconductor electrode. *nature* **238**, 37-38 (1972).
- 59 Walter, M. G. *et al.* Solar water splitting cells. *Chemical reviews* **110**, 6446-6473 (2010).
- 60 Li, J. & Wu, N. Semiconductor-based photocatalysts and photoelectrochemical cells for solar fuel generation: a review. *Catalysis Science & Technology* **5**, 1360-1384 (2015).
- 61 Chen, S. & Wang, L.-W. Thermodynamic oxidation and reduction potentials of photocatalytic semiconductors in aqueous solution. *Chemistry of Materials* **24**, 3659-3666 (2012).
- 62 McEvoy, A., Etman, M. & Hemming, M. Interface charging and intercalations effects on d-band transition metal diselenide photoelectrodes. *Journal of electroanalytical chemistry and interfacial electrochemistry* **190**, 225-241 (1985).
- 63 Yang, X., Du, C., Liu, R., Xie, J. & Wang, D. Balancing photovoltage generation and charge-transfer enhancement for catalyst-decorated photoelectrochemical water splitting: A case study of the hematite/MnO<sub>x</sub> combination. *Journal of catalysis* **304**, 86-91 (2013).
- 64 Bard, A. J., Bocarsly, A. B., Fan, F. R. F., Walton, E. G. & Wrighton, M. S. The concept of Fermi level pinning at semiconductor/liquid junctions. Consequences for energy conversion efficiency and selection of useful solution redox

- couples in solar devices. *Journal of the American Chemical Society* **102**, 3671-3677 (1980).
- 65 Sivula, K. Metal oxide photoelectrodes for solar fuel production, surface traps, and catalysis. *J. Phys. Chem. Lett* **4**, 1624-1633 (2013).
- 66 Prévot, M. S. *et al.* Evaluating Charge Carrier Transport and Surface States in CuFeO<sub>2</sub> Photocathodes. *Chemistry of Materials* (2017).
- 67 Du, C. *et al.* Hematite-based water splitting with low turn-on voltages. *Angewandte Chemie International Edition* **52**, 12692-12695 (2013).
- 68 Mayer, M. T. Photovoltage at semiconductor–electrolyte junctions. *Current Opinion in Electrochemistry* (2017).
- 69 Stubbe, J., Nocera, D. G., Yee, C. S. & Chang, M. C. Radical initiation in the class I ribonucleotide reductase: long-range proton-coupled electron transfer? *Chemical reviews* **103**, 2167-2202 (2003).
- 70 Nozik, A. J. & Memming, R. Physical chemistry of semiconductor– liquid interfaces. *The Journal of Physical Chemistry* **100**, 13061-13078 (1996).
- 71 Shockley, W. & Queisser, H. J. Detailed balance limit of efficiency of p-n junction solar cells. *Journal of applied physics* **32**, 510-519 (1961).
- 72 Werner, J. H., Kolodinski, S. & Queisser, H. J. Novel optimization principles and efficiency limits for semiconductor solar cells. *Physical review letters* **72**, 3851 (1994).
- 73 Fountaine, K. T., Lewerenz, H. J. & Atwater, H. A. Efficiency limits for photoelectrochemical water-splitting. *Nature communications* **7** (2016).
- 74 Mooradian, A. Photoluminescence of metals. *Physical Review Letters* **22**, 185 (1969).
- 75 Apell, P., Monreal, R. & Lundqvist, S. Photoluminescence of noble metals. *Physica Scripta* **38**, 174 (1988).
- 76 Noginov, M. *et al.* Stimulated emission of surface plasmon polaritons. *Physical review letters* **101**, 226806 (2008).
- 77 Shahbazyan, T. V. Theory of plasmon-enhanced metal photoluminescence. *Nano letters* **13**, 194-198 (2012).
- 78 Govorov, A. O., Zhang, H., Demir, H. V. & Gun'ko, Y. K. Photogeneration of hot plasmonic electrons with metal nanocrystals: Quantum description and potential applications. *Nano Today* **9**, 85-101 (2014).
- 79 Cushing, S. K., Bristow, A. D. & Wu, N. Theoretical maximum efficiency of solar energy conversion in plasmonic metal–

- semiconductor heterojunctions. *Physical Chemistry Chemical Physics* **17**, 30013-30022 (2015).
- 80 Valenti, M., Jonsson, M., Biskos, G., Schmidt-Ott, A. & Smith, W. Plasmonic nanoparticle-semiconductor composites for efficient solar water splitting. *Journal of Materials Chemistry A* **4**, 17891-17912 (2016).
- 81 Liu, G. *et al.* Plasmon-dominated photoelectrodes for solar water splitting. *Journal of Materials Chemistry A* **5**, 4233-4253 (2017).
- 82 Tatsuma, T., Nishi, H. & Ishida, T. Plasmon-induced charge separation: chemistry and wide applications. *Chemical Science* **8**, 3325-3337 (2017).
- 83 Cushing, S. K. *et al.* Photocatalytic activity enhanced by plasmonic resonant energy transfer from metal to semiconductor. *Journal of the American Chemical Society* **134**, 15033-15041 (2012).
- 84 Wu, K., Chen, J., McBride, J. R. & Lian, T. Efficient hot-electron transfer by a plasmon-induced interfacial charge-transfer transition. *Science* **349**, 632-635 (2015).
- 85 Zhang, X., Chen, Y. L., Liu, R.-S. & Tsai, D. P. Plasmonic photocatalysis. *Reports on Progress in Physics* **76**, 046401 (2013).
- 86 Ingram, D. B. & Linic, S. Water splitting on composite plasmonic-metal/semiconductor photoelectrodes: evidence for selective plasmon-induced formation of charge carriers near the semiconductor surface. *Journal of the American Chemical Society* **133**, 5202-5205 (2011).
- 87 Christopher, P., Xin, H., Marimuthu, A. & Linic, S. Singular characteristics and unique chemical bond activation mechanisms of photocatalytic reactions on plasmonic nanostructures. *Nature materials* **11**, 1044-1050 (2012).
- 88 Linic, S., Christopher, P. & Ingram, D. B. Plasmonic-metal nanostructures for efficient conversion of solar to chemical energy. *Nature materials* **10**, 911-921 (2011).
- 89 Beversluis, M. R., Bouhelier, A. & Novotny, L. Continuum generation from single gold nanostructures through near-field mediated intraband transitions. *Physical Review B* **68**, 115433 (2003).
- 90 Sönnichsen, C. *et al.* Drastic reduction of plasmon damping in gold nanorods. *Physical review letters* **88**, 077402 (2002).
- 91 Dulkeith, E. *et al.* Plasmon emission in photoexcited gold nanoparticles. *Physical Review B* **70**, 205424 (2004).
- 92 Sarina, S. *et al.* Viable Photocatalysts under Solar-Spectrum Irradiation: Nonplasmonic Metal Nanoparticles. *Angewandte Chemie International Edition* **53**, 2935-2940 (2014).

- 93 Zhu, H. *et al.* Mechanism of supported gold nanoparticles as photocatalysts under ultraviolet and visible light irradiation. *Chemical Communications*, 7524-7526 (2009).
- 94 Yan, J., Wu, G., Guan, N. & Li, L. Synergetic promotion of the photocatalytic activity of TiO<sub>2</sub> by gold deposition under UV-visible light irradiation. *Chemical Communications* **49**, 11767-11769 (2013).
- 95 Lin, Z. *et al.* On the role of localized surface plasmon resonance in UV-Vis light irradiated Au/TiO<sub>2</sub> photocatalysis systems: pros and cons. *Nanoscale* **7**, 4114-4123 (2015).
- 96 Hung, S. F. *et al.* Iridium Oxide-Assisted Plasmon-Induced Hot Carriers: Improvement on Kinetics and Thermodynamics of Hot Carriers. *Advanced Energy Materials* **6** (2016).
- 97 Liu, Z., Hou, W., Pavaskar, P., Aykol, M. & Cronin, S. B. Plasmon resonant enhancement of photocatalytic water splitting under visible illumination. *Nano letters* **11**, 1111-1116 (2011).
- 98 Brennan, L. J. *et al.* Hot plasmonic electrons for generation of enhanced photocurrent in gold-TiO<sub>2</sub> nanocomposites. *Nanoscale research letters* **10**, 38 (2015).
- 99 Thomann, I. *et al.* Plasmon enhanced solar-to-fuel energy conversion. *Nano letters* **11**, 3440-3446 (2011).
- 100 Warren, S. C. & Thimsen, E. Plasmonic solar water splitting. *Energy & Environmental Science* **5**, 5133-5146 (2012).
- 101 Maier, S. A. & Atwater, H. A. Plasmonics: Localization and guiding of electromagnetic energy in metal/dielectric structures. *Journal of Applied Physics* **98**, doi:Artn 01110110.1063/1.1951057 (2005).
- 102 Liz-Marzan, L. M. Tailoring surface plasmons through the morphology and assembly of metal nanoparticles. *Langmuir* **22**, 32-41, doi:10.1021/la0513353 (2006).
- 103 Chen, H., Liu, G. & Wang, L. Switched photocurrent direction in Au/TiO<sub>2</sub> bilayer thin films. *Scientific reports* **5** (2015).
- 104 Cushing, S. K. *et al.* Photocatalytic Activity Enhanced by Plasmonic Resonant Energy Transfer from Metal to Semiconductor. *Journal of the American Chemical Society* **134**, 15033-15041, doi:10.1021/ja305603t (2012).
- 105 Li, J. T. *et al.* Plasmon-induced resonance energy transfer for solar energy conversion. *Nature Photonics* **9**, 601-+, doi:10.1038/Nphoton.2015.142 (2015).
- 106 Wu, K., Chen, J., McBride, J. & Lian, T. Efficient hot-electron transfer by a plasmon-induced interfacial charge-transfer transition. *Science* **349**, 632-635 (2015).

- 107 Liu, Z. W., Hou, W. B., Pavaskar, P., Aykol, M. & Cronin, S. B. Plasmon Resonant Enhancement of Photocatalytic Water Splitting Under Visible Illumination. *Nano Letters* **11**, 1111-1116, doi:10.1021/nl104005n (2011).
- 108 Thimsen, E., Le Formal, F., Gratzel, M. & Warren, S. C. Influence of Plasmonic Au Nanoparticles on the Photoactivity of Fe<sub>2</sub>O<sub>3</sub> Electrodes for Water Splitting. *Nano Letters* **11**, 35-43, doi:10.1021/nl1022354 (2011).
- 109 Thomann, I. *et al.* Plasmon Enhanced Solar-to-Fuel Energy Conversion. *Nano Letters* **11**, 3440-3446, doi:10.1021/nl201908s (2011).
- 110 Zhang, N., Yang, M.-Q., Liu, S., Sun, Y. & Xu, Y.-J. Waltzing with the versatile platform of graphene to synthesize composite photocatalysts. *Chemical reviews* **115**, 10307-10377 (2015).
- 111 Liu, S., Han, C., Tang, Z.-R. & Xu, Y.-J. Heterostructured semiconductor nanowire arrays for artificial photosynthesis. *Materials Horizons* (2016).
- 112 Han, C., Zhang, N. & Xu, Y.-J. Structural diversity of graphene materials and their multifarious roles in heterogeneous photocatalysis. *Nano Today* (2016).
- 113 Zhan, Z. Y., An, J. N., Zhang, H. C., Hansen, R. V. & Zheng, L. X. Three-Dimensional Plasmonic Photoanodes Based on Au-Embedded TiO<sub>2</sub> Structures for Enhanced Visible-Light Water Splitting. *Acs Applied Materials & Interfaces* **6**, 1139-1144, doi:10.1021/am404738a (2014).
- 114 Xu, Z. *et al.* Understanding the Enhancement Mechanisms of Surface Plasmon-Mediated Photoelectrochemical Electrodes: A Case Study on Au Nanoparticle Decorated TiO<sub>2</sub> Nanotubes. *Advanced Materials Interfaces* **2**, doi:Artn 150016910.1002/Admi.201500169 (2015).
- 115 Lee, J., Mubeen, S., Ji, X. L., Stucky, G. D. & Moskovits, M. Plasmonic Photoanodes for Solar Water Splitting with Visible Light. *Nano Letters* **12**, 5014-5019, doi:10.1021/nl302796f (2012).
- 116 Govorov, A. O., Zhang, H. & Gun'ko, Y. K. Theory of photoinjection of hot plasmonic carriers from metal nanostructures into semiconductors and surface molecules. *The Journal of Physical Chemistry C* **117**, 16616-16631 (2013).
- 117 Walter, M. G. *et al.* Solar Water Splitting Cells. *Chemical Reviews* **110**, 6446-6473, doi:10.1021/cr1002326 (2010).
- 118 Jain, P. K., Lee, K. S., El-Sayed, I. H. & El-Sayed, M. A. Calculated absorption and scattering properties of gold nanoparticles of different size, shape, and composition:

- Applications in biological imaging and biomedicine. *Journal of Physical Chemistry B* **110**, 7238-7248, doi:10.1021/jp057170o (2006).
- 119 Govorov, A. O., Zhang, H., Demir, H. V. & Gun'ko, Y. K. Photogeneration of hot plasmonic electrons with metal nanocrystals: Quantum description and potential applications. *Nano Today* **9**, 85-101, doi:10.1016/j.nantod.2014.02.006 (2014).
- 120 Kim, H. J. *et al.* Plasmon-Enhanced Photoelectrochemical Water Splitting with Size-Controllable Gold Nanodot Arrays. *ACS nano* **8**, 10756-10765 (2014).
- 121 Pu, Y. C. *et al.* Au Nanostructure-Decorated TiO<sub>2</sub> Nanowires Exhibiting Photoactivity Across Entire UV-visible Region for Photoelectrochemical Water Splitting. *Nano Letters* **13**, 3817-3823, doi:10.1021/nl4018385 (2013).
- 122 Archana, P. S., Pachauri, N., Shan, Z. C., Pan, S. L. & Gupta, A. Plasmonic Enhancement of Photoactivity by Gold Nanoparticles Embedded in Hematite Films. *Journal of Physical Chemistry C* **119**, 15506-15516, doi:10.1021/acs.jpcc.5b02357 (2015).
- 123 Zhang, N. *et al.* Near-field dielectric scattering promotes optical absorption by platinum nanoparticles. *Nature Photonics* (2016).
- 124 Kazuma, E. & Tatsuma, T. Photoelectrochemical Analysis of Allowed and Forbidden Multipole Plasmon Modes of Polydisperse Ag Nanorods. *Journal of Physical Chemistry C* **117**, 2435-2441, doi:10.1021/jp300175y (2013).
- 125 Kundu, S. A new route for the formation of Au nanowires and application of shape-selective Au nanoparticles in SERS studies. *Journal of Materials Chemistry C* **1**, 831-842 (2013).
- 126 Barman, T., Hussain, A. A., Sharma, B. & Pal, A. R. Plasmonic Hot Hole Generation by Interband Transition in Gold-Polyaniline. *Scientific reports* **5** (2015).
- 127 Hung, S. F. *et al.* Iridium Oxide-Assisted Plasmon-Induced Hot Carriers: Improvement on Kinetics and Thermodynamics of Hot Carriers. *Advanced Energy Materials* (2016).
- 128 Atwater, H. A. & Polman, A. Plasmonics for improved photovoltaic devices. *Nature materials* **9**, 205-213 (2010).
- 129 Jain, P. K., Lee, K. S., El-Sayed, I. H. & El-Sayed, M. A. Calculated absorption and scattering properties of gold nanoparticles of different size, shape, and composition: applications in biological imaging and biomedicine. *The Journal of Physical Chemistry B* **110**, 7238-7248 (2006).
- 130 Wang, Y.-C., Engelhard, M. H., Baer, D. R. & Castner, D. G. Quantifying the Impact of Nanoparticle Coatings and Nonuniformities on XPS Analysis: Gold/Silver Core-Shell Nanoparticles. *Analytical chemistry* **88**, 3917-3925 (2016).

- 131 Morgan, T. T., Goff, T. M. & Adair, J. H. The colloidal stability of fluorescent calcium phosphosilicate nanoparticles: the effects of evaporation and redispersion on particle size distribution. *Nanoscale* **3**, 2044-2053 (2011).
- 132 Hinterwirth, H. *et al.* Quantifying thiol ligand density of self-assembled monolayers on gold nanoparticles by inductively coupled plasma–mass spectrometry. *ACS nano* **7**, 1129-1136 (2013).
- 133 Trasatti, S. Electrocatalysis by oxides—attempt at a unifying approach. *Journal of Electroanalytical Chemistry and Interfacial Electrochemistry* **111**, 125-131 (1980).
- 134 Kanan, M. W. & Nocera, D. G. In situ formation of an oxygen-evolving catalyst in neutral water containing phosphate and  $\text{Co}^{2+}$ . *Science* **321**, 1072-1075 (2008).
- 135 Gaspar, D. *et al.* Influence of the layer thickness in plasmonic gold nanoparticles produced by thermal evaporation. *Scientific reports* **3** (2013).
- 136 Khatri, O. P., Murase, K. & Sugimura, H. Structural organization of gold nanoparticles onto the ITO surface and its optical properties as a function of ensemble size. *Langmuir* **24**, 3787-3793 (2008).
- 137 Archana, P. S., Pachauri, N., Shan, Z., Pan, S. & Gupta, A. Plasmonic Enhancement of Photoactivity by Gold Nanoparticles Embedded in Hematite Films. *The Journal of Physical Chemistry C* **119**, 15506-15516 (2015).
- 138 Andoshe, D. M. *et al.* A wafer-scale antireflective protection layer of solution-processed  $\text{TiO}_2$  nanorods for high performance silicon-based water splitting photocathodes. *Journal of Materials Chemistry A* **4**, 9477-9485, doi:10.1039/C6TA02987F (2016).
- 139 Subramanian, V., Wolf, E. & Kamat, P. V. Semiconductor-metal composite nanostructures. To what extent do metal nanoparticles improve the photocatalytic activity of  $\text{TiO}_2$  films? *The Journal of Physical Chemistry B* **105**, 11439-11446 (2001).
- 140 Reguera, J. *et al.* Synthesis of Janus plasmonic-magnetic, star-sphere nanoparticles, and their application in SERS detection. *Faraday Discussions* (2016).
- 141 Bard, A. J. & Faulkner, L. R. Fundamentals and applications. *Electrochemical Methods, 2nd ed.*; Wiley: New York (2001).
- 142 Hong, S. J., Lee, S., Jang, J. S. & Lee, J. S. Heterojunction  $\text{BiVO}_4/\text{WO}_3$  electrodes for enhanced photoactivity of water oxidation. *Energy & Environmental Science* **4**, 1781-1787 (2011).
- 143 Tran, P. D., Wong, L. H., Barber, J. & Loo, J. S. Recent advances in hybrid photocatalysts for solar fuel production. *Energy & Environmental Science* **5**, 5902-5918 (2012).

- 144 Gray, H. B. Powering the planet with solar fuel. *Nature chemistry* **1**, 7-7 (2009).
- 145 Dahl, S. & Chorkendorff, I. Solar-fuel generation: towards practical implementation. *Nature materials* **11**, 100-101 (2012).
- 146 Listorti, A., Durrant, J. & Barber, J. Artificial photosynthesis: solar to fuel. *Nature materials* **8**, 929-930 (2009).
- 147 Tang, D. *et al.* Carbon quantum dots enhance the photocatalytic performance of BiVO<sub>4</sub> with different exposed facets. *Dalton Transactions* **42**, 6285-6289 (2013).
- 148 Paracchino, A., Laporte, V., Sivula, K., Grätzel, M. & Thimsen, E. Highly active oxide photocathode for photoelectrochemical water reduction. *Nature materials* **10**, 456-461 (2011).
- 149 Cowan, A. J. *et al.* Activation energies for the rate-limiting step in water photooxidation by nanostructured  $\alpha$ -Fe<sub>2</sub>O<sub>3</sub> and TiO<sub>2</sub>. *Journal of the American Chemical Society* **133**, 10134-10140 (2011).
- 150 Kay, A., Cesar, I. & Grätzel, M. New benchmark for water photooxidation by nanostructured  $\alpha$ -Fe<sub>2</sub>O<sub>3</sub> films. *Journal of the American Chemical Society* **128**, 15714-15721 (2006).
- 151 Sivula, K., Le Formal, F. & Grätzel, M. Solar water splitting: progress using hematite ( $\alpha$ -Fe<sub>2</sub>O<sub>3</sub>) photoelectrodes. *ChemSusChem* **4**, 432-449 (2011).
- 152 Wang, G. *et al.* Facile synthesis of highly photoactive  $\alpha$ -Fe<sub>2</sub>O<sub>3</sub>-based films for water oxidation. *Nano letters* **11**, 3503-3509 (2011).
- 153 Zhong, D. K. & Gamelin, D. R. Photoelectrochemical water oxidation by cobalt catalyst ("Co- Pi")/ $\alpha$ -Fe<sub>2</sub>O<sub>3</sub> composite photoanodes: oxygen evolution and resolution of a kinetic bottleneck. *Journal of the American Chemical Society* **132**, 4202-4207 (2010).
- 154 Kim, T. W. & Choi, K.-S. Nanoporous BiVO<sub>4</sub> photoanodes with dual-layer oxygen evolution catalysts for solar water splitting. *Science* **343**, 990-994 (2014).
- 155 Park, Y., McDonald, K. J. & Choi, K.-S. Progress in bismuth vanadate photoanodes for use in solar water oxidation. *Chemical Society Reviews* **42**, 2321-2337 (2013).
- 156 Huang, Z.-F., Pan, L., Zou, J.-J., Zhang, X. & Wang, L. Nanostructured bismuth vanadate-based materials for solar-energy-driven water oxidation: a review on recent progress. *Nanoscale* **6**, 14044-14063 (2014).
- 157 Seabold, J. A. & Choi, K.-S. Efficient and stable photo-oxidation of water by a bismuth vanadate photoanode coupled with an iron oxyhydroxide oxygen evolution catalyst. *Journal of the American Chemical Society* **134**, 2186-2192 (2012).

- 158 Lee, M. G. *et al.* Conformally coated BiVO<sub>4</sub> nanodots on porosity-controlled WO<sub>3</sub> nanorods as highly efficient type II heterojunction photoanodes for water oxidation. *Nano Energy* **28**, 250-260 (2016).
- 159 Zhong, D. K., Choi, S. & Gamelin, D. R. Near-complete suppression of surface recombination in solar photoelectrolysis by “Co-Pi” catalyst-modified W: BiVO<sub>4</sub>. *Journal of the American Chemical Society* **133**, 18370-18377 (2011).
- 160 Chatchai, P., Murakami, Y., Kishioka, S.-y., Nosaka, A. Y. & Nosaka, Y. Efficient photocatalytic activity of water oxidation over WO<sub>3</sub>/BiVO<sub>4</sub> composite under visible light irradiation. *Electrochimica Acta* **54**, 1147-1152 (2009).
- 161 Rao, P. M. *et al.* Simultaneously efficient light absorption and charge separation in WO<sub>3</sub>/BiVO<sub>4</sub> core/shell nanowire photoanode for photoelectrochemical water oxidation. *Nano letters* **14**, 1099-1105 (2014).
- 162 Bae, E.-J. *et al.* Glucocerebrosidase depletion enhances cell-to-cell transmission of  $\alpha$ -synuclein. *Nature communications* **5** (2014).
- 163 Chae, S. Y. *et al.* Morphology control of one-dimensional heterojunctions for highly efficient photoanodes used for solar water splitting. *Journal of Materials Chemistry A* **2**, 11408-11416 (2014).
- 164 Liang, Y., Tsubota, T., Mooij, L. P. & Van de Krol, R. Highly improved quantum efficiencies for thin film BiVO<sub>4</sub> photoanodes. *The Journal of Physical Chemistry C* **115**, 17594-17598 (2011).
- 165 Saito, R., Miseki, Y. & Sayama, K. Highly efficient photoelectrochemical water splitting using a thin film photoanode of BiVO<sub>4</sub>/SnO<sub>2</sub>/WO<sub>3</sub> multi-composite in a carbonate electrolyte. *Chemical Communications* **48**, 3833-3835 (2012).
- 166 Long, M., Cai, W. & Kisch, H. Visible light induced photoelectrochemical properties of n-BiVO<sub>4</sub> and n-BiVO<sub>4</sub>/p-Co<sub>3</sub>O<sub>4</sub>. *The Journal of Physical Chemistry C* **112**, 548-554 (2008).
- 167 Pihosh, Y. *et al.* Nanostructured WO<sub>3</sub>/BiVO<sub>4</sub> photoanodes for efficient photoelectrochemical water splitting. *Small* **10**, 3692-3699 (2014).
- 168 Zhang, L., Herrmann, L. O. & Baumberg, J. J. Size dependent plasmonic effect on BiVO<sub>4</sub> photoanodes for solar water splitting. *Scientific reports* **5** (2015).
- 169 Li, J. *et al.* Plasmon-induced photonic and energy-transfer enhancement of solar water splitting by a hematite nanorod array. *Nature communications* **4**, 2651 (2013).

- 170 Chen, H. M. *et al.* Plasmon inducing effects for enhanced  
photoelectrochemical water splitting: X-ray absorption approach  
to electronic structures. *ACS nano* **6**, 7362-7372 (2012).
- 171 Halas, N. J., Lal, S., Chang, W.-S., Link, S. & Nordlander, P.  
Plasmons in strongly coupled metallic nanostructures. *Chem. Rev*  
**111**, 3913-3961 (2011).
- 172 Hu, D., Diao, P., Xu, D. & Wu, Q. Gold/WO<sub>3</sub> nanocomposite  
photoanodes for plasmonic solar water splitting. *Nano Research*  
**9**, 1735-1751 (2016).
- 173 Chatchai, P., Kishioka, S.-y., Murakami, Y., Nosaka, A. Y. &  
Nosaka, Y. Enhanced photoelectrocatalytic activity of FTO/WO<sub>3</sub>/BiVO<sub>4</sub>  
electrode modified with gold nanoparticles for water  
oxidation under visible light irradiation. *Electrochimica Acta* **55**,  
592-596 (2010).
- 174 Abdi, F. F., Dabirian, A., Dam, B. & van de Krol, R. Plasmonic  
enhancement of the optical absorption and catalytic efficiency of  
BiVO<sub>4</sub> photoanodes decorated with Ag@ SiO<sub>2</sub> core-shell  
nanoparticles. *Physical Chemistry Chemical Physics* **16**, 15272-  
15277 (2014).
- 175 Bai, S., Jiang, J., Zhang, Q. & Xiong, Y. Steering charge kinetics  
in photocatalysis: intersection of materials syntheses,  
characterization techniques and theoretical simulations.  
*Chemical Society Reviews* **44**, 2893-2939 (2015).
- 176 Moon, C. W. *et al.* Plasmonic Octahedral Gold Nanoparticles of  
Maximized Near Electromagnetic Fields for Enhancing Catalytic  
Hole Transfer in Solar Water Splitting. *Particle & Particle  
Systems Characterization* **34** (2017).
- 177 Wang, M., Ye, M., Iocozzia, J., Lin, C. & Lin, Z. Plasmon-  
Mediated Solar Energy Conversion via Photocatalysis in Noble  
Metal/Semiconductor Composites. *Advanced Science* **3** (2016).
- 178 Zheng, X. & Zhang, L. Photonic nanostructures for solar energy  
conversion. *Energy & Environmental Science* **9**, 2511-2532  
(2016).
- 179 Cao, S.-W. *et al.* Preparation of Au-BiVO<sub>4</sub> heterogeneous  
nanostructures as highly efficient visible-light photocatalysts.  
*ACS applied materials & interfaces* **4**, 418-423 (2011).
- 180 Pu, Y.-C. *et al.* Au nanostructure-decorated TiO<sub>2</sub> nanowires  
exhibiting photoactivity across entire UV-visible region for  
photoelectrochemical water splitting. *Nano letters* **13**, 3817-3823  
(2013).
- 181 Chandrasekar, M. & Pushpavanam, M. Pulse and pulse reverse  
plating—Conceptual, advantages and applications.  
*Electrochimica Acta* **53**, 3313-3322 (2008).

- 182 Qu, N., Zhu, D., Chan, K. & Lei, W. Pulse electrodeposition of  
nanocrystalline nickel using ultra narrow pulse width and high  
peak current density. *Surface and Coatings Technology* **168**, 123-  
128 (2003).
- 183 Mudunkotuwa, I. A. & Grassian, V. H. Citric acid adsorption on  
TiO<sub>2</sub> nanoparticles in aqueous suspensions at acidic and  
circumneutral pH: surface coverage, surface speciation, and its  
impact on nanoparticle–nanoparticle interactions. *Journal of the  
American Chemical Society* **132**, 14986-14994 (2010).
- 184 Daniel, M.-C. & Astruc, D. Gold nanoparticles: assembly,  
supramolecular chemistry, quantum-size-related properties, and  
applications toward biology, catalysis, and nanotechnology.  
*Chemical reviews* **104**, 293-346 (2004).
- 185 Liu, Y. *et al.* Synergistic Effect of Surface Plasmonic particles  
and Surface Passivation layer on ZnO Nanorods Array for  
Improved Photoelectrochemical Water Splitting. *Scientific  
reports* **6**, 29907 (2016).
- 186 Cushing, S. K. *et al.* Controlling plasmon-induced resonance  
energy transfer and hot electron injection processes in Metal@  
TiO<sub>2</sub> core–shell nanoparticles. *The Journal of Physical  
Chemistry C* **119**, 16239-16244 (2015).
- 187 Li, J. *et al.* Plasmon-induced resonance energy transfer for solar  
energy conversion. *Nature Photonics* **9**, 601-607 (2015).
- 188 Zhang, L. *et al.* Plasmonic enhancement in BiVO<sub>4</sub> photonic  
crystals for efficient water splitting. *small* **10**, 3970-3978 (2014).
- 189 Stoughton, S. *et al.* Adsorption-controlled growth of BiVO<sub>4</sub> by  
molecular-beam epitaxy. *APL Materials* **1**, 042112 (2013).
- 190 Dickerson, E. B. *et al.* Gold nanorod assisted near-infrared  
plasmonic photothermal therapy (PPTT) of squamous cell  
carcinoma in mice. *Cancer letters* **269**, 57-66 (2008).
- 191 Jokerst, J. V., Lobovkina, T., Zare, R. N. & Gambhir, S. S.  
Nanoparticle PEGylation for imaging and therapy.  
*Nanomedicine* **6**, 715-728 (2011).
- 192 Lin, F. *et al.* Laser synthesis of gold/oxide nanocomposites.  
*Journal of Materials Chemistry* **20**, 1103-1106 (2010).
- 193 Yeo, J. *et al.* Laser-induced hydrothermal growth of  
heterogeneous metal-oxide nanowire on flexible substrate by  
laser absorption layer design. *ACS nano* **9**, 6059-6068 (2015).
- 194 Gogurla, N., Sinha, A. K., Santra, S., Manna, S. & Ray, S. K.  
Multifunctional Au-ZnO plasmonic nanostructures for enhanced  
UV photodetector and room temperature NO sensing devices.  
*Scientific reports* **4**, 6483 (2014).
- 195 Xia, W. *et al.* Nanoplate-built ZnO hollow microspheres  
decorated with gold nanoparticles and their enhanced

- photocatalytic and gas-sensing properties. *ACS applied materials & interfaces* **7**, 11824-11832 (2015).
- 196 Lee, J., Mubeen, S., Ji, X., Stucky, G. D. & Moskovits, M. Plasmonic photoanodes for solar water splitting with visible light. *Nano letters* **12**, 5014-5019 (2012).
- 197 Pu, Y.-C. *et al.* Au nanostructure-decorated TiO<sub>2</sub> nanowires exhibiting photoactivity across entire UV-visible region for photoelectrochemical water splitting. *Nano letters* **13**, 3817-3823 (2013).
- 198 Jain, P. K., Lee, K. S., El-Sayed, I. H. & El-Sayed, M. A. Calculated absorption and scattering properties of gold nanoparticles of different size, shape, and composition: applications in biological imaging and biomedicine. *Journal of Physical Chemistry B* **110**, 7238 (2006).
- 199 Xiao, M. *et al.* Plasmon-enhanced chemical reactions. *Journal of Materials Chemistry A* **1**, 5790-5805 (2013).
- 200 Sajanlal, P., Subramaniam, C., Sasanpour, P., Rashidian, B. & Pradeep, T. Electric field enhancement and concomitant Raman spectral effects at the edges of a nanometre-thin gold mesotriangle. *Journal of Materials Chemistry* **20**, 2108-2113 (2010).
- 201 Zhang, X., Liu, Y., Lee, S.-T., Yang, S. & Kang, Z. Coupling surface plasmon resonance of gold nanoparticles with slow-photon-effect of TiO<sub>2</sub> photonic crystals for synergistically enhanced photoelectrochemical water splitting. *Energy & Environmental Science* **7**, 1409-1419 (2014).
- 202 Lee, M. G. *et al.* Dominance of Plasmonic Resonant Energy Transfer over Direct Electron Transfer in Substantially Enhanced Water Oxidation Activity of BiVO<sub>4</sub> by Shape-Controlled Au Nanoparticles. *Small* (2017).
- 203 Shi, X., Ueno, K., Takabayashi, N. & Misawa, H. Plasmon-enhanced photocurrent generation and water oxidation with a gold nanoisland-loaded titanium dioxide photoelectrode. *The Journal of Physical Chemistry C* **117**, 2494-2499 (2012).
- 204 Cifuentes, A., Bernal, J. L. & Diez-Masa, J. C. Determination of critical micelle concentration values using capillary electrophoresis instrumentation. *Analytical Chemistry* **69**, 4271-4274 (1997).
- 205 Hu, X., Tian, J., Xue, Y., Li, Y. & Cui, H. Au Nanorods Decorated Bi<sub>2</sub>WO<sub>6</sub> Nanosheets with Enhanced Near-Infrared Photocatalytic Property Based on Surface Plasmon Resonance Effects and Wide Range Near-Infrared Light Harvesting. *ChemCatChem* (2017).

- 206 Karakoti, A. S., Das, S., Thevuthasan, S. & Seal, S. PEGylated inorganic nanoparticles. *Angewandte Chemie International Edition* **50**, 1980-1994 (2011).
- 207 OckáPark, J. & YongáLee, S. A foolproof method for phase transfer of metal nanoparticles via centrifugation. *Chemical Communications* **52**, 1625-1628 (2016).
- 208 BaniáYaseen, A. Facile phase transfer of gold nanoparticles from aqueous solution to organic solvents with thiolated poly (ethylene glycol). *RSC Advances* **4**, 52676-52679 (2014).
- 209 Parimi, S., Barnes, T. J. & Prestidge, C. A. PAMAM dendrimer interactions with supported lipid bilayers: a kinetic and mechanistic investigation. *Langmuir* **24**, 13532-13539 (2008).
- 210 Boca, S. C. & Astilean, S. Detoxification of gold nanorods by conjugation with thiolated poly (ethylene glycol) and their assessment as SERS-active carriers of Raman tags. *Nanotechnology* **21**, 235601 (2010).
- 211 Lee, S., Anderson, L. J., Payne, C. M. & Hafner, J. H. Structural transition in the surfactant layer that surrounds gold nanorods as observed by analytical surface-enhanced Raman spectroscopy. *Langmuir* **27**, 14748-14756 (2011).
- 212 Santhosh, P. B., Thomas, N., Sudhakar, S., Chadha, A. & Mani, E. Phospholipid stabilized gold nanorods: towards improved colloidal stability and biocompatibility. *Physical Chemistry Chemical Physics* **19**, 18494-18504 (2017).
- 213 Gökce, H. & Bahçeli, S. The molecular structures, vibrational spectroscopies (FT-IR and Raman) and quantum chemical calculations of n-alkyltrimethylammonium bromides. *Optics and Spectroscopy* **115**, 632-644 (2013).
- 214 Tebbe, M., Kuttner, C., Männel, M., Fery, A. & Chanana, M. Colloidally stable and surfactant-free protein-coated gold nanorods in biological media. *ACS applied materials & interfaces* **7**, 5984-5991 (2015).
- 215 Kuo, C.-H., Chiang, T.-F., Chen, L.-J. & Huang, M. H. Synthesis of highly faceted pentagonal-and hexagonal-shaped gold nanoparticles with controlled sizes by sodium dodecyl sulfate. *Langmuir* **20**, 7820-7824 (2004).
- 216 Dutta, A., Paul, A. & Chattopadhyay, A. The effect of temperature on the aggregation kinetics of partially bare gold nanoparticles. *RSC Advances* **6**, 82138-82149 (2016).
- 217 Di Landro, L., Pegoraro, M. & Bordogna, L. Interactions of polyether—polyurethanes with water vapour and water—methane separation selectivity. *Journal of membrane science* **64**, 229-236 (1991).

- 218 Gu, F. *et al.* Luminescent properties of Mn 2+-doped SnO 2 nanoparticles. *Inorganic Chemistry Communications* **6**, 882-885 (2003).
- 219 Schulz, F. *et al.* Effective PEGylation of gold nanorods. *Nanoscale* **8**, 7296-7308 (2016).
- 220 Feng, J. *et al.* Adsorption mechanism of single amino acid and surfactant molecules to Au {111} surfaces in aqueous solution: design rules for metal-binding molecules. *Soft Matter* **7**, 2113-2120 (2011).
- 221 Wright, L. B., Palafox-Hernandez, J. P., Rodger, P. M., Corni, S. & Walsh, T. R. Facet selectivity in gold binding peptides: exploiting interfacial water structure. *Chemical Science* **6**, 5204-5214 (2015).

---

## Closing Remarks

The problem of solar water splitting is now in the insufficient photoelectrochemical conversion efficiency. Even the theoretical efficiency is quite high in semiconductor, the method for the aim is not discovered and unknown. For the highly efficiency photoelectrode, incorporation of plasmonic octahedral gold nanoparticle is essential to overcome the theoretical photoelectrochemical efficiency. The goal is achievable via the profound understanding for plasmon-carrier interaction semiconductor physics over the semiconductor in solar water splitting.

At the first time, I made a simple assumption that shape controlled gold nanoparticle would contribute the photocurrent enhancement of photoelectrode. I have met several adversities to synthesize and attach gold nanoparticles on the semiconductor surface during the journey. For example, unreproducible data at first, measurement errors and analysis of the result would be the part of them. I felt delight when the advancement has observed after the hardships. Through the process, I acquired the technical skills for the experiment and understanding of nanoparticle plasmonics.

I recognized the potential of octahedral gold nanoparticles in various applications. The journey is not finished. The further investigations will be driven from the combination with fellows.

## List of Publications

1. H. J. Gwon, P. Yensil, C. W. Moon, S. Nahm, S. -J. Yoon, S. Y. Kim and H. W. Jang, "Superhydrophobic and antireflective nanoglass-coated glass for high performance solar cells", *Nano Research* 7, 670-678 (2014),
2. S. Y. Moon, C. W. Moon, H. J. Chang, T. Kim, C. Y. Kang, H. J. Choi, J. S. Kim, S. H. Baek, and H. W. Jang, "Comprehensive study on critical role of surface oxygen vacancies for 2DEG formation and annihilation in  $\text{LaAlO}_3/\text{SrTiO}_3$  heterointerfaces", *Electronic Materials Letters* 12, 243-250 (2016), <Co-first>
3. S.Y. Moon, C. W. Moon, H. J. Chang, T. Kim, C. Y. Kang, H. J. Choi, J. S. Kim, S. H. Baek, and H. W. Jang, "Thermal stability of 2DEG at amorphous  $\text{LaAlO}_3$ /crystalline  $\text{SrTiO}_3$  heterointerfaces", *Nano Convergence* 3, 7 (2016), <Co-first>
4. K. C. Kwon, S. Choi, K. Hong, C. W. Moon, Y.-S. Shim, D. H. Kim, T. Kim, W. Sohn, J.-M. Jeon, C. H. Lee, K. T. Nam, S. Han, S. Y. Kim, and H. W. Jang, "Wafer-scale transferable molybdenum disulphide thin-film catalyst for photoelectrochemical hydrogen production" *Energy & Environmental Science* 9, 2240-2248 (2016)
5. J. Choi, S. Park, J. Lee, K. Hong, D.-H. Kim, C. W. Moon, G. D. Park, J. Suh, J. Hwang, S. Y. Kim, H. S. Jung, N.-G. Park, S. Han, K. T. Nam, and H. W. Jang, "Organolead Halide Perovskites for Low Operating

- Voltage Multilevel Resistive Switching", *Advanced Materials* 28, 6562-6567 (2016)
6. D. M. Andoshe, S. Choi, Y.-S. Shim, S. H. Lee, Y. Kim, C. W. Moon, D. H. Kim, S. Y. Lee, T. Kim, H. K. Park, M. G. Lee, J.-M. Jeon, K. T. Nam, M. Kim, J. K. Kim, J. Oh, and H. W. Jang, "A wafer-scale antireflective protection layer of solution-processed TiO<sub>2</sub> nanorods for high performance silicon-based water splitting photocathodes", *Journal of Materials Chemistry A* 4, 9477-9485 (2016)
  7. M. G. Lee, D. H. Kim, W. Sohn, C. W. Moon, H. Park, S. Lee, and H. W. Jang, "Conformally Coated BiVO<sub>4</sub> Nanodots on Porosity-Controlled WO<sub>3</sub> Nanorods as Highly Efficient Type II Heterojunction photoanodes for Water Oxidation", *Nano Energy* 28, 250-260 (2016)
  8. D. H. Kim, D. M. Andoshe, Y. S. Shim, C. W. Moon, W. Sohn, S. Choi, T. L. Kim, M. Lee, H. K. Park, K. T. Hong, K. C. Kwon, J. M. Suh, J. S. Kim, J. H. Lee, and H. W. Jang "Toward High Performance Hematite Nanotube Photoanodes: Charge Transfer Engineering at Heterointerfaces", *ACS Applied Materials & Interfaces* 8, 23793-23800 (2016)
  9. C. W. Moon, S. Y. Lee, W. Sohn, D. M. Andoshe, D. H. Kim, K. Hong, and H. W. Jang, "Plasmonic Octahedral Gold Nanoparticles of Maximized Near Electromagnetic Fields for Enhancing Catalytic Hole Transfer in Solar Water Splitting", *Particle & Particle Systems Characterization* 34, 1600340 (2017) <Cover>

10. M. G. Lee, C. W. Moon, H. Park, W. Sohn, S. B. Kang, S. Lee, K. J. Choi, H. W. Jang "Dominance of Plasmonic Resonant Energy Transfer over Direct Electron Transfer in Substantially Enhanced Water Oxidation Activity of BiVO<sub>4</sub> by Shape-Controlled Au Nanoparticles", *Small* 13, 1701644 (2017), <Co-first> <Cover>
11. J. H. Choi, Q. V. Le, K. T. Hong, C. W. Moon, J. S. Han, K.C. Kwon, P. R. Cha, Y. W. Kwon, S. Y. Kim, and H. W. Jang "Enhanced endurance organolead halide perovskite resistive switching memories operable under an extremely low bending radius", *ACS Applied Materials & Interfaces* 9, 30764-30771 (2017)
12. J. S. Han, Q. V. Le, J. Choi, K. Hong, C. W. Moon, T. L. Kim, H. Kim, S. Y. Kim and H. W. Jang "Air-stable cesium lead iodide perovskite for ultra-low operating voltage resistive switching", *Advanced Functional Materials*, Accepted (2017).
13. C. W. Moon, J. S. Park, S.-P. Hong, W. Sohn, D. M. Andoshe and H. W. Jang "Anchoring Electric-field Amplifying Plasmonic Octahedral Gold Nanoparticles via PEGylation on Au (111) Facet", In preparation (2017)

## **Research interest**

- Synthesis of shape-controlled Au nanoparticles
- Functionalization of plasmonic gold nanoparticles
- Au NPs decoration methods for decoration on semiconductors
- Plasmonic photoelectrodes for solar to chemical fuel conversion
- 2-dimensional electron gas (2DEG) & plasmon interaction
- Active plasmonics
- Plasmon enhanced gas sensor
- Colorimetric plasmonic sensor
- Finite-difference time-domain simulation (FDTD) for electromagnetic field

## 국문초록

### 물분해 응용을 위한 팔면체 금나노입자 표면 기능화

가시광선영역에서의 국부적 표면 플라즈몬 공명 (localized surface plasmon resonance, LSPR) 으로 인해서 금속 나노입자는 밴드갭이 큰 반도체 산화물 반도체의 광활성도를 증진시키는 것으로 여겨져 왔다. 그러한 산화물 반도체 물질에서의 광활성도 증가는 열전자 주입 (hot electron injection) 혹은 공명 에너지 전달 (resonant energy transfer) 과 같은 표면 플라즈몬의 완화 (relaxation) 작용들에 기인한다. 그러나, 플라즈몬을 이용한 근거리장 기반 (near-field) 의 물분해 과정의 자세한 것들은 아직 잘 이해 되어있지 않다. 현재까지 연구되어온 플라즈몬 금 나노입자/산화물 반도체 계면은 금 나노입자의 반도체 표면의 작은 부피로의 빛 한정작용 (light confinement) 및 표면 전자 밴드 구조 (bandstructure) 변화로 인해 광활성도 증가에 있어서 큰 가능성을 보여주고 있다. 모양 조절된 나노 입자는 강한 밴드간 전이 (interband transition) 와 밴드 내 전이 (intraband transition) 으로 인해 반도체의 흡수 파장 경계 (absorption edge)의 위와 아

래에 겹쳐질 수 있어, 산화물 반도체 물질 적용을 통한 물분해 시스템에 적용을 위해 필수적이다.

이 졸업논문은 플라즈몬을 통해 향상된 산화물 반도체 기반 태양광 물분해 시스템에 대해서 3개의 챕터에서 다루고 있다. 첫번째 챕터는 국부 플라즈몬 공명 (LSPR) 에너지 이상의 밴드갭 에너지를 가진 산화물 반도체에 국부 플라즈몬 공명 (LSPR)을 보이는 팔면체 금 나노입자를 붙여 태양광 물분해 효율을 증진시키는 연구를 담고 있다 (주로  $\text{TiO}_2$ ). 두번째 챕터는 비슷하지만, 국부 플라즈몬 공명 (LSPR) 에너지 이하의 밴드갭 에너지를 가진 산화물 반도체에 국부 플라즈몬 공명 (LSPR)을 보이는 팔면체 금 나노입자를 붙여 태양광 물분해 효율을 증진시키는 연구를 담고 있다 (주로  $\text{BiVO}_4$ ). 마지막 챕터는, 높은 표면 입자 밀도를 가진 (high-coverage) 팔면체 입자를 물에서 유기로의 상변화 (phase transfer) 를 통한 리간드 변환 (ligand exchange) 을 통해 산화물 반도체 표면에 코팅하는 방법을 다루고 있으며 이를 적용하여 (111)표면으로 인해 리간드 변환이 잘 되지 않던 팔면체 나노입자를 균일하게 코팅에 성공하여 광전극  $\text{BiVO}_4$ 의 이론 효율을 넘는 광특성을 가진 전극을 얻었다.

첫번째 챕터에서는 모양 조절된 금 나노입자의 큰 밴드갭 산화물 반도체에 적용해 물분해 광활성도를 밴드갭 이하의 에너지보다 밴드갭 이상의 에너지에서 효율 증진을 이끌어내는 결과를 담고 있다. 연구를 통해 플라즈몬 완화 (relaxation) 작용을 통해 형성된 열정공(hot hole)의 산소 발생 전위로의 주입이 반응 속도를 결정하게되는 중요한 과정이라는 것이 밝혀졌다. 연구에서 제안된 잘 정돈된 표면 모서리 및 꼭지점으로부터의 열정공 주입의 컨셉은 여러 광촉매 반도체 입자 시스템에 적용 가능하며, 새로운 플라즈몬 기반의 광촉매 시스템에 응용 가능하다.

두번째 챕터에서는 모양 조절된 입자의  $\text{BiVO}_4$  산화물 반도체의 적용을 통한 플라즈몬 기반 물분해 효과를 확인하고자 하였다. 모양 조절된 팔면체 입자 도입을 통해 상당히 크게 향상된 광활성도를 가진 광전극을 얻을 수 있었다. 팔면체 금 나노입자- $\text{BiVO}_4$  산화물 반도체 구조를 통해 물이 분해되는 전위인 1.23 V vs. RHE에서  $2.4 \text{ mA/cm}^2$ 의 광전류를 얻었으며 이는 팔면체 금 나노입자가 없는 경우에 비해 3배정도의 증가 효과를 보이는 것이다. 이 값은, 국부 표면 플라즈몬 진동 (LSPR)을 이용한 어떠한 기준에 보고된 논문보다 높은 값이다. 이 높은 광전류는 표면 직접 전자 전

달 (direct electron transfer, DET)과 플라즈몬 기반 공명 에너지 전달 (plasmon resonant energy transfer, PRET) 에 기반한다. 적당한 반도체 밴드갭을 생각할 때, 플라즈몬 기반 공명 에너지 전달 (plasmon resonant energy transfer, PRET) 과정은 직접 전자 전달 (direct electron transfer, DET) 과정을 뛰어넘어 발생할 수 있다. 이러한 모양 조절된 입자로부터의 물분해 효율 증진은 다른 적당한 반도체 밴드갭을 가진 산화물 반도체에 적용이 가능하다. 이 연구는 새로운 플라즈몬 기반 태양광 물분해를 연구하는데 좋은 시스템이 될 수 있다.

마지막연구는, 금 나노입자의 가장 큰 장점이 플라즈몬 형성을 통해 빛 에너지를 효율적으로 바꿀 수 있다는 가장 큰 장점에서 시작한다. 플라즈몬이 감쇄하면서 (decay) 열 생성, 근거리장 세기 증가 (near-field enhancement), 열전자 주입 (hot electron injection) 그리고 공명 에너지 전달 (resonant energy transfer)과 같은 여러 작용을 할 수 있다. 모양이 조절된 팔면체 나노입자는 이 과정을 극대화 할 수 있는 가능성을 가지고 있다. 실용적인 응용을 위해서는 진공 증착법에 의해 만들 수 있는 금 나노입자에 개수에 필적할 수 있도록 금 나노입자를 꾸밀 수 있는 높은 표면 밀도

(high-coverage)의 금 나노 입자 부착 방법이 요구된다. 이를 위해서는 리간드 변환 (ligand exchange)을 통한 금나노입자의 표면 기능화가 요구되는데, 특히 팔면체 금 나노입자 같은 경우에는 (111) 표면에 매우 밀집되어 (densely-packed) 붙어있는 CTAB 물질 이중층 때문에 이 과정이 잘 일어나지 않는다. 세번째 주제에서는 산화물 반도체 나노구조에 높은 표면 밀도를 가지고 금 나노입자를 부착하기 위해, 이 문제를 해결하기 위한 과정이 담겨있다. 물에서 유기 (에탄올-디클로로메탄 혼합액, ethanol-dichloroethane mixture) 로의 상변화 (phase transfer) 를 통해 Thiol로 기능화 된 polyethylene glycol (PEG) 의 팔면체 금나노입자 (111) 표면에 효과적으로 부착하는 과정이 활성화 되었다. 이런 과정을 통해 얻어진 기술을 BiVO<sub>4</sub>표면에 적용해 보았고, 이 결과는 광전극의 이론적 수치를 넘는 효율을 가진 광전극의 제작이 가능하게 하였다. 이 결과는 미래 금 나노입자 응용에 큰 영향을 줄 것으로 예상된다.

**키워드:** 광-물분해, 플라즈몬, 국부 표면 플라즈몬, 플라즈몬 기반 광-물 분해, 팔면체 금 나노입자, 촉매작용 홀 전달, 열전자 주입, 공명 전자 전달, 표면 PEG 기능화, thiol 작용기로 기능화된 PEG, (111)면, 리간드 변환, FDTD 시뮬레이션

**학번:** 2012-23142

**문천우**